
Electronic Thesis and Dissertation Repository

4-27-2023 2:00 PM

In vivo multi-modal imaging approaches for cancer, stem and immune cells

Nourhan Shalaby,

Supervisor: Scholl, Timothy J., *The University of Western Ontario*

Joint Supervisor: Ronald, John A., *The University of Western Ontario*

A thesis submitted in partial fulfillment of the requirements for the Doctor of Philosophy degree
in Medical Biophysics

© Nourhan Shalaby 2023

Follow this and additional works at: <https://ir.lib.uwo.ca/etd>



Part of the [Medical Biophysics Commons](#), [Medical Cell Biology Commons](#), and the [Medical Molecular Biology Commons](#)

Recommended Citation

Shalaby, Nourhan, "In vivo multi-modal imaging approaches for cancer, stem and immune cells" (2023).
Electronic Thesis and Dissertation Repository. 9275.
<https://ir.lib.uwo.ca/etd/9275>

This Dissertation/Thesis is brought to you for free and open access by Scholarship@Western. It has been accepted for inclusion in Electronic Thesis and Dissertation Repository by an authorized administrator of Scholarship@Western. For more information, please contact wlsadmin@uwo.ca.

Abstract

Introduction: Molecular imaging allows for non-invasive longitudinal visualization of cellular functions *in vivo*. This area of research has provided better understanding of fundamental molecular and biochemical processes, enabled optimization of pre-clinical and clinical assessments for new treatments, and allowed for more accurate and early detection of many pathologies. Extensive research for novel imaging techniques and emerging technologies have rapidly advanced the field. However, an ideal single imaging modality or approach does not exist. Alternatively, multi-modal imaging approaches are commonly applied to overcome limitations of individual technologies. In this thesis, we design, develop, validate, and image various cell tracking systems using complementary multi-modal imaging approaches such as bioluminescence imaging (BLI), magnetic resonance imaging (MRI), magnetic particle imaging (MPI), and positron emission tomography (PET) to maximize the strengths of each technology. **Methods and Results:** First, we develop a multi-modal imaging approach to track breast cancer cells in a safe, sensitive, and quantitative manner *in vivo*. We have subsequently optimized and applied our multi-modal system further to visualize mesenchymal stem cells (MSCs), a clinically-relevant cell type, with more sensitivity. Furthermore, we have validated this imaging approach in an emerging cellular immunotherapy for the treatment of a rodent model of ovarian cancer. Specifically, using a safe dual human reporter-gene imaging approach, breast cancer cells were detectable in mice with PET and MRI - two clinical imaging modalities. Next, MSCs were genetically modified with a PET reporter gene and labelled with iron oxide nanoparticles for longitudinal imaging with clinical PET and sensitive MPI. Finally, we demonstrate chimeric antigen receptor natural killer (CAR-NK) cells slowed tumor progression in an ovarian cancer model using BLI, and were able to track

the CAR-NK cells using reporter-based BLI and PET. **Conclusion:** The studies reported in this thesis contribute new multi-modal non-invasive molecular imaging tools to track various cell types in preclinical models to reveal complementary information on cell localization, proliferation, viability, and therapeutic response. Continued development of the clinically-relevant imaging tools we have built for tracking MSCs and CAR-NK cells may one day provide valuable information on cell therapy response/non-response or side effects in individual patients – important goals in the era of precision medicine.

Keywords

Molecular imaging, Positron Emission Tomography, Magnetic Resonance Imaging, Bioluminescence Imaging, Magnetic Particle Imaging, cellular tracking, Mesenchymal Stem Cells, breast cancer, ovarian cancer, natural killer cells, immunotherapy, reporter genes

Summary for Lay Audience

Traditional imaging primarily focuses on imaging structural changes in the body. Molecular imaging (MI) allows one to visualize particular molecules and cells in the body in a non-invasive and sensitive manner and works by labeling of cells of interest with imaging labels to enable their visualization with various imaging scanners. There are many applications of these approaches, ranging from better understanding of basic cellular-cellular interactions and functions, to providing more knowledge on new medicine, as well as extending to earlier diagnosis of many diseases. In this thesis, we use MI approaches to non-invasively track cancer cells, stem cells, and immune cells in a safe, sensitive, and quantitative approach using numerous imaging technologies: positron emission tomography (PET), magnetic resonance imaging (MRI), bioluminescence imaging (BLI) and magnetic particle imaging (MPI). The first cell system we describe uses safe genetic modifications of breast cancer cells to enable their detection with MRI and PET longitudinally. Next, we combined MPI and PET to track stem cells, a therapeutic cell type, to allow for sensitive cell tracking for a long time after their implantation into mice. Finally, we combined BLI and PET to track a novel cellular immunotherapy that was able to successfully treat ovarian cancer in mice. This thesis adds to the rapidly growing field of non-invasive detection of cells in the body to better understand where they localize, if they persist, expand, die, or how they interact in preclinical models.

Co-Authorship Statement

This thesis is presented in an integrate article format. Chapters 2 and 3 are adapted from manuscripts that have been published in peer-reviewed journals and Chapter 4 is adapted from a study in preparation for submission. Nourhan Shalaby was the first author on the aforementioned manuscripts and was involved in all aspects of manuscript preparation (study design, data collection, data analysis and interpretation, manuscript compilation).

Chapter 2 is adapted from the original research article, titled “A Human-Derived Dual MRI/PET Reporter Gene System with High Translational Potential for Cell Tracking” by Shalaby, N., Kelly, J., Francisco, M., Fox, M., Qi, Q., Thiessen, J., Hicks, J., Scholl, T.J., Ronald, J.A. *Molecular Imaging and Biology*. 2022 April 24 (2): 341-351. This study was designed by NS, TJS, and JAR. Data acquisition was performed by NS with help from JK, FM, MF, and QQ. Results were analyzed and interpreted by NS, with input from TJS and JAR. All authors edited and reviewed the manuscript. This study was supervised by TJS and JAR.

Chapter 3 is adapted from the original research article, titled “Complementary Early-Phase Magnetic Particle Imaging and Late-Phase Positron Emission Tomography Reporter Imaging of Mesenchymal Stem Cells In Vivo” by Shalaby, N., Kelly, J., Sehl, O.C., Geavert, J.J., Fox, M., Qi, Q., Foster, P., Thiessen, J., Hicks, J., Scholl, T.J., Ronald, J.A. *Nanoscale* January 2023. This study was designed by NS, TJS, and JAR. Data acquisition was performed by NS, with help from OCS, JJG, JK, MF, and QQ. Results were analyzed and interpreted by NS, with input from TJS and JAR. All authors edited and reviewed the manuscript. This study was supervised by TJS and JAR.

Chapter 4 is currently in preparation for submission, titled “Non-invasive imaging of a HER2-specific CAR NK-92 cell immunotherapy with Bioluminescence Imaging (BLI) and Positron Emission Tomography (PET)” by Shalaby, N., Xia, Y., Kelly, J., Sanchez, R.P., Martinez, F., Fox, M., Qi, Q., Thiessen, J., Hicks, J., Scholl, T.J., Ronald, J.A. *Manuscript in preparation*. This study was designed by NS, TJS and JAR. Data acquisition was performed by NS, with help from YX, JK, RPS, FM, and MF. Data were analyzed and interpreted by NS with input from TJS and JAR. All authors edited and reviewed the manuscript. This study was supervised by TJS and JAR.

Acknowledgments

I would like to express my utmost gratitude for the privilege of having been a PhD student at Western University, where I had the opportunity to work in the esteemed Department of Medical Biophysics, under the joint supervision on Dr. John Ronald and Dr. Timothy Scholl. The past few years have been an exceptional journey, during which I have had the honor of working with brilliant scientists, acquiring professional and personal skills, and creating unforgettable memories with exceptional colleagues.

I wish to acknowledge the individuals below for their significant impact on my academic and research growth, as well as my personal and professional developments, and overall graduate school experience.

Dr. John Ronald, I am extremely thankful for your consistent guidance, supervision, and mentorship. You have created and fostered a welcoming environment in the lab that made my training and learning experiences enjoyable. Your passion for science is both inspirational and contagious, and I aspire to have such passion in my future endeavors. I am deeply grateful that you provided me with the opportunity to work in your lab despite my lack of wet lab experience at the time, and for allowing me to be a part of your team, which ultimately became like family. Thank you, John.

Dr. Timothy Scholl, I would like to express my appreciation for your invaluable expertise, guidance, enthusiasm and constructive feedback throughout the past few years. I am particularly grateful for your continuous support and availability, even amidst your busy schedule. Your ability to view problems from different perspectives, critically analyze work

and creatively troubleshoot has been an inspiration to me. I hope I have learned some of those traits from you. Thank you, Tim.

Dr. Francisco Martinez, I can't thank you enough for your contributions to this work. First, for your assistance with MRI, both theoretical and practical. Moreover, I am deeply appreciative of the numerous instances where you have gone above and beyond to assist me with problems outside the scope of your job description. Your expertise, patience, and kindness have been instrumental in helping me navigate many challenging situations throughout the past few years. Lastly, I would like to thank you for bringing your delightful garden flowers to work, which were a source of joy during challenging times. Thank you, Paco.

Dr. John Kelly, I am immensely grateful for the support and guidance you have provided during this academic journey. Your expertise has been fundamental in developing my research skills, and your endless patience in answering all my questions is really appreciated. You are an incredible research associate with so much dedication. I also really cherish your willingness to listen when I needed to vent. Finally, I must thank you for the delightful baked goods you often bring in, which are always delicious. Thank you, JK.

Dr. Ying Xia, I am grateful for your kindness and invaluable assistance, especially throughout my NK project. Your leadership in initiating the NK set up in the lab was crucial to the success of my project. Thank you for your support and guidance with experimental planning as well as your help with the animal work.

I want to thank Dr. Rafael Sanchez, for his insightful feedback and innovative ideas which have elevated my data. Raf, your meticulous attention to detail and thoroughness have provided invaluable input to my work.

I would like to extend a special thanks to Dr. Amanda Hamilton for the exceptional mentorship in teaching me wet lab and 2+ skills. Thank you, Amanda.

I would like to express my deepest gratitude to my advisory committee members for their invaluable support and guidance throughout my academic journey. Your mentorship has been critical to the success of my projects, and I am honored to have had the opportunity to learn from exceptional scientists. Dr. Donna Murrell, I want to thank you for your support, positive feedback, and encouragement since the beginning. I also want to express my admiration for you as a role model for women in the medical physics field. Dr. Jonathan Thiessen, I am thankful for the opportunity to work under your supervision at St. Joseph's hospital. I am particularly grateful for your dedication to attending my presentations and providing me with invaluable feedback that has helped me improve my work.

A special thanks to Dr. Charles McKenzie, for their role as the department chair and Dr. Paula Foster for leading the Molecular Imaging program. Thank you for being a great mentor, and always lightening up the mood. I am appreciative of all your efforts with CMIG. Dr. Aaron Ward, while you were not my direct supervisor, you have always been my mentor. I am particularly thankful for the time you took to assist me with my residency applications. I can't thank you enough for your words of encouragement and how they have motivated me to keep going when times were tough. You have been one of the most influential individuals in my PhD journey.

The PET colleagues: Dr. Matthew Fox, I appreciate your assistance with all things PET related, from scheduling, and last-minute cancellations, accommodations to our non-traditional image acquisitions and experimental set up, and your help with image analysis. Dr. Qi Qi: I am grateful for all the times you went out of your way to ensure my experiments went as smoothly

as possible. Thank you for taking time out of your schedule to help me with the gamma counter, and PET experiments. Many thanks to Dr. Justin Hicks for developing the tracer for all our PET experiments. A special thanks to Dr. Savita Dhanvantari for giving me access to the lab space. This work is not possible without all of you.

My amazing (past and present) lab colleagues, Dr. Katie Parkins, Nivin Nystrom, and Dr. Tian Duo Wang: You have set the standards exceptionally high for everyone in this lab and I am thankful for your mentorship and grateful for everything you have taught me. Veronica Dubois, Xin Yue Wang, Melissa Evans, Shirley Liu, Josephine Tan, Sean McRae, Jerry Fu. You have all contributed to an unforgettable experience in my graduate school journey and I am really excited to see where you all venture out. Julia Gevaert, Natasha Knier and Olivia Sehl, thank you for your friendship. I am so grateful you were a part of this experience and for the memories we have made together. I am excited to make more.

I would also like to acknowledge my funding sources from the Natural Sciences and Engineering Research Council, Translational Breast Cancer Regional Unit and Schulich School of Medicine and Dentistry.

Finally, I would like to give a very special thanks to my loved ones who were the ultimate support during this journey. Many thanks to my mother, who is my endless source of power as well as my father, who is the most empathetic listener. Thank you to my incredible siblings for your continuous encouragements, and support. My lifelong friends who have always pushed and encouraged me to go further. You have all been a tremendous support system and I am blessed for having you apart of this experience.

Table of Contents

Abstract.....	ii
Summary for Lay Audience.....	iv
Co-Authorship Statement.....	v
Acknowledgments.....	vi
Table of Contents.....	x
List of Tables	xv
List of Figures	xvi
List of Abbreviations	xxi
CHAPTER 1	1
1 General Introduction	1
1.1 Motivation and Overview	1
1.2 Molecular Imaging.....	3
1.2.1 Cell Tracking	6
1.2.2 Methods to cell tracking.....	6
1.2.3 Cancer	11
1.2.4 Stem cells	14
1.2.5 Immune cells.....	21
1.3 Imaging Modalities	28
1.3.1 Positron Emission Tomography.....	28
1.3.2 Magnetic Resonance Imaging.....	35
1.3.3 Bioluminescence Imaging.....	41
1.3.4 Magnetic Particle Imaging.....	46
1.3.5 Multi-modal imaging	51
1.4 Purpose of thesis	52
1.4.1 Rationale	52

1.4.2	Hypotheses.....	53
1.4.3	Overview of studies	53
1.5	References.....	55
CHAPTER 2		78
2	A Human-derived Dual MRI/PET Reporter Gene System with High Translational Potential for Cell Tracking.....	78
2.1	Introduction.....	79
2.2	Materials and Methods.....	81
2.2.1	Cell Lines and Cell Cultures	81
2.2.2	Cloning and Lentiviral Production.....	82
2.2.3	Cell Transduction.....	82
2.2.4	Western Blots.....	83
2.2.5	In Vitro Gd-EOB-DTPA Uptake and MRI.....	84
2.2.6	In Vitro [¹⁸ F]TFB Tracer Uptake.....	85
2.2.7	Animal Model	86
2.2.8	In Vivo Gd-EOB-DTPA- enhanced MRI	86
2.2.9	In Vivo [¹⁸ F]TFB PET	88
2.2.10	Histology and Immunofluorescence Staining.....	88
2.2.11	Statistics	89
2.3	Results.....	89
2.3.1	In-Vivo Gd-EOB-DTPA- enhanced OATP1B3 MRI: Intravenous (IV) versus Intraperitoneal (IP) Gd-EOB-DTPA administration	93
2.3.2	In-Vivo [¹⁸ F]TFB NIS PET	99
2.4	Discussion.....	101
2.5	References.....	105
CHAPTER 3		112

3	Complementary Early-Phase Magnetic Particle Imaging and Late-Phase Positron Emission Tomography Reporter Imaging of Mesenchymal Stem Cells In Vivo	112
3.1	Introduction.....	113
3.2	Materials and Methods.....	116
3.2.1	Cloning and Lentiviral Production.....	116
3.2.2	MSC Culture and Transduction	116
3.2.3	MSC Iron Labelling	117
3.2.4	In Vitro Magnetic Particle Imaging	117
3.2.5	MPI Image Analysis and Quantification.....	118
3.2.6	Animal Models.....	118
3.2.7	In Vivo Magnetic Particle Imaging.....	119
3.2.8	In Vivo Bioluminescence Imaging	119
3.2.9	In Vivo [^{18}F]TFB Positron Emission Tomography	120
3.2.10	Ex Vivo Staining and Fluorescence Microscopy.....	120
3.2.11	Statistical Analysis.....	121
3.3	Results.....	121
3.4	Discussion.....	131
3.5	References.....	136
	CHAPTER 4	145
4	Imaging CAR-NK cells Targeted to HER2 Ovarian Cancer with Sodium Iodide Symporter-Based Positron Emission Tomography	145
4.1	Introduction.....	146
4.2	Materials and Methods.....	150
4.2.1	Cell Lines	150
4.2.2	Cloning and Lentiviral Production.....	150
4.2.3	Lentiviral Transductions	151
4.2.4	HER2 Analysis.....	152

4.2.5	Cytotoxicity Assay.....	152
4.2.6	Animal Model	153
4.2.7	Fluc BLI of Tumour Burden	153
4.2.8	Antares BLI of NIS ⁺ Antares ⁺ CAR NK cells	154
4.2.9	[¹⁸ F]TFB PET	154
4.2.10	Peritoneal Lavage.....	155
4.2.11	Histology and Microscopy	155
4.2.12	Statistical Analysis.....	156
4.3	Results.....	156
4.4	Discussion	168
4.4.1	Limitations	172
4.4.2	Conclusions.....	173
4.5	References	175
CHAPTER 5	184
5	Summary	184
5.1	Summary and Discussion.....	185
5.1.1	Chapter 2: Clinically translatable dual human-derived PET and MRI reporter genes.....	185
5.1.2	Chapter 3: Early- and Late- Phase Multi-Modal Tracking of Mesenchymal Stem Cells	185
5.1.3	Chapter 4: Imaging a CAR NK cell-based therapy against HER2 ovarian cancer	186
5.2	Challenges and Limitations.....	187
5.2.1	Limitations of reporter genes	187
5.2.2	Lentiviral transduction of genes.....	188
5.2.3	Dose Optimization	189
5.3	Future work.....	190

5.3.1 Optimization of CAR NK therapy	190
5.3.2 CAR design.....	191
5.3.3 Genetic engineering methods.....	192
5.3.4 Safety switches.....	192
5.3.5 Conclusion	193
5.4 References	195
APPENDICES	199
Appendix A: Supplemental Figures.....	199
Appendices B: Permissions.....	212
Appendices C: Curriculum Vitae.....	214

List of Tables

Table 2.1: MRI sequence parameters used for *in vitro* uptake of Gd-EOB-DTPA. 85

Table 2.2: MRI sequence parameters used for *in vivo* mice imaging. 87

List of Figures

Figure 2.1: (A) Diagram of hEF1a-hNIS-T2A-OATP1B3-P2A-zsG lentiviral construct used to engineer MDA-MB-231 triple negative cells. (B) Flow cytometry showing naïve cells with no zsG expression and transduced MRI/PET cells with 93% transduction efficiency post-sort. (C) Fluorescence microscopy images showing no zsG in naïve cells and MRI/PET cells showing zsG fluorescence signal. (D) Western Blots of naïve and transduced cells showing the NIS and OATP1B3 bands at their corresponding sizes (100 and 90 kDa, respectively) and their absence in the naïve cells..... 90

Figure 2.2: (A) An average *R1* map in naïve and MRI/PET cells without and with incubation of Gd-EOB-DTPA. (B) *R1* values (38% higher) in MRI/PET cells incubated with the Gd-EOB-DTPA was found significantly higher ($p < 0.05$) compared to the naïve cells incubated with the agent. (C) [^{18}F]TFB percent uptake was calculated as $0.31 \pm 0.18\%$ in naïve cells, whereas significantly higher uptake was seen in MRI/PET cells ($14.2 \pm 1.3\%$; * $p < 0.001$)..... 92

Figure 2.3: (A) Dynamic coronal *T1*-w MRI images of lower mammary fat pads of an NSG mouse after IV Gd-EOB-DTPA injection. Manual segmentation showing naïve (left; blue outline) and MRI/PET (right; orange outline) tumors pre- and post-IV administration of Gd-EOB-DTPA. (B) Enhanced contrast and higher normalized (to muscle tissue) signal intensities are shown in the MRI/PET tumor. (C) Contrast enhancement was also observed in endogenous tissue and clearance into the intestines. 94

Figure 2.4: (A) Dynamic coronal *T1*-w MRI images of lower mammary fat pads of an NSG mouse after IP Gd-EOB-DTPA injection. Manual segmentation showing naïve (left) and NIS-OATP1B3 (right) tumors pre- and post-IP administration of Gd-EOB-DTPA. (B) Higher normalized (to muscle tissue) signal intensities are shown in the NIS-OATP1B3 tumor compared to the naïve tumor. (C) Contrast enhancement was also observed in the liver. 96

Figure 2.5: (A) Representative *T1*-weighted MRI images showing pre- and approximately 5 hours post- IV (top) and IP (bottom) injection of Gd-EOB-DTPA in two different mice. (B) Contrast enhancement observed in MRI/PET tumors post- Gd-EOB-DTPA injection, with both IV and IP administration methods. No contrast enhancement was observed in the naïve tumors

post agent administration. Significantly higher average signal intensity between MRI/PET tumors and naïve tumors was observed, for both IV and IP agent administration and no significant difference in average signal intensity between IV and IP delivery methods was observed for either naïve or MRI/PET tumors (n=3) at 5 hours post injection. 98

Figure 2.6: (A) Dynamic MAPs showing whole body PET coronal images and uptake of [¹⁸F]TFB for 40 minutes. (B) Average SUV (g/mL) for 3 mice at different time points showed significantly higher for MRI/PET tumors compared to naïve tumors (p<0.05) using repeated measures of ANOVA. (C) Displaying [¹⁸F]TFB uptake in NIS-expressing tissue (salivary glands, thyroid, stomach), MRI/PET tumor (denoted with arrowhead), and the bladder ([¹⁸F]TFB clearance). 100

Figure 3.1: A) The genetic constructs containing (top) the zsGreen fluorescent gene followed by the cleaving peptide T2A and then then PET reporter gene NIS; and (bottom) the tdTomato fluorescent gene followed by T2A and the BLI reporter gene Akaluc. Flow cytometry showing naïve non-transduced MSCs (B), initial transduction with the lentiviral plasmid containing zsG-NIS (C), and second transduction with the lentiviral plasmid containing tdt-Akaluc (D). Microscopy showing unlabeled MSCs (E.) and MSCs labelled with Synomag-D® (>95% labelling efficiency) (F.) at 40x. 122

Figure 3.2: *In-vivo* detection of MSCs in the left hind limb with MPI (top), BLI (middle) and PET (bottom) in a representative mouse over a 30-day period. MPI shows the brightest signal on day 0 and steadily decreases over time. BLI signal shows reduced radiance on day 9 (likely due to cell death), followed by an increase in BLI signal thereafter. ¹⁸F-TFB PET SUV shows a similar pattern to BLI radiance at the comparable imaging timepoints of the engineered MSCs (arrows). ¹⁸F-TFB uptake also present in thyroid and stomach (organs with endogenous NIS expression). Imaging data in the graph on the right are for this mouse. 124

Figure 3.3: A) MPI-measured iron content (mg) decreased monotonically over time for all 5 mice. B) Average BLI radiance (p/sec/cm²/sr) showed slight initial decrease over first 15 days and then increased over remaining experimental timepoints in 3 mice. BLI radiance in the remaining 2 mice remained low at all timepoints after the initial decline. Note the scale is divided into low and high-value ranges for the BLI data. C) ¹⁸F-TFB PET SUV values (g/mL) exhibited the same trends as BLI for individual mice (i.e., mice with high BLI signal at a

particular timepoint had high PET SUV values, and vice versa). (D-F) MPI, BLI, and PET measurements normalized to their initial measurement, respectively. (G-I) Grouped averages of the normalized data. Error bars represent +/- SD. G) a significant decrease of MPI signal at all imaging timepoints compared to day 0 was found ($p < 0.001$; $n = 5$). H) due to the high variability in BLI data across mice, significant differences over time were not found. I) significant increases in SUV values between MSC-injected hind limbs and control hind limbs were found on days 10, 17 and 30 ($p < 0.05$; $n = 3$). 126

Figure 3.4: MPI (A) and BLI (B) signal from early imaging timepoints (days 0-9 post MSC injection), and correlational analysis of this data (C). ^{18}F -TFB PET SUV values (D) and BLI signal (E) from later imaging timepoints (days 10-30 post MSC injection), and correlational analysis of this data (F). 128

Figure 3.5: A) PPB iron staining with nuclear fast red counter stain of a control limb showing striated muscle cells and B) MSCs shown as darker and more dense cells with intracellular iron (white arrow) surrounded by muscle cells (black arrow) of the hind limb tissue harvested post-mortem (day 30). C) and D) show the DAPI staining of control and MSC cells, respectively. E) and G) shows the absence of tTomato and zsGreen fluorescence in the control hind limb, while F) and H) show the presence of both fluorescence signals in the MSC-injected limb. 130

Figure 4.1: A) Lentiviral construct used to engineer SKOV3-ip1 ovarian cancer cells containing the human elongation factor 1 alpha promoter (pEF1a) to drive expression of tdTomato (tdT) and Firefly luciferase (Fluc) separated by a T2A peptide sequence. Flow plots showing $\text{Fluc}^+\text{tdT}^+$ SKOV3-ip1 cells (B) without or with HER2 immunostaining. C) Flow plots showing naïve SKOV3-ip1 and $\text{Fluc}^+\text{tdT}^+$ SKOV3-ip1. D) Lentiviral constructs used to engineer NK-92 cells. Describe constructs. E-H) Flow plots confirming the expression of zsG and Antares in NK-92 cells engineered with both constructs in D. I) Cytotoxicity assays by BLI-Fluc showing various levels of ovarian cancer killing upon co-culturing of $\text{Fluc}^+\text{tdT}^+$ SKOV3-ip1 with NK cells at different effector to target ratios. Naïve NK and zsG^+NIS^+ NK effectors showed no significant difference in cancer killing at all ratios, while CAR Antares⁺ NK and NIS^+ Antares⁺ CAR NK cells showed more cancer killing (significantly higher than non-CAR-expressing NK effectors), especially at higher ratios (J.). There was no

significant difference in killing abilities between CAR Antares⁺ NK and NIS⁺ Antares⁺ CAR NK effector cells (J)..... 158

Figure 4.2: A) Experimental design of mouse studies. B) Fluc BLI images of tumor burden from a representative mouse from each cohort (PBS, Naïve NK and NIS⁺ Antares⁺ CAR NK). C) Average Fluc BLI radiance from all mice showed significantly lower tumour burden in mice receiving NIS⁺ Antares⁺ CAR NK cells compared to both other control cohorts at day 14, 18, 23 and 28 (*p<0.05). D) Kaplan-Meier curve analysis showed significantly increased survival in mice receiving NIS⁺ Antares⁺ CAR NK cells compared to mice receiving PBS or Naïve NK cells (***p<0.001). 161

Figure 4.3: A) Longitudinal Antares BLI images of a representative mouse receiving NIS⁺ Antares⁺ CAR NK cells. B) Average radiance from Antares BLI images from all mice receiving NIS⁺ Antares⁺ CAR NK cells. Ceasing daily injections of IL-2 at day 35 resulted in stable Antares BLI signal from NIS⁺ Antares⁺ CAR NK cells. C and D) ¹⁸F[TFB] PET images of control mice (CM) receiving sham (PBS) injections and treated mice (TM) receiving NIS⁺ Antares⁺ CAR NK cells on day 27 post cancer cell inoculation. ¹⁸F[TFB] uptake is noted in NIS-expressing tissues and clearance routes (salivary glands (SG), thyroid (Th.), stomach (St.) and bladder (Bl.)) shows uptake of ¹⁸F[TFB]. Additional ¹⁸F[TFB] uptake is noted in the peritoneal of all mice receiving NIS⁺ Antares⁺ CAR NK cells. E) Significantly higher peritoneal PET signal (SUV) was measured in mice receiving NIS⁺ Antares⁺ CAR NK cells compared to mice receiving PBS injections (*p<0.05). 163

Figure 4.4: A) Peritoneal lavages performed with PBS injections into the peritoneal space followed by aspiration to collect and assess cellular composition. B) Control mouse receiving PBS injections showed larger cancer mass (white arrow) and ascites (blue arrow) within the peritoneal spaces. D) Mouse receiving the NIS⁺ Antares⁺ CAR NK cell therapy showed smaller tumour mass (white arrow) and no signs of ascites. C and E) Flow cytometry assessment of peritoneal lavage fluid showed tdTomato positive cells in both mice with additional zsGreen positive cells only in the mouse receiving the NIS⁺ Antares⁺ CAR NK cell therapy..... 165

Figure 4.5: Tissue sections of tumour masses (A-B) and ovaries (C-D) stained with Hematoxylin and Eosin (H&E) of a control mouse and a mouse receiving the NIS⁺ Antares⁺ CAR NK therapy. Fluorescence images showing DAPI (nuclei; E-H), TdTomato

(Fluc⁺tdT⁺SKOV3-ip1 cells; I-L), zsGreen (NIS⁺ Antares⁺ CAR NK; M-P), and the merged images (Q-T). ZsGreen positive cells are shown on the periphery of the ovaries in mice receiving the NK therapy (T). Few zsG positive cells are seen infiltrating inside the ovaries.

..... 167

List of Abbreviations

ADCC	Antibody dependent cell mediated cytotoxicity
Akaluc	Akaluciferase
ASC	Adult stem cells
ATP	Adenosine triphosphate
BLI	Bioluminescence Imaging
CAR	Chimeric antigen receptor
Cas9	CRISPR-associated protein 9
CRISPR	Clustered regularly interspaced short palindromic repeats
CRS	Cytokine release syndrome
DNA	Deoxyribonucleic acid
E:T	Effector to target
eDHFR	Escherichia coli dihydrofolate reductase enzyme
FDG	Fluorodeoxyglucose
FLI	Fluorescence imaging
Fluc	Firefly luciferase
Gd-EOB-DTPA	Gadolinium ethoxybenzyl diethylenetriamine pentaacetic acid
GFP	Green fluorescent protein
GvHD	Graft versus host disease
HER2	Human epidermal growth factor receptor 2
HSV-tk1	Herpes simplex virus- thymidine kinase 1

ICANS	Immune effector cell-associated neurotoxicity syndrome
ICG	Indocyanine green
IM	Intramuscular
IP	Intraperitoneal
iPSC	Induced pluripotent stem cells
IV	Intravenous
MAP	Maximum activity projection
MIP	Maximum intensity projection
MOI	Multiplicity of infection
MPI	Magnetic particle imaging
MPIO	Microparticle iron oxide
MRI	Magnetic resonance imaging
MSC	Mesenchymal stem cells
NIS	Sodium iodide symporter
NK	Natural killer
NSC	Neural stem cells
NSG	NOD scid gamma
OATP1B3	Organic anion transporter polypeptide 1B3
OSEM	Ordered subset expectation maximization
PAI	Photoacoustic imaging

pEF1 α	Human elongation factor-1 alpha promoter
PET	Positron emission tomography
PPB	Pearl Prussian blue
PSMA	Prostate specific membrane antigen
RF	Radiofrequency
ROI	Region of interest
SNR	Signal to noise ratio
SPECT	Single photon emission computed tomography
SSRT	Somatostatin receptor
SUV	Standardized uptake value
tdT	tdTomato
UPSIO	Ultra-small superparamagnetic iron oxide
US	Ultrasound
zsG	zsGreen

CHAPTER 1

1 General Introduction

The goal of this thesis is to develop complementary multi-modal imaging approaches that provide important knowledge of the fate of implanted cells *in vivo*. These methods show the benefit of using multiple imaging technologies for different applications, namely cancer and cell-based therapy tracking as well as assessing therapeutic efficacy for cancer therapies. Chapter 1 provides a focused overview of molecular imaging (MI), different approaches used to accomplish cell tracking that have been performed pre-clinically and clinically in cancer, stem, and immune cells. Finally, this chapter provides a brief introduction into the imaging modalities that were used in this thesis. The background provided in this chapter introduces the studies within this thesis.

1.1 Motivation and Overview

Cell-based therapy is the administration of cells to treat or fight a disease. Globally, there are currently 58 approved cell-based therapies used for oncological, neurological, cardiological, inflammatory and regenerative applications. The clinical and commercial success of these living drugs has caused great interest in the development of novel cell therapeutics, with hundreds of cell-based products currently in clinical trials (clinicaltrials.gov). However, there are many hurdles facing these therapies along the path to clinical translation, mainly associated with the development, manufacturing, and safety of the cell therapy. One particular challenge hindering the clinical integration of cell therapies is the limited knowledge on their fate post administration into patients. This is a major obstacle as it is essential to understand if the therapy has reached its target site, and if so, in what amounts. Furthermore, patients may be non-responsive or may respond differently to the cell therapy. In severe cases, some patients may experience adverse effects to these therapeutics. Thus, to accelerate the implementation of these promising living drugs,

methods to non-invasively visualize these therapies over their entire existence once they are in the body are needed. While different methods to visualize cell therapies are being performed in clinical practice (discussed in chapter 1), they lack sensitivity and do not provide complete insight into the effects of cell therapies in the body. Thus, the focus of this thesis is to develop cell labeling techniques that can accomplish non-invasive imaging of cells in the body to provide safe, sensitive, quantitative information using multi-modality imaging technologies. We develop a cell tracking system in chapter 2 that utilizes human-derived reporter genes which are safe, sensitive and provide quantifiable information on gene-modified breast cancer cells, rendering them detectable with two widely used clinical imaging modalities (PET and MRI). This system has high clinical translatability in that it uses human-derived reporter genes with a clinically approved probe and contrast agent to provide information on the cells location(s), proliferation, and intratumoral distribution. The PET part of this system was then introduced into a therapeutic cell type and optimized to include a labeling method that is highly sensitive and quantifiable. This labeling system enabled tracking of mesenchymal stem cells which are used clinically for the treatment of many pathologies. A multi-modal imaging approach, with PET and MPI, is used for longitudinal tracking of the stem cells for the entirety of their *in vivo* lifespan. Such labeling technique has the potential to report to clinicians on the success or failure of cell-therapy administration, provide information on the number of therapeutic cells delivered successfully, and report on the cell therapy's *in vivo* persistence and survival. In chapter 4, we used PET and optical imaging together in another multi-modal imaging approach to visualize a cellular immunotherapy in an ovarian cancer disease model and evaluate the response of the therapy in treatment of the disease. These works validate the use of multi-modal detection systems to successfully visualize cell fate in the

body in a non-invasive and sensitive approach that can track cells over the span of their in-vivo persistence.

1.2 Molecular Imaging

Molecular imaging (MI) is a field that combines molecular biology and biomedical imaging to non-invasively visualize cellular and subcellular processes within living subjects to provide information on proliferation, apoptosis, localization, distribution, and cell-cell interactions [1]. Advancements in the field of MI are attributed to innovations in imaging technologies, development of novel imaging agents, and optimization of molecular and cellular labeling techniques, such as evolving tools for genetic engineering. MI can extend knowledge beyond information provided by in-vitro or ex-vivo biopsy or standard cell culture laboratory techniques, in a non-invasive, sensitive, and quantifiable manner.

Applications of MI have included both preclinical and clinical functions. Pre-clinical MI in animal models has become an integral step in the development and evaluation of novel targets, probes, contrast agents and drugs prior to their clinical implementation. With a focus on cancer, these studies have aided in finding new molecular targets for cancer imaging and therapy. Furthermore, MI can enable non-invasive imaging of cancer cells to not only provided better understanding of disease mechanisms and its progression (*i.e.*, metastasis) but can also assist in disease screening to facilitate early diagnosis and improve interventions, and thus patient outcomes [2]. MI of cell-based therapies (*i.e.*, immune or stem cells) on the other hand aims to monitor treatment response and to better evaluate therapeutic efficacy or assess any potential side effects.

In the clinic, MI techniques have been accomplished with computed tomography (CT), positron emission tomography (PET), single photon emission computed tomography (SPECT), magnetic

resonance imaging (MRI), and ultrasound (US) in applications such as oncology, neurology, cardiology, and musculoskeletal diseases [3].

The ideal criteria for clinical MI applications includes safe non-toxic, bio-compatible and highly specific labels which are also reversible, and can report on the cells of interest for the entirety of their lifespan [4]. Additionally, MI benefits from modalities capable of sensitive and quantitative detection of probes that interact with the target at pico- or nanomolar concentrations [5]. Thus, sensitive nuclear imaging techniques (PET and SPECT) have been at the forefront of MI as they provide sensitive and quantitative whole-body imaging. Moreover, many targeted radiopharmaceutical agents for both SPECT and PET are available for both imaging and theranostic purposes. However, radionuclide imaging is expensive, involves ionizing radiation and unless coupled with another modality (CT or MRI), is associated with either limited spatial resolution or lack of anatomical context [5]. In recent years, MI has extended and advanced beyond the field of nuclear medicine and now other imaging technologies such as MRI, optical imaging and ultrasound are being employed. Anatomical context with MRI offers superb spatial resolution, unlimited depth penetration with exceptional soft tissue contrast [5]. However, MR imaging of targets with micromolar concentrations is challenging and requires enhancements from the labels, usually with the aid of contrast agents (i.e., positive or negative contrast agents). Optical techniques such as bioluminescence and fluorescence are also effective modalities for molecular imaging. Optical techniques are extremely sensitive with detection of agents at the pico- and even femtomolar concentrations [6]. Specifically, for BLI and near-infrared (NIR) fluorescence imaging, a low background is observed, providing enhanced signal-to-noise (SNR) ratios. However, a key limitation for optical imaging is the limited resolution and depth penetration due to light scatter and attenuation by tissues which is why optical imaging techniques have been

primarily used for research in preclinical models [6]. Nonetheless, there are several areas in which optical molecular imaging can translate to clinical applications, with current clinical applications restricted to surface (skin), intraoperative, or ocular imaging [7]. Pre-clinical optical imaging has been used to assess contrast agents, test novel drugs, and to better understand basic biological processes. However, clinical translation of optical imaging approaches still requires refinement of the instrumentation and assessment of contrast agents. Ultrasound is another appealing molecular imaging strategy that is relatively inexpensive, is non-ionizing, safe, and offers real-time high-resolution images which are widely used for anatomical and functional imaging. Contrast-enhanced ultrasound mainly involves the use of micron-sized gas-filled bubbles which can recognize and bind to inflamed or highly vascularized cancer cells [8]. For example, in 2017, Wijkstra, *et al.*, developed the first clinical grade contrast agent for US targeting the vascular endothelial growth factor receptor type 2; VEGFR2, associated with neoangiogenesis in many cancers [9]. While microbubbles provide sensitive detection (in picomolar concentrations) and have additional therapeutic capabilities, they suffer from poor stability caused by core gas diffusion across the cell [10].

While each modality has its strengths and weaknesses, combining imaging systems for cell tracking has been a common approach that has been shown to provide a more holistic overview on the cells of interest and has shown to be more complementary than competitive. In this thesis, cell tracking is accomplished via multi-modal imaging approaches to visualize various cell types (cancer cells, stem cells and immune cells) and report on their fate post administration in preclinical models.

1.2.1 Cell Tracking

The use of medical imaging techniques for non-invasive visualization of cell biodistribution and trafficking throughout a living subject, is referred to as cell tracking. Cell tracking provides valuable information for disease progression and diagnosis (i.e., infection and inflammation), fundamental biological mechanisms, as well as the development, evaluation, and optimization of cell-based therapies. Cell tracking has been utilized in many preclinical settings and has enabled understanding of tumour development and metastasis, tracking of cancer cell fate in preclinical animal models, and supported evaluations of cancer therapies. Additionally, cell tracking has many clinical applications in a variety of medical settings (report on patient received dosing, patient response to treatment, or report on possible severe cytotoxicities). Thus, it is essential to fully understand the biodistribution, accumulation, localization of therapeutic cells for both pre-clinical and clinical applications. There are various methods and strategies for cell labeling to enable non-invasive imaging with medical imaging techniques. In the next section, different methods for cell tracking are summarized.

1.2.2 Methods to cell tracking

There are two general methods for cellular tracking: (1) direct labeling and (2) indirect labeling. Direct cell labeling is a relatively straightforward and well-established technique that involves the introduction of a labeling tag into the cell to allow for visualization with a suitable imaging tool. Indirect imaging approaches, also often referred to as reporter gene imaging, typically integrates the reporter gene(s) into the cells genome via either viral or non-viral gene delivery methods. In the following subsections, common direct and indirect labeling approaches will be discussed.

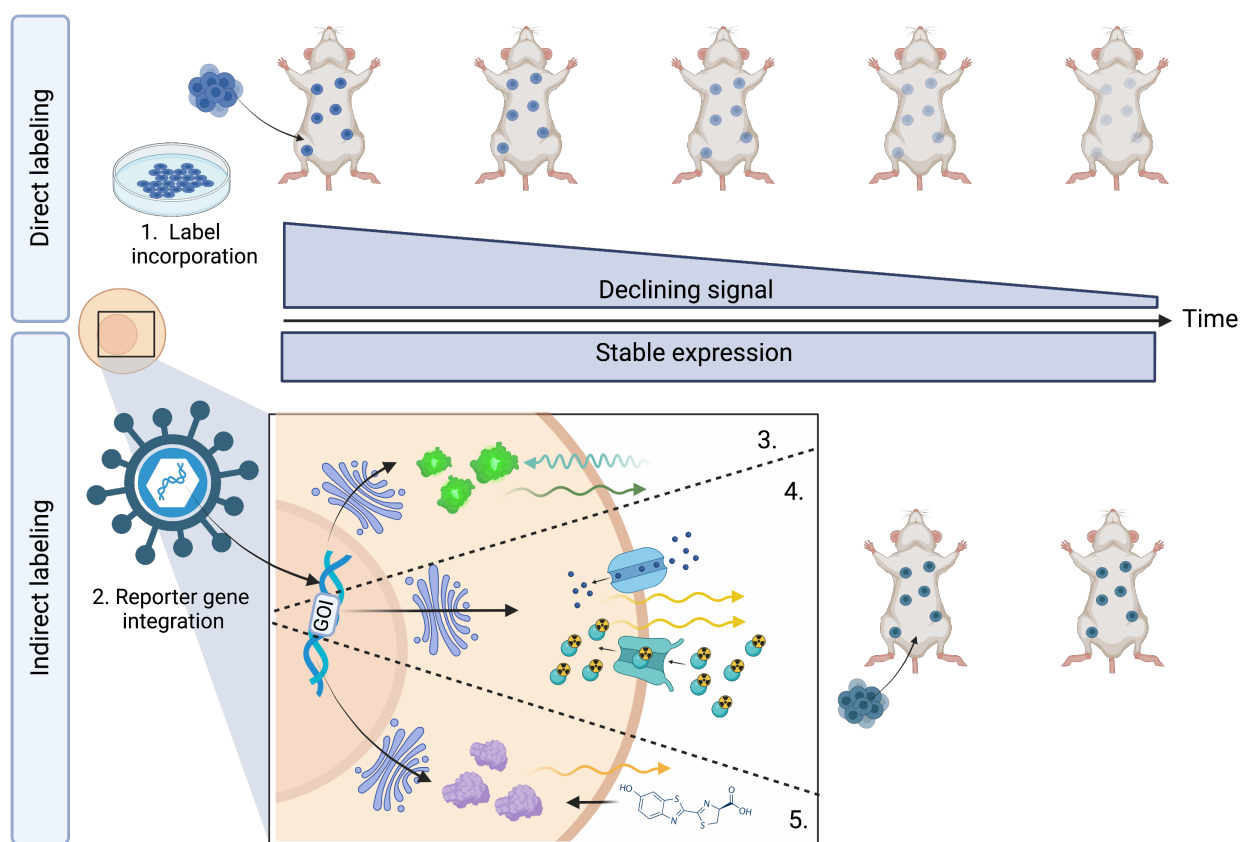


Figure 1.2.1 : Methods of cellular labeling techniques. In direct labeling, probes, contrast agents or tracers are incubated with cells (1) prior to their administration into animal models. Proliferation of labelled cells, or clearance of agent, results in declining signal over time. In indirect labeling techniques, (2) reporter genes are integrated into the cellular genome via lentiviral transductions. Other delivery methods for genetic transfer exist (viral and non-viral methods). Reporter genes can encode for fluorescent proteins which require excitation by photons within a specific range of wavelengths to emit detectable photons (3). Reporter genes can encode for transporters and symporters that uptake specific imaging agents, tracers, or contrast agents to produce a detectable signal (4). Reporter genes can encode to enzymes that catalyze an administered substrate and result in the emission of detectable photons (5).

1.2.2.1 Direct Labeling

In principle, direct cell labeling is a relatively uncomplicated technique that requires a labeling agent (probe) to enter inside a cell, or attach to the cellular membrane, typically via incubation of the labeling probe with the cell. Some cells are labeled by natural processes such as phagocytosis (engulfing the probe) or pinocytosis, direct attachment of the probe to the cell membrane, or uptake of an imaging agent through a transporter expressed on the cell surface. Some cell types require the addition of a labeling agent such as a transfection agent to induce the cell to take up the imaging probe. Once cells are labeled *in vitro*, they can be administered into the subjects and the subject is imaged to enable cell detection *in vivo*. One of the major advantages of direct labeling techniques is that the cells do not require genetic modification (as opposed to indirect labeling discussed in the following section) and thus this approach is commonly used in clinical practice as it poses lower regulatory scrutiny.

Direct cell labeling long been performed in white blood cells with Indium-111 (^{111}In)-oxine or Technetium-99m ($^{99\text{m}}\text{Tc}$)-hexamethylpropylene amine oxime ($^{99\text{m}}\text{Tc}$]HMPAO) to image sites of inflammation with SPECT [11][12]. However, SPECT sensitivity is 2-3 orders of magnitude lower than PET, which makes PET imaging of Fluorine-18- , Copper-64- , Iodine-124- and Zirconium-89- labeled cells more attractive. Furthermore, PET provides superior image quality, sensitivity, spatial resolution, and quantification compared to SPECT. Alternative to radiolabeling, MRI tracking of human cells in the clinic was first reported in 2005, where dendritic cells were labeled with superparamagnetic iron oxides (SPIOs) [13]. Since then, the use of SPIOs has dominated the field of MRI-based cell tracking and has even shown its capability of single cell detection in mice [14]. Nuclei other than ^1H for MRI has been employed for cell tracking. The use of Fluorine-19 (^{19}F) MRI has been used to detect perfluorocarbon nanoparticles (PFCs), or ^{19}F -

labeled cells. ^{19}F -MR imaging of labeled cells produces high specificity, since ^{19}F is not endogenous to the body. Furthermore, ^{19}F detection is quantitative since the ^{19}F content is proportional to the signal generated [15]. While this is an effective technique for cell labeling, its main limitation is low sensitivity [16].

One of the main limitations associated with direct labeling is the potential efflux of the labeling probe from labeled cells over time, which can lead to a reduction in imaging signal, or misinterpretation of the signal. Another drawback of this labeling technique is its restriction in indefinite visualization of labeled cells as the cells proliferate, resulting in imaging agent dilution over time and reduced sensitivity. Also, when cells die the agent may still be present in the extracellular space or taken up by bystander cells. These limitations can result in issues in quantitation and false-positive results which can hinder imaging at time points long after cell injection for evaluation of cell proliferation, activation, or death. Indirect labeling is a labeling approach that can overcome these limitations, and provide quantitative measurements for the entirety of the cell's lifetime.

1.2.2.2 Indirect Labeling

Indirect labeling involves genetically modifying cells by the introduction of a reporter gene into the cell's genome. A reporter gene will encode for expression of a reporter protein, which through different mechanisms, can result in a detectable signal. Most reporter proteins are cell surface receptors/transporters or intracellular enzymes, whereby the use of an injected imaging agent will specifically interact with these proteins, resulting in detectable signal. Reporter proteins can also inherently provide signal (i.e., GFP) or take up endogenous material (such as iron) to provide contrast. Reporter genes have played a major role in MI and have revolutionized non-invasive visualization of many dynamic processes, including cellular tracking, gene replacement therapy,

and protein-protein interactions. The discovery and development of the first reporter gene, the green fluorescent protein (GFP), by Martin Chalfie, Osamu Shimomura and Roger Y. Tsien, received the 2008 Nobel Prize award in Chemistry. GFP is derived from jellyfish *Aequoria Victoria* and has been used as a versatile reporter in many applications (i.e. monitoring gene expression). Since then, many reporter genes have been developed for detection with BLI, MRI, PET, SPECT and PAI [17][18][19][20][21].

The main advantage of incorporating reporter genes in cells is their ability to be inherited by daughter cells, resulting in the stable expression of reporter proteins in the progeny of the original engineered cell. Ideally, this enables imaging for the entire lifespan of the engineered cell and all daughter cells, which can provide information on cell proliferation. It is important to acknowledge that for longitudinal imaging of many reporter genes, repeated administration of the imaging agent is required. Another benefit of using reporter genes, is their ability to report on cell viability since reporter proteins are not expressed by dead cells. For example, the sodium iodide symporter, which can function as a PET reporter protein, is ATP-dependent and will not function in dead cells. Likewise, some, but not all BLI reporter genes require catalytic reactions which are oxygen- and ATP-dependent, thus enabling BLI detection of only viable cells [22]. Despite these advantages, the genetic manipulation of cells is viewed as a challenge in clinical translation. However, with the emergence of genetically modified cellular therapies (i.e., chimeric antigen receptor T (CAR-T) cell therapies), and safer ways to engineer cells, this concern is less of an issue.

Genetic incorporation of the reporter gene into the cell of interest can be accomplished via viral or nonviral methods. Viral delivery of the reporter gene uses the biology of viruses to integrate the reporter gene into the cell's genome. Retroviral and lentiviral methods are the most frequently used methods for genetic alteration of cells, although novel viral mechanisms are developed.

Certain viral integration methods are associated with risks, such as the random integration of the reporter genes within the genome, leading to insertional mutagenesis. However, studies have identified genomic safe harbors which can accommodate incorporation of new genetic material without causing functional perturbations [23][24]. Nonviral gene delivery can be accomplished by numerous strategies, including nanoparticles, polymers, electroporation, chemical vectors or cationic transfection agents [15]. In this thesis, lentiviral transduction methods are used to integrate the reporter genes into the cell of interest. We used reporter genes that are compatible with both preclinical (BLI) and clinical (PET and MRI) imaging modalities. The specifics of the each of the used reporter genes used are discussed in section 1.3. In the next section, cell tracking for cancer, stem and immune cells will be covered.

1.2.3 Cancer

Cancer is a leading cause of death worldwide, responsible for one in six deaths (World Health Organization). The hallmarks of cancer as defined by Hanahan and Weinberg include sustained proliferative signaling, evasion of growth suppression signals, resistance of death, replicative immortality, induction of angiogenesis, activation of invasion and metastasis, reprogramming of energy metabolism, and evasion of immune destruction [25]. While cancer can be a debilitating disease, diagnosis of stage I cancer is associated with >90% 5-year survival [26]. However, cancer metastasis, or the spread of cancer cells from the primary tumour to distant sites, is responsible for 90% of cancer deaths. It is crucial to advance and improve the detection of early cancer to reduce these related mortalities.

Cancer diagnosis is a sequential process that begins with an initial assessment such as a physical examination for detection of palpable tumours (such as in breast or prostate cancer), blood tests to detect abnormal levels of cancer-associated biomarkers (such as prostate specific antigen; PSA),

and biopsies which can assist in the classification and staging of cancer. Imaging is also an indispensable tool for diagnosis and has a key role in cancer screening, staging, treatment monitoring, recurrence, and prognosis. Currently, the main imaging modalities used for cancer imaging and detection are MRI, PET, SPECT, CT, OI, US. Each of these conventional imaging technologies are associated with strengths and limitations which has made way for hybrid or multi-modal imaging. Although these imaging modalities still represent the mainstay of cancer imaging in the clinic, conventional imaging techniques typically detect lesions when they are large (> 1 cm) at which point they consist of approximately $>10^9$ cells [26]. Thus, there is enormous incentive for developing techniques that are more sensitive and specific for early cancer detection using these technologies. The field of MI can have a key role in this setting as it allows for the detection of key molecular targets associated with preliminary stages of metastasis or even prior to metastatic transformation. Furthermore, some MI approaches have shown sensitivity as fine as single cell detection [27][28][29].

1.2.3.1 Tracking cancer cells

Cancer cell tracking with molecular imaging techniques has advanced our understanding of disease progression and its metastasis. Molecular imaging approaches can either target cancer-related processes such as metastasis, proliferation, hypoxia, increased metabolism and inflammation, or cancer-associated markers that are typically overexpressed (i.e., receptors or antigens) [15]. One of the main imaging approaches used for detection of cancer metabolism is ^{18}F -Fluorodeoxyglucose (^{18}F -FDG)- PET. ^{18}F -FDG is a radiolabeled glucose analog that works on the principle that many cancers exhibit a shift in their metabolism as a result of the Warburg effect, thus enhancing cancer cell uptake of ^{18}F -FDG, and enabling detection with PET [30]. The development of radiolabeled nucleoside analogs (i.e. thymidine compounds), which can integrate

into DNA can serve as a means to image cancer cell proliferation [31]. ^{18}F -FDG-PET has other applications for cancer diagnosis, staging, and monitoring therapeutic response in many cancers [32]. However, this technique is not cancer-specific as other pathologies (i.e., infection and inflammation), are also associated with an increase in glucose uptake [33]. A more specific PET molecular imaging approach is targeting tumour-specific antigens, such as the prostate specific membrane antigen (PSMA), which is typically overexpressed in 90-95% of prostate cancers [34]. PSMA-PET has shown more sensitive and specific detection of PSMA positive cancers, compared to ^{18}F -FDG-PET [35].

Optical imaging modalities have also been widely used to elucidate cancer cell trafficking, invasion, angiogenesis, and metastatic development. Bioluminescence imaging (BLI) can be used to detect both the primary tumour as well as the metastatic lesions, which are frequently too small to be detected by macroscopic observations, in live animals. Once cells are genetically engineered to express a luciferase, imaging with BLI can be accomplished. BLI is a technique that uses a cooled-charged device (CCD) camera to image the expression levels luciferase enzymes with an exogenously administered substrate (i.e., a luciferin). Luciferase-expressing cells can be repeatedly imaged with BLI easily with simple substrate re-administration. This technique enables effective temporal evaluation of tumor burden and regression through a course of treatment [36][37][38]. BLI has shown to be an extremely sensitive imaging tool with single cell detection capabilities [39].

Magnetic Resonance Imaging (MRI), along with the use of small molecule paramagnetic agents (i.e., gadolinium-based contrast agents; GBCA) or superparamagnetic iron oxide nanoparticles (i.e., SPIONs) can report on cancer staging as well as different tumour processes such as angiogenesis, invasion and apoptosis [44]. As an example, Ferumoxytol (a SPION) has been used

in MRI to locate lymph node metastases <7 mm in size in patients with prostate cancer. SPIONs were taken up by macrophages which travel to benign lymph nodes to appear dark on T2-weighted MRI, while metastatic lymph nodes showed a paucity of macrophages and appeared bright [45]. Sipkins et al., showed paramagnetic liposomes for the delivery of gadolinium to endothelial markers associated with neovascularization to visualize tumour angiogenesis [46]. Furthermore, molecular biomarkers associated with apoptosis have been linked to both iron oxide nanoparticles or gadolinium to allow for *in vivo* detection of therapy induced apoptosis, assisting in assessing therapeutic response [47][48].

Multimodal imaging approaches to harness the advantages from each technology have also been performed in cancer cell tracking. A technique using ^{99m}Tc -labeled nanoparticles also carrying Gd-chelates was used to image 3D neovascular mapping using SPECT-CT and MRI to improve sensitivity and provide high-resolution characterization of tumour angiogenesis [49]. Other studies have tracked tumour-associated markers overexpressed on cancer cells using a combination of different imaging modalities such as MRI and optical imaging [50][51], or fluorescence, radionuclide and MR imaging [52], or PET and fluorescence imaging [53]. Multi-modal imaging has also been used to track cancer cell metastasis (i.e., using PET and BLI [54], or MPI and BLI [55]), tumour necrosis (i.e., using SPECT and optical imaging [56][57]), and tracking cancer cellular processes, such as response to a cancer therapeutic (i.e., using a trimodal BLI technique [58]). In chapter 2 of this thesis, the viability and proliferation of cancer cells are tracked using two clinically relevant reporter genes for PET and MRI.

1.2.4 Stem cells

Stem cells (SCs) are undifferentiated cells within multicellular organisms that are characterized with a long-term capability for differentiation and self-renewal [59]. Stem cells can be classified

into two types: embryonic stem cells (ESCs), and adult stem cells (ASCs). ESCs are derived from the inner cell mass of pre-implanted embryos while ASCs can be found in various tissues and organs [60]. Stem cells are also classified based on their differentiation capabilities as either totipotent, pluripotent, multipotent, and unipotent. Unlike ESCs, which can differentiate into any cell type (pluripotent), ASCs are multipotent, meaning are more restricted in their differentiation capacity (can differentiate into bone, cartilage and fat). Nonetheless, ASCs can develop into all cell types within one lineage and have had significant applications in the treatment of many diseases such as autoimmune diseases, multiple sclerosis, rheumatoid arthritis, cardiovascular disease, Parkinson's disease, Alzheimer's disease and spinal cord injury. Due to ethical concerns and controversial views with ESCs, ASCs are preferred for stem cell therapies [61]. It is also noteworthy to mention the discovery of induced pluripotent stem cells (iPSCs). In 2006 Shinya Takahashi achieved a breakthrough in stem cell research through the development of iPSCs from fibroblasts, which showed similar properties and differentiation capabilities to ESCs, without the associated ethical dilemmas [62]. However, this thesis will focus on ASCs.

ASCs include hematopoietic stem cells (HSCs), mesenchymal stem cells (MSCs) and neural stem cells (NSCs). Mesenchymal stem cells are one of the most frequently used multipotent stem cell types for cell therapy and clinical applications. MSCs are applicable for a wide variety of pathologies due to unique characteristics they possess. MSCs are trophic and express chemokines and growth factors, such as transforming growth factor-alpha (TGF- α), hepatocyte growth factor, epithelial growth factor (EGF), insulin-like growth factor-1 (IGF-1), and vascular epithelial growth factor (VEGF) to induce proliferation and angiogenesis. MSCs are also immunomodulatory and can also secrete anti-inflammatory proteins such as interleukin-1 (IL-1), IL-2, IL-12, TNF- α and interferon-gamma (INF- γ). This immunomodulatory property is an especially unique feature

of MSCs for transplantation as it reduces the chances of transplant rejection [63]. MSCs also possess anti-apoptotic capabilities which have not been fully elucidated but have been linked to their ability to secrete IL-6 and IGF-1 [60].

There are many stem cell-based therapies available globally, but only a few cord blood-derived blood forming stem cell therapies are FDA approved for use in patients with blood disorders [64]. Currently, there are also more than 3,000 trials involving the use of stem cells in the World Health Organization International Clinical Trials Registry. While stem cell therapies hold promise for many diseases, the FDA has warned against unapproved stem cell therapies as they may be associated with potential risks such as ineffective therapeutic outcome, displacement from the desired site, differentiation into inappropriate cell types, and development into teratomas.

It is not surprising that the potent abilities of stem cells to replenish damaged cells and their wide applicability to regenerative medicine has led to the enormous interest in better understanding their mechanisms for self-renewal and differentiation. Innovative labeling and monitoring strategies have been widely established to track the biodistribution, viability, and proliferation of transplanted stem cells. The next section summarizes common labeling and imaging techniques used to track various stem cells.

1.2.4.1 Tracking stem cells

Stem cell therapy in transplant and regenerative medicine has proven to be effective and promising treatments for many pathologies, as mentioned above. Effective monitoring of stem cells is an essential step in further advancing these therapies in the clinic since most stem cell-based therapies are still in experimental stages. There are several hurdles that need to be overcome for these therapies before routine application in the clinic. Some of these hurdles include: side effects such

as failure of therapy; immune responses and cell rejection; carcinogenesis; differentiation into an undesirable tissue type; delivery route of stem cells; and determination of the ideal dose. In addition, understanding of the biology of stem cells once they are inside the living subject remains a challenge [63].

Along with the advancements in stem cell research, it is also important to develop appropriate methods to track these therapies after their transplantation. Non-invasive tracking of transplanted stem cells provides a means to visualize these therapies to understand their fate and behaviour inside a living subject. Several non-invasive molecular imaging approaches have been previously used to follow stem cells after transplantation, such as SPECT, PET, and MRI. In this section, a summary of different stem cell labeling techniques will be discussed.

Magnetically labeling stem cells with SPIONs for MRI detection has shown several advantages compared to other imaging modalities. MRI lacks ionizing radiation, can provide soft tissue contrast which assists in monitoring accuracy of cell delivery to target tissue, and can provide relatively longer duration of stem cell tracking (days to weeks using iron nanoparticles compared to the short half-lives of radionuclides such as 6 hours for [^{99m}Tc]-HMPAO and 1.83 h for [^{18}F]-FDG) [63]. Furthermore, ionizing radiation of radionuclides can increase DNA damage, stem cell death, or carcinogenesis.

Directly labeling stem cells with magnetic nanoparticles, Fluorine-19, or Gadolinium agents has repeatedly shown to not have adverse effects on the survival, migration, and differentiation of stem cells [63][65][66][67]. The first MRI studies used iron oxide compounds to label stem cells. Iron oxide particles are frequently used in stem cell tracking as they produce a signal void in T2/T2* weighted MR images and have shown sensitive single cell detection [27]. Ferumoxytol, which is

an FDA approved formulation used to treat anemia patients with chronic kidney disease, consists of a solution of superparamagnetic iron oxide nanoparticles and has been repurposed as an MRI cell tracking agent due to its biocompatibility and biodegradability. Ferumoxytol has also been shown to be capable of stem cell detection for weeks to months after transplantation [68]. Castaneda et al. used the transfection agent protamine sulfate (PS) to improve the uptake of ferumoxytol in stem cells and showed as few as 10,000 stem cells in T2-weighted MRI [69]. Using heparin in combination with PS and ferumoxytol to label stem cells has also been shown by Thu et al. and has improved sensitivity to as few as 1,000 labeled cells on T2*-weighted MRI [70]. Importantly, this nanocomplex contained three FDA approved components which facilitated its use as an MRI cell labeling probe. Although negative contrast agents are extremely sensitive, they are difficult to quantify when compared to positive contrast agents [3].

^{19}F is another contrast agent used for MRI cell tracking and has been used in both clinical and experimental studies. This mechanism is more specific than iron nanoparticles since only labeled cells are detectable, and there is no detectable endogenous fluorine signal in the body resulting in little to no background. Perfluorocarbons (PFCs) are compounds containing ^{19}F which have been shown to not possess toxic qualities, even at high doses. Furthermore, ^{19}F is linearly proportional to the MR signal which has significant applications in quantifying stem cells after implantation [71][72]. A study by Gaudet et al. imaged ^{19}F labelled human and mice stem cells with MRI at days 0, 3, 9 and 16 after implantation [72].

Gadolinium based contrast agents (GBCAs) are commonly used for T1-weighted MRI enhancement. More specifically, gadolinium diethylenetriamine pentaacetic acid (Gd-DTPA) is the most frequently used Gd agent in MRI examinations. Gd-DTPA is fast in its elimination in dead or interstitial spaces allowing better separation between viable and necrotic cells. However,

Gd-DTPA is unable to pass through stem cell membrane and studies have developed efforts in other Gd-containing compounds to improve cellular uptake. One modification developed was to complex Gd-DTPA with a positively charged transfection agent called JetPEI, which efficiently labeled MSCs and allowed their detection for up to 14 days post stem cell transplantation [73]. However, it is important to note that there is no apparent relationship between signal intensity and the number of injected cells from these Gd agents.

The use of radionuclides for imaging with PET and SPECT has also been used for stem cell tracking. One of the simplest and most established methods to label and track stem cell distribution is though *in vitro* pre-labeling with the glucose analog 2-deoxy-2- ^{18}F fluoro-D-glucose (^{18}F -FDG), followed by cell implantation and PET imaging. ^{18}F -FDG is taken up and entrapped by cells allowing PET detection. Nose et al. used this ^{18}F -FDG labeling technique to track stem cells with PET in various species using different administration routes and noted that distribution varied based on delivery route, highlighting the potential of this technique to optimize stem cell therapies [74]. Another study by Wolfs et al. wanted to investigate the radiotoxic effects using transmission electron microscopy and determined that the main cellular ultrastructural properties of MSCs were not affected by ^{18}F -FDG labeling [75].

The use of Technetium $^{99\text{m}}$ -hexamethyl-propylene amine oxime [$^{99\text{m}}\text{Tc}$]HMPAO for labeling stem cells is one of the most common methods for SPECT detection. $^{99\text{m}}\text{Tc}$ is a widely used radiotracer used in the clinic for scintigraphy in nuclear medicine. [$^{99\text{m}}\text{Tc}$]HMPAO is a lipophilic complex that internalizes inside the cell and converts into a hydrophilic complex to provide stable labeling of cells for up to 24 hours [76]. Likewise, ^{111}In Oxine (^{111}In Oxine) has also been used to radiolabel stem cells and has shown longer SPECT detection (up to 10 days post cell injection) when compared with [$^{99\text{m}}\text{Tc}$]HMPAO [76][77].

While the MRI, PET and SPECT labels have been invaluable for stem cell research, these probes are not able to report on cell retention of probe, signal loss due to exocytosis and cell division. Thus, reporter gene tracking of stem cells offers a way to longitudinally track these stem cells and their progeny. Moreover, reporter genes can be inserted downstream of a specific promoter that permits gene expression only if the stem cell differentiates into a specific phenotype [78].

Several reporter genes have been used to track MSCs. Sun et al. engineered MSCs with the ferritin heavy chain (FTH) MRI reporter gene whose expression was mediated by a tumour specific promoter. This served to report on MSCs that had undergone malignant transformation, which is a serious limitation of MSC-based therapies [79]. In another study by Wolfs et al., MSCs were engineered with the human sodium iodide symporter (NIS) and imaged mice with PET post ^{124}I administration to track MSCs and their ability to differentiate *in vivo*. The observable drawback of this was the significant efflux of the ^{124}I , although stem cell detection was still achieved [80]. Optical modalities such as BLI, have been applied in various preclinical applications, including tracking adipose-derived stem cell distribution in myocardial infarction mouse models [81], tracking viability and distribution in pancreatectomized mice [82] and tracking activation and differentiation of transplanted stem cells as they graft [83].

Multi-modal imaging of stem cells is also common. Many studies have combined two or even three imaging tools to track the biodistribution, viability, proliferation, and differentiation of stem cells. In one study, the divalent metal transporter 1 (DMT1) was used as a dual-imaging reporter gene to track human stem cells in a rat brain using [^{18}F]-FDG and $^{52}\text{Manganese}$ with PET and MRI, respectively [84]. Other studies have incorporated more than one reporter gene to accomplish multi-modal imaging. Cao et al., transduced murine embryonic stem cells with a triple-fusion reporter gene consisting of firefly luciferase, red fluorescent protein, and truncated thymidine

kinase to assess the viability, proliferation and differentiation [85]. Other studies have tracked stem cells multimodally with direct labeling approaches. Sehl et al., used Ferumoxytol-labeled stem cells to allow for detection with MRI and MPI. ^{19}F -PFC was also administered intravenously for uptake by macrophages to show the relative persistence of both stem cells and macrophages using ^{19}F -MRI [86]. Alternatively, there have been double and even triple luciferase systems which are multiplexed and can catalyze orthogonal substrates which enable BLI detection of stem cells [87][58]. Mezzanote et al., showed the feasibility of using two different luciferase reporter genes (Luc2 and Renilla Luciferase) for dual color and dual substrate BLI tracking of neuronal stem cells [87]. In Chapter 3, multi-modal tracking of mesenchymal stem cells was performed with direct labeling and reporter gene imaging, using MPI, BLI and PET.

1.2.5 Immune cells

Using immune cells for treating a variety of diseases originates from early centuries of history as evident by the fight against smallpox and cowpox [88]. Since then, immune cells have been extensively studied to better understand their biological role. Over the last few years, cancer immunotherapy has been an area of impressive development which has led to novel targets and breakthrough therapeutic approaches.

Immune cells such as T cells, natural killer (NK) cells, dendritic cells (DC) and macrophages, have been used to develop various immunotherapies against different pathologies [89][90]. In this thesis, NK cells were used to develop a cell-based immunotherapy for the treatment of ovarian cancer. NK cells are large granular lymphocytes that belong to the innate immune system and function to control microbial infections and stressed or cancer cells. Primary NK cells are derived from peripheral blood (PB), umbilical cord blood (UCB), or induced pluripotent stem cells (iPSCs) [91]. Primary NK cells are difficult to isolate and expand but several NK cell lines are well

established and commercially available with the NK-92 cell line being the most widely used and first to enter clinical trials [92][93]. The NK-92 cell line is derived from peripheral blood mononuclear cells from a 50-year-old, white male with rapidly progressive non-Hodgkin's lymphoma. NK-92 cells are easier to expand, transduce and result in pure population of cells with less contamination with T cells, when compared with primary NK cells [94].

NK cells are mediated by a set of inhibitory and activation receptors, where inhibitory receptors such as the inhibitory killer immunoglobulin receptors (KIRs) and NKG2A/CD94 receptors maintain the inactive state of NK cells via the constitutive recognition of self-MHC class I molecules, expressed on healthy cells [91]. Activation receptors such as NKG2D, CD16 and natural cytotoxicity receptors (NCRs) and activating KIRs, result in activation of NK cell through the recognition of pathogen-encoded antibodies or proteins. NK activation can be accomplished by several mechanisms. Since MHC-I molecule binding to NK inhibitory receptors inhibit NK function, a downregulation of MHC-I molecules (a common characteristic seen in cancer cells) will trigger NK activation due to this missing-self recognition. Another mechanism to activate NK cells is through their response to proinflammatory interferons ($\text{INF-}\alpha$, $-\beta$, $-\gamma$) or cytokines (IL-12, IL-15 and IL-18). NK cells can also mediate antibody-dependent cellular cytotoxicity (ADCC) where the CD16 of NK cells binds to the Fc portion of various antibodies. ADCC can also be mediated by Fas ligand (FasL) or TNF-related apoptosis-inducing ligand (TRAIL). Upon NK activation, perforins and granzymes are secreted which will trigger apoptosis in target cells. Furthermore, chemokines and cytokines as well as granulocyte macrophage colony stimulating factor (GM-CSF) secreted by NK cells can modulate other immune cell activation.

Although there are several NK lytic mechanisms, cancer cells have evolved different defense mechanisms to evade NK recognition and killing. Tumour cells can upregulate MHC-I molecule

expression [95], release immunosuppressive cytokines (IL-10) [96], and downregulate tumour associated antigens (TAAs) [97]. Thus, NK enhancements to overcome these cancer evasion mechanisms would enhance lytic functions and improve therapeutic response. One effective mechanism to enhance NK recognition and killing of tumour cells is through genetic engineering of a chimeric antigen receptor (CAR). There are a few CAR-based immunotherapies approved by the Food and Drug Administration (FDA) for the treatment of various hematological malignancies.

CARs are synthetic hybrid receptors that comprise of a variable portion of an antibody with the constant portion of a T cell receptor. The single chain antibody variable fragment (scFv) of the CAR is derived from a tumour-specific antibody and serves to target the tumour antigen. Antigen binding domains in CARs are not restricted to scFv. Some CARs have incorporated ligand-based, receptor-based, nanobody-based and designed ankyrin repeat proteins (DARPs) for recognition of tumour cells [98]. The intracellular signaling domain of the CAR is derived from the immunoreceptor tyrosine-based activation motifs (ITAMs) of the T cell receptor (TCR). Upon antigen recognition, intracellular phosphorylation of ITAMs recruits signaling molecules to activate downstream signaling pathways resulting in an immune cell response [99].

There are several generations of CARs with first-generation CARs only containing the CD3 ξ signaling domain subunit derived from the T cell receptor. First generation CARs were not effective in fully activating cells or in complete tumour eradication as they lacked intracellular co-stimulatory domains. Second generation CARs added either CD28, 4-1BB (CD137), ICOS, or OX40 (CD134) co-stimulatory domains to the original CD3 ξ domain of the first-generation CAR which improved immune cell activation [99]. In third generation CARs, two co-stimulatory domains were included in receptor although this did not consistently show an improvement in

cytotoxicity[91]. However different costimulatory molecules resulted in drastically different effector functions. For example, CD28 favored effector memory activation which resulted in quick onset, robust cytolytic performance, and enhanced expansion, while 4-1BB favored central memory cell differentiation which led to higher persistence, safer profile and less exhaustive behavior [91]. There are other efforts to build more effective CARs including the development of CARs to target multiple proteins or TAAs [100][101], CAR-modified immune cells to secrete enzymes, interleukins or chemokines (Armored CARs) [102][103] , or converter CARs which convert an immunosuppressive action into desirable proinflammatory functions [104][105].

1.2.5.1 Tracking Immune cells

Traditionally, most of the information acquired on immune cell fate is obtained with flow cytometry and confocal microscopy [106]. However, flow cytometry is only useful for *ex vivo* samples and does not provide spatial information while confocal microscopy is not readily applicable for real-time *in vivo* monitoring of cells in deep organs, especially in patients. Recent advances in non-invasive molecular imaging strategies are aimed to optimize therapeutic efficacy and maximize safety in preclinical and clinical studies by monitoring biodistribution and functional changes related to viability, proliferation and migration [106].

Preclinically, BLI has been used to track migration of T cells towards inflammation sites [107][108]. FLI has also been used to track the migration of dendritic cells into lymph nodes [109] and track primary macrophages towards inflammation [110]. Optical imaging modalities have also been used to track NK cells with the use of fluorescence [111] and luciferase reporter genes [38] in preclinical models. While these optical tools offer high through-put with the potential for single cell detection, they are limited in spatial resolution, offer poor tissue penetration and are restricted

to preclinical models [112]. Thus, clinical imaging modalities for cell tracking applications have been used to track various immune cells with higher clinical potential.

For decades, labeling immune cells, such as white blood cells (WBCs) with $^{111}\text{Indium}$ and $^{99\text{m}}\text{Technetium}$ has been used to image inflammation with SPECT [112][11][113]. Radiolabeling immune cells with $^{18}\text{Fluorine}$ [114], $^{68}\text{Gallium}$ or $^{89}\text{Zirconium}$ [115] has also been extensively performed to enable sensitive detection and provide temporal biodistribution information with PET and have played a vital role in understanding the treatment response. Nuclear medicine imaging techniques are appealing as they offer highly sensitive information using low radiotracer concentrations (pmol- μmol), provide quantifiable information with unlimited penetration depths [112]. Reporter gene imaging of immune cells with PET has also been performed with the Herpes Simplex Virus 1-thymidine kinase (HSV1-tk) being the first to be used in glioblastoma patients as shown by Sam Gambhir's group [116]. Martin Pomper's group also engineered CAR T cells to express truncated prostate specific membrane antigen (PSMA) which enabled PET detection with ^{18}F 2-(3-{1-carboxy-5-[(6-[^{18}F]fluoro-pyridine-3-carbonyl)-amino]-pentyl}-ureido)-pentanedioic acid, ^{18}F DCFPyL administration [117]. Similarly, Sellmyer's lab engineered CAR T cells to express E. coli dihydrofolate reductase enzyme (eDHFR) which enabled PET imaging with its $^{18}\text{Fluorine}$ substrate trimethoprim (TMP) and showed residency of T cells in the spleen followed by redistribution to targeted lesions [118]. The Somatostatin Receptor 2 (SSRT2) has been engineered into CAR T cells to permit longitudinal PET tracking of cells and has revealed biphasic expansion of T cells at tumour sites [119]. The sodium iodide symporter (NIS) was also engineered on pan-EbB- targeted CAR T cells and showed a 3,000 cell sensitivity with PET when ^{18}F -tetrafluoroborate (^{18}F -TFB) was administered [120]. NIS- labeled CAR T cells were also imaged with SPECT/CT when used with $^{99\text{m}}\text{Tc}$ -pertechnetate [$^{99\text{m}}\text{Tc}$]TCO $_4^-$ [121]. Shortcomings

of SPECT and PET include the use of ionizing radiotracers and limited spatial resolution (4-5 mm for clinical scanners [122] and 1.5-2.5 mm for preclinical scanners [123]).

Unlike PET and SPECT, MRI offers exquisite spatial resolution in images without the use of ionizing radiation. MRI has also been used as a clinical tool to track various immune cells. Engineered CAR NK cells that target HER2 positive mammary tumours have been labelled with ferucarbotran and ferumoxides to allow tracking with MRI revealing sensitivity of 250,000 labeled cells [124]. Moreover, perfluorocarbons (PFC) are FDA approved and have been tagged with Fluorine-19 to label T, NK and DCs to allow detection with ^{19}F MRI, although this technique suffers from lower sensitivity using clinical gradient strength scanners [125][126][127][128].

Several multimodal imaging approaches have been performed to track immune cells to provide more informative results. In 2022, Daldrup-Link's group developed a clinically translatable approach for CAR T cell labeling using iron oxide nanoparticles (ferumoxytol) enabling iron-labeled T cell detection with MRI, photoacoustic imaging (PAI) and MPI. They were able to show successful homing of T cells to osteosarcomas while preserving T cell proliferation, viability and function post labeling [129]. While ferumoxytol is FDA approved, it has shown to be associated with rare but severe anaphylactic reactions. Thus, in December 2022 another group labelled CD70-targeting CAR T cells with a novel MegaPro-nanoparticles (NP) which showed an improved safety profile compared to ferumoxytol. These CD70 CAR T cells were also luciferase-expressing, enabling multi-modal detection with BLI while MegaPro-NP enabled imaging with MRI [130]. Similarly, another study by Simonetta et al., labeled CD19-targeted CAR T cells with a ^{89}Zr -based tracer in addition to engineering CAR T cells with luciferase to allow for detection with PET and BLI, respectively [131].

While many studies have shown cell tracking of various cell types using one or more imaging modality, it is important to consider each modality for its strengths and limitations to select the ideal tool(s) for the desired application. In the following section, a basic overview of the imaging modalities used in this thesis will be discussed.

1.3 Imaging Modalities

1.3.1 Positron Emission Tomography

Positron Emission Tomography (PET) is a clinical imaging technique that provides images of metabolic activity in the body and is widely used in research, monitoring, and diagnosis of many pathologies. PET is extensively used in oncology to noninvasively monitor and stage tumours, determine tumour recurrences as well as observe therapeutic treatment outcomes.

1.3.1.1 Introduction to PET

For image acquisition, patients are injected with a radioactive agent, or a radiotracer, which is designed to target specific cells or tissues of interest in the body. Radiotracers are composed of a positron-emitting radionuclide in conjugation with a targeting moiety. The most frequent positron-emitting radionuclides used in PET include ^{15}O , ^{13}N , ^{11}C and ^{18}F , while less commonly used radionuclides include ^{14}O , ^{64}Cu , ^{62}Cu , ^{124}I , ^{76}Br , ^{82}Rb (rubidium) and ^{68}Ga (gallium), most of which are produced in a cyclotron, except for ^{82}Rb and ^{68}Ga which are produced with a radionuclide generator [32]. By far, the most frequently used radiotracer is [^{18}F]Fluorodeoxyglucose, [^{18}F]FDG, a radioactive glucose analog that reports on sites of abnormal glucose metabolism, a characteristic of typical tumours, termed the Warburg Effect [30]. Typical administered activity is about 10^{13} - 10^{15} labelled molecules. Inside a patient, the positron emitting radionuclide will emit high-energy photons that can escape the body and be detected by a PET scanner.

PET takes advantage of radionuclides that decay through positron emission. When a nucleus is unstable (contains either too many protons or too many neutrons), it will undergo a decay process to achieve a more stable configuration. In the case of proton excess in the nucleus, a proton will

be converted into a neutron releasing a positron (e^+) and a neutrino (ν) in the process (eq.1) [132]. Positron emission decay is the basis for PET imaging.

$$Parent \rightarrow Daughter + e^+ + \nu \quad \text{Eq.1}$$

In accordance with the law of conservation of energy, the energy released by this process is shared between the resulting daughter nucleus, the positron and the neutrino, giving the emitted positron a range of energies possible energies up to a maximum endpoint E_{\max} . The mean kinetic energy of the positron however is about 33% of the maximum energy [132]. After the positron is ejected, it quickly loses its kinetic energy within electron rich tissue, increasing the probability that it will combine with an orbital electron in the tissue. Their masses are converted into electromagnetic energy in a process known as electron-positron annihilation. This results in a combined energy release of 1022 keV. Conservation of momentum results in the division of this energy among two annihilation photons, each with 511 keV, travelling roughly 180° apart. It is the two annihilation photons with their precise geometric relationship that are detected by the PET scanners. This process is shown in figure 1.3.1.1 (E) below.

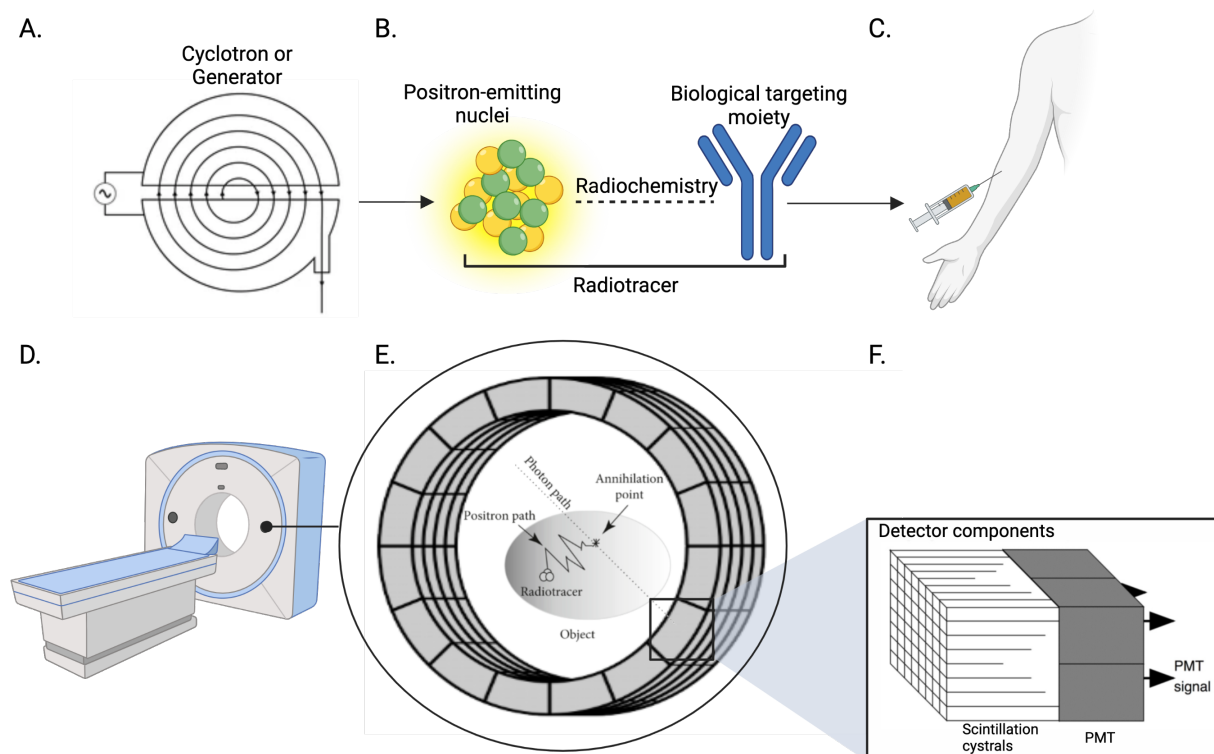


Figure 1.2: (A) A cyclotron or a generator is required for the production of radioactive nuclei which are conjugated with targeting molecules to produce radiotracers (B). Radiotracers injected into patients prior to imaging with PET (C & D). The PET scanner contains a ring of scintillation detectors (E) which can detect the 511 keV photons emitted 180° apart resulting from the annihilation of the positron and electrons (present within the tissue) (E). The positron emitted travels a small distance before combining with an electron. (F) Detector component showing the array of scintillation crystals coupled with the position-sensitive photomultiplier tubes (PMTs).

A PET scanner is designed to collect the simultaneous back-to-back annihilation photons emitted by a radionuclide from a subject. A typical small-animal PET scanner, such as the one used in this thesis, contains a detector ring which comprises 16 detector blocks, each of which contains a row of four lutetium oxyorthosilicate (LSO) detectors, for a total of 64 detectors, with a 16.1-cm ring diameter and a 12.7-cm axial length. Each detector block consists of a 20 by 20 LSO crystal array of 1.51 by 1.51 by 10.0 mm elements. When thousands of annihilation photons are incident on a specific crystal, the software can map the detected photon to the physical location of the respective crystal. Scintillation detectors respond to the absorption of photon energy by emitting visible light, facilitated by impurities within the crystals that alter the energy levels of electrons. This light output is then incident on a photomultiplier tube (PMT), where the visible light is converted to an electronic signal. It is the size of the scintillation crystals that primarily determines the spatial resolution of the PET scanner. Preclinical PET scanners have typical spatial resolutions of 1-2 mm in contrast to approximately 1 cm spatial resolution of clinical scanners [133]. In a typical scan, 10^6 to 10^9 decay events are detected. Mathematical algorithms then construct the corrected events into 3-D image volume. The signal intensity in a particular voxel is proportional to the amount of radionuclide in that voxel, allowing the spatial distribution of radiolabeled tracers to be quantitatively measured. The standardized uptake value (SUV) is a measure of relative tracer uptake in a region of interest and can be calculated based on the precise knowledge of the injection dose, time of injection and weight of the subject [134]. If a series of images are taken over time, the concentration of the radiolabelled molecules as a function of time, can be measured and the rate of specific biological processes, such as cancer, can be determined [132].

While PET has demonstrated high accuracy in diagnosing a variety of infections and inflammatory diseases, it also presents some limitations. Stand-alone PET scanners do not include anatomical

information, and only report on the concentration of radiotracer, which results in difficulty in localizing lesions. Thus, hybrid PET systems typically combine PET with computed tomography (CT) or MRI, which are imaging modalities that complement PET's metabolic information with their high-resolution anatomical information. Another limitation of PET, is that since all radionuclides, independent of the element, result in the emission of 2 photons at the same distinctive energy of 511 keV, it is impossible to distinguish two molecular probes for multiple radionuclide studies [132]. Furthermore, due to the use of radioactive tracers, patients receive radiation exposures. Therefore, it is important for clinicians to evaluate the risks and benefit for each patient prior to performing PET imaging. It should be noted that for most oncological PET indications, the benefit to the patient outweighs the risk of radiation exposure[135]. PET is also relatively more expensive when compared to other imaging technologies. Another limitation of PET is its reduced accessibility in hospitals and clinical settings. There is also the requirement for a nearby generator or cyclotron for production of the short-lived radiotracers, making imaging with PET relatively less feasible compared to other modalities.

1.3.1.2 PET reporter genes

Radiotracer labeling of cells *in vitro* has been the most translatable for cell tracking due to its technique simplicity, sensitivity (with cellular detection limit of 100,000-1,000,000 cells [136]), and a plethora of labeling probes for nuclear medicine have been reported. Despite this, probe labeling of cells is a technique that is limited to short-term cell tracking as the probe will dilute when cells proliferate resulting in reduced imaging signal that is no longer an accurate reflection of cell number, and eventually over time, a non-detectable probe signal. This limitation restricts probe cell labeling techniques to short-term studies for dividing cell populations and could be more useful for non-proliferating or terminally differentiated cell types. Alternatively, genetic

engineering of cells with PET reporter genes that are passed on to daughter cells, allows for long-term cellular tracking.

By far, the herpes simplex virus type 1 thymidine kinase (HSV1-tk) gene and HSV1-sr39tk, its more potent mutated derivative, have been the most used PET reporter genes [7][8]. These viral kinases were originally developed to serve as therapeutic genes as they are able to phosphorylate nucleoside analogues or prodrugs, such as acyclovir, ganciclovir, and penciclovir, administered at pharmaceutical doses [137]. Later, they were utilized as PET reporter genes by radiolabeling the nucleosides, most commonly 9-(4-(18F)-Fluoro-3-[hydroxymethyl]butyl) guanine, [¹⁸F]-FHBG, 2'-fluoro-2'-deoxy-1 β -D- arabinofuranosyl-5-[¹²⁴I]iodouracil, [¹²⁴I]-FIAU, and 2'- [¹⁸F]fluoro-5-ethyl-1-beta-D-arabino-furanosyluracil, [¹⁸F]-FEAU, and administered at non-pharmaceutical doses to allow for PET detection [139]. This reporter gene system has been in development for over 20 years, and more recently the Gambhir group and colleagues were first to report its use for cell based immunotherapy tracking in patients [116]. A major concern for reporter proteins such as the virally-derived HSV1-tk is the non-human origin, which has the potential to trigger an immune response and induce the death of therapeutic cells [140]. This propelled the interest and development of human-derived reporter systems for cell tracking. Doubrovin *et al.* utilized the human norepinephrine transporter (hNET) as a PET reporter gene to track T cells with both SPECT and PET using a clinical grade metaiodobenzylguanidine (MIBG) tracer radiolabeled with either [¹²³I] or [¹²⁴I] [141]. Another PET reporter gene with human-origin is somatostatin transporter 2 (SSRT2), which has limited background expression in the kidneys and cerebrum, making it desirable for detection and tracking cell therapies targeting a variety of tumours [142]. SSRT2 can also serve as a suicide gene when administered with high-energy radioisotopes such as ¹⁷⁷lutetium,

^{90}Y yttrium, or ^{213}Bi bismuth, which would result in the destruction of cell therapeutics in case of cell toxicity.

The prostate-specific membrane antigen (PSMA) has also been used as a human PET reporter gene. PSMA is a transmembrane protein that possesses many properties that make it a desirable PET reporter for cell tracking. It has low background since it is primarily expressed in the prostate, the proximal tubules of the kidney, and the brain. Truncated versions of PSMA have also been developed to prolong PET probe binding and increase imaging sensitivity, showing a detection limit of approximately 2000 cells [117].

Another PET human reporter gene is the human sodium iodide symporter (NIS). NIS is endogenously expressed in the thyroidal tissue, stomach, as well as the salivary glands and functions to actively uptake iodide for thyroid hormone production (T_3 , T_4) [143]. This symporter belongs to a family of more than 60 members in both prokaryotic and eukaryotic species with very high genomic sequence similarity as well as functionality. NIS, as well as many other family members, use an electrochemical Na^+ gradient to drive negatively-charged solutes, such as iodide, into the cytoplasm. Radioiodines, such as ^{123}I and ^{124}I , as well as $^{99\text{m}}\text{Tc}$ Technetium ($^{99\text{m}}\text{Tc}$) have been used for thyroidal imaging of NIS for over half a century [144]. This mechanism inspired the development of NIS as an imaging reporter gene systems for detection with PET and SPECT [145][146][147]. In addition to being a reporter gene, NIS also has the potential to serve as a therapeutic gene when administered with ^{131}I , ^{186}Re , ^{188}Re , ^{211}At [112]. NIS detection with SPECT can also be accomplished by $^{99\text{m}}\text{TcO}_4^-$ radiotracer administration [121]. Imaging of NIS using ^{123}I or $^{99\text{m}}\text{Tc}$ showed limited resolution and sensitivity in detecting low volumes with SPECT, while the use of ^{124}I for NIS/PET detection showed limitations in availability and possess physical properties that are unfavorable, such as complex production, a longer than clinically necessary half-life,

which leads to a larger absorbed dose, low positron yield (23%), as well as high positron energy ($E_{\max}=2.14$ MeV) [144]. Thus, the readily available ^{18}F Fluorine (^{18}F) which has a high positron emission yield (97%), a low positron energy ($E_{\max}=0.634$ MeV), and a clinically-compatible half-life of 110 minutes, is a much more desirable radionuclide for NIS imaging. ^{18}F -tetrafluoroborate, [^{18}F]TFB, was developed in the early 1960's, before the cloning of the NIS gene, and only in the 21st century did it make its way into the clinic with the first [^{18}F]TFB human studies taking place in 2017 [145]. Since then, several studies have used [^{18}F]TFB for imaging NIS with PET for cell tracking applications [147][148][149][150]. In this thesis we exploit the NIS with [^{18}F]TFB for cell tracking with PET.

1.3.2 Magnetic Resonance Imaging

Magnetic Resonance Imaging (MRI) is a non-invasive clinical imaging technology that produces 3D high-resolution images, with detailed anatomical information for a variety of medical applications. MRI has applications for disease diagnosis, detection and treatment monitoring [151] [152]. Many groups have also used MRI for cell tracking applications [153][154][155]. The following section provides an overview of the fundamental basis of MRI and MRI reporter genes.

1.3.2.1 Introduction to MRI

MRI depends on the magnetization of atomic nuclei exposed to radiofrequency (RF) pulses within a large magnetic field. The most frequently used nuclei for conventional MRI is the proton (^1H). There are other less frequently used nuclei for MRI such as ^3He , ^{13}C , ^{19}F , ^{23}Na , and ^{31}P [156]. Each of these nuclei have different nuclear charge distributions, giving rise to a physical property known as a magnetic dipole moment. When placed in an external magnetic field, B_0 the magnetic dipole moments precess around the magnetic field direction. The angles of the cones of precession are slightly skewed along B_0 leading to a net magnetization vector (M_0) along the direction of B_0 . The

nuclei precess about B_0 , with a frequency known as the Larmor frequency, ω , modelled by the following equation:

$$\omega = \bar{\gamma}_n B_0 \quad \text{Eq. 1.3.2.1 [156]}$$

where γ_n is the gyromagnetic ratio for a given nuclei and is proportional to the nuclei's magnetic dipole moment. For protons, $\bar{\gamma}$ is 42.575 MHz/T, which is the largest γ amongst nuclei that might be considered for MRI. When an RF pulse at the Larmor frequency is applied to the ensemble of precessing nuclei, this causes M_0 to be tipped away from B_0 so that they are no longer aligned. In addition, the excited net magnetization precesses around B_0 . In this way, the longitudinal magnetization (M_0) is tipped into the plane transverse from the magnetic field. In a rotating reference frame at the Larmor frequency, the resulting transverse magnetization M_t looks stationary but soon seems to spread out as it is composed of individual spins rotating at slightly different Larmor frequencies due to small differences in their local magnetic fields. This “dephases” M_t causing an exponential decrease in its magnitude. At the same time, the net magnetization of the sample is re-growing along B_0 . It is the precession of the transverse magnetization around B_0 , which results in detectable MRI signal. Tissues are characterized by two different relaxation times. The spin-lattice (longitudinal) relaxation time, T_1 , is the time constant which characterizes the asymptotic regrowth of the longitudinal magnetization after excitation by the RF pulse. More precisely, T_1 is defined as the time it takes for the net magnetization (M_z) to reach 63% of the final magnetization M_0 . T_2 is the transverse relaxation time constant, also called spin-spin relaxation, which characterizes the exponentially dephasing of the transverse magnetization. By definition, T_2 is the time it takes for the transverse magnetization to be reduced

to 37%. Various tissue types, such as fat, water and bone have different T1 and T2 relaxation rates which allows their distinction and produces contrast on the MR image [151].

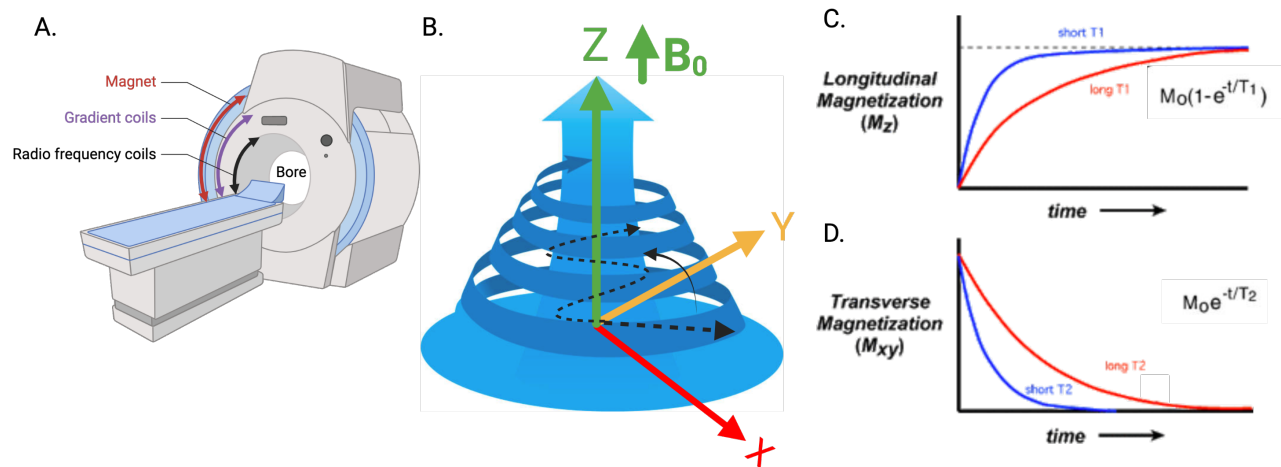


Figure 1.3: A depiction of a clinical MRI scanner including the magnet, the gradient coils, and radio frequency coils (A). A radiofrequency pulse will tip the longitudinal magnetization, M_z away from the magnetic field direction and onto the transverse (xy) plane. When the RF pulse is removed, the magnetization vector (M_{xy}) will dephase and re-align with B_0 . The re-alignment, or relaxation is termed longitudinal relaxation, or T1 relaxation and corresponds of the time required for M_z to grow to approximately 63% of its final M_0 value (C.). Spin-spin relaxation, or T2 relaxation corresponds to the time required for M_{xy} to decay to approximately 37% of the initial values.

Generally, MR images are acquired to highlight differences of tissues related to their intrinsic T1 and T2 values. These images are said to be either T1- or T2-weighted. T1-weighted scans are predominantly resultant from T1 properties of tissue, where tissues with short T1 values (such as fat), appear bright due to their quicker magnetization recovery, while tissues with long T1 values (such as water or air) appear dark. T2- weighted images are determined by T2 tissue properties, where tissues with short T2 (such as fat) appear dark and tissues with long T2 (such as cerebrospinal fluid) appear bright. T1-weighted images are produced by using short time to echo (TE) and Repetition Time (TR) times. TE is the time between the RF pulse delivery and the reception of the echo signal, while TR is the time between successive RF pulse sequences applied to a slice [151]. Conversely, T2-weighted images result from using longer TE and TR times.

MRI contrast agents containing gadolinium or other paramagnetic contrast enhancement agents, such as manganese, can be used to further improve contrast on T1-weighted images. These agents work by shortening the T1 relaxation of protons within the vicinity which results in hyperintense regions on the MR image leading to enhanced contrast. Paramagnetic gadolinium (III) chelates are effective contrast agents due to their unpaired electrons which confer a magnetic moment that confers a high relaxivity to this agent and allowing it to effectively decrease the longitudinal relaxation time (T1) of neighboring tissue to enhance contrast. While many clinical and pre-clinical MRI agents are available, in this work we use a clinically approved agent called, gadolinium ethoxybenzyl diethylenetriamine pentaacetic acid (Gd-EOB-DTPA), clinically known as Primovist ® (Bayer, Inc. Germany).

1.3.2.2 MRI reporter genes

Several MRI reporter genes have been developed to enable longitudinal tracking of different cell populations *in vivo*. MRI reporter genes include genes that translate to enzymes which undergo

catalytic reactions to produce MRI contrast, genes that translate to cell membrane transporters which can uptake contrast agents, or genes that sequester endogenous compounds to produce MR contrast [112]. The majority of MRI reporters rely on negative contrast, or hypointense regions to distinguish labelled cells within the MR image. Such MRI reporter genes include ferritin [157], transferrin [158], tyrosinase [159], and bacterial magnetosomes, magA, genes [160]. The main obstacle with reporters that generate negative contrast on the MRI, is the difficulty in defining labelled cells within regions that are naturally dark on MRI (lungs, lymph nodes). Alternatively, positive contrast MRI reporters have been developed and can overcome this limitation, including a β -galactosidase enzyme [161], a divalent metal transporter (DMT1) [162], and organic anion transporter polypeptides (OATPs) [163]. In this thesis, a specific OATP is used as an MRI reporter gene to enable complementary multi-modal imaging to track cancer cells.

The Organic Anion Transporter Polypeptides are a superfamily of transporter proteins that are expressed on a variety of tissues (liver, kidneys, intestines, brain, and testes) to mediate the uptake of endogenous and exogenous compounds, including hormones and drugs [164]. In humans, the exclusive expression of the OATP1B3 on the membrane of hepatocytes, has been exploited for MRI liver imaging via its uptake of the clinical MRI contrast agent Primovist ® (Bayer) [165]. The analogous rat-derived OATP1A1 transporter was first developed into an MRI reporter system which enabled cell tracking of OATP1A1-expressing cells post gadolinium administration, leading to enhanced contrast on T1-weighted MRI [163]. Other groups extended this mechanism to the OATP1B3 for use as an MRI reporter gene [166][167]. OATP1B3 is advantageous over OATP1A1 mainly due to its human-origins, limiting immunogenic effects. Furthermore, OATP1B3 can uptake several other imaging agents, such as indocyanine green and Indium-111 to

enable detection with photoacoustic imaging [168] or SPECT [163], respectively. In chapter 3, breast cancer cells are engineered to express OATP1B3 to enable their detection with MRI.

1.3.3 Bioluminescence Imaging

Bioluminescence imaging (BLI) is a sensitive optical imaging technique that refers to the process of detecting light emissions from living organisms [17]. This technique, first described in 1995 [169] as a powerful tool for molecular imaging, has enabled non-invasive, real-time imaging of biological processes *in vivo* at relatively low cost. BLI technology has been extensively used to monitor tumour progression and metastasis, transgene expression, infection, gene therapy, as well as track a variety of different cell types [170][171][172][173][174].

1.3.3.1 Introduction to BLI

BLI signal results from visible light that is produced by a catalytic reaction between an enzyme and a substrate. More specifically, oxidation of the substrate (luciferin) mediated by the enzyme (luciferase), emits detectable light peaking at 612 nm, enabling imaging as deep as several centimeters (figure 1.2.2.3 A) [169]. Furthermore, the catalytic reaction is dependent on the presence of ATP and magnesium ions, resulting in specific detection of viable cells.

Since BLI does not require excitation photons, rather an oxidation catalytic reaction cause an electronic excitation that relaxes to result in photonic emissions, minimal background signal is observed in BLI as signal is only generated through enzyme/substrate catalysis. While there may be spontaneous substrate emissions, they are negligible compared to the expected emissions from typical substrates used, resulting in high signal-to-noise ratios [175].

To enable detection of cells with BLI, cells are first genetically modified to stably express a BLI reporter gene. Transgenic cells are then implanted into a pre-clinical model. Upon substrate administration, the catalytic reaction will result in a BLI detectable signal (figure 1.2.2.3 B).

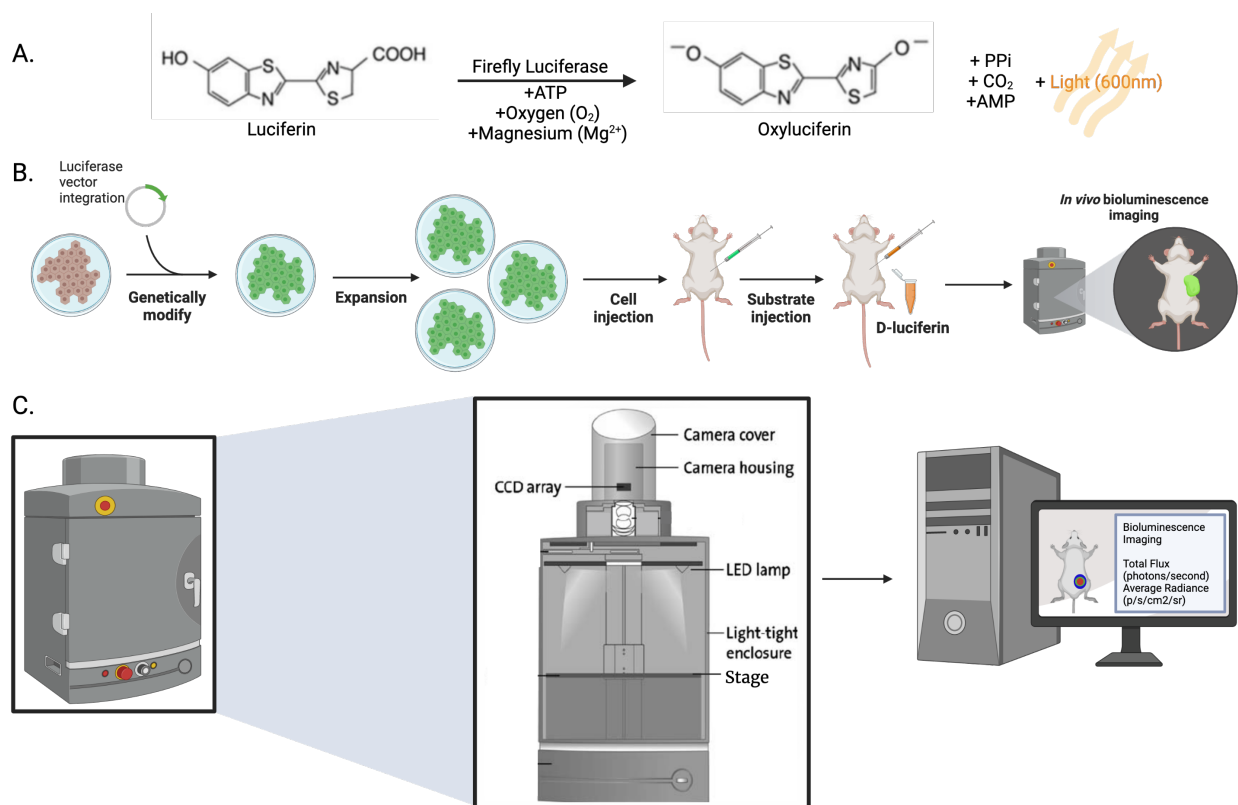


Figure 1.4: (A) The oxidative catalytic reaction of luciferin mediated by luciferase in the presence of ATP, oxygen and magnesium to produce oxyluciferin, PPI, carbon dioxide, AMP, and bioluminescent light (600nm). (B) Cells are genetically modified to incorporate a luciferase gene, expanded and injected into a preclinical model. Upon administration of the compatible substrate (D-luciferin), detectable signal is produced and imaged with BLI. (C) The light-tight enclosure containing the CCD array required for photon to electron conversion, and photon spatial localization connected to a computer for image acquisition and interpretation.

The sensitivity of detecting the emitted photons depends on several factors, including the expression levels of the reporters, the depth of the labelled cells in the model (travelling distance of photons), as well as the sensitivity of the imaging system. Typical BLI detection systems involve a bench-top light-tight box containing a sensitive charged coupled device (CCD) imaging sensor which can detect bioluminescent photons. CCDs convert emitted bioluminescent photons into photoelectrons in the photoactive region of the sensor. The array of photoelectrons are read out by shift registers and converted to a voltage signal for digitization. CCDs are typically cooled to reduce their thermal noise and reduce image background signal. These imaging sensors are connected to a computer for image acquisition, reconstruction, and analysis (figure 1.2.2.3 C).

While BLI is successful in many molecular imaging applications, there are some limitations associated with this modality. One major limitation is the wavelength-dependent detection of emitted photons through the animal tissue. Generally, a 10-fold loss of photons occurs with every centimeter depth of tissue [17]. This results in less detection of photons coming from deeper tissue and brighter signal from light closer to the surface. Bioluminescent light can also be attenuated, through absorption (mainly by hemoglobin) and scatter by surrounding tissue, leading to reduced detectable signal and spatial location.

It is also important to consider the biochemical limitations of BLI. Due to the oxygen and ATP-dependent catalytic reactions, insufficient availability of any of the reagents or administered substrate, via reduced vascularization and poor oxygenation, can result in an underestimate of true signal, providing semiquantitative information. Furthermore, the non-human derivation of these BLI reporters may pose immunogenicity effects [176]. These restrictions limit BLI imaging to preclinical applications and severely hinder the translatability of BLI reporters into clinical settings.

1.3.3.2 BLI reporter genes

Many bioluminescence reporters (enzyme and substrate pairs) have been identified in natural biological systems. The first discovered BLI reporter is Firefly Luciferase (Fluc), derived from the North American firefly (*Photinus pyralis*). Other BLI reporter systems have been derived from organisms including jellyfish (*Aequorea*), sea pansy (*Renilla*; RLuc), corals (*Tenilla*), and click beetle (*Pyrophorus plagiophthalmus*). While Fluc is the most commonly used reporter with an emission peak at 612 nm at 37°C and a quantum yield of 0.41, it has a low oxidation catalytic rate of 1.6 reactions per second [175]. For *in vivo* imaging, emission above 600 nm is ideal as longer photons avoid absorption by hemoglobin and enable deep tissue imaging. NanoLuc (Nano Luciferase), on the other hand, is derived from shrimp *Oplophorus* and has a catalytic rate that is approximately 100 times faster than Fluc, but has peak emission at 460 nm. An ideal luciferase would combine high enzymatic rates, red shifted emissions for deep tissue imaging, and produce optimal brightness. Akaluc (Aka Luciferase) and its substrate Akalumine-HCl were engineered from Fluc and D-Luc, respectively to produce more sensitive BLI signal. Akalumine-HCl is an analog to D-Luciferin while Akaluc is a mutated version of Fluc, resulting in significantly higher signal (52-fold more sensitive than Fluc) [177]. Akalumine-HCl catalysis results in emitted light in the near-infrared range (650 nm) resulting in better detection from deeper tissues, compared to blue and green photon-emitting substrates [177]. Fusion of luciferase-luciferin pairs with electron accepting molecules, such as fluorescent proteins, is a rapidly growing area of research which enables deep tissue imaging of living subjects. Bioluminescence Resonance Energy Transfer (BRET) is the transfer of energy between luciferase-luciferin pairs and an energy accepting chromophore to develop red-shifted fusion proteins that are less affected by light attenuation and scattering [178]. An example of such fusion is Antares, a fusion protein of two orange-red

fluorescent proteins, CyOFP1, to a blue-emitting luciferase, NanoLuc. Antares enables sensitive and deep tissue BLI tracking in-vivo when administered with its optimized substrate fluoroflurimazine (FFZ).

1.3.4 Magnetic Particle Imaging

Magnetic Particle Imaging (MPI) is an emerging non-invasive imaging technology that was first introduced by Gleich and Weizenecker in 2005 [179]. While MPI uses similar hardware to that of MRI, the physics and imaging concepts are different. MPI has been very promising in molecular imaging applications due to its ability to directly quantify and map the distribution of nanoparticles. MPI has been used for disease imaging and monitoring in applications including cardiovascular[180], lung perfusion imaging [181], cancer diagnosis [182], and stem cell labeling[183]. The next section discusses the basics of MPI, and different probes used in MPI cell tracking.

1.3.4.1 Introduction to MPI

MPI uses external magnetic fields to exploit the unique properties of superparamagnetic iron oxide nanoparticles (SPIOs) to produce 3D images of high contrast and high sensitivity with high spatial and temporal resolution [184]. Although magnetic nanoparticles are primarily used to shorten T2 relaxation rates in MRI to produce hypointense contrast (as mentioned in section 1.3.2), SPIOs can be exploited for their superparamagnetic characteristics to produce positive contrast in MPI. Furthermore, endogenous tissues are diamagnetic and thus appear transparent in MPI. This results in “hot spot” tracer detection of SPIO-labelled cells only to produce an image with virtually no background and excellent positive contrast, similar to radiotracer detection in nuclear medicine [185].

MPI is composed of two permanent opposing magnets which produce a strong magnetic field gradient everywhere besides a single field free point (FFP). In response to the non-zero externally applied magnetic field, SPIOs produce a nonlinear magnetization, as a result of their higher order harmonics of their excitation frequency, and are considered “saturated”. However, nanoparticles within the field free region (FFP) are unsaturated and will generate harmonics that contribute to the MPI signal detected since the receiver coil can only detect time-varying magnetizations and thus only SPIOs in the FFP are detected. To cover the imaging field of view (FOV), the FFP rapidly scans throughout the sample to generate a full tomographic image of SPIOs distribution [186]. The MPI signal is proportional to the nanoparticle concentration which results in a quantitative image of nanoparticle distribution.

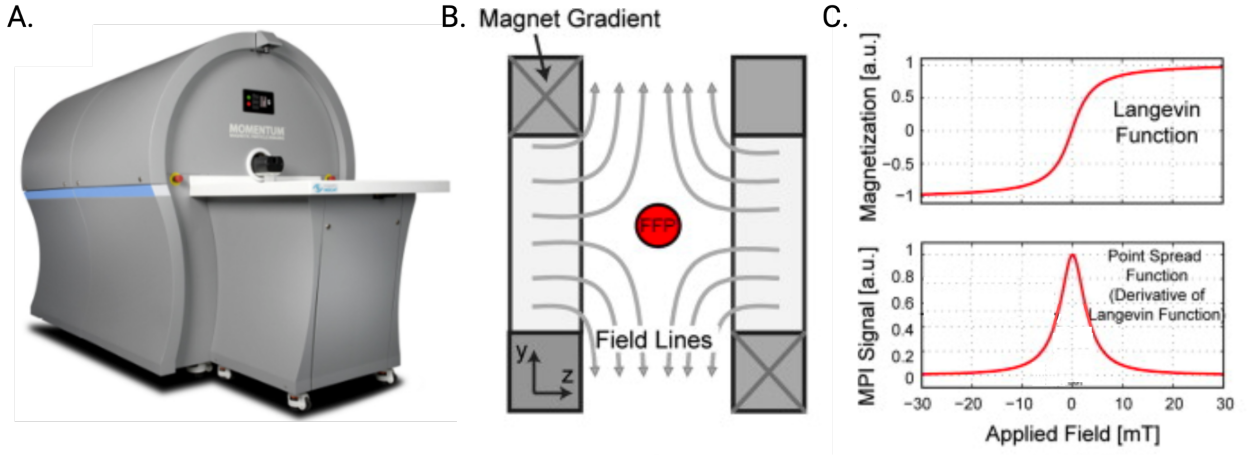


Figure 1.5: (A) MPI preclinical scanner. (B) Two opposing magnets generating a strong magnetic field gradient and a field free point (FFP). (C) SPIO magnetization produces a nonlinear (Langevin function) response to the magnetic field gradient. The unsaturation of the SPIOs in the FFP is detected by the receiver coil to generate the MPI signal. The MPI signal is modeled by a point spread function (derivative of the Langevin function). Figure adapted from [187].

The image quality of other medical imaging technologies, such as MRI and CT, heavily relies on the hardware as well as the reconstruction algorithms. However in MPI, the characteristics of the nanoparticles (such as the core size, size distribution, anisotropy of the magnetic core, and the surface modification), in addition to the strength of the magnetic field gradient, govern the spatial resolution and the sensitivity of MPI [188].

Compared to paramagnetic agents, such as gadolinium (III), SPIOs have a larger effect on MRI relaxivity which enables the detection of lower concentration of cells relative to gadolinium-labeled cells. In fact, studies have shown single cell detection using SPIOs for cell labeling [189]. SPIOs cause inhomogeneities in the local magnetic field and affect spin-spin dephasing, leading to shortening of T_2/T_2^* relaxation times, resulting in negative contrast on T_2 weighted MRI. Iron oxide particles come in different sizes, ranging from 10-50 nm (ultrasmall superparamagnetic iron oxides; USPIOs), to 50-100 nm SPIOs and up to >1 μm (micrometer-sized iron oxides; MPIOs). SPIO magnetization gradually increases with nanoparticle core size, up until a point of a sharp decrease. Larger nanoparticle core diameters result in a steeper magnetization curve which leads to better spatial resolution. However, the size distribution properties are also crucial factors for the spatial resolution of MPI, where a monodisperse and narrow size distribution for the entire nanoparticle ensemble produces higher MPI signal and better spatial resolution and SNR [190]. Magnetic anisotropy of SPIOs also influences the performance of SPIOs in MPI, where high anisotropy may diminish the performance and low anisotropy may enhance it. Surface modifications, such as coatings that form a barrier between the physiological environment and the hydrophobic nanoparticle cores, also serve to enhance MPI image quality. These coatings also contribute to the blood half-life and biodistribution of SPIOs (smaller hydrodynamic core results

in increased half-life) to ensure optimized core performance for relevant *in vivo* systems (such as prevent rapid clearance for steady state imaging) [191].

1.3.4.2 MPI Probes

Most SPIONs for MPI are preclinical, with the exception of the FDA-approved MRI contrast agents Resovist®, Feridex®, and Endorem® [192]. Due to their slower renal clearance and higher relaxation values, in comparison to gadolinium-based contrast agents (GBCAs), SPIONs are more favorable for imaging applications. Resovist was the first probe used for MPI which resulted in two-dimensional images with a very high spatial resolution but at the cost of its sensitivity and is used as the reference tracer for other probes in development. Resovist, with median diameter of 5 nm and a size distribution of $\sigma = 0.37$ nm, similar to Feridex®, only contributed to 3% of MPI signal which was a result from nanoparticle ensembles of 30 nm diameter, making these SPIONs far from ideal for MPI. Thus, nanoparticle size optimization has been integral in improving MPI sensitivity [190]. Magnetite nanoparticles, with a size of 20 nm core diameter and $\sigma = 0.26$ performed at 4 times higher sensitivity than Resovist [190], while iron oxide nanoparticles micelles (ION-Michelles) outperformed Resovist® in spatial resolution by a factor of 4-6 [179]. Another SPION available for MPI is Synomag®-D which has shown better performance compared to Resovist® [193]. Synomag®-D has been previously used for *in vivo* tracking of erythrocytes and cancer cells [194][195]. Synomag®-D, with a mean core diameter of 28.6 nm and $\sigma = 9.4$, contains heterogeneous nanocrystal clusters and is polyethylene glycol (PEG)-coated, to prolong its circulation time [193]. In this thesis, Synomag®-D was used for stem cell labeling to allow cell tracking with MPI.

1.3.5 Multi-modal imaging

Multi-modal imaging is the use of multiple imaging modalities which has been used for several applications. In this thesis, multi-modal imaging for cell tracking applications will be discussed. Multi-modal imaging provides a particularly beneficial advantage of providing comprehensive information of labelled cells as harnessing the strengths of different modalities can be maximized. Multimodal tracking of cells can be accomplished by either using a single label that is detectable by multiple imaging technologies, or by combining different labeling probes or tracers [196]. Typical modalities used for cell tracking include SPECT, PET, MRI, FLI and BLI. Nuclear medicine modalities (SPECT and PET) require the use of radiolabeled tracers, such as ^{111}In and $^{99\text{m}}\text{Tc}$ for SPECT and ^{89}Zr and ^{18}F for PET [196][77][197]. While nuclear medicine imaging techniques provide sensitive and quantitative information, the radio-labelled probes result in radiation exposure and dose administration for repeat imaging is tightly regulated. MRI does not use radiotracers, but rather iron oxide nanoparticles (IONs), gadolinium (Gd)- or manganese (Mn)-based contrast agents to generate contrast. It is important to note that MRI contrast agents are also regulated and are not officially approved for cell labeling. MRI cell tracking studies that have used ^{19}F for cell labeling have shown quantitative tracking but limitations with respect to sensitivity while imaging with IONs have can be very sensitive and have shown single cell detection [198]. Finally, optical-based techniques such as FLI and BLI are the most frequently used owing to their ease of use. These techniques are limited by their depth penetration and are thus limited to preclinical models with low potential for translatability in humans. The use of fluorescent proteins is well established and in addition to FLI, is useful for microscopy and flow cytometry. Thus, it is common to combine fluorescence with other imaging techniques. Multimodal imaging serves several roles. By combining modalities and/or probes and understanding their strengths and

shortcomings, allows better and accurate interpretation on cell fate. For example, the presence or absence of a label used to directly label cells may not accurately represent live cells, whereas reporter gene imaging reports only on viable cells. Several combinations of modalities are common. For example, MRI can be used for its spatial resolution in combination with SPECT for its quantification strengths. This has been performed in the clinic to track dendritic cells in melanoma patients [13]. Additionally, the use of an established labeling and imaging technique is essential for developing novel labeling agents and technologies. Thus, combining an established modality with an emergent one allows for comparisons and enables optimizations required for further development. Multimodal imaging also has significant roles for cellular therapy and many studies have demonstrated the importance of multimodal imaging for cellular therapy optimization [13][199][200][201].

1.4 Purpose of thesis

1.4.1 Rationale

As discussed, there are many direct and indirect cell labeling techniques that have been historically used for non-invasive imaging of various cell types. This has advanced the field of molecular imaging by providing information on the in-vivo biodistribution, trafficking, proliferation, and viability of labeled cells, in both preclinical and clinical applications. The purpose of this thesis was to combine, develop and evaluate various cell labeling approaches, including both direct and indirect labeling techniques, to non-invasively track cancer, stem and immune cells, in a multimodal imaging approach.

1.4.2 Hypotheses

In Chapters 2-4, novel multi-modal imaging approaches are investigated for tracking cancer, stem and immune cells. The below three hypotheses will be investigated:

1. Breast cancer cells engineered to express human-derived MRI and PET reporter genes can be non-invasively visualized, post administration of their compatible imaging probes/tracers. This system is highly translatable, combining complementary information from PET (sensitivity and quantification) and MRI (high tissue contrast and intratumoral spatial information);
2. Mesenchymal stem cells (MSCs), directly labeled with a SPIO, and engineered to express a PET reporter gene can be detected with MPI and PET, respectively. Complementary information to provide superior sensitivity at early time points post MSC-injection can be accomplished by MPI, while PET provides longitudinal imaging of MSCs.
3. Natural killer cells, engineered to target and kill HER2 positive ovarian cancer, and co-engineered to express a PET reporter gene can be effective against ovarian cancer lysis and be visualized with PET, respectively.

1.4.3 Overview of studies

This thesis aims to extend the field of molecular imaging by using different multi-modal imaging techniques. Chapter 2 is the first study to report on a PET and MRI multi-modal imaging approach for cell tracking, using human-derived reporter genes, and clinically-used imaging probes. This chapter has been peer reviewed and published: Shalaby, N., Kelly, J., Martinez, F., Fox, M., Qi, Q., Thiessen, J., Hicks, J., Scholl, T., Ronald, J. A Human-derived Dual MRI/PET Reporter Gene System with High Translational Potential for Cell Tracking. *Molecular Imaging and Biology*. 2022 Apr;24(2):341-351. Chapter 3 is the first study to combine MPI and PET for multi-modal detection

of stem cells to provide complementary information on stem cell fate for a duration of 30 days post injection. This chapter has been peer reviewed and published: Shalaby, N., Kelly, J., Sehl, O., Gevaert, J., Fox, M., Qi, Q., Foster, P., Thiessen, J., Hicks, J., Scholl, T., Ronald, J. Complementary early-phase magnetic particle imaging and late-phase positron emission tomography reporter imaging of mesenchymal stem cells *in vivo*. *Nanoscale*. 2023. Jan; 26(15):3408-3418. Chapter 4 integrates a multi-modal imaging approach in a cancer immunotherapy, CAR-NK therapy, used to treat a HER2 positive ovarian cancer model. CAR-NK cells were co-engineered to express BLI and PET reporter genes to enable multi-modal imaging. This chapter is currently being prepared as a manuscript for journal submission.

1.5 References

- [1] Stanford Medicine, "What is Molecular Imaging?" .
- [2] J. Liu, W. X. Ren, un J. Shu, "Multimodal molecular imaging evaluation for early diagnosis and prognosis of cholangiocarcinoma", *Insights Imaging*, sēj. 13, nr. 1, 2022, doi: 10.1186/s13244-021-01147-7.
- [3] M. L. James un S. S. Gambhir, "A Molecular Imaging Primer: Modalities, Imaging Agents, and Applications", *Physiol. Rev.*, sēj. 92, nr. 2, lpp. 897–965, apr. 2012, doi: 10.1152/physrev.00049.2010.
- [4] H. Youn un K.-J. Hong, " In Vivo Non Invasive Molecular Imaging for Immune Cell Tracking in Small Animals ", *Immune Netw.*, sēj. 12, nr. 6, lpp. 223, 2012, doi: 10.4110/in.2012.12.6.223.
- [5] A. Hengerer un J. Grimm, "Molecular magnetic resonance imaging", 2006, doi: 10.2349/biij.2.2.e8.
- [6] F. On un M. Imaging, "Optical Imaging : Current Applications and Future Directions", lpp. 1–4, 2008, doi: 10.2967/jnumed.107.045799.
- [7] P. Beard, "Biomedical photoacoustic imaging", nr. June, lpp. 602–631, 2011.
- [8] 2011 Xuefeng Chen, et al, P. L. Reiter, un A.-L. McRee, "Ultrasound Molecular Imaging: Moving Towards Clinical Translation", *Physiol. Behav.*, sēj. 176, nr. 10, lpp. 139–148, 2011, doi: 10.1016/j.ejrad.2015.03.016.Ultrasound.
- [9] M. Smeenge *u.c.*, "First-in-Human Ultrasound Molecular Imaging With a VEGFR2-Specific Ultrasound Molecular Contrast Agent (BR55) in Prostate Cancer: A Safety and Feasibility Pilot Study", *Invest. Radiol.*, sēj. 52, nr. 7, 2017, [Tiešsaiste]. Pieejams: https://journals.lww.com/investigativeradiology/Fulltext/2017/07000/First_in_Human_Ultrasound_Molecular_Imaging_With_a.5.aspx.

- [10] H. Lee *u.c.*, "Microbubbles used for contrast enhanced ultrasound and theragnosis: a review of principles to applications", *Biomed. Eng. Lett.*, sēj. 7, nr. 2, lpp. 59–69, 2017, doi: 10.1007/s13534-017-0016-5.
- [11] B. Meller *u.c.*, "Monitoring of a new approach of immunotherapy with allogenic ¹¹¹In-labelled NK cells in patients with renal cell carcinoma", *Eur. J. Nucl. Med. Mol. Imaging*, sēj. 31, nr. 3, lpp. 403–407, 2004, doi: 10.1007/s00259-003-1398-4.
- [12] R. Ridolfi *u.c.*, "Evaluation of in vivo labelled dendritic cell migration in cancer patients", *J. Transl. Med.*, sēj. 2, nr. 1, jūl. 2004, doi: 10.1186/1479-5876-2-27.
- [13] I. J. M. De Vries *u.c.*, "Magnetic resonance tracking of dendritic cells in melanoma patients for monitoring of cellular therapy", *Nat. Biotechnol.*, sēj. 23, nr. 11, lpp. 1407–1413, nov. 2005, doi: 10.1038/nbt1154.
- [14] C. Heyn, C. V. Bowen, B. K. Rutt, un P. J. Foster, "Detection threshold of single SPIO-labeled cells with FIESTA", *Magn. Reson. Med.*, sēj. 53, nr. 2, lpp. 312–320, 2005, doi: 10.1002/mrm.20356.
- [15] M. F. Kircher, S. S. Gambhir, un J. Grimm, "Noninvasive cell-tracking methods", *Nat. Rev. Clin. Oncol.*, sēj. 8, nr. 11, lpp. 677–688, 2011, doi: 10.1038/nrclinonc.2011.141.
- [16] E. T. Ahrens, R. Flores, H. Xu, un P. A. Morel, "In vivo imaging platform for tracking immunotherapeutic cells", *Nat. Biotechnol.*, sēj. 23, nr. 8, lpp. 983–987, 2005, doi: 10.1038/nbt1121.
- [17] R. T. Sadikot un T. S. Blackwell, "Bioluminescence imaging", *Proc. Am. Thorac. Soc.*, sēj. 2, nr. 6, lpp. 537–540, 2005, doi: 10.1513/pats.200507-067DS.
- [18] A. A. Gilad, K. Ziv, M. T. McMahon, P. C. M. van Zijl, M. Neeman, un J. W. M. Bulte, "MR REPORTER GENES", *J. Nucl. Med.*, sēj. 49, nr. 12, lpp. 1905, dec. 2008, doi: 10.2967/JNUMED.108.053520.

- [19] S. S. Yaghoubi, D. O. Campbell, C. G. Radu, un J. Czernin, "Positron emission tomography reporter genes and reporter probes: Gene and cell therapy applications", *Theranostics*, sēj. 2, nr. 4, lpp. 374–391, 2012, doi: 10.7150/thno.3677.
- [20] "Imaging reporter genes for cell tracking with PET and SPECT". <https://www.minervamedica.it/en/journals/nuclear-med-molecular-imaging/article.php?cod=R39Y2005N04A0349> (skatīts sept. 17, 2019).
- [21] Z. Lei, Y. Zeng, X. Zhang, X. Wang, un G. Liu, "Photoacoustic reporter genes for noninvasive molecular imaging and theranostics", *J. Innov. Opt. Health Sci.*, sēj. 13, nr. 3, lpp. 1–11, 2020, doi: 10.1142/S1793545820300050.
- [22] M. Li, Y. Wang, M. Liu, un X. Lan, "Multimodality reporter gene imaging: Construction strategies and application", *Theranostics*, sēj. 8, nr. 11. Ivyspring International Publisher, lpp. 2954–2973, 2018, doi: 10.7150/thno.24108.
- [23] J. J. Kelly *u.c.*, "Safe harbor-targeted CRISPR-Cas9 homology-independent targeted integration for multimodality reporter gene-based cell tracking", *Sci. Adv.*, sēj. 7, nr. 4, lpp. eabc3791, janv. 2021, doi: 10.1126/sciadv.abc3791.
- [24] V. P. Dubois *u.c.*, "Safe Harbor Targeted CRISPR-Cas9 Tools for Molecular-Genetic Imaging of Cells in Living Subjects", *Cris. J.*, sēj. 1, nr. 6, lpp. 440–449, 2018, doi: 10.1089/crispr.2018.0030.
- [25] D. Hanahan un R. A. Weinberg, "Hallmarks of Cancer: The Next Generation", *Cell*, sēj. 144, nr. 5, lpp. 646–674, mar. 2011, doi: 10.1016/j.cell.2011.02.013.
- [26] W. a Weber, "Molecular imaging in cancer", *Bundesgesundheitsblatt. Gesundheitsforschung. Gesundheitsschutz*, sēj. 53, nr. 8, lpp. 810–7, 2010, [Tiešsaiste]. Pieejams: <http://www.ncbi.nlm.nih.gov/pubmed/20870460>.
- [27] E. M. Shapiro, K. Sharer, S. Skrtic, un A. P. Koretsky, "In vivo detection of single cells by MRI", *Magn. Reson. Med.*, sēj. 55, nr. 2, lpp. 242–249, 2006, doi: 10.1002/mrm.20718.

- [28] S. Iwano *u.c.*, "Single-cell bioluminescence imaging of deep tissue in freely moving animals.", *Science*, sēj. 359, nr. 6378, lpp. 935–939, febr. 2018, doi: 10.1126/science.aag1067.
- [29] C. Heyn *u.c.*, "In vivo magnetic resonance imaging of single cells in mouse brain with optical validation", *Magn. Reson. Med.*, sēj. 55, nr. 1, lpp. 23–29, janv. 2006, doi: 10.1002/mrm.20747.
- [30] M. V. Liberti un J. W. Locasale, "The Warburg Effect: How Does it Benefit Cancer Cells?", *Trends Biochem. Sci.*, sēj. 41, nr. 3, lpp. 211–218, mar. 2016, doi: 10.1016/J.TIBS.2015.12.001.
- [31] A. F. Shields, J. R. Grierson, S. M. Kozawa, un M. Zheng, "Development of labeled thymidine analogs for imaging tumor proliferation", *Nucl. Med. Biol.*, sēj. 23, nr. 1, lpp. 17–22, 1996, doi: 10.1016/0969-8051(95)02005-5.
- [32] S. S. Gambhir, "Molecular imaging of cancer with positron emission tomography", *Nat. Rev. Cancer*, sēj. 2, nr. 9, lpp. 683–693, 2002, doi: 10.1038/nrc882.
- [33] R. L. Wahl, V. Dilsizian, un C. J. Palestro, "At last, 18F-FDG for inflammation and infection!", *J. Nucl. Med.*, sēj. 62, nr. 8, lpp. 1048–1049, 2021, doi: 10.2967/jnumed.121.262446.
- [34] K. A. Plichta, S. A. Graves, un J. M. Buatti, "Prostate-Specific Membrane Antigen (PSMA) Theranostics for Treatment of Oligometastatic Prostate Cancer", *Int. J. Mol. Sci.*, sēj. 22, nr. 22, lpp. 12095, nov. 2021, doi: 10.3390/ijms222212095.
- [35] T. Maurer, M. Eiber, M. Schwaiger, un J. E. Gschwend, "Current use of PSMA-PET in prostate cancer management", *Nat. Rev. Urol.*, sēj. 13, nr. 4, lpp. 226–235, 2016, doi: 10.1038/nrurol.2016.26.
- [36] D. E. Jenkins *u.c.*, "Bioluminescent imaging (BLI) to improve and refine traditional murine models of tumor growth and metastasis", *Clin. Exp. Metastasis*, sēj. 20, nr. 8, lpp. 733–744, 2003, doi: 10.1023/B:CLIN.0000006815.49932.98.

- [37] S. Bhaumik, X. Z. Lewis, un S. S. Gambhir, "Optical imaging of Renilla luciferase, synthetic Renilla luciferase, and firefly luciferase reporter gene expression in living mice", *J. Biomed. Opt.*, sēj. 9, nr. 3, lpp. 578, 2004, doi: 10.1117/1.1647546.
- [38] M. Edinger, Y. A. Cao, M. R. Verneris, M. H. Bachmann, C. H. Contag, un R. S. Negrin, "Revealing lymphoma growth and the efficacy of immune cell therapies using in vivo bioluminescence imaging", *Blood*, sēj. 101, nr. 2, lpp. 640–648, janv. 2003, doi: 10.1182/BLOOD-2002-06-1751.
- [39] J. Nakayama *u.c.*, "High sensitivity in vivo imaging of cancer metastasis using a near-infrared luciferin analogue seMpai", *Int. J. Mol. Sci.*, sēj. 21, nr. 21, lpp. 1–8, 2020, doi: 10.3390/ijms21217896.
- [40] R. M. Hoffman, "Visualization of GFP-expressing tumors and metastasis in vivo", *Biotechniques*, sēj. 30, nr. 5, lpp. 1016–1026, 2001, doi: 10.2144/01305bi01.
- [41] A. P. Savitsky *u.c.*, "Noninvasive and Real-Time Fluorescence Imaging of Peritoneal Metastasis in Nude Mice", sēj. 872, lpp. 97–114, 2012, doi: 10.1007/978-1-61779-797-2.
- [42] C. Chi *u.c.*, "Use of indocyanine green for detecting the sentinel lymph node in breast cancer patients: From preclinical evaluation to clinical validation", *PLoS One*, sēj. 8, nr. 12, lpp. 24–28, 2013, doi: 10.1371/journal.pone.0083927.
- [43] M. Ogawa, N. Kosaka, P. L. Choyke, un H. Kobayashi, "In vivo Molecular Imaging of Cancer with a Quenching Near Infrared Fluorescent Probe Using Conjugates of Monoclonal Antibodies and Indocyanine Green", *Cancer Res*, sēj. 69, nr. 4, lpp. 1268–1272, 2009, doi: 10.1158/0008-5472.CAN-08-3116.In.
- [44] C. Albanese *u.c.*, "Preclinical magnetic resonance imaging and systems biology in cancer research: Current applications and challenges", *Am. J. Pathol.*, sēj. 182, nr. 2, lpp. 312–318, 2013, doi: 10.1016/j.ajpath.2012.09.024.
- [45] R. Muteganya, S. Goldman, F. Aoun, T. Roumeguère, un S. Albisinni, "Current imaging techniques for lymph node staging in prostate cancer: A review", *Front. Surg.*, sēj. 5, nr. December, 2018, doi: 10.3389/fsurg.2018.00074.

- [46] A. Bogdanov un M. L. Mazzanti, "Molecular magnetic resonance contrast agents for the detection of cancer: Past and present", *Semin. Oncol.*, sēj. 38, nr. 1, lpp. 42–54, 2011, doi: 10.1053/j.seminoncol.2010.11.002.
- [47] E. A. Schellenberger, D. Högemann, L. Josephson, un R. Weissleder, "Annexin V-CLIO: A nanoparticle for detecting apoptosis by MRI", *Acad. Radiol.*, sēj. 9, nr. SUPPL. 2, lpp. 102–107, 2002, doi: 10.1016/S1076-6332(03)80212-X.
- [48] A. A. Neves *u.c.*, "A paramagnetic nanoprobe to detect tumor cell death using magnetic resonance imaging.", *Nano Lett.*, sēj. 7, nr. 5, lpp. 1419–1423, mai. 2007, doi: 10.1021/nl070126v.
- [49] M. Lijowski *u.c.*, "High Sensitivity: High-Resolution SPECT-CT/MR Molecular Imaging of Angiogenesis in the Vx2 Model", *Invest. Radiol.*, sēj. 44, nr. 1, 2009, [Tiešsaiste]. Pieejams: https://journals.lww.com/investigativeradiology/Fulltext/2009/01000/High_Sensitivity__High_Resolution_SPECT_CT_MR.3.aspx.
- [50] A. Moore, Z. Medarova, A. Potthast, un G. Dai, "In Vivo Targeting of Underglycosylated MUC-1 Tumor Antigen Using a Multimodal Imaging Probe", *Cancer Res.*, sēj. 64, nr. 5, lpp. 1821–1827, 2004, doi: 10.1158/0008-5472.CAN-03-3230.
- [51] K. M. Parkins, A. M. Hamilton, A. V. Makela, Y. Chen, P. J. Foster, un J. A. Ronald, "A multimodality imaging model to track viable breast cancer cells from single arrest to metastasis in the mouse brain", *Sci. Rep.*, sēj. 6, nr. October, lpp. 1–9, 2016, doi: 10.1038/srep35889.
- [52] D. W. Hwang *u.c.*, "A nucleolin-targeted multimodal nanoparticle imaging probe for tracking cancer cells using an aptamer", *J. Nucl. Med.*, sēj. 51, nr. 1, lpp. 98–105, 2010, doi: 10.2967/jnumed.109.069880.
- [53] K. M. Lin, C.-H. Hsu, W.-S. W. Chang, C.-T. Chen, T.-W. Lee, un C.-T. Chen, "Human Breast Tumor Cells Express Multimodal Imaging Reporter Genes", *Mol. Imaging Biol.* 2008 105, sēj. 10, nr. 5, lpp. 253–263, jūn. 2008, doi: 10.1007/S11307-008-0147-2.
- [54] T. H *u.c.*, "Radio-deoxynucleoside Analogs used for Imaging tk Expression in a Transgenic Mouse Model of Induced Hepatocellular Carcinoma", *Theranostics*, sēj. 2, nr. 6, lpp. 597–606, 2012, doi: 10.7150/THNO.3371.

- [55] R. J. Williams *u.c.*, "Dual Magnetic Particle Imaging and Akaluc Bioluminescence Imaging for Tracking Cancer Cell Metastasis", *Tomography*, sēj. 9, nr. 1, lpp. 178–194, 2023, doi: 10.3390/tomography9010016.
- [56] M. A. Stammes *u.c.*, "Pre-clinical Evaluation of a Cyanine-Based SPECT Probe for Multimodal Tumor Necrosis Imaging", *Mol. Imaging Biol.* 2016 186, sēj. 18, nr. 6, lpp. 905–915, jūn. 2016, doi: 10.1007/S11307-016-0972-7.
- [57] M. A. Stammes *u.c.*, "The Necrosis-Avid Small Molecule HQ4-DTPA as a Multimodal Imaging Agent for Monitoring Radiation Therapy-Induced Tumor Cell Death", *Front. Oncol.*, sēj. 0, nr. OCT, lpp. 221, okt. 2016, doi: 10.3389/FONC.2016.00221.
- [58] C. A. Maguire *u.c.*, "Triple bioluminescence imaging for in vivo monitoring of cellular processes", *Mol. Ther. - Nucleic Acids*, sēj. 2, nr. April 2014, 2013, doi: 10.1038/mtna.2013.25.
- [59] X. Yang *u.c.*, "Cellular and molecular imaging for stem cell tracking in neurological diseases", *Stroke Vasc. Neurol.*, sēj. 6, lpp. 408, 2021, doi: 10.1136/svn-2020-000408.
- [60] "View of Multipotent Stem Cell and Current Application". <https://acta.tums.ac.ir/index.php/acta/article/view/4962/4885> (skatīts febr. 22, 2023).
- [61] R. M. Aly, "Current state of stem cell-based therapies: An overview", *Stem Cell Investig.*, sēj. 7, nr. May, lpp. 1–10, 2020, doi: 10.21037/sci-2020-001.
- [62] K. Takahashi un S. Yamanaka, "Induction of pluripotent stem cells from mouse embryonic and adult fibroblast cultures by defined factors", *Cell*, sēj. 126, nr. 4, lpp. 663–676, aug. 2006, doi: 10.1016/J.CELL.2006.07.024.
- [63] R. Yahyapour *u.c.*, "Stem Cell Tracing Through MR Molecular Imaging", *Tissue Eng. Regen. Med.*, sēj. 15, nr. 3, lpp. 15, 2018, doi: 10.1007/s13770-017-0112-8.
- [64] "Approved Cellular and Gene Therapy Products | FDA". <https://www.fda.gov/vaccines-blood-biologics/cellular-gene-therapy-products/approved-cellular-and-gene-therapy-products> (skatīts febr. 22, 2023).

- [65] R. Guzman *u.c.*, "Long-term monitoring of transplanted human neural stem cells in developmental and pathological contexts with MRI", *Proc. Natl. Acad. Sci. U. S. A.*, sēj. 104, nr. 24, lpp. 10211–10216, 2007, doi: 10.1073/pnas.0608519104.
- [66] A. K. Srivastava, D. K. Kadayakkara, A. Bar-Shir, A. A. Gilad, M. T. McMahon, un J. W. M. Bulte, "Advances in using MRI probes and sensors for in vivo cell tracking as applied to regenerative medicine", *DMM Dis. Model. Mech.*, sēj. 8, nr. 4, lpp. 323–336, 2015, doi: 10.1242/dmm.018499.
- [67] E. J. Ngen un D. Artemov, "Advances in monitoring cell-based therapies with magnetic resonance imaging: Future perspectives", *Int. J. Mol. Sci.*, sēj. 18, nr. 1, lpp. 14–22, 2017, doi: 10.3390/ijms18010198.
- [68] Y. Huang, J. C. Hsu, H. Koo, un D. P. Cormode, "Repurposing ferumoxytol: Diagnostic and therapeutic applications of an FDA-approved nanoparticle", *Theranostics*, sēj. 12, nr. 2, lpp. 796–816, 2022, doi: 10.7150/thno.67375.
- [69] R. T. Castaneda, A. Khurana, R. Khan, un H. E. Daldrup-Link, "Labeling stem cells with ferumoxytol, an FDA-approved iron oxide nanoparticle", *J. Vis. Exp.*, nr. 57, 2011, doi: 10.3791/3482.
- [70] M. S. Thu *u.c.*, "Self-assembling nanocomplexes by combining ferumoxytol, heparin and protamine for cell tracking by magnetic resonance imaging", *Nat. Med.*, sēj. 18, nr. 3, lpp. 463–467, mar. 2012, doi: 10.1038/NM.2666.
- [71] A. M. Morawski *u.c.*, "Quantitative "magnetic resonance immunohistochemistry" with ligand-targeted ¹⁹F nanoparticles", *Magn. Reson. Med.*, sēj. 52, nr. 6, lpp. 1255–1262, 2004, doi: 10.1002/mrm.20287.
- [72] J. M. Gaudet, E. J. Ribot, Y. Chen, K. M. Gilbert, un P. J. Foster, "Tracking the fate of stem cell implants with fluorine-19 MRI", *PLoS One*, sēj. 10, nr. 3, lpp. 1–11, 2015, doi: 10.1371/journal.pone.0118544.

- [73] Y. Liu *u.c.*, "Evaluation of cell tracking effects for transplanted mesenchymal stem cells with jetPEI/Gd-DTPA complexes in animal models of hemorrhagic spinal cord injury", *Brain Res.*, sēj. 1391, lpp. 24–35, mai. 2011, doi: 10.1016/J.BRAINRES.2011.03.032.
- [74] N. Nose *u.c.*, "[18F]FDG-labelled stem cell PET imaging in different route of administrations and multiple animal species", *Sci. Rep.*, sēj. 11, nr. 1, lpp. 1–8, 2021, doi: 10.1038/s41598-021-90383-4.
- [75] E. Wolfs *u.c.*, "18F-FDG labeling of mesenchymal stem cells and multipotent adult progenitor cells for PET imaging: Effects on ultrastructure and differentiation capacity", *J. Nucl. Med.*, sēj. 54, nr. 3, lpp. 447–454, 2013, doi: 10.2967/jnumed.112.108316.
- [76] O. Detante *u.c.*, "Intravenous administration of 99mTc-HMPAO-labeled human mesenchymal stem cells after stroke: In vivo imaging and biodistribution", *Cell Transplant.*, sēj. 18, nr. 12, lpp. 1369–1379, 2009, doi: 10.3727/096368909X474230.
- [77] A. Gholamrezanezhad *u.c.*, "In vivo tracking of 111In-oxine labeled mesenchymal stem cells following infusion in patients with advanced cirrhosis", *Nucl. Med. Biol.*, sēj. 38, nr. 7, lpp. 961–967, 2011, doi: 10.1016/j.nucmedbio.2011.03.008.
- [78] D. L. Kraitchman un J. W. M. Bulte, "Imaging of stem cells using MRI", *Basic Res. Cardiol.*, sēj. 103, nr. 2, lpp. 105–113, 2008, doi: 10.1007/s00395-008-0704-5.
- [79] J. Sun *u.c.*, "MRI detection of the malignant transformation of stem cells through reporter gene expression driven by a tumor-specific promoter", *Stem Cell Res. Ther.*, sēj. 12, nr. 1, lpp. 1–14, 2021, doi: 10.1186/s13287-021-02359-w.
- [80] E. Wolfs *u.c.*, "Optimization of Multimodal Imaging of Mesenchymal Stem Cells Using the Human Sodium Iodide Symporter for PET and Cerenkov Luminescence Imaging", *PLoS One*, sēj. 9, nr. 4, lpp. e94833, apr. 2014, doi: 10.1371/JOURNAL.PONE.0094833.
- [81] J. R. Bagó *u.c.*, "Bioluminescence imaging of cardiomyogenic and vascular differentiation of cardiac and subcutaneous adipose tissue-derived progenitor cells in fibrin patches in a myocardium infarct model", *Int. J. Cardiol.*, sēj. 169, nr. 4, lpp. 288–295, nov. 2013, doi: 10.1016/J.IJCARD.2013.09.013.

- [82] S. Lee *u.c.*, "In vivo bioluminescence imaging of transplanted mesenchymal stem cells as a potential source for pancreatic regeneration", *Mol. Imaging*, sēj. 13, nr. 8, lpp. 1–12, 2014, doi: 10.2310/7290.2014.00023.
- [83] H. J. Oh, D. W. Hwang, H. Youn, un D. S. Lee, "In vivo bioluminescence reporter gene imaging for the activation of neuronal differentiation induced by the neuronal activator neurogenin 1 (Ngn1) in neuronal precursor cells", *Eur. J. Nucl. Med. Mol. Imaging*, sēj. 40, nr. 10, lpp. 1607–1617, 2013, doi: 10.1007/s00259-013-2457-0.
- [84] C. M. Lewis *u.c.*, "52Mn production for PET/MRI tracking of human stem cells expressing divalent metal transporter 1 (DMT1)", *Theranostics*, sēj. 5, nr. 3, lpp. 227–239, 2015, doi: 10.7150/thno.10185.
- [85] F. Cao *u.c.*, "In vivo visualization of embryonic stem cell survival, proliferation, and migration after cardiac delivery", *Circulation*, sēj. 113, nr. 7, lpp. 1005–1014, 2006, doi: 10.1161/CIRCULATIONAHA.105.588954.
- [86] O. C. Sehl, A. V. Makela, A. M. Hamilton, un P. J. Foster, "Trimodal cell tracking in vivo: Combining iron-and fluorine-based magnetic resonance imaging with magnetic particle imaging to monitor the delivery of mesenchymal stem cells and the ensuing inflammation", *Tomography*, sēj. 5, nr. 4, lpp. 367–376, 2019, doi: 10.18383/j.tom.2019.00020.
- [87] L. Mezzanotte, M. Aswendt, A. Tennstaedt, R. Hoebe, M. Hoehn, un C. Löwik, "Evaluating reporter genes of different luciferases for optimized in vivo bioluminescence imaging of transplanted neural stem cells in the brain", *Contrast Media Mol. Imaging*, sēj. 8, nr. 6, lpp. 505–513, 2013, doi: 10.1002/cmmi.1549.
- [88] J. Perrin *u.c.*, "Cell Tracking in Cancer Immunotherapy", *Front. Med.*, sēj. 0, lpp. 34, febr. 2020, doi: 10.3389/FMED.2020.00034.
- [89] M. Schuster, A. Nechansky, H. Loibner, un R. Kircheis, "Cancer immunotherapy", *Biotechnol. J.*, sēj. 1, nr. 2, lpp. 138–147, 2006, doi: 10.1002/biot.200500044.

- [90] T. Hinz, C. J. Buchholz, T. Van Der Stappen, K. Cichutek, un U. Kalinke, "Manufacturing and quality control of cell-based tumor vaccines: A scientific and a regulatory perspective", *J. Immunother.*, sēj. 29, nr. 5, lpp. 472–476, sept. 2006, doi: 10.1097/01.CJI.0000211305.98244.56.
- [91] A. Yilmaz, H. Cui, M. A. Caligiuri, un J. Yu, "Chimeric antigen receptor-engineered natural killer cells for cancer immunotherapy", *J. Hematol. Oncol.*, sēj. 13, nr. 1, lpp. 1–22, 2020, doi: 10.1186/s13045-020-00998-9.
- [92] M. Cheng, J. Zhang, W. Jiang, Y. Chen, un Z. Tian, "Natural killer cell lines in tumor immunotherapy", *Front. Med. China*, sēj. 6, nr. 1, lpp. 56–66, mar. 2012, doi: 10.1007/S11684-012-0177-7/METRICS.
- [93] T. Tonn *u.c.*, "Treatment of patients with advanced cancer with the natural killer cell line NK-92", *Cytotherapy*, sēj. 15, nr. 12, lpp. 1563–1570, dec. 2013, doi: 10.1016/J.JCYT.2013.06.017.
- [94] H. Klingemann, "Challenges of cancer therapy with natural killer cells", *Cytotherapy*, sēj. 17, nr. 3, lpp. 245–249, mar. 2015, doi: 10.1016/J.JCYT.2014.09.007.
- [95] A. M. Cornel, I. L. Mimpem, un S. Nierkens, "cancers MHC Class I Downregulation in Cancer: Underlying Mechanisms and Potential Targets for Cancer Immunotherapy", doi: 10.3390/cancers12071760.
- [96] E. Sheikhpour, P. Noorbakhsh, E. Foroughi, S. Farahnak, R. Nasiri, un H. Neamatzadeh, "A Survey on the Role of Interleukin-10 in Breast Cancer: A Narrative", *Reports Biochem. Mol. Biol.*, sēj. 7, nr. 1, 2018, Skatīts: febr. 21, 2023. [Tiešsaiste]. Pieejams: www.RBMB.net.
- [97] N. P. Restifo, K. R. Irvine, B. R. Mineev, A. S. Taggarse, B. J. Mcfariand, un M. Wang, "Enhancing the recognition of tumor associated antigens".
- [98] N. Albinger, J. Hartmann, un E. Ullrich, "Current status and perspective of CAR-T and CAR-NK cell therapy trials in Germany", *Gene Ther.* 2021 289, sēj. 28, nr. 9, lpp. 513–527, mar. 2021, doi: 10.1038/s41434-021-00246-w.

- [99] R. C. Sterner un R. M. Sterner, "CAR-T cell therapy: current limitations and potential strategies", *Blood Cancer J.*, sēj. 11, nr. 4, 2021, doi: 10.1038/s41408-021-00459-7.
- [100] M. Hegde *u.c.*, "Tandem CAR T cells targeting HER2 and IL13R α 2 mitigate tumor antigen escape", *J. Clin. Invest.*, sēj. 126, nr. 8, lpp. 3036–3052, aug. 2016, doi: 10.1172/JCI83416.
- [101] E. Walseng *u.c.*, "A TCR-based Chimeric Antigen Receptor", *Sci. Rep.*, sēj. 7, nr. 1, lpp. 1–10, 2017, doi: 10.1038/s41598-017-11126-y.
- [102] O. O. Yeku, T. J. Purdon, M. Koneru, D. Spriggs, un R. J. Brentjens, "Armored CAR T cells enhance antitumor efficacy and overcome the tumor microenvironment", *Sci. Rep.*, sēj. 7, nr. 1, lpp. 1–14, 2017, doi: 10.1038/s41598-017-10940-8.
- [103] F. Borrego, C. Rossig, A. Di Stasi, M. Carlsten, un R. W. Childs, "Genetic manipulation of NK cells for cancer immunotherapy: techniques and clinical implications", *Article*, sēj. 6, lpp. 1, 2015, doi: 10.3389/fimmu.2015.00266.
- [104] S. Mohammed *u.c.*, "Improving Chimeric Antigen Receptor-Modified T Cell Function by Reversing the Immunosuppressive Tumor Microenvironment of Pancreatic Cancer", *Mol. Ther.*, sēj. 25, nr. 1, lpp. 249–258, janv. 2017, doi: 10.1016/J.YMTHE.2016.10.016.
- [105] C. Lu *u.c.*, "A novel chimeric PD1-NKG2D-41BB receptor enhances antitumor activity of NK92 cells against human lung cancer H1299 cells by triggering pyroptosis", *Mol. Immunol.*, sēj. 122, lpp. 200–206, jūn. 2020, doi: 10.1016/J.MOLIMM.2020.04.016.
- [106] H. W. Lee, P. Gangadaran, S. Kalimuthu, un B.-C. Ahn, "Advances in Molecular Imaging Strategies for In Vivo Tracking of Immune Cells", *Biomed Res. Int.*, sēj. 2016, 2016, doi: 10.1155/2016/1946585.
- [107] G. L. Costa *u.c.*, "Adoptive Immunotherapy of Experimental Autoimmune Encephalomyelitis Via T Cell Delivery of the IL-12 p40 Subunit", *J. Immunol.*, sēj. 167, nr. 4, lpp. 2379–2387, aug. 2001, doi: 10.4049/JIMMUNOL.167.4.2379.

- [108] B. A. Rabinovich *u.c.*, "Visualizing fewer than 10 mouse T cells with an enhanced firefly luciferase in immunocompetent mouse models of cancer", 2008, Skatīts: febr. 16, 2023. [Tiešsaiste]. Pieejams: www.pnas.org/cgi/content/full/.
- [109] Y. Noh, Y. T. Lim, un B. H. Chung, "Noninvasive imaging of dendritic cell migration into lymph nodes using near-infrared fluorescent semiconductor nanocrystals", *FASEB J.*, sēj. 22, nr. 11, lpp. 3908–3918, nov. 2008, doi: 10.1096/FJ.08-112896.
- [110] S. Kang *u.c.*, "Combined Fluorescence and Magnetic Resonance Imaging of Primary Macrophage Migration to Sites of Acute Inflammation Using Near-Infrared Fluorescent Magnetic Nanoparticles", *Mol Imaging Biol.*, sēj. 17, lpp. 643–651, 2015, doi: 10.1007/s11307-015-0830-z.
- [111] "Optical imaging of cellular immunotherapy against prostate cancer - PubMed". <https://pubmed.ncbi.nlm.nih.gov/19344572/> (skatīts febr. 21, 2023).
- [112] N. Shalaby, V. P. Dubois, un J. Ronald, "Molecular imaging of cellular immunotherapies in experimental and therapeutic settings", *Cancer Immunol. Immunother.*, sēj. 71, nr. 6, lpp. 1281–1294, 2022, doi: 10.1007/s00262-021-03073-5.
- [113] J. M. Brand *u.c.*, "Kinetics and Organ Distribution of Allogeneic Natural Killer Lymphocytes Transfused into Patients Suffering from Renal Cell Carcinoma", <https://home.liebertpub.com/scd>, sēj. 13, nr. 3, lpp. 307–314, jūl. 2004, doi: 10.1089/154732804323099235.
- [114] R. Meier *u.c.*, "Tracking of [18F]FDG-labeled natural killer cells to HER2/neu-positive tumors", *Nucl. Med. Biol.*, sēj. 35, nr. 5, lpp. 579–588, jūl. 2008, doi: 10.1016/j.nucmedbio.2008.02.006.
- [115] M. R. Weist *u.c.*, "PET of adoptively transferred chimeric antigen receptor T Cells with 89Zr-Oxine", *J. Nucl. Med.*, sēj. 59, nr. 10, lpp. 1531–1537, okt. 2018, doi: 10.2967/jnumed.117.206714.
- [116] K. V. Keu *u.c.*, "Reporter gene imaging of targeted T cell immunotherapy in recurrent glioma", *Sci. Transl. Med.*, sēj. 9, nr. 373, janv. 2017, doi: 10.1126/scitranslmed.aag2196.

- [117] I. Minn *u.c.*, "Imaging CAR T cell therapy with PSMA-targeted positron emission tomography", *Sci. Adv.*, sēj. 5, nr. 7, lpp. eaaw5096, jūl. 2019, doi: 10.1126/sciadv.aaw5096.
- [118] M. A. Sellmyer *u.c.*, "Imaging CAR T Cell Trafficking with eDHFR as a PET Reporter Gene", *Mol. Ther.*, sēj. 28, nr. 1, lpp. 42, janv. 2020, doi: 10.1016/J.YMTHE.2019.10.007.
- [119] Y. Vedvyas *u.c.*, "Longitudinal PET imaging demonstrates biphasic CAR T cell responses in survivors", *Ref. Inf. JCI Insight*, sēj. 1, nr. 19, lpp. 90064, 2016, doi: 10.1172/jci.insight.90064.
- [120] A. Volpe *u.c.*, "Spatiotemporal PET Imaging Reveals Differences in CAR-T Tumor Retention in Triple-Negative Breast Cancer Models", *Mol. Ther.*, sēj. 28, nr. 10, lpp. 2271–2285, okt. 2020, doi: 10.1016/j.ymthe.2020.06.028.
- [121] N. Emami-Shahri *u.c.*, "Clinically compliant spatial and temporal imaging of chimeric antigen receptor T-cells", *Nat. Commun.*, sēj. 9, nr. 1, lpp. 1–12, dec. 2018, doi: 10.1038/s41467-018-03524-1.
- [122] K. Wang, "Feasibility of High Spatial Resolution Working Modes for Clinical PET Scanner", *Int. J. Med. Physics, Clin. Eng. Radiat. Oncol.*, sēj. 07, nr. 04, lpp. 539–552, nov. 2018, doi: 10.4236/ijmpcero.2018.74045.
- [123] C. Kuntner un D. Stout, "Quantitative preclinical PET imaging: Opportunities and challenges", *Front. Phys.*, sēj. 2, lpp. 1–12, febr. 2014, doi: 10.3389/fphy.2014.00012.
- [124] H. E. Daldrup-Link *u.c.*, "In vivo tracking of genetically engineered, anti-HER2/neu directed natural killer cells to HER2/neu positive mammary tumors with magnetic resonance imaging", *Eur. Radiol.*, sēj. 15, nr. 1, lpp. 4–13, janv. 2005, doi: 10.1007/s00330-004-2526-7.
- [125] M. N. Bouchlaka *u.c.*, "(19)F-MRI for monitoring human NK cells in vivo", *Oncoimmunology*, sēj. 5, nr. 5, mai. 2016, doi: 10.1080/2162402X.2016.1143996.
- [126] B. A. Kennis *u.c.*, "Monitoring of intracerebellarly-administered natural killer cells with fluorine-19 MRI", *J. Neurooncol.*, sēj. 142, nr. 3, lpp. 395–407, mai. 2019, doi: 10.1007/s11060-019-03091-5.

- [127] C. Gonzales *u.c.*, "In-vivo detection and tracking of T cells in various organs in a melanoma tumor model by ¹⁹F-fluorine MRS/MRI", *PLoS One*, sēj. 11, nr. 10, lpp. 1–18, 2016, doi: 10.1371/journal.pone.0164557.
- [128] E. T. Ahrens, B. M. Helfer, C. F. O'Hanlon, un C. Schirda, "Clinical cell therapy imaging using a perfluorocarbon tracer and fluorine-19 MRI", *Magn. Reson. Med.*, sēj. 72, nr. 6, lpp. 1696–1701, 2014, doi: 10.1002/mrm.25454.
- [129] L. Kiru *u.c.*, "In vivo imaging of nanoparticle-labeled CAR T cells", *Proc. Natl. Acad. Sci. U. S. A.*, sēj. 119, nr. 6, 2022, doi: 10.1073/pnas.2102363119.
- [130] T. Cells *u.c.*, "Multimodal In Vivo Tracking of Chimeric Antigen Receptor T cells in Preclinical Glioblastoma Models", sēj. 00, nr. 00, lpp. 1–8, 2022, doi: 10.1097/RLI.0000000000000946.
- [131] F. Simonetta *u.c.*, "Molecular Imaging of Chimeric Antigen Receptor T Cells by ICOS-ImmunoPET", *Clin. Cancer Res.*, sēj. 27, nr. 4, lpp. 1058–1068, 2021, doi: 10.1158/1078-0432.CCR-20-2770.
- [132] S. R. Cherry un M. Dahlbom, "PET: Physics, Instrumentation, and Scanners", *Pet*, lpp. 1–117, 2006, doi: 10.1007/0-387-34946-4_1.
- [133] M. N. McCracken, R. Tavaré, O. N. Witte, un A. M. Wu, "Advances in PET Detection of the Antitumor T Cell Response", *Adv. Immunol.*, sēj. 131, lpp. 187–231, janv. 2016, doi: 10.1016/BS.AI.2016.02.004.
- [134] K. Mah un C. B. Caldwell, "chapter 4 - Biological Target Volume", no *PET-CT in Radiotherapy Treatment Planning*, A. C. Paulino un B. S. Teh, Red. Philadelphia: Elsevier, 2008, lpp. 52–89.
- [135] T. Derlin, V. Grünwald, J. Steinbach, H.-J. Wester, un T. L. Ross, "M E D I C I N E Molecular Imaging in Oncology Using Positron Emission Tomography", doi: 10.3238/arztebl.2018.0175.

- [136] B. M. Fischer *u.c.*, "How few cancer cells can be detected by positron emission tomography? A frequent question addressed by an in vitro study", *Eur. J. Nucl. Med. Mol. Imaging*, sēj. 33, nr. 6, lpp. 697–702, jūn. 2006, doi: 10.1007/s00259-005-0038-6.
- [137] J. G. Tjuvajev *u.c.*, "Imaging herpes virus thymidine kinase gene transfer and expression by positron emission tomography", *Cancer Res.*, sēj. 58, nr. 19, lpp. 4333–4341, 1998.
- [138] E. H. Gschwend *u.c.*, "HSV-sr39TK positron emission tomography and suicide gene elimination of human hematopoietic stem cells and their progeny in humanized mice", *Cancer Res.*, sēj. 74, nr. 18, lpp. 5173–5183, jūl. 2014, doi: 10.1158/0008-5472.CAN-14-0376.
- [139] J. Perrin *u.c.*, "Cell Tracking in Cancer Immunotherapy", *Frontiers in Medicine*, sēj. 7. Frontiers Media S.A., lpp. 34, febr. 14, 2020, doi: 10.3389/fmed.2020.00034.
- [140] S. R. Riddell *u.c.*, "T-cell mediated rejection of gene-modified HIV-specific cytotoxic T lymphocytes in HIV-infected patients", *Nat. Med.*, sēj. 2, nr. 2, lpp. 216–223, 1996, doi: 10.1038/nm0296-216.
- [141] M. M. Doubrovin, E. S. Doubrovina, P. Zanzonico, M. Sadelain, S. M. Larson, un R. J. O'Reilly, "In vivo imaging and quantitation of adoptively transferred human antigen-specific T cells transduced to express a human norepinephrine transporter gene", *Cancer Res.*, sēj. 67, nr. 24, lpp. 11959–11969, dec. 2007, doi: 10.1158/0008-5472.CAN-07-1250.
- [142] Y. Vedvyas *u.c.*, "Longitudinal PET imaging demonstrates biphasic CAR T cell responses in survivors", *JCI Insight*, sēj. 1, nr. 19, nov. 2016, doi: 10.1172/jci.insight.90064.
- [143] M. Hingorani *u.c.*, "The biology of the sodium iodide symporter and its potential for targeted gene delivery.", *Curr. Cancer Drug Targets*, sēj. 10, nr. 2, lpp. 242–67, mar. 2010, Skatīts: mar. 11, 2019. [Tiešsaiste]. Pieejams: <http://www.ncbi.nlm.nih.gov/pubmed/20201784>.
- [144] M. Jauregui-Osoro *u.c.*, "Synthesis and biological evaluation of [18F]tetrafluoroborate: A PET imaging agent for thyroid disease and reporter gene imaging of the sodium/iodide symporter", *Eur. J. Nucl. Med. Mol. Imaging*, sēj. 37, nr. 11, lpp. 2108–2116, nov. 2010, doi: 10.1007/S00259-010-1523-0/FIGURES/6.

- [145] H. Jiang un T. R. DeGrado, "[18F]Tetrafluoroborate ([18F]TFB) and its analogs for PET imaging of the sodium/iodide symporter.", *Theranostics*, sēj. 8, nr. 14, lpp. 3918–3931, 2018, doi: 10.7150/thno.24997.
- [146] A. R. Penheiter, S. J. Russell, un S. K. Carlson, "The Sodium Iodide Symporter (NIS) as an Imaging Reporter for Gene, Viral, and Cell-based Therapies", *Curr. Gene Ther.*, sēj. 12, nr. 1, lpp. 33, 2012, doi: 10.2174/156652312799789235.
- [147] J. H. Kang *u.c.*, "Development of a Sodium/Iodide Symporter (NIS)-Transgenic Mouse for Imaging of Cardiomyocyte-Specific Reporter Gene Expression".
- [148] J. Terrovitis *u.c.*, "Ectopic expression of the sodium-iodide symporter enables imaging of transplanted cardiac stem cells in vivo by single-photon emission computed tomography or positron emission tomography", *J. Am. Coll. Cardiol.*, sēj. 52, nr. 20, lpp. 1652–1660, nov. 2008, doi: 10.1016/J.JACC.2008.06.051.
- [149] J. W. Ostrominski *u.c.*, "CRISPR/Cas9-mediated introduction of the sodium/iodide symporter gene enables noninvasive in vivo tracking of induced pluripotent stem cell-derived cardiomyocytes", *Stem Cells Transl. Med.*, sēj. 9, nr. 10, lpp. 1203, okt. 2020, doi: 10.1002/SCTM.20-0019.
- [150] S. B. Lee *u.c.*, "Tracking dendritic cell migration into lymph nodes by using a novel PET probe 18F-tetrafluoroborate for sodium/iodide symporter", *EJNMMI Res.*, sēj. 7, nr. 1, dec. 2017, doi: 10.1186/s13550-017-0280-5.
- [151] D. W. McRobbie, E. A. Moore, un M. J. Graves, *MRI from picture to proton*. 2017.
- [152] K. L. McMahon, G. Cowin, un G. Galloway, "Magnetic resonance imaging: The underlying principles", *J. Orthop. Sports Phys. Ther.*, sēj. 41, nr. 11, lpp. 806–819, nov. 2011, doi: 10.2519/JOSPT.2011.3576/ASSET/IMAGES/LARGE/JOSPT-806-FIG009.JPEG.
- [153] E. T. Ahrens un J. Zhong, "In vivo MRI Cell Tracking Using Perfluorocarbon Probes And Fluorine-19 Detection", *NMR Biomed.*, sēj. 26, nr. 7, lpp. 860–871, jül. 2013, doi: 10.1002/nbm.2948.

- [154] J. W. M. Bulte, "In vivo MRI cell tracking: Clinical studies", *Am. J. Roentgenol.*, sēj. 193, nr. 2, lpp. 314–325, 2009, doi: 10.2214/AJR.09.3107.
- [155] M. Hoehn *u.c.*, "Cell tracking using magnetic resonance imaging", *J. Physiol.*, sēj. 584, nr. 1, lpp. 25–30, 2007, doi: 10.1113/jphysiol.2007.139451.
- [156] "Larmor frequency - Questions and Answers in MRI". <https://mriquestions.com/who-was-larmor.html> (skatīts janv. 16, 2023).
- [157] H. S. Kim *u.c.*, "In vivo Tracking of Dendritic Cell using MRI Reporter Gene, Ferritin", *PLoS One*, sēj. 10, nr. 5, lpp. e0125291, 2015, doi: 10.1371/journal.pone.0125291.
- [158] A. Moore, L. Josephson, R. M. Bhorade, J. P. Babilion, un R. Weissleder, "Human transferrin receptor gene as a marker gene for MR imaging", *Radiology*, sēj. 221, nr. 1, lpp. 244–250, okt. 2001, doi: 10.1148/RADIOL.2211001784/ASSET/IMAGES/LARGE/R01OC42T1X.JPEG.
- [159] R. Weissleder un W. S. Enochs, "and of Gene Expression Scintigraphy Induction ", *MR Imaging Scintigr. Gene Expr. through Melanin Induction*, sēj. 204, nr. 2, lpp. 425–429, 1997.
- [160] S. Shantanam un MUELLER, "MagA is sufficient for producing magnetic nanoparticles in mammalian cells, making it an MRI reporter", *Physiol. Behav.*, sēj. 176, nr. 1, lpp. 139–148, 2018, doi: 10.1002/mrm.21606.MagA.
- [161] A. Y. Louie *u.c.*, "In vivo visualization of gene expression using magnetic resonance imaging", *Nat. Biotechnol.*, sēj. 18, nr. 3, lpp. 321–325, 2000, doi: 10.1038/73780.
- [162] B. B. Bartelle, K. U. Szulc, G. A. Suero-Abreu, J. J. Rodriguez, un D. H. Turnbull, "Divalent metal transporter, DMT1: A novel MRI reporter protein", *Magn. Reson. Med.*, sēj. 70, nr. 3, lpp. 842–850, 2013, doi: 10.1002/MRM.24509.
- [163] E. Jacquemin *u.c.*, "Expression cloning of a rat liver Na(+)-independent organic anion transporter.", *PNAS*, sēj. 91, nr. 1, lpp. 133–137, janv. 2014, doi: 10.1073/pnas.91.1.133.

- [164] Y. Ali *u.c.*, "The involvement of human organic anion transporting polypeptides (OATPs) in drug-herb/food interactions", *Chinese Med. (United Kingdom)*, sēj. 15, nr. 1, lpp. 1–10, jūl. 2020, doi: 10.1186/S13020-020-00351-9/TABLES/1.
- [165] C. N. Caraiani, M. Dan, D. I. Fenesan, un R. Badea, "Description of focal liver lesions with Gd-EOB-DTPA enhanced MRI", *Clujul Med.*, sēj. 88, nr. 4, lpp. 438–448, 2015, doi: 10.15386/cjmed-414.
- [166] S. E. Baek *u.c.*, "Human organic anion transporting polypeptide 1B3 applied as an MRI-based reporter gene", *Korean J. Radiol.*, sēj. 21, nr. 6, lpp. 726–735, jūn. 2020, doi: 10.3348/kjr.2019.0903.
- [167] M.-R. Wu *u.c.*, "Organic anion-transporting polypeptide 1B3 as a dual reporter gene for fluorescence and magnetic resonance imaging", *FASEB J.*, sēj. 32, nr. 3, lpp. 1705–1715, mar. 2018, doi: 10.1096/fj.201700767R.
- [168] N. N. Nyström, L. C. M. Yip, J. J. L. Carson, T. J. Scholl, un J. A. Ronald, "Development of a Human Photoacoustic Imaging Reporter Gene Using the Clinical Dye Indocyanine Green", *Radiol. Imaging Cancer*, sēj. 1, nr. 2, lpp. e190035, nov. 2019, doi: 10.1148/rycan.2019190035.
- [169] C. H. Contag, P. R. Contag, J. I. Mullins, S. D. Spilman, D. K. Stevenson, un D. A. Benaron, "Photonic detection of bacterial pathogens in living hosts", *Mol. Microbiol.*, sēj. 18, nr. 4, lpp. 593–603, 1995, doi: 10.1111/J.1365-2958.1995.MMI_18040593.X.
- [170] D. A. Benaron, P. R. Contag, un C. H. Contag, "Imaging brain structure and function, infection and gene expression in the body using light", *Philos. Trans. R. Soc. B Biol. Sci.*, sēj. 352, nr. 1354, lpp. 755–761, 1997, doi: 10.1098/rstb.1997.0059.
- [171] C. CH *u.c.*, "Visualizing gene expression in living mammals using a bioluminescent reporter", *Photochem. Photobiol.*, sēj. 66, nr. 4, lpp. 523–531, 1997, doi: 10.1111/J.1751-1097.1997.TB03184.X.
- [172] P. Ray, A. De, J. J. Min, R. Y. Tsien, un S. S. Gambhir, "Imaging Tri-Fusion Multimodality Reporter Gene Expression in Living Subjects", *Cancer Res.*, sēj. 64, nr. 4, lpp. 1323–1330, febr. 2004, doi: 10.1158/0008-5472.CAN-03-1816.

- [173] A. Rehemtulla *u.c.*, "Rapid and quantitative assessment of cancer treatment response using in vivo bioluminescence imaging", *Neoplasia*, sēj. 2, nr. 6, lpp. 491–495, 2000, doi: 10.1038/SJ.NEO.7900121.
- [174] M. Edinger, T. J. Sweeney, A. A. Tucker, A. B. Olomu, R. S. Negrin, un C. H. Contag, "Noninvasive Assessment of Tumor Cell Proliferation in Animal Models", *Neoplasia*, sēj. 1, nr. 4, lpp. 303–310, 1999, doi: 10.1038/SJ.NEO.7900048.
- [175] J. Chu *u.c.*, "A bright cyan-excitable orange fluorescent protein facilitates dual-emission microscopy and enhances bioluminescence imaging in vivo", *Nat. Biotechnol.*, sēj. 34, nr. 7, lpp. 760–767, 2016, doi: 10.1038/nbt.3550.
- [176] A. M. Ansari *u.c.*, "Cellular GFP Toxicity and Immunogenicity: Potential Confounders in in Vivo Cell Tracking Experiments", *Stem Cell Rev. Reports*, sēj. 12, nr. 5, lpp. 553–559, 2016, doi: 10.1007/s12015-016-9670-8.
- [177] D. Bozec *u.c.*, "Akalic bioluminescence offers superior sensitivity to track in vivo glioma expansion", *Neuro-Oncology Adv.*, sēj. 2, nr. 1, lpp. 1–10, janv. 2020, doi: 10.1093/NOAJNL/VDAA134.
- [178] F. Weihs un H. Dacres, "Red-shifted bioluminescence Resonance Energy Transfer: Improved tools and materials for analytical in vivo approaches", *TrAC - Trends Anal. Chem.*, sēj. 116, lpp. 61–73, jūl. 2019, doi: 10.1016/J.TRAC.2019.04.011.
- [179] P. Peng, L. Long, un B. Smith, "Magnetic particle imaging: current developments and future clinical", *Chinese J. Radiol.*, sēj. 53, nr. 5, lpp. 426–430, 2019, doi: 10.3760/cma.j.issn.1005-1201.2019.05.029.
- [180] A. C. Bakenecker, M. Ahlborg, C. Debbeler, C. Kaethner, T. M. Buzug, un K. Lüdtke-Buzug, "Magnetic particle imaging in vascular medicine", *Innov. Surg. Sci.*, sēj. 3, nr. 3, lpp. 179–192, 2020, doi: 10.1515/iss-2018-2026.
- [181] X. Y. Zhou *u.c.*, "First in vivo magnetic particle imaging of lung perfusion in rats", *Phys. Med. Biol.*, sēj. 62, nr. 9, lpp. 3510–3522, 2017, doi: 10.1088/1361-6560/aa616c.

- [182] Z. W. Tay *u.c.*, "Magnetic particle imaging: An emerging modality with prospects in diagnosis, targeting and therapy of cancer", *Cancers (Basel)*., sēj. 13, nr. 21, lpp. 1–27, 2021, doi: 10.3390/cancers13215285.
- [183] B. Zheng *u.c.*, "Magnetic Particle Imaging tracks the long-term fate of in vivo neural cell implants with high image contrast", *Sci. Reports 2015 51*, sēj. 5, nr. 1, lpp. 1–9, sept. 2015, doi: 10.1038/srep14055.
- [184] M. H. Publico-Lansigan, S. F. Situ, un A. C. S. Samia, "Magnetic particle imaging: Advancements and perspectives for real-time in vivo monitoring and image-guided therapy", *Nanoscale*, sēj. 5, nr. 10, lpp. 4040–4055, 2013, doi: 10.1039/c3nr00544e.
- [185] J. W. M. Bulte, "Superparamagnetic iron oxides as MPI tracers: A primer and review of early applications", *Adv. Drug Deliv. Rev.*, sēj. 138, lpp. 293–301, 2019, doi: 10.1016/j.addr.2018.12.007.
- [186] E. U. Saritas *u.c.*, "Magnetic particle imaging (MPI) for NMR and MRI researchers", *J. Magn. Reson.*, sēj. 229, lpp. 116–126, 2013, doi: 10.1016/j.jmr.2012.11.029.
- [187] P. W. Goodwill *u.c.*, "X-Space MPI: Magnetic nanoparticles for safe medical imaging", *Adv. Mater.*, sēj. 24, nr. 28, lpp. 3870–3877, 2012, doi: 10.1002/adma.201200221.
- [188] G. M. Lekha un S. George, Colloidal magnetic metal oxide nanocrystals and their applications. Elsevier Inc., 2020.
- [189] C. Heyn *u.c.*, "In vivo MRI of cancer cell fate at the single-cell level in a mouse model of breast cancer metastasis to the brain", *Magn. Reson. Med.*, sēj. 56, nr. 5, lpp. 1001–1010, nov. 2006, doi: 10.1002/mrm.21029.
- [190] Y. Du, P. T. Lai, C. H. Leung, un P. W. T. Pong, "Design of superparamagnetic nanoparticles for magnetic particle imaging (MPI)", *Int. J. Mol. Sci.*, sēj. 14, nr. 9, lpp. 18682–18710, 2013, doi: 10.3390/ijms140918682.

- [191] S. Shantanam un MUELLER, "Tuning surface coatings of optimized magnetite nanoparticle tracers for in vivo Magnetic Particle Imaging", *Physiol. Behav.*, sēj. 176, nr. 1, lpp. 139–148, 2018, doi: 10.1109/TMAG.2014.2321096.Tuning.
- [192] M. Mahmoudi, S. Sant, B. Wang, S. Laurent, un T. Sen, "Superparamagnetic iron oxide nanoparticles (SPIONs): Development, surface modification and applications in chemotherapy", *Adv. Drug Deliv. Rev.*, sēj. 63, nr. 1–2, lpp. 24–46, 2011, doi: 10.1016/j.addr.2010.05.006.
- [193] S. Liu *u.c.*, "Long circulating tracer tailored for magnetic particle imaging", *Nanotheranostics*, sēj. 5, nr. 3, lpp. 348–361, 2021, doi: 10.7150/ntno.58548.
- [194] A. Antonelli *u.c.*, "Development of long circulating magnetic particle imaging tracers: use of novel magnetic nanoparticles and entrapment into human erythrocytes.", *Nanomedicine*, sēj. 15, nr. 8, lpp. 739–753, apr. 2020, doi: 10.2217/NNM-2019-0449.
- [195] H. Paysen *u.c.*, "Cellular uptake of magnetic nanoparticles imaged and quantified by magnetic particle imaging", *Sci. Rep.*, sēj. 10, nr. 1, dec. 2020, doi: 10.1038/S41598-020-58853-3.
- [196] M. Srinivas, I. Melero, E. Kaempgen, C. G. Figdor, un I. J. M. de Vries, "Cell tracking using multimodal imaging", *Contrast Media Mol. Imaging*, sēj. 8, nr. 6, lpp. 432–438, nov. 2013, doi: 10.1002/cmmi.1561.
- [197] P. J. Gawne, F. Man, P. J. Blower, un R. T. M. De Rosales, "Direct Cell Radiolabeling for in Vivo Cell Tracking with PET and SPECT Imaging", *Chem. Rev.*, sēj. 122, nr. 11, lpp. 10266–10318, 2022, doi: 10.1021/acs.chemrev.1c00767.
- [198] J. H. Cho *u.c.*, "Detection of iron-labeled single cells by MR imaging based on intermolecular double quantum coherences at 14 T", *J. Magn. Reson.*, sēj. 217, lpp. 86–91, 2012, doi: 10.1016/j.jmr.2012.02.014.
- [199] M. Srinivas *u.c.*, "Imaging of cellular therapies", *Adv. Drug Deliv. Rev.*, sēj. 62, nr. 11, lpp. 1080–1093, 2010, doi: 10.1016/j.addr.2010.08.009.

- [200] H. Zaidi, M. L. Montandon, un A. Alavi, "The Clinical Role of Fusion Imaging Using PET, CT, and MR Imaging", *Magn. Reson. Imaging Clin. N. Am.*, sēj. 18, nr. 1, lpp. 133–149, febr. 2010, doi: 10.1016/J.MRIC.2009.09.010.
- [201] B. Bybel, R. C. Brunken, F. P. DiFilippo, D. R. Neumann, G. Wu, un M. D. Cerqueira, "SPECT/CT Imaging: Clinical Utility of an Emerging Technology¹", <https://doi.org/10.1148/rg.284075203>, sēj. 28, nr. 4, lpp. 1097–1113, jūl. 2008, doi: 10.1148/RG.284075203.

CHAPTER 2

2 A Human-derived Dual MRI/PET Reporter Gene System with High Translational Potential for Cell Tracking

Reporter gene imaging has been extensively used to longitudinally report on whole-body distribution and viability of transplanted engineered cells. Multi-modal cell tracking can provide complementary information on cell fate. Typical multi-modal reporter gene systems often combine clinical and preclinical modalities. A multi-modal reporter gene system for magnetic resonance imaging (MRI) and positron emission tomography (PET), two clinical modalities, would be advantageous by combining the sensitivity of PET with the high-resolution morphology and non-ionizing nature of MRI. We developed and evaluated a dual MRI/PET reporter gene system composed of two human-derived reporter genes that utilize clinical reporter probes for engineered cell detection. As a proof-of-concept, breast cancer cells were engineered to co-express the human organic anion transporter polypeptide 1B3 (OATP1B3) that uptakes the clinical MRI contrast agent gadolinium ethoxybenzyl-diethylenetriaminepentaacetic acid (Gd-EOB-DTPA), and the human sodium iodide symporter (NIS) which uptakes the PET tracer, [^{18}F] tetrafluoroborate ([^{18}F] TFB). T_1 -weighted MRI results in mice exhibited significantly higher MRI signals in reporter-gene-engineered mammary fat pad tumors versus contralateral naïve tumors ($p < 0.05$). No differences in contrast enhancement were observed at 5 h after Gd-EOB-DTPA administration using either intravenous or intraperitoneal injection. We also found significantly higher standard uptake values (SUV) in engineered tumors in comparison to the naïve tumors in [^{18}F]TFB PET images ($p < 0.001$). Intratumoral heterogeneity in signal enhancement was more conspicuous in relatively higher resolution MR images compared to PET images. Our study demonstrates the ability to noninvasively track cells engineered with our human-derived dual MRI/PET reporter system, enabling a more comprehensive evaluation of transplanted cells. Future work is focused

on applying this tool to track therapeutic cells, which may one day enable the broader application of cell tracking within the healthcare system.

2.1 Introduction

Reporter genes are highly advantageous tools for *in vivo* cell tracking in that only viable cells are detected and they allow for life-long tracking capability because they are passed on to daughter cells [1]. Reporter genes have been developed for many *in vivo* preclinical and clinical imaging modalities such as fluorescence imaging (FLI) [2][3][4], bioluminescence imaging (BLI) [5][6], magnetic resonance imaging (MRI) [7][8][9], ultrasound [10][11], photoacoustic imaging [12], single photon emission computed tomography (SPECT), and positron emission tomography (PET) [13][14][15]. Notably, first-in-man clinical cell tracking has been achieved using a virally-derived PET reporter gene engineered into therapeutic T cells infused intracranially in glioma patients [14][16].

A multiple modality reporter gene system would be beneficial as it would combine the strengths of each modality to hopefully mitigate individual weaknesses. Typical multi-modal reporter gene imaging systems incorporate optical imaging via fluorescence and/or bioluminescence in combination with nuclear imaging, [17][18][19][20][21][22][23]. While FLI and BLI provide great sensitivity (10^{-15} mol/L for BLI) [24], and high throughput at a relatively lower cost, they suffer from low spatial resolution at depth, light scattering, and are not compatible for imaging larger subjects, thus limiting their potential for clinical translation. For multimodal tracking of cellular therapeutics in patients, a human-derived reporter gene system combining two clinical modalities would be of great benefit. MRI provides excellent soft tissue contrasts with high spatial resolution, lacks ionizing radiation, is relatively cost-effective and readily available in the clinic, while PET can offer sensitive and quantitative information on administered cells. Here we develop

a clinically-relevant dual modality reporter gene system for cellular imaging with both MRI and PET. Our main interest in combining these two modalities is that the fine spatial resolution of MRI can provide information about intratumoral heterogeneity of viable cells while PET's sensitivity would be valuable when MRI is not sufficiently sensitive to detect smaller lesions. Moreover, combining both modalities may allow more widespread use within the healthcare system where one modality may not be as readily available (e.g., PET).

The organic anion transporter polypeptide (OATP) is a superfamily of membrane transporters that can uptake a variety of multi-specific anionic substrates, both endogenous and exogenous, from the blood and into the cells for their absorption, distribution, metabolism and excretion [25]. Brindle *et al.* were the first to demonstrate specific uptake of a clinically approved Gd^{3+} MRI agent by rat-derived OATP1A1 transport, showing a rapid, reversible and strong increase in signal enhancement of OATP1A1-expressing cells on T_1 -weighted MRI [26]. Additionally, OATP1A1 was established as a multi-modal reporter gene as it was also shown to uptake the $^{111}\text{Indium}$ -EOB-DTPA analog for detection with SPECT [27], as well as the clinical agent, indocyanine green (ICG) for detection with photoacoustic imaging [12]. OATP1B3 is a human-derived transporter of the OATP1 family, with restricted background expression, mainly in the basolateral membrane of hepatocytes in the liver [25]. In addition to a wide variety of compatible substrates, OATP1B3 can uptake the MRI contrast agent Gd-EOB-DTPA, developed for liver imaging, enabling the OATP1B3 to serve as an MRI reporter gene [28][29][30]. Importantly, the human origin of this gene overcomes safety limitations such as potential immunogenicity of analogous rodent-derivatives, or alternative prokaryotic-derived reporter genes.

The human sodium iodide symporter (NIS) has been previously demonstrated as a reporter gene for SPECT or PET detection [31][32][33][34]. This symporter is naturally expressed on the

basolateral surface of follicular cells of the thyroid and functions to uptake plasma iodide for either oxidation or entrapment and storage for eventual catabolism into thyroid hormones [35]. Lower expression levels of NIS have also been reported in the salivary glands, stomach, and lactating mammary glands with no ability for entrapment and hormone production [36]. Additionally, a wide selection of tracers have been developed for diagnostic or therapeutic purposes involving NIS expressing tissue [37][38][39]. [^{18}F]tetrafluoroborate ([^{18}F]TFB), has been extensively evaluated as a PET reporter probe for imaging NIS expression in both transfected [40][34] and transduced cells [41]. In comparison to other NIS compatible probes, [^{18}F]TFB is an ideal PET tracer as it is a fundamental NIS substrate without any other metabolic interactions [42]. Furthermore, Fluorine-18 tracers having high positron yield of 97%, with a short diffusion range in tissue (< 2.4 mm), a clinically compatible half-life of 110 minutes and may be routinely synthesized in medical centers with cyclotrons [39].

In this research, we have designed, developed, and evaluated a dual MRI/PET human reporter gene system for *in vivo* cellular imaging. This system uses two human-derived reporter genes (NIS and OATP1B3), with their respective clinical imaging probes, ([^{18}F]TFB and Gd-EOB-DTPA, respectively) to enable detection with two clinical imaging technologies, giving this system high translational potential.

2.2 Materials and Methods

2.2.1 Cell Lines and Cell Cultures

Human triple negative breast cancer cells (MDA-MB-231), obtained from (American Type Culture Collection, Manassas, Virginia, United States), were maintained in Dulbecco's modified Eagle's medium (DMEM) containing 10% fetal bovine serum (Wisent BioProducts, Quebec,

Canada), 1% penicillin, and 1% streptomycin (Waltham, Thermo Fisher Scientific Inc., Massachusetts, United States). All cells were kept in a humidified incubator with 5% CO₂ at 37 °C. Cells were routinely confirmed to be mycoplasma negative using the MycoAlert mycoplasma detection kit (Lonza Group, Basel, Switzerland).

2.2.2 Cloning and Lentiviral Production

A third-generation lentiviral transfer plasmid was engineered to express the NIS gene (Origene technologies, Inc. NM_000453), OATP1B3 (sequence acquired from the hOATP1B3/SLCO1B3 VersaClone cDNA vector, Cat. RDC0870, R&D Systems, Minneapolis, Minnesota, United States), along with the zsGreen (zsG) fluorescence reporter gene, driven by a constitutive hEF1 α promoter. NIS, OATP1B3 and zsG are separated with the self-cleaving peptides T2A and P2A respectively. P2A and T2A are reported to have the highest (>90%) cleaving efficiencies amongst other 2As [43][44] warranting equimolar expression of each reporter gene (Figure 1A). Third-generation packaging and envelop plasmids pMDLg/pRRE, and pRSV-Rev, and pMD2.G (Addgene plasmids #12251, #12253, and #12259, respectively) were combined with the transfer plasmid for the In-Fusion Cloning reaction (Takara Bio USA, Inc.) to transfect human embryonic kidney (HEK 293T) (American Type Culture collection; ATCC) cells with the aid of Lipofectamine 3000 (Thermo Fisher Scientific, Massachusetts, USA) in accordance to the manufacturer's lentiviral production protocol (Thermo Fisher Scientific Inc., Waltham, Massachusetts, United States). Viral-containing supernatant was collected 24 and 48 hours after transfection, filtered with a 0.45 μ m filter and frozen at -80 °C until use.

2.2.3 Cell Transduction

MDA-MB-231 cells were seeded at a density of 5×10^5 cells per well in a 6-well plate on day 0 and then transduced for 6 h on day 1 with the prepared lentivirus and Polybrene (8 μ g/mL; Sigma) at

a multiplicity of infection (MOI) of one. On day 4, naïve and transduced cells were harvested and assessed for zsG expression and sorted using a FACSAria III fluorescence-activated cell sorter (BD Biosciences) to acquire a highly purified population of engineered cells, which we call our MRI/PET cells throughout. Fluorescence microscopy was performed on a LSM Meta 510 microscope (Carl Zeiss AG, Oberkochen, Germany) to confirm the presence of zsG in the MRI/PET cells.

2.2.4 Western Blots

Western blot analysis for both OATP1B3 and NIS was performed using naïve MDA-MB-231 cells, MDA-MB-231 cells expressing OATP1B3 alone and our MRI/PET cells. Cells were incubated with 200- μ L 4 °C RIPA buffer and protease inhibitors for 30 minutes. Lysates were collected and sonicated with three 5.0-s, 40-kHz bursts before centrifugation at 13,000G for 20 minutes at 4 °C. Supernatants were collected and quantified using the Pierce BCA Protein Assay (23225, Thermo Fisher Scientific, Massachusetts, USA). A 40- μ g protein sample was loaded into an acrylamide gel composed of a 4.0% stacking layer buffered at pH 6.8 and a 15% separation layer buffered at pH 8.8. Gel electrophoresis was performed for 20 minutes at 90 V and 1 hour at 110 V. Protein was transferred to a nitrocellulose membrane for 7.5 minutes via the iBlot™ 2 Gel Transfer Device (IB21001, Thermo Fisher Scientific, Waltham, Massachusetts, United States) and blocked with 0.05% Tween-20, 3% w/v BSA solution for 30 minutes. For OATP1B3, a primary purified rabbit antibody against OATP1B3 (1:500 dilution, ab139120, Abcam, Cambridge, United Kingdom) was added for overnight incubation at 4 °C. For the myc-tagged NIS, a mouse anti-myc (9B11, Cell Signaling Technology, Massachusetts, USA) was added at a dilution of 1:1000 for one hour at room temperature. After washing the blot three times with 0.05% Tween-20 solution for 5 minutes, the OATP1B3 secondary antibody, Goat anti-Rabbit IgG (H+L) Highly Cross-Adsorbed

Secondary Antibody, Alexa Fluor 790 was used with a dilution of 1:10,000 (A11369, Thermo Fisher Scientific, Massachusetts, USA) was added for one hour. The blot was washed three times with 0.05% Tween-20 solution for 5 minutes before application of the Goat anti-Mouse IgG (H+L) High Cross-Adsorbed Secondary Antibody, Alexa Fluor Plus 488 with a dilution of 0.1-0.4 µg/mL (A32723, Thermo Fisher Scientific, Massachusetts, USA) for one hour. Lastly, the blot was stripped for GAPDH staining. A primary mouse anti-GAPDH antibody (MAB374, Sigma-Aldrich, Missouri, USA) at a dilution of 1:1000 was applied for one hour at room temperature with subsequent application of secondary antibodies IRDye-800CW and 680RD (Thermo Fisher Scientific, Massachusetts, USA) at dilutions of (1:15,000). Finally, imaging on the Odyssey CLx Imaging System (LI-COR Biosciences, Lincoln, Nebraska, United States) was performed.

2.2.5 In Vitro Gd-EOB-DTPA Uptake and MRI

One million naïve or MRI/PET cells/mL were seeded in two 15-cm-diameter dishes. At 95% cell confluency, a 1.6-mM dose of Gd-EOB-DTPA (Eovist/Primovist®, Bayer Health Care Pharma, Berlin, Germany) was added to each dish and incubated for 60 minutes. Each cell type also had a dish with no Gd-EOB-DTPA addition to serve as the negative control. Media was aspirated and cells were thoroughly washed with $1 \times$ phosphate-buffered saline (PBS) (pH 7.4) three times. Subsequent trypsinization, collection and centrifugation of cells formed cell pellets in 0.2mL Eppendorf tubes. Tubes were imbedded into a 1% agarose gel phantom for MRI imaging with a 3T GE clinical MR scanner (General Electric Healthcare Discovery MR750 3.0 T, Milwaukee, Wisconsin, United States) using a 16-channel head RF coil. A fast spin-echo inversion-recovery pulse sequence, with the below parameters (Table 1), was used to determine spin-lattice relaxation rates by sampling with the following 17 inversion times (TI): 50, 60, 68, 80, 94, 128, 175, 239, 327, 447, 612, 836, 1144, 1564, 2139, 2925, and 4000 ms.

Table 2.1: MRI sequence parameters used for *in vitro* uptake of Gd-EOB-DTPA.

Imaging matrix size	256 x 256
Repetition time (TR)	5000 ms
Echo time (TE)	19.1 ms
Echo train length (ETL)	4
Number of averages (NEX)	1
Receiver bandwidth	24.4 kHz
In-plane resolution	0.27 mm x 0.27 mm
Slice thickness	2.0 mm

MatLab (R2018a, MathWorks, Natick, Massachusetts, United States) was used to evaluate spin-lattice relaxation rates by overlaying the image series of the different inversion times and computing the average signal intensity for each cell pellet. The data were fitted with Equation 1 to determine the spin lattice relaxation time (T_1).

$$S = M_0(1 - 2e^{(-\frac{TI}{T_1})} + e^{(-\frac{TR}{T_1})}) \quad \text{Equation 1}$$

Here, S represents the acquired signal intensity, M_0 is the magnetization in steady state, TI is the inversion time, and TR is the repetition time.

2.2.6 In Vitro [^{18}F]TFB Tracer Uptake

[^{18}F]TFB was synthesized as described previously [41] with 98.7±2% purity. [^{18}F]TFB uptake studies were performed with naïve and MRI/PET cells. Cells were seeded in a 6-well dish (5×10^5 cells/well) and incubated (37 °C with 5% CO_2) overnight. DMEM was aspirated and cells were

washed with $1 \times$ PBS. Fresh DMEM was added (2mL/well) followed by addition of 0.1MBq of ^{18}F -TFB to each well. Cells were incubated for 30 minutes prior to their collection. Activity of harvested cells as well as the activity in the supernatant was measured using a gamma counter. Counts were decay-corrected and tracer uptake was calculated as the average counts per minute (cpm) of activity detected using the following equation.

$$Uptake (\%) = \frac{CPM_{cells}}{(CPM_{cells} + CPM_{supernatant})} \times 100\% \quad \text{Equation 2}$$

2.2.7 Animal Model

All applicable institutional and/or national guidelines for the care and use of animals were followed. Naïve and MRI/PET MDA-MB-231 cells were implanted into the left and right mammary fat pad, respectively, of female nod scid gamma (NSG) mice (n=3). Tumors were allowed to form for ~2-3 weeks and imaging was performed on days 19 with PET, 31 and 35 with MRI post-implantation.

2.2.8 In Vivo Gd-EOB-DTPA- enhanced MRI

T_1 -weighted 3T-MRI was performed pre and 4.5h post tail-vein injection of 1 mmol/kg Gd-EOB-DTPA. To evaluate signal resulting from agent uptake and retention, one mouse implanted with separate naïve and engineered tumors was serially imaged for approximately 5 hours after Gd-EOB-DTPA intravenous and intraperitoneal injections on separate days. Gd-EOB-DTPA was administered by IV tail injections on day 31 post tumor implantation and by IP injections on day 35 post-tumor implantation in 3 NSG mice, to assess different delivery methods. All mice were anesthetized with 1-2% isoflurane during imaging sessions with the use of a nose cone attached to a carbon charcoal filter for passive scavenging. Mice respiration rates during acquisition were between 40-70 bpm and body temperature was maintained between 37 and 38 °C using a regulated

heating pad. A 3D Spoiled Gradient Recalled Acquisition in Steady State (SPRG) pulse sequence with a 3.5-cm diameter birdcage RF coil (Morris Instruments, Ottawa, ON, Canada) and a custom-built gradient insert were used with the below parameters (Table 2) for a scan time of approximately 15 minutes.

Table 2.2: MRI sequence parameters used for *in vivo* mice imaging.

Imaging matrix size	250x250
Repetition time (TR)	14.7 ms
Echo time (TE)	3.3 ms
Number of averages (NEX)	3
Flip angle	60°
Field of view (FOV)	50 mm
Bandwidth	24.4 kHz
In-plane Resolution	0.2 mm x 0.2 mm
Slice thickness	0.2 mm

Horos Project software v3.3.6 (horosproject.org, Nimble Co LLC d/b/a Purview, Annapolis, Maryland, United States) was used to manually segment regions-of-interest (ROIs) to acquire measures of signal intensity on pre-contrast and post-contrast images in naïve, MRI/PET tumors as well as other organs (muscle, kidney, liver, and bladder).

2.2.9 In Vivo [¹⁸F]TFB PET

Nineteen days post cell implantation, mice were anesthetized with 2% isoflurane, injected with 13-15 MBq of [¹⁸F]TFB in 50-150 μ L and imaged dynamically with a microPET system (Siemens Inveon ©2011 by Siemens Medical Solutions USA, Inc.). Animal breathing rate and body temperature were monitored and maintained between 40-70 bpm and at 37 °C, respectively. Dynamic PET data were acquired for 40 minutes, and images were reconstructed using 2D filtered back projection. Quantification of PET signal was performed by manual segmentation of ROIs using Horos Project software v3.3.6. Maximum Activity Projections (MAPs) were generated. SUV was calculated with the below equation:

$$SUV \left(\frac{g}{mL} \right) = \frac{Pixel\ value \left(\frac{Bq}{mL} \right) * weight\ (kg)}{Dose\ (Bq)} * 1000 \left(\frac{g}{kg} \right). \quad Equation\ 3$$

2.2.10 Histology and Immunofluorescence Staining

Appendices figure 2.1 shows the H&E staining of both naïve and MRI/PET cells on the left panels. Cells were grown on a coverslip, fixed in 4% PFA, permeabilized with Triton X-100 for 10 minutes and incubated for one hour at room temperature with rabbit anti-SLCO1B3 (OATP1B3) primary antibody (2- μ g/mL working concentration, HPA004943, Sigma-Aldrich Canada, Oakville, Ontario, Canada). Secondary Goat anti-rabbit AlexaFluor 647-conjugated secondary antibody was then applied for one hour (1:500 dilution; 4- μ g/ml working concentration, ab150079, Lot E114795, Abcam, Cambridge, Massachusetts, United States). Mouse anti-NIS primary antibody was used at a dilution of 1:100 (113168, SLC5A5 Polyclonal Antibody, Thermo Fisher Scientific Inc., Massachusetts, United States) for 2 hours at room temperature. Coverslips were washed three times with PBS and secondary antibody Goat anti-rabbit at a dilution of 1:200 (Alexa Fluor® 488, Thermo Fisher Scientific Inc., Massachusetts, United States) was used for one hour. Cells were

counterstained with DAPI for 5 minutes and imaged with the LSM Meta 510 microscope (Carl Zeiss AG, Oberkochen, Germany).

2.2.11 Statistics

Unpaired two-tailed t tests were performed using Graphpad Prism software (Version 7.00 for Mac OS X, GraphPad Software Inc., La Jolla California USA, www.graphpad.com) for cell characterization after Gd-EOB-DTPA and [^{18}F]TFB incubation and comparing MRI data between IP and IV at 5 hours. Repeated measures of ANOVA were used for SUV comparisons. All data are expressed as mean \pm standard deviation, of at least three independent experiments. P-values <0.05 were considered statistically significant.

2.3 Results

Human breast cancer cells were engineered to stably co-express NIS, OATP1B3, and zsG using a lentivirus produced using the transfer plasmid shown in Fig. 2.1A. Flow cytometry showed no zsG expression in naïve cells and a 93% transduction efficiency in the dual reporter gene system containing zsG (Fig. 2.1B). Fluorescence microscopy confirmed zsG positive cells in the MRI/PET cells and no zsG in naïve cells (Fig. 2.1C). Western blots confirmed the presence of both transporters in the MRI/PET cells with a band at 100 kDa corresponding to NIS and a 90 kDa band for the OATP1B3 protein (Fig. 2.1 D). These bands were not observed for the naïve cells.

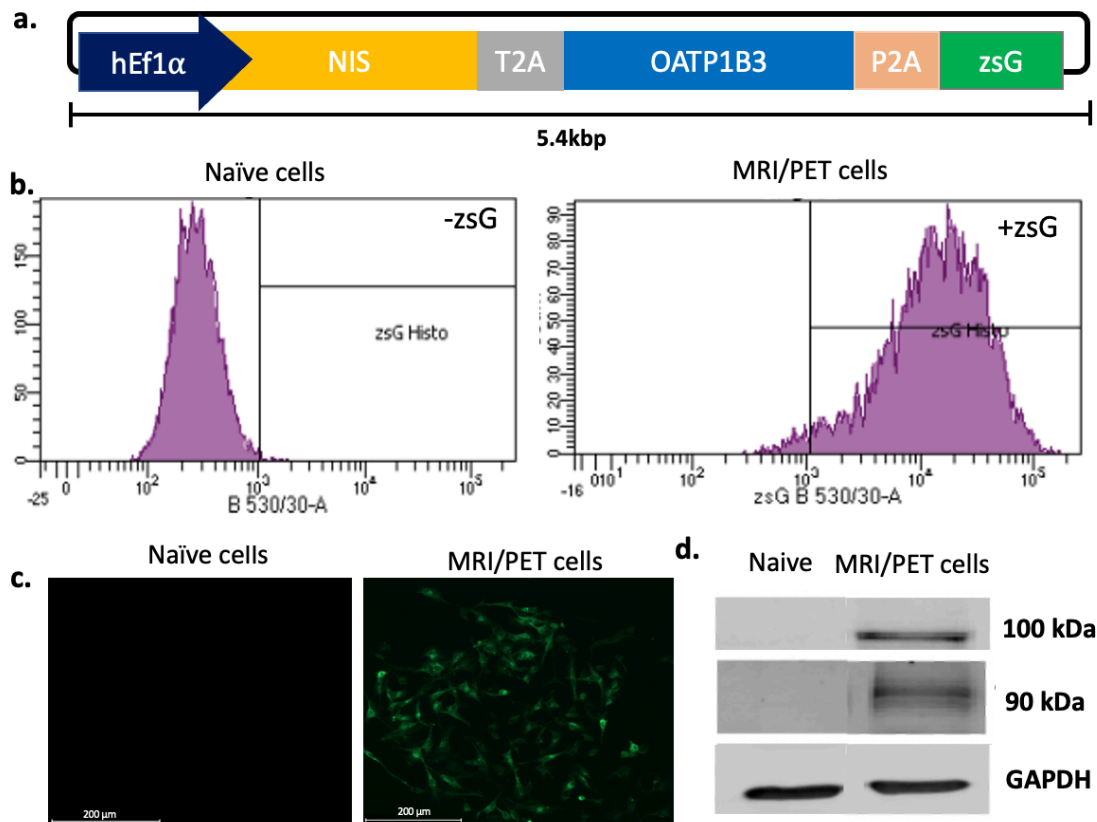


Figure 2.1: (A) Diagram of hEf1α-hNIS-T2A-OATP1B3-P2A-zsG lentiviral construct used to engineer MDA-MB-231 triple negative cells. (B) Flow cytometry showing naïve cells with no zsG expression and transduced MRI/PET cells with 93% transduction efficiency post-sort. (C) Fluorescence microscopy images showing no zsG in naïve cells and MRI/PET cells showing zsG fluorescence signal. (D) Western Blots of naïve and transduced cells showing the NIS and OATP1B3 bands at their corresponding sizes (100 and 90 kDa, respectively) and their absence in the naïve cells.

Next, we evaluated reporter gene functionality *in vitro*. MRI/PET cells incubated with Gd-EOB-DTPA resulted in a 38% higher R_1 value compared to naïve cells incubated with Gd-EOB-DTPA ($p<0.05$). Average R_1 for naïve cells was 0.76 ± 0.08 Hz, compared to 1.05 ± 0.12 Hz for MRI/PET cells (Fig. 2.2B). Similarly, cells were also incubated with 0.1 MBq of [^{18}F]TFB for one hour and the percentage activity uptake was retrieved with a gamma counter. NIS-OATP1B3 cells incubated with [^{18}F]TFB had uptake of $14.2\pm1.3\%$ compared to $0.31 \pm 0.18\%$ uptake of naïve cells, revealing a 45-fold higher ($p<0.001$) uptake in the dual-reporter gene cells as shown in Fig. 2.2C. Additionally, functionality test results for Gd-EOB-DTPA uptake in Naïve, NIS/zsG, OATP1B3/zsG and NIS/OATP1B3/zsG cells, showing non-significant uptake between OATP1B3/zsG and NIS/OATP1B3/zsG cells is shown in Appendices figure 2.2.

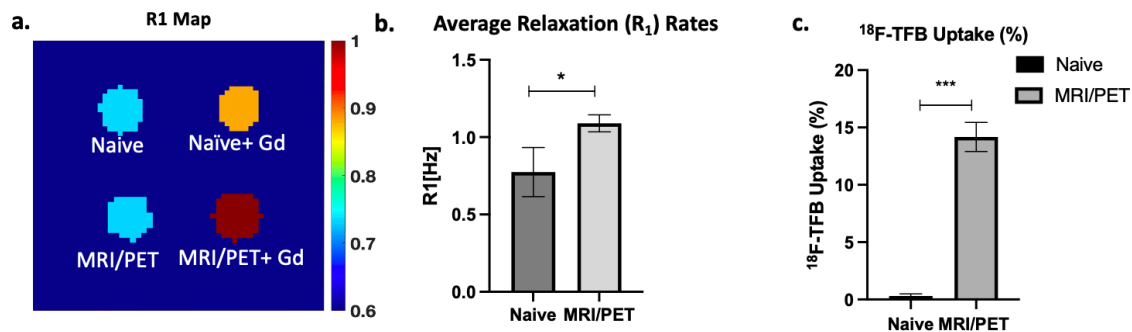


Figure 2.2: (A) An average R_1 map in naïve and MRI/PET cells without and with incubation of Gd-EOB-DTPA. (B) R_1 values (38% higher) in MRI/PET cells incubated with the Gd-EOB-DTPA was found significantly higher ($p < 0.05$) compared to the naïve cells incubated with the agent. (C) [^{18}F]TFB percent uptake was calculated as $0.31 \pm 0.18\%$ in naïve cells, whereas significantly higher uptake was seen in MRI/PET cells ($14.2 \pm 1.3\%$; * $p < 0.001$).

2.3.1 In-Vivo Gd-EOB-DTPA- enhanced OATP1B3 MRI: Intravenous (IV) versus Intraperitoneal (IP) Gd-EOB-DTPA administration

Typical OATP1/Gd-EOB-DTPA reporter gene imaging is performed ~4-6 hours post IV administration[27]. Several studies have compared contrast enhancement in MRI using both an IP and IV method of agent administration, and have shown IP as an alternative delivery route that yields comparable contrast enhancement to IV [45][46]. The dynamics of the MRI/PET cells to accumulate Gd-EOB-DTPA *in-vivo* through IV or IP administration was investigated 30 days post tumor implantation in one mouse. This longitudinal study was only performed on one mouse as per our institution requirements. Fig.3A shows dynamic coronal images over the course of ~4.5 hours with both naïve (left) and MRI/PET (right) tumors post IV administration of the Gd-EOB-DTPA with a dose of 1 mmol/kg. As expected, no differences in signal were apparent between the tumors in the pre-contrast image. Post-contrast images showed obvious contrast enhancement only in the MRI/PET tumor, with enhancement being heterogenous within the tumor (Fig. 2.3C). Image analysis revealed higher signal intensity in the dual MRI/PET compared to naïve tumor (Fig. 2.3B) within one-hour post injection of Gd-EOB-DTPA with relatively constant uptake for the remaining of the imaging period. Contrast enhancement was also observed in the liver presumably through uptake by endogenous murine OATP1A1 expression (Appendices Figure 2.3).

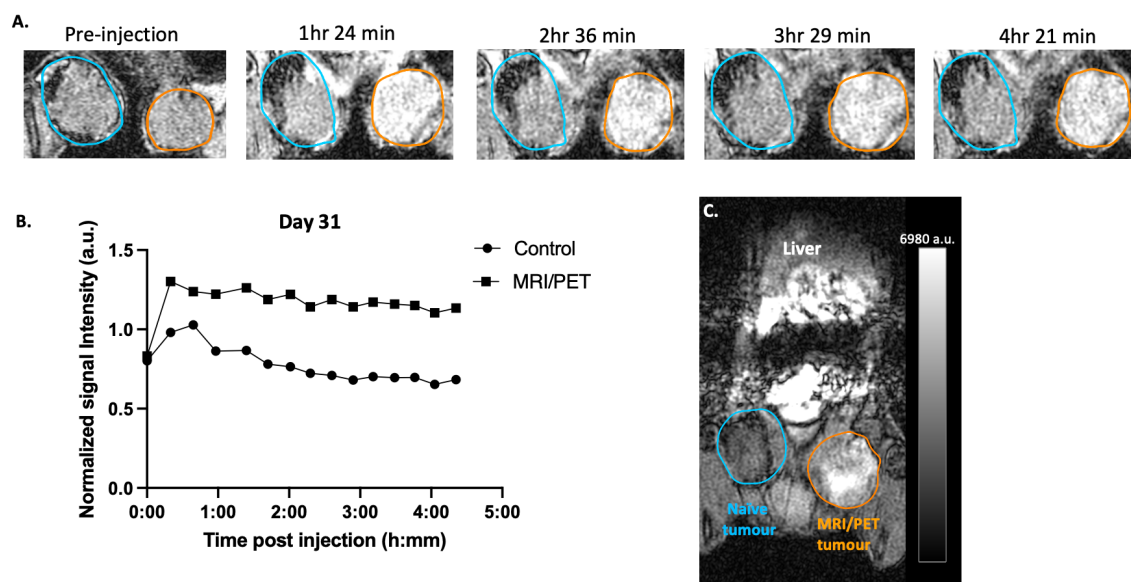


Figure 2.3: (A) Dynamic coronal $T1$ -w MRI images of lower mammary fat pads of an NSG mouse after IV Gd-EOB-DTPA injection. Manual segmentation showing naïve (left; blue outline) and MRI/PET (right; orange outline) tumors pre- and post-IV administration of Gd-EOB-DTPA. (B) Enhanced contrast and higher normalized (to muscle tissue) signal intensities are shown in the MRI/PET tumor. (C) Contrast enhancement was also observed in endogenous tissue and clearance into the intestines.

The same mouse in Fig. 2.3 was dynamically imaged again at 34 days post tumor implantation for about 5.5 hours using the same MR imaging parameters but with an IP delivery of Gd-EOB-DTPA (1 mmol/kg). It should be noted that due to the mean clearance half-life of Gd-EOB-DTPA (55-57 minutes), <1% of the agent amount is expected to remain 24 hours post administration. Figure 4A shows select MRI images pre-and post-Gd-EOB-DTPA administration with IP injection. At around 1.5 hours, contrast enhancement surrounding both naïve and MRI/PET mammary fat pad tumors is present. Over time, more agent accumulates intratumorally in the MRI/PET tumor compared to the naïve tumor, corresponding to higher T_1 -weighted signal intensities (Fig.2.5B). Again, heterogeneous enhancement within the MRI/PET tumors was noted. Contrast enhancement in the liver with natural OATP1 expression was also observed (Appendices Figure 2.3). Appendices figure 2.5 shows the difference in signal intensity between MRI/PET and naïve tumours in our dynamic imaging, for both IV and IP injection, showing the highest difference after approximately 2.5 hours for IV and 5 hours for IP injection.

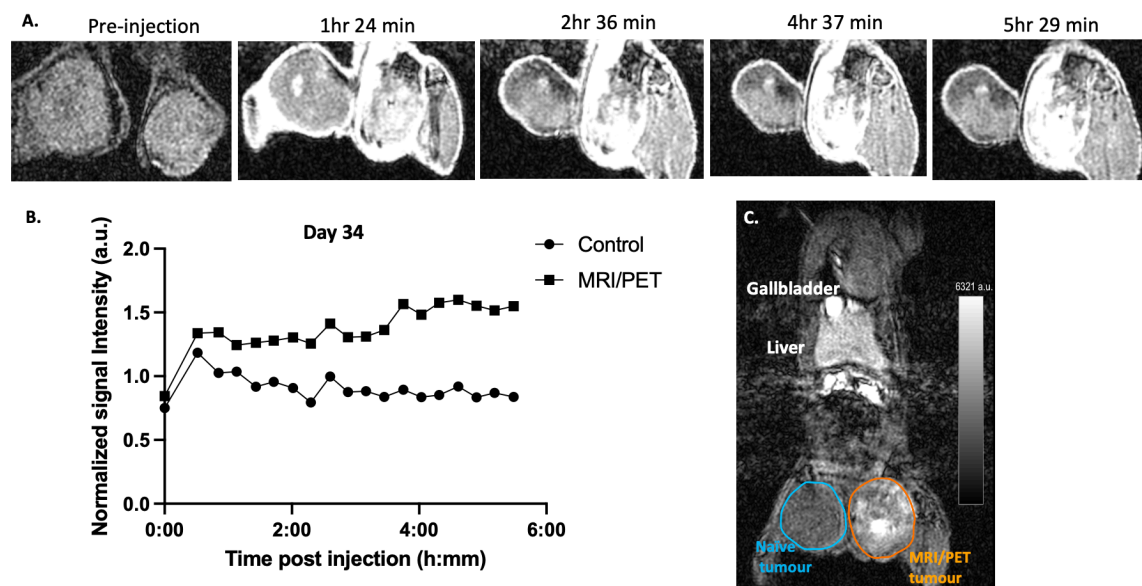


Figure 2.4: (A) Dynamic coronal $T1$ -w MRI images of lower mammary fat pads of an NSG mouse after IP Gd-EOB-DTPA injection. Manual segmentation showing naïve (left) and NIS-OATP1B3 (right) tumors pre- and post-IP administration of Gd-EOB-DTPA. (B) Higher normalized (to muscle tissue) signal intensities are shown in the NIS-OATP1B3 tumor compared to the naïve tumor. (C) Contrast enhancement was also observed in the liver.

Figure 2.5 shows pre- and approximately 5 hours post-Gd-EOB-DTPA injection with both IV (top) and IP (bottom) delivery routes (Appendices Figure 2.4 shows representative examples at selective time points). Differences in signal enhancement are evident between the naïve and the MRI/PET tumor approximately 5 hours post agent administration with both delivery methods. Significantly higher ($p<0.05$) average signal intensity was observed in MRI/PET tumors compared to naïve tumors in all three mice for both IV and IP administration of Gd-EOB-DTPA (B). No differences in signal intensity were seen between IV or IP injection route at this time point post-Gd-EOB-DTPA injection.

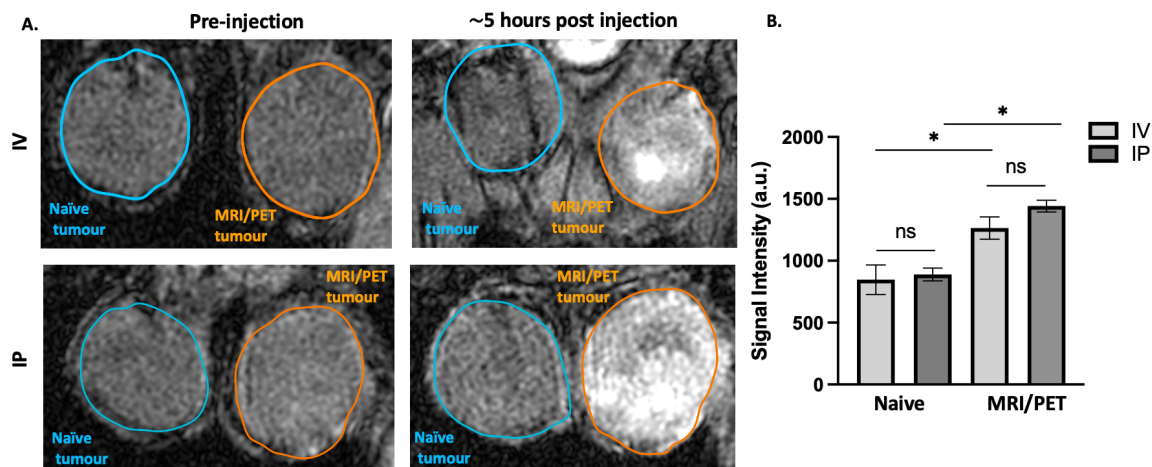


Figure 2.5: (A) Representative *T1*-weighted MRI images showing pre- and approximately 5 hours post- IV (top) and IP (bottom) injection of Gd-EOB-DTPA in two different mice. (B) Contrast enhancement observed in MRI/PET tumors post- Gd-EOB-DTPA injection, with both IV and IP administration methods. No contrast enhancement was observed in the naïve tumors post agent administration. Significantly higher average signal intensity between MRI/PET tumors and naïve tumors was observed, for both IV and IP agent administration and no significant difference in average signal intensity between IV and IP delivery methods was observed for either naïve or MRI/PET tumors (n=3) at 5 hours post injection.

In-Vivo [¹⁸F]TFB NIS PET

Mice bearing contralateral naïve and MRI/PET mammary fat pad tumors received 13-15 MBq of [¹⁸F]TFB via tail vein injection, and dynamic PET imaging was performed for 40 minutes (Fig. 2.6). Rapid accumulation of [¹⁸F]TFB in NIS expressing tissue was observed within 10 minutes of injection (Fig. 2.6A/B). As expected, whole body PET mean activity projections (MAPs) displayed regions of [¹⁸F]TFB uptake in the salivary glands, thyroid, and stomach which correspond to sites of endogenous mouse NIS expression. SUV values in the thyroid and stomach over time are shown in Appendices Figure 2.6. Tracer uptake was also observed in the engineered MRI/PET tumor, but not in the naïve tumor (Fig. 2.6A and 2.6 C). Qualitatively, unlike with our MRI results, local differences in tracer uptake in different regions within tumors were difficult to visualize in our PET images due to the image resolution. The average SUV was calculated for mice at different time-points during the 40-minute scan (Fig. 2.3B). Significantly higher SUVs were observed for MRI/PET tumor compared to naïve tumors 10, 15, 20, 25, 30, 35, and 40 minutes after tracer injection ($p < 0.05$).

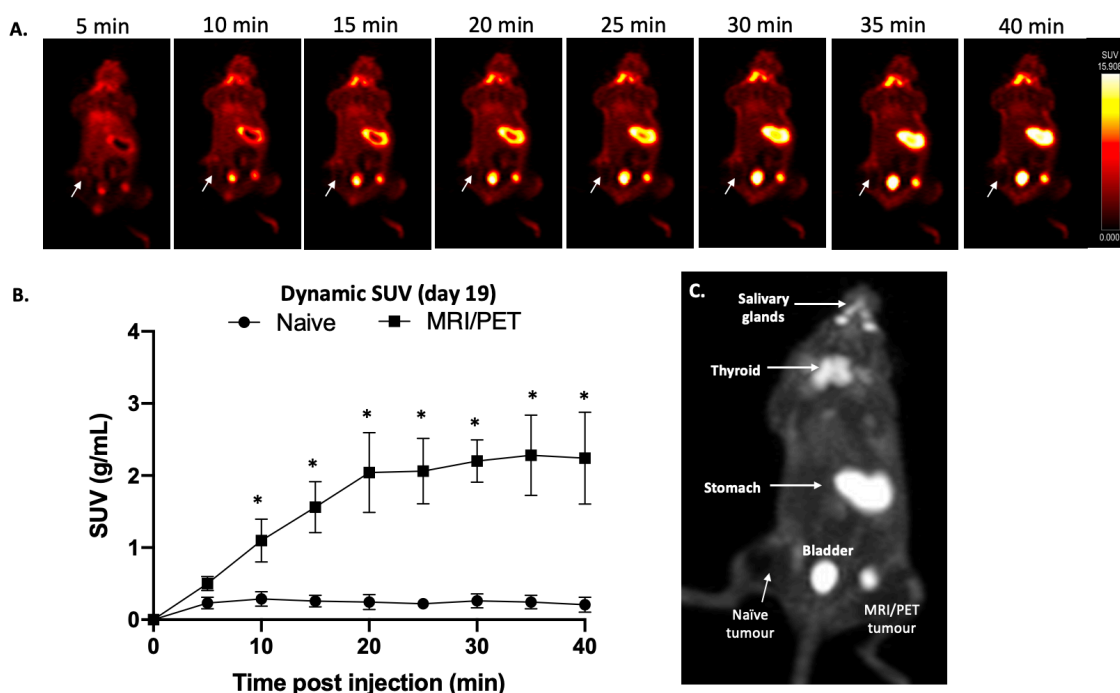


Figure 2.6: (A) Dynamic MAPs showing whole body PET coronal images and uptake of [^{18}F]TFB for 40 minutes. (B) Average SUV (g/mL) for 3 mice at different time points showed significantly higher for MRI/PET tumors compared to naïve tumors ($p < 0.05$) using repeated measures of ANOVA. (C) Displaying [^{18}F]TFB uptake in NIS-expressing tissue (salivary glands, thyroid, stomach), MRI/PET tumor (denoted with arrowhead), and the bladder ([^{18}F]TFB clearance).

2.4 Discussion

The use of multiple modalities is advantageous as it harnesses complementary information from individual modalities to provide more comprehensive assessment of the activity and fate of administered cells. Sensitive imaging modalities often suffer from relatively lower resolution (BLI, PET, SPECT), whereas less sensitive modalities may provide fine spatial resolution (MRI) [24]. As a result, multi-modal tracking is often undertaken with a combination of a sensitive and spatially resolving modalities [47]. However, current multi-modal cell tracking methods possess limitations either in their safety profiles [14][48], their imaging sensitivity [49][50][51], their preclinical status [19][52] or their ability for long-term tracking [53][54], limiting their translational potential.

For this work, we combine two clinical systems to exploit the sensitivity and quantification of PET and the higher spatial resolution and soft-tissue contrast of MRI. We have developed a novel multi-modal cell tracking system using MRI and PET human-derived reporter genes that can provide safe, sensitive, and quantitative information for longitudinal tracking.

We employed the human-derived OATP1B3 gene as an MRI reporter gene for our system. This transporter can transport the clinical Gd-EOB-DTPA MRI contrast agent into cells. Once internalized, the Gd-EOB-DTPA enhances contrast on T_1 -weighted images to improve the conspicuity of engineered cells. Previous work by Brindle's group showed maximal contrast enhancement in T_1 -weighted images 5 hours post IV injection of Gd-EOB-DTPA in OATP1A1-expressing cells [55]. In this work, we performed dynamic imaging to determine the optimal timing of the maximum contrast uptake within our OATB1B3-engineered tumors.

We also compared the contrast enhancement of the Gd-EOB-DTPA agent via two administration routes: intravenously (IV) and intraperitoneally (IP). Although probes are typically administered intravenously, IP administration is a technically easier injection that has shown comparable contrast enhancement and can be used as a substitute to IV injections in small animal models for targeting and trapping agents [45][46]. However, IP pharmacokinetics dictate that the contrast material would be absorbed into the peritoneal cavity and eventually drain into the portal vein for hepatic metabolism before reaching systemic circulation, resulting in slower delivery of the agent when compared to IV injection routes. Maximum contrast enhancement was achieved approximately two hours post both IV and IP injection routes, and significant enhancement endured for the remaining of the imaging period (~5 hours). Thus, the OATP1B3 gene demonstrated genuine potential for cell tracking in gadolinium-enhanced MRI with both IV and IP delivery methods of the Gd-EOB-DTPA contrast agent.

NIS was employed as the PET reporter gene for this system and its expression was imaged with PET following administration of its clinical tracer, [^{18}F]TFB. Our dual MRI/PET reporter system also showed significant uptake of [^{18}F]TFB ($p < 0.001$) *in vitro*, and higher ($p < 0.05$) *in vivo* SUV in the NIS-expressing tumors compared to the naïve tumors.

An additional qualitative difference between the PET and MRI images is the ability to distinguish intratumoral heterogeneity of signal enhancement. While PET is more sensitive, we were only able to see heterogenous contrast enhancement in the OATP1B3-expressing tumours in the MRI images. Previous work from our lab has shown this variation in contrast enhancement corresponds to the spatial distribution of viable OATP1A1-expressing cells [56].

Advances in cellular therapies have demonstrated anti-tumor effects by modifying a variety of cell types to boost their targeting and killing abilities [57]. *In vivo* tracking of these therapeutic cells can reveal information regarding their cellular interactions, therapeutic efficacy as well as potential side effects [47]. In addition to assessing the number of therapeutic cells within tumors, it is also important to evaluate their tumour localization and distribution. Thus, combining the quantitative nature of PET and the fine resolution of MRI can produce information on both the cell numbers, and their location, respectively.

Ideally for safety concerns, reporter genes should be human-derived genes as opposed to exogenous reporter genes (luciferase or fluorescent protein) which can trigger an immune response. Indeed the virally-derived PET reporter gene herpes simplex virus thymidine kinase has been shown to be immunogenic in human [58], highlighting a need to reduce immunogenicity via protein engineering or utilizing human-derived reporter genes. NIS and OATP1B3 are both endogenous human genes, making them non-immunogenic to facilitate clinical translation. Furthermore, both imaging probes ($[^{18}\text{F}]\text{TFB}$ and Gd-EOB-DTPA) are already widely in clinical use with PET and MRI respectively, further giving this system high translational potential. Repeated administration of these imaging probes allows for longitudinal tracking to be accomplished in reporter gene systems for a specific application. Administration of $[^{18}\text{F}]\text{TFB}$ for detection of NIS expression with PET can provide sensitive and quantifiable information, and detection at an earlier timepoint but may be limited by cost, availability and perceived concerns regarding radiation. In contrast, Gd-EOB-DTPA can be repetitively administered to facilitate longitudinal tracking of engineered cells with MRI. Moreover, the fine spatial resolution of MRI images can show intratumoral heterogeneity of the viable engineered cells. Heterogeneity due to differences in biodistribution within the control tumour is most likely seen during the early phases

after Gd-EOB-DTPA administration, when non-specific uptake into the extracellular space is dominant. At earlier time points, there is non-specific uptake in both control and MRI/PET tumours (following both IV- and IP- injections). Over time, there is no significant Gd-EOB-DTPA enhancement in control tumours and uptake is specific to OATP1B3-expressing cells.

This study validates a new dual PET and MRI reporter gene system for *in vivo* cell tracking. Future incorporation of this dual reporter gene system in other cell types, such as T lymphocytes, natural killer (NK) cells, mesenchymal stem cells, or dendritic cells, could provide valuable information for more clinically relevant applications. Additionally, novel gene integration systems such as CRISPR/Cas with the ability to target safe genomic sites could further improve the safety of this cell-tracking multi-modal reporter gene system while reducing the chances of unwanted biological effects on the cells [59].

In this work, MRI and PET were used to detect cells longitudinally. To our knowledge this is the first time this combination of clinical imaging modalities has been used, with reporter gene imaging. We demonstrated that we could use multi-modal imaging system to visualize human-derived MRI/PET reporter gene- expressing cells, enabling more comprehensive understanding of administered cells. Future applications of such systems can be used for tracking therapeutic cells.

2.5 References

1. Ashmore-Harris C, Iafrate M, Saleem A, Fruhwirth GO (2020) Non-invasive Reporter Gene Imaging of Cell Therapies, including T Cells and Stem Cells. *Mol Ther* 28:. <https://doi.org/10.1016/j.ymthe.2020.03.016>
2. Yang Z, Wang Y, Li Y, et al (2014) Options for tracking GFP-Labeled transplanted myoblasts using in vivo fluorescence imaging: Implications for tracking stem cell fate. *BMC Biotechnol* 14:1–8. <https://doi.org/10.1186/1472-6750-14-55>
3. Xu X, Yang Z, Liu Q, Wang Y (2010) In vivo fluorescence imaging of muscle cell regeneration by transplanted EGFP-labeled myoblasts. *Mol Ther* 18:835–842. <https://doi.org/10.1038/mt.2010.3>
4. Winnard PT, Kluth JB, Raman V (2006) Noninvasive optical tracking of red fluorescent protein-expressing cancer cells in a model of metastatic breast cancer. *Neoplasia* 8:796–806. <https://doi.org/10.1593/neo.06304>
5. Conway M, Xu T, Kirkpatrick A, et al (2020) Real-time tracking of stem cell viability, proliferation, and differentiation with autonomous bioluminescence imaging. *BMC Biol* 18:79. <https://doi.org/10.1186/s12915-020-00815-2>
6. Parkins KM, Dubois VP, Kelly JJ, et al (2020) Engineering circulating tumor cells as novel cancer theranostics. *Theranostics* 10:7925–7937. <https://doi.org/10.7150/thno.44259>
7. Bar-Shir A, Alon L, Korrer MJ, et al (2018) Quantification and tracking of genetically engineered dendritic cells for studying immunotherapy. *Magn Reson Med* 79:1010–1019. <https://doi.org/10.1002/mrm.26708>
8. Kim HS, Woo J, Lee JH, et al (2015) In vivo Tracking of Dendritic Cell using MRI Reporter Gene, Ferritin. *PLoS One* 10:e0125291. <https://doi.org/10.1371/journal.pone.0125291>
9. Nyström NN, Hamilton AM, Xia W, et al (2019) Longitudinal Visualization of Viable Cancer Cell Intratumoral Distribution in Mouse Models Using Oatp1a1 -Enhanced

- Magnetic Resonance Imaging. *Invest Radiol* 54:302–311.
<https://doi.org/10.1097/RLI.0000000000000542>
10. Bourdeau RW, Lee-Gosselin A, Lakshmanan A, et al (2018) Acoustic reporter genes for noninvasive imaging of microorganisms in mammalian hosts. *Nature* 553:86–90.
<https://doi.org/10.1038/nature25021>
 11. Farhadi A, Ho GH, Sawyer DP, et al (2019) Ultrasound imaging of gene expression in mammalian cells. *Science* (80-) 365:1469–1475. <https://doi.org/10.1126/science.aax4804>
 12. Nyström NN, Yip LCM, Carson JJJ, et al (2019) Development of a Human Photoacoustic Imaging Reporter Gene Using the Clinical Dye Indocyanine Green. *Radiol Imaging Cancer* 1:e190035. <https://doi.org/10.1148/rycan.2019190035>
 13. Yaghoubi SS, Campbell DO, Radu CG, Czernin J (2012) Positron emission tomography reporter genes and reporter probes: Gene and cell therapy applications. *Theranostics* 2:374–391
 14. Keu KV, Witney TH, Yaghoubi S, et al (2017) Reporter gene imaging of targeted T cell immunotherapy in recurrent glioma. *Sci Transl Med* 9:.
<https://doi.org/10.1126/scitranslmed.aag2196>
 15. Gschwend EH, McCracken MN, Kaufman ML, et al (2014) HSV-sr39TK positron emission tomography and suicide gene elimination of human hematopoietic stem cells and their progeny in humanized mice. *Cancer Res* 74:5173–5183.
<https://doi.org/10.1158/0008-5472.CAN-14-0376>
 16. Yaghoubi SS, Jensen MC, Satyamurthy N, et al (2009) Noninvasive detection of therapeutic cytolytic T cells with ¹⁸F-FHBG PET in a patient with glioma. *Nat Clin Pract Oncol* 6:53–58. <https://doi.org/10.1038/ncponc1278>
 17. Pomper MG, Hammond H, Yu X, et al (2008) Serial imaging of human embryonic stem-cell engraftment and teratoma formation in live mouse models. *Cell Res* 2009 193 19:370–379. <https://doi.org/10.1038/cr.2008.329>

18. Y W, WY Z, S H, et al (2012) Genome editing of human embryonic stem cells and induced pluripotent stem cells with zinc finger nucleases for cellular imaging. *Circ Res* 111:1494–1503. <https://doi.org/10.1161/CIRCRESAHA.112.274969>
19. Z L, F W, J D, et al (2007) Imaging of mesenchymal stem cell transplant by bioluminescence and PET. *J Nucl Med* 48:2011–2020. <https://doi.org/10.2967/JNUMED.107.043166>
20. E W, B H, L O, et al (2017) Molecular Imaging of Human Embryonic Stem Cells Stably Expressing Human PET Reporter Genes After Zinc Finger Nuclease-Mediated Genome Editing. *J Nucl Med* 58:1659–1665. <https://doi.org/10.2967/JNUMED.117.189779>
21. H T, X L, H G, et al (2012) Radio-deoxynucleoside Analogs used for Imaging tk Expression in a Transgenic Mouse Model of Induced Hepatocellular Carcinoma. *Theranostics* 2:597–606. <https://doi.org/10.7150/THNO.3371>
22. Lin KM, Hsu C-H, Chang W-SW, et al (2008) Human Breast Tumor Cells Express Multimodal Imaging Reporter Genes. *Mol Imaging Biol* 2008 105 10:253–263. <https://doi.org/10.1007/S11307-008-0147-2>
23. Yan X, Ray P, Paulmurugan R, et al (2013) A Transgenic Tri-Modality Reporter Mouse. *PLoS One* 8:e73580. <https://doi.org/10.1371/JOURNAL.PONE.0073580>
24. Xing Y, Zhao J, Conti PS, Chen K (2014) Radiolabeled nanoparticles for multimodality tumor imaging. *Theranostics* 4:290–306
25. Zhou Y, Yuan J, Li Z, et al (2015) Genetic Polymorphisms and Function of the Organic Anion-Transporting Polypeptide 1A2 and Its Clinical Relevance in Drug Disposition. *Pharmacology* 95:201–208. <https://doi.org/10.1159/000381313>
26. Jacquemin E, Hagenbuch B, Stieger B, et al (1994) Dual-modality gene reporter for in vivo imaging. *Proc Natl Acad Sci U S A* 91:133–7. <https://doi.org/10.1073/pnas.91.1.133>
27. Jacquemin E, Hagenbuch B, Stieger B, et al (2014) Expression cloning of a rat liver Na(+)-independent organic anion transporter. *PNAS* 91:133–137.

<https://doi.org/10.1073/pnas.91.1.133>

28. Leonhardt M, Keiser M, Oswald S, et al (2010) Hepatic uptake of the magnetic resonance imaging contrast agent Gd-EOB-DTPA: Role of human organic anion transporters. *Drug Metab Dispos* 38:1024–1028. <https://doi.org/10.1124/dmd.110.032862>
29. Wu M-R, Liu H-M, Lu C-W, et al (2018) Organic anion-transporting polypeptide 1B3 as a dual reporter gene for fluorescence and magnetic resonance imaging. *FASEB J* 32:1705–1715. <https://doi.org/10.1096/fj.201700767R>
30. Baek SE, Ul-Haq A, Kim DH, et al (2020) Human organic anion transporting polypeptide 1B3 applied as an MRI-based reporter gene. *Korean J Radiol* 21:726–735. <https://doi.org/10.3348/kjr.2019.0903>
31. Sharif-Paghaleh E, Sunassee K, Tavaré R, et al (2011) In vivo SPECT reporter gene imaging of regulatory T cells. *PLoS One* 6:. <https://doi.org/10.1371/journal.pone.0025857>
32. Punzón I, Mauduit D, Holvoet B, et al (2020) In Vivo Myoblasts Tracking Using the Sodium Iodide Symporter Gene Expression in Dogs. *Mol Ther - Methods Clin Dev* 17:317–327. <https://doi.org/10.1016/j.omtm.2019.12.011>
33. Volpe A, Man F, Lim L, et al (2018) Radionuclide-fluorescence Reporter Gene Imaging to Track Tumor Progression in Rodent Tumor Models. *J Vis Exp*. <https://doi.org/10.3791/57088>
34. Lee SB, Lee HW, Lee H, et al (2017) Tracking dendritic cell migration into lymph nodes by using a novel PET probe 18F-tetrafluoroborate for sodium/iodide symporter. *EJNMMI Res* 7:. <https://doi.org/10.1186/s13550-017-0280-5>
35. Ahn BC (2012) Sodium iodide symporter for nuclear molecular imaging and gene therapy: From bedside to bench and back. *Theranostics* 2:392–402
36. Penheiter AR, Russell SJ, Carlson SK (2012) The Sodium Iodide Symporter (NIS) as an Imaging Reporter for Gene, Viral, and Cell-based Therapies. *Curr Gene Ther* 12:33. <https://doi.org/10.2174/156652312799789235>

37. Willhauck MJ, Sharif Samani B-R, Gildehaus F-J, et al (2007) Application of ¹⁸⁸Rhenium as an Alternative Radionuclide for Treatment of Prostate Cancer after Tumor-Specific Sodium Iodide Symporter Gene Expression. *J Clin Endocrinol Metab* 92:4451–4458. <https://doi.org/10.1210/jc.2007-0402>
38. Smit JWA, Schröder-Van Der Elst JP, Karperien M, et al (2002) Iodide kinetics and experimental ¹³¹I therapy in a xenotransplanted human sodium-iodide symporter-transfected human follicular thyroid carcinoma cell line. *J Clin Endocrinol Metab* 87:1247–1253. <https://doi.org/10.1210/jcem.87.3.8307>
39. Jiang H, DeGrado TR (2018) [¹⁸F]Tetrafluoroborate ([¹⁸F]TFB) and its analogs for PET imaging of the sodium/iodide symporter. *Theranostics* 8:3918–3931. <https://doi.org/10.7150/thno.24997>
40. Weeks AJ, Jauregui-Osoro M, Cleij M, et al (2011) Evaluation of [¹⁸F]-tetrafluoroborate as a potential PET imaging agent for the human sodium/iodide symporter in a new colon carcinoma cell line, HCT116, expressing hNIS. *Nucl Med Commun* 32:98–105. <https://doi.org/10.1097/MNM.0b013e3283419540>
41. Jiang H, Bansal A, Pandey MK, et al (2016) Synthesis of ¹⁸F-Tetrafluoroborate via radiofluorination of boron trifluoride and evaluation in a murine C6-Glioma tumor model. *J Nucl Med* 57:1454–1459. <https://doi.org/10.2967/jnumed.115.170894>
42. Diocou S, Volpe A, Jauregui-Osoro M, et al (2017) [¹⁸F]tetrafluoroborate-PET/CT enables sensitive tumor and metastasis in vivo imaging in a sodium iodide symporter-expressing tumor model. *Sci Rep* 7:946. <https://doi.org/10.1038/s41598-017-01044-4>
43. Liu Z, Chen O, Wall JBJ, et al (2017) Systematic comparison of 2A peptides for cloning multi-genes in a polycistronic vector. *Sci Rep* 7:2193. <https://doi.org/10.1038/s41598-017-02460-2>
44. Wang Y, Wang F, Wang R, et al (2015) 2A self-cleaving peptide-based multi-gene expression system in the silkworm *Bombyx mori*. *Sci Rep* 5:16273. <https://doi.org/10.1038/srep16273>

45. Jing Ye, Liu X, Xu Y, Lü G (2006) Targeted magnetic resonance imaging with intraperitoneal and intravenous streptavidin (SA)-DTPA-Gd: a comparative study in tumor-bearing nude mice. <https://pubmed.ncbi.nlm.nih.gov/16503514/>. Accessed 15 dec 2020
46. Moreno H, Hua, F, Brown T, Small S (2006) Longitudinal mapping of mouse cerebral blood volume with MRI. *NMR Biomed* 19:535–543. <https://doi.org/10.1002/nbm.1022>
47. Perrin J, Capita M, Mougin-Degraef M, et al (2020) Cell Tracking in Cancer Immunotherapy. *Front. Med.* 7:34
48. C B, ME F, EH W, SR R (2006) Analysis of transgene-specific immune responses that limit the in vivo persistence of adoptively transferred HSV-TK-modified donor T cells after allogeneic hematopoietic cell transplantation. *Blood* 107:2294–2302. <https://doi.org/10.1182/BLOOD-2005-08-3503>
49. Fruhwirth GO, Diocou S, Blower PJ, et al (2014) A whole-body dual-modality radionuclide optical strategy for preclinical imaging of metastasis and heterogeneous treatment response in different microenvironments. *J Nucl Med* 55:686–694. <https://doi.org/10.2967/jnumed.113.127480>
50. Stammes MA, Knol-Blanckevoort VT, Cruz LJ, et al (2016) Pre-clinical Evaluation of a Cyanine-Based SPECT Probe for Multimodal Tumor Necrosis Imaging. *Mol Imaging Biol* 2016 186 18:905–915. <https://doi.org/10.1007/S11307-016-0972-7>
51. Stammes MA, Maeda A, Bu J, et al (2016) The Necrosis-Avid Small Molecule HQ4-DTPA as a Multimodal Imaging Agent for Monitoring Radiation Therapy-Induced Tumor Cell Death. *Front Oncol* 0:221. <https://doi.org/10.3389/FONC.2016.00221>
52. Pool SE, Hagen TLM ten, Koelewijn S, et al (2012) Multimodality Imaging of Somatostatin Receptor–Positive Tumors with Nuclear and Bioluminescence Imaging: <http://dx.doi.org/102310/7290201100024> 11:27–32. <https://doi.org/10.2310/7290.2011.00024>
53. Bhattacharya A, Kochhar R, Sharma S, et al (2014) PET/CT with 18F-FDG–Labeled

- Autologous Leukocytes for the Diagnosis of Infected Fluid Collections in Acute Pancreatitis. *J Nucl Med* 55:1267–1272. <https://doi.org/10.2967/JNUMED.114.137232>
54. Hofmann M, Wollert KC, Meyer GP, et al (2005) Monitoring of Bone Marrow Cell Homing Into the Infarcted Human Myocardium. *Circulation* 111:2198–2202. <https://doi.org/10.1161/01.CIR.0000163546.27639.AA>
 55. Jacquemin E, Hagenbuch B, Stieger B, et al (2014) Expression cloning of a rat liver Na(+)-independent organic anion transporter. *PNAS* 91:133–137. <https://doi.org/10.1073/pnas.91.1.133>
 56. Nyström NN, Hamilton AM, Xia W, et al (2019) Longitudinal Visualization of Viable Cancer Cell Intratumoral Distribution in Mouse Models Using Oatp1a1-Enhanced Magnetic Resonance Imaging. *Invest Radiol* 54:302–311. <https://doi.org/10.1097/RLI.0000000000000542>
 57. Guedan S, Ruella M, June CH (2018) Emerging Cellular Therapies for Cancer. <https://doi.org/10.1146/annurev-immunol-042718-041407> 37:145–171. <https://doi.org/10.1146/ANNUREV-IMMUNOL-042718-041407>
 58. R G, G O, MT S, et al (2015) Improving the safety of cell therapy with the TK-suicide gene. *Front Pharmacol* 6:. <https://doi.org/10.3389/FPHAR.2015.00095>
 59. Dubois VP, Zotova D, Parkins KM, et al (2018) Safe Harbor Targeted CRISPR-Cas9 Tools for Molecular-Genetic Imaging of Cells in Living Subjects. *Cris J* 1:440–449. <https://doi.org/10.1089/crispr.2018.0030>

CHAPTER 3

3 Complementary Early-Phase Magnetic Particle Imaging and Late-Phase Positron Emission Tomography Reporter Imaging of Mesenchymal Stem Cells In Vivo

Stem cell-based therapies have demonstrated significant potential in clinical applications for many debilitating diseases. The ability to non-invasively and dynamically track the location and viability of stem cells post administration could provide important information on individual patient response and/or side effects. Multi-modal cell tracking provides complementary information that can offset the limitations of a single imaging modality to yield a more comprehensive picture of cell fate. In this study, mesenchymal stem cells (MSCs) were engineered to express human sodium iodide symporter (NIS), a clinically relevant positron emission tomography (PET) reporter gene, as well as labeled with superparamagnetic iron oxide nanoparticles (SPIOs) to allow for detection with magnetic particle imaging (MPI). MSCs were additionally engineered with a preclinical bioluminescence Imaging (BLI) reporter gene for comparison of BLI cell viability data to both MPI and PET data over time. MSCs were implanted into the hind limbs of immunocompromised mice and imaging with MPI, BLI and PET was performed over a 30-day period. MPI showed sensitive detection that steadily declined over the 30-day period, while BLI showed initial decreases followed by later rapid increases in signal. PET signal of MSCs was significantly higher than the background at later timepoints. Early-phase imaging (Day 0-9 post MSC injections) showed correlation between MPI and BLI data ($R^2=0.671$), while PET and BLI showed strong correlation for late-phase (day 10-30 post MSC injections) imaging timepoints ($R^2=0.9817$). We report the first use of combined MPI and PET for cell tracking and show the complementary benefits of MPI for sensitive detection of MSCs early after implantation and PET for longer-term measurements of cell viability.

3.1 Introduction

Cell-based therapies are an expanding class of medicine that have shown significant success in the treatment of numerous pathologies [1][2]. These living drugs offer a therapeutic advantage over conventional drugs as they can perform complex and dynamic biological functions such as tissue regeneration, biological function restoration, malignancy killing, and heightening of immune responses. The global cell therapy market size is expected to reach \$23.0 billion USD by 2028 [3], with stem cells and tissue-specific cells accounting for approximately 36% of this market [2]. Mesenchymal stem cells (MSCs) comprise 46% of approved stem cell therapies for numerous diseases such as graft versus host disease, osteoarthritis, inflammatory bowel diseases, myocardial infarctions, liver cirrhosis, limb ischemia, and spinal cord injury [4][5]. The therapeutic potential of MSCs arise from their innate ability to differentiate into a variety of different tissue types for regenerative medicine purposes [6], and for control of inflammation as they can modulate the proliferation and cytokine production of immune cells [4]. To enable clinicians to better evaluate MSC therapies in terms of patient response or unwanted side effects, cell tracking tools to quantitatively monitor the longitudinal fate of administered MSCs would be highly valuable.

One popular cell tracking approach is to directly label cultured cells with imaging probes prior to their administration to a living subject. For MSCs, probes for various clinical imaging modalities have been utilized including positron emission tomography (PET) [7][8], photoacoustic imaging (PAI) [9][10], and superparamagnetic iron oxide nanoparticles (SPIOs) for magnetic resonance imaging (MRI) [11][12]. While the latter technique is highly sensitive, SPIOs provide negative contrast in MR images which can obscure the ability to see cells in tissues that appear dark (e.g., lungs), and quantitation of SPIOs is challenging with MRI. Recently, magnetic particle imaging (MPI), a relatively newer modality, has also been used to image SPIO-labeled MSCs [4][13]. MPI

provides radiation-free and positive contrast ‘hotspot’ images of the SPIOs without signal attenuation in biological tissues [14], allowing for unambiguous identification of labelled cells. MPI is currently limited to preclinical systems for imaging of small animals, but development of clinical MPI systems for humans is under active development [15][16]. MPI cell tracking is sensitive with reported detection limit of 1000 ferucarbotran-labeled stem cells *in vitro* with signal-to-noise ratio of ~ 5 [17]. Synomag-D is a novel SPIO which has enhanced MPI sensitivity compared to ferucarbotran and its use for cell tracking is gaining momentum [18][19][20][21]. Numerous *in vivo* studies have also used the MPI signal from SPIOs as a surrogate for cell number. However, for proliferating cell populations the amount of SPIO per cell can diminish which compromises cellular detection sensitivity and quantification. Moreover, SPIOs can be lost from dead cells and taken up by resident macrophages, further confounding the MPI estimate of cell number over time. Therefore, MPI quantification of cell number is most accurate and valuable at early timepoints after cell administration.

A complementary approach for longer term cell tracking is to engineer cells with imaging reporter genes. Unlike probe strategies, the reporter genes are passed to cell progeny and not able to be transferred to bystander cells, allowing for life-long specific imaging of proliferating viable cells. Various reporter genes for different clinical imaging modalities exist including MRI, PAI, and PET [22][23][24]. PET reporter gene cell tracking has received the most attention in terms of clinical translation due to the low dose required of the PET tracer and the high sensitivity of PET to low cell numbers (in the 10,000 cell range in mice [25]). As such, PET reporter genes have been used to track whole-body survival, proliferation and quantification of transgenic cells over time in animals [26], and clinical PET reporter-based tracking of therapeutic T cells has been successfully performed in glioma patients [24]. While numerous PET reporter genes exist, the

human sodium iodide symporter (NIS), an intrinsic membrane transporter, has received significant attention as its human-origin alleviates the risk of immunogenicity, it has a wide variety of compatible imaging probes, and it can additionally serve as a therapeutic gene [27][26][28]. The fluorine-18-based PET tracer, ^{18}F -tetrafluoroborate (^{18}F -TFB), provides high positron yield, short diffusion range in tissue (< 2.4 mm), and a clinically compatible half-life (110 minutes), when compared to radioiodine probes compatible with NIS [29]. Jiang, H., *et al.* performed the first imaging study of 8 healthy human subjects to assess the pharmacokinetics, safety, biodistribution and stability, showing ^{18}F -TFB to be overall well-tolerated [30]. Thus, ^{18}F -TFB/NIS imaging has high translational potential, and numerous groups have used it in preclinical models to track cells such as dendritic cells [31], CAR T cells [32], and induced pluripotent stem cells [33].

In this work, MSCs were genetically modified to express NIS for PET detection followed by direct labelling with Synomag-D for MPI. In addition, MSCs were engineered to co-express a bioluminescence imaging (BLI) reporter gene called Akaluciferase (Akaluc) to serve as an independent imaging measure of cell viability over time. Akaluc BLI has been shown to be able to detect single cells in mice [34][35]. MSCs were then implanted intramuscularly in mice as described before [36], and longitudinal trimodal imaging was performed with ^{18}F -TFB PET, BLI and MPI, and imaging measures for each modality were compared over time. Our work highlights the benefits of using the combination of MPI and PET for tracking cells, allowing highly sensitive early-phase imaging of cells with MPI and sensitive late-phase imaging with PET.

3.2 Materials and Methods

3.2.1 Cloning and Lentiviral Production

Using In-Fusion Cloning (Takara Bio USA, Inc. CA, USA), two third-generation lentiviral transfer plasmids were engineered (Figure 1A): one expressing NIS gene (Origene technologies, Inc. MD, USA NM_000453) and zsGreen (zsG) both driven by a human elongation factor α (hEF1 α) promoter; and another to co-express tdTomato (tdT) (from Addgene plasmid #48688) and Akaluc (obtained from the pcDNA3-Venus-Akaluc Vector (Cat. RDB15781, RIKEN BioResource Research Center, Ibaraki, Japan). For the NIS construct, lentivirus was produced by a commercial vendor at a titre of 10^8 IFU/ml (Origene technologies, Inc. MA, USA: custom made). For the Akaluc construct, lentivirus was produced in-house using the packaging and envelope plasmids pMDLg/pRRE, pRSV-Rev, and pMD2.G (Addgene MA, USA plasmids #12251, #12253, and #12259, respectively). Briefly, human embryonic kidney (HEK 293T; ATCC) cells were transfected with Lipofectamine 3000 (Thermo Fisher Scientific, MA, USA) in accordance with the manufacturer's lentiviral production instructions (Thermo Fisher Scientific Inc., MA, USA). Viral-containing supernatant was collected 24 and 48 hours after transfection, filtered with a 0.45- μ m filter and frozen at -80 °C until use. Our tdT-Akaluc lentivirus was produced at a titre of 10^8 IFU/ml, as assessed by flow cytometry.

3.2.2 MSC Culture and Transduction

Bone marrow-derived murine MSCs were purchased from Cyagen (CA, USA MUBMX 01001) and maintained in Dulbecco's Modified Eagle's Medium-low glucose (D6046, Sigma-Aldrich, MI, USA) containing 10% fetal bovine serum (Wisent BioProducts, QC, Canada). All cells were kept in a humidified incubator with 5% CO₂ at 37°C and routinely confirmed to be mycoplasma-free using the MycoAlert mycoplasma detection kit (Lonza Basel, Switzerland LT07-318).

MSCs were seeded at a density of 3.33×10^4 cells in a 48-well plate on day 0 and then transduced for 6 h with the above zsG-NIS lentivirus at a multiplicity of infection (MOI) of 75 along with Polybrene (8 mg/ml; Sigma Aldrich MI, USA SML0517). On day 4 after transduction, naïve and transduced cells were harvested and sorted using a FACS Aria III fluorescence-activated cell sorter (BD Biosciences, NJ, USA) for zsG expression. MSCs were expanded prior to additional transduction with the tdT-Akaluc-containing lentivirus at an MOI of 75 along with Polybrene. Cells were then re-sorted for dual zsG/tdT expression.

3.2.3 MSC Iron Labelling

Engineered MSCs were seeded at a density of 2×10^6 cells in T-75 flasks and grown until 80-90% confluency was reached. In a 15 ml falcon tube (tube A), 180 μ l of protamine sulfate (12 μ g/mL) was added to 7.5 mL of low-glucose serum free media and vortexed. In another 15 ml falcon tube (tube B) containing 7.5 ml of serum free media, 270 μ l of Synomag-D (180 μ g Fe/mL) (Micromod Rostock, Germany Product code: 104-00-501 Lot: 02721104-01), and 60 μ l of heparin (3 U/mL) were added and vortexed. Protamine sulfate and heparin were used as transfection agents to increase the iron uptake in cells. Tube A was then added to tube B, and vortexed thoroughly. MSCs were washed with HBSS and incubated with the SPIO-containing mixture for 4 hours. Serum-containing media (5 ml) was added to the MSC flasks and incubated overnight for next day collection. Upon collection, cell counting, and viability was determined using the trypan-blue exclusion assay (Countess Automated Cell Counter; Invitrogen, MA, USA). Perls Prussian Blue (PPB) staining was then performed to assess iron labeling.

3.2.4 In Vitro Magnetic Particle Imaging

Cell pellets containing 2.5×10^5 , 1×10^5 , 5×10^4 , 2.5×10^4 , 1.2×10^4 , 6×10^3 Synomag-D labeled MSCs were individually imaged on a Momentum™ MPI scanner (Magnetic Insight Inc.).

Images were acquired in 2D (~2 min) and 3D (~ 30 min) using a 3.0 T/m selection field gradient and drive field strengths of 22 mT and 26 mT in the X and Z axes, respectively, with a 12 x 6 cm field of view (FOV). Single projection images were used for 2D and 35 projections were used for 3D images (Appendices Figure 3.1).

3.2.5 MPI Image Analysis and Quantification

All MPI images were imported and viewed with a custom MPI colour look-up table (CLUT) using the open-source Horos™ image analysis software (version 3.3.6, Annapolis, MD USA). MPI signal was measured using a semi-automatic segmentation tool within a region of interest (ROI) selecting for signal exceeding 5 times the standard deviation of system noise. Total MPI signal for an ROI was calculated by multiplying the ROI area (2D) or volume (3D) by the mean signal. Calibration lines (2D and 3D) for Synomag-D were made to determine the relationship between iron content and MPI signal using previously established methods. Iron content of the cell samples was calculated by dividing the total MPI signal by the slope of the calibration line. A cellular sensitivity calibration line was made by correlating measured MPI signal with the number of cells in the sample. A simple linear regression was performed to determine this relationship between iron content and cell number.

3.2.6 Animal Models

Animals were cared for in accordance with the standards of the Canadian Council on Animal Care, and experiments were conducted as specified in an animal use protocol (AUP 2020-025). MSCs (3×10^5) were intramuscularly (IM) injected in the left hind limb of NOD scid gamma (NSG) mice. NSG mice (n=5) were chosen due to their highly immunodeficient nature and are most supportive to stem cell engraftment expressing non-murine reporter genes (NIS and Akaluc).

3.2.7 In Vivo Magnetic Particle Imaging

On day 0, post MSC injections, mice were anesthetized with 2% isoflurane using a nose cone and inserted into the MPI MOMENTUM system (Magnetic Insight Inc., Alameda, California). Full body (mouse) MPI was acquired in 2D (for visualization) and 3D (for quantification). For 2D images, imaging parameters were: field of view (FOV) = 12 cm x 6 cm, gradient strength = 3.0 T/m, excitation amplitude = 22 mT (X-channel) and 26 mT (Z-channel), imaging time = 2.8 minutes. For 3D imaging (28 minutes), the FOV = 12 cm x 6 cm x 6 cm with 35 projections, using the same gradient strength and excitation amplitude. A 3D image of an empty sample holder was used to measure background signal, as defined by standard deviation (SD) of the signal in air. For image quantification in 3D, a minimum threshold of 5 times the background signal was used for region-of-interest (ROI) delineation, following the Rose criteria for signal-to-noise ratio (SNR)³⁷. MPI signal was calculated as the mean signal intensity (a.u.) in the ROI multiplied by the area of the ROI (mm³). The calibration curve generated in Appendices Figure 3.1 was used to convert MPI signal to iron content.

3.2.8 In Vivo Bioluminescence Imaging

Mice were anesthetized with 2% isoflurane, injected intraperitoneally with 100 μ l of 5 mM Akalumine-HCl (Sigma Aldrich, Missouri, USA 808350) and imaged with an IVIS Lumina XRMS In Vivo Imaging System (PerkinElmer). Images with auto exposure times were captured every 60 seconds for 30 minutes, with a field of view of 12 cm. Regions of interest were drawn manually around the MSC implant using the LivingImage software (PerkinElmer) to measure the average radiance (p/s/cm²/sr). The peak average radiance over the 30-minute imaging session was used for data analysis.

3.2.9 In Vivo [¹⁸F]TFB Positron Emission Tomography

¹⁸F-TFB was synthesized as described previously³⁸. Mice were anesthetized with 2% isoflurane, injected with 15-20 MBq of ¹⁸F-TFB in 50-150 µl via the tail vein, and imaged with a Siemens Inveon™ microPET system (Siemens Medical Solutions USA, Inc.). Animal breathing rate and body temperature were monitored and kept between 40-70 bpm and at 37 °C, respectively. Static PET data were acquired 30 minutes post ¹⁸F-TFB injections. Images were reconstructed using ordered subset expectation maximization (OSEM). Quantification of PET signal was performed by manual segmentation of ROIs using Horos Project software v3.3.6. Maximum Activity Projections (MAPs). Standard Uptake Value (SUV) was calculated with the below equation:

$$SUV \left(\frac{g}{mL} \right) = \frac{Pixel\ value \left(\frac{Bq}{mL} \right) * weight\ (kg)}{Dose\ (Bq)} * 1000 \left(\frac{g}{kg} \right) \quad Equation\ 1$$

3.2.10 Ex Vivo Staining and Fluorescence Microscopy

Following final imaging session on day 30, animals were euthanized by isoflurane overdose, followed by perfusion-fixation with 4% paraformaldehyde (PFA). Both left and right hind limbs were harvested from each animal and stored in 4% paraformaldehyde until use. Tissues were then either embedded in paraffin for PPB staining or frozen in a 30% sucrose solution for evaluating fluorescence protein expression. Paraffin-embedded tissues were sectioned at 5-micron thickness, stained with PPB³⁹ to identify the presence of Synomag-D and counterstained with nuclear fast red. Frozen tissues were sectioned at 10-micron thickness and imaged with a Revolve Fluorescence microscope (Echo Microscopes, California, USA).

3.2.11 Statistical Analysis

One-way Analysis of Variance (ANOVA) and Tukey's post-hoc multiple comparisons were performed on the grouped averages for MPI and PET in-vivo studies. Two-tailed Pearson correlation coefficient were performed on MPI and BLI at early timepoints as well as BLI and PET at later imaging timepoints. Statistical analysis used GraphPad Prism Software (Version 7.00 for Mac OS X, GraphPad Software Inc., La Jolla California USA, www.graphpad.com). For all tests, a p-value less than 0.05 was considered statistically significant.

3.3 Results

Cells were transduced with a zsG-NIS lentiviral vector and then sorted to collect a purified population of 96% zsG+ cells (Figure 3.1C). This population of zsG+ MSCs were subsequently transduced with a second tdT-Akaluc lentivirus and sorted again to obtain a purified population (96%) of zsG-NIS-tdt-Akaluc MSCs (Figure 3.1D). Engineered MSCs were then efficiently labeled with Synomag-D® (>95%; Figure 3.1F). Appendices figure 3.1 shows 2D MPI cellular detection limit of <8,000 cells, and a 3D MPI detection limit of <4,000 cells.

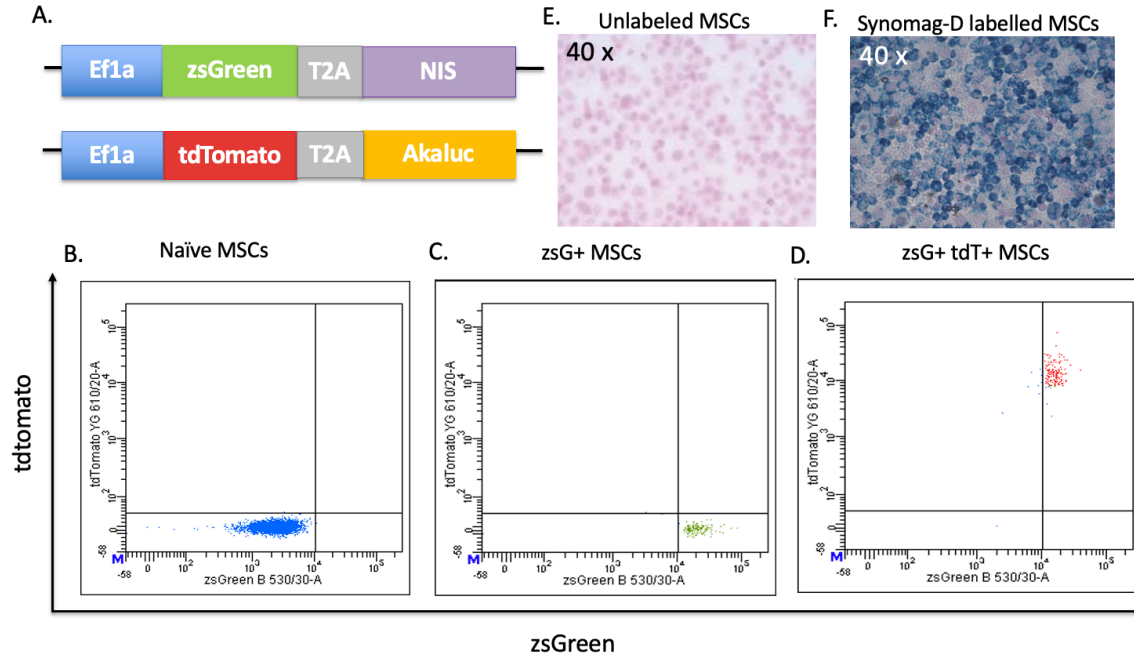


Figure 3.1: A) The genetic constructs containing (top) the *zsGreen* fluorescent gene followed by the cleaving peptide T2A and then then PET reporter gene *NIS*; and (bottom) the *tdtomato* fluorescent gene followed by T2A and the BLI reporter gene *Akaluc*. Flow cytometry showing naïve non-transduced MSCs (B), initial transduction with the lentiviral plasmid containing *zsG-NIS* (C), and second transduction with the lentiviral plasmid containing *tdt-Akaluc* (D). Microscopy showing unlabeled MSCs (E.) and MSCs labelled with Synomag-D® (>95% labelling efficiency) (F.) at 40x.

Engineered and Synomag-D loaded MSCs (1×10^6) were implanted into the hind limb muscle of NSG mice. Post cell implantation, mice were imaged with MPI (Day 0). Mice were then imaged with BLI and PET on day 1 and day 2 post MSC implantation, respectively, and repeated imaging of mice was performed over the duration of 30 days. A representative mouse imaged over the course of 30 days is shown in Figure 3.2 (For images from the additional 4 mice please see Appendices Figures 3.2-3.5). For all mice at all timepoints, MPI showed positive signal in the limb where the MSCs were injected. Qualitatively, a decrease in MPI signal was observed over the 30-day period for all mice. BLI signal was also detected at the same site as MPI signal and generally showed an initial decrease in signal from days 1 to 9 post-injection (in all mice) followed by a rapid increase from days 16 to 29 (in 3 mice). Qualitatively, among the 5 mice, higher PET signal was seen in the injected limb compared to the contralateral limb on days 2, 10, 17 and 30 for 3 of the 5 mice. While the other two mice showed BLI and MPI signal at all timepoints, obvious PET signal was not seen.

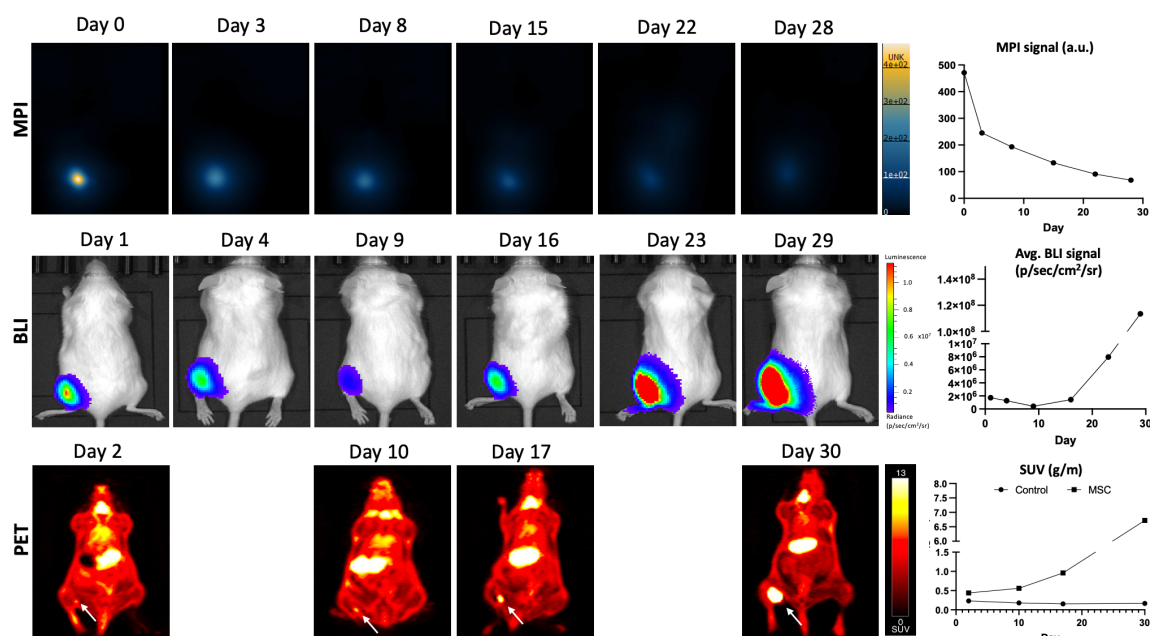


Figure 3.2: *In-vivo* detection of MSCs in the left hind limb with MPI (top), BLI (middle) and PET (bottom) in a representative mouse over a 30-day period. MPI shows the brightest signal on day 0 and steadily decreases over time. BLI signal shows reduced radiance on day 9 (likely due to cell death), followed by an increase in BLI signal thereafter. ^{18}F -TFB PET SUV shows a similar pattern to BLI radiance at the comparable imaging timepoints of the engineered MSCs (arrows). ^{18}F -TFB uptake also present in thyroid and stomach (organs with endogenous NIS expression). Imaging data in the graph on the right are for this mouse.

Analysis of BLI, MPI and PET images revealed significant changes in imaging signal over time and relationships between these signal changes between different modalities (Figures 3.3 and 3.4). Quantification of signal from MPI, BLI and PET systems over the 30-day tracking period for the individual 5 mice is shown in Figure 3.3.

Figure 3.3A shows longitudinal MPI measurements of iron content (mg) in the hind limbs implanted with Synomag-D-labelled MSCs. Post MSC implantation, iron content averaged 2.77 ± 1.53 mg between mice on day 0 and 0.43 ± 0.36 mg between mice on day 28, showing a steady decline over time in all 5 mice. Average MPI signal (n=5) significantly decreased ($p < 0.001$) on days 3, 8, 15, 22 and 28 compared to the initial day of injection (day 0) (Fig. 3.3G). BLI initial radiance ranged from 10^6 - 10^7 p/sec/cm²/sr on day 1 post MSC administration. In 3 of the 5 mice, BLI signal decreased at earlier timepoints (on day 9 for one mouse and day 16 for two mice) and a rapid increase in signal with signal in one mouse reaching $>10^8$ p/sec/cm²/sr, was seen (Fig. 3B). BLI signal was lower (in the 10^6 p/sec/cm²/sr range) for the remaining two mice throughout the entire imaging study. From days 17 to 30, ¹⁸F-TFB PET SUV values showed a similar upward trend to the BLI signal for the 3 mice showing higher radiance (in the 10^7 - 10^8 p/sec/cm²/sr range), while no tracer uptake above background was noted for two mice with BLI radiance in the 10^6 p/sec/cm²/sr range (Figure 3.3C and Appendices Figures 3.4 and 3.5). No significant difference in tracer uptake was noted on day 2 post cell transplantation between the MSC-injected and control hind limbs, while significantly higher ($p < 0.05$) SUV values were detected on days 10, 17, and 30 in the MSC-injected versus control limbs for the same 3 mice that displayed the highest BLI signal (Fig. 3.3I).

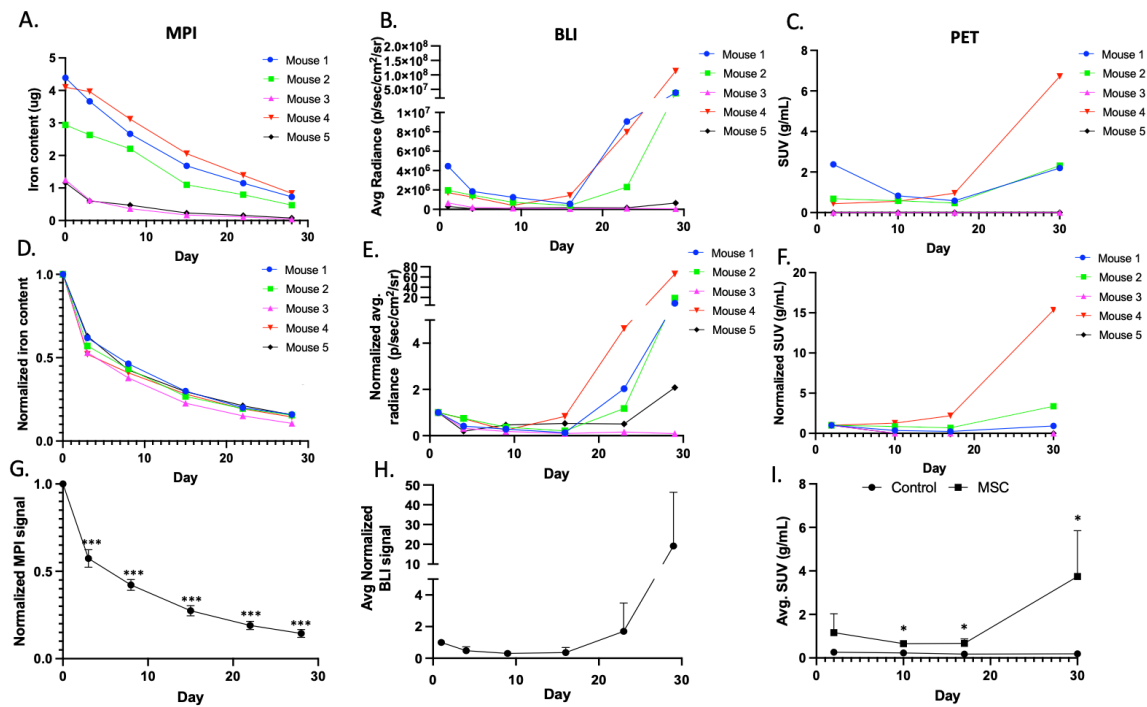


Figure 3.3: A) MPI-measured iron content (mg) decreased monotonically over time for all 5 mice. B) Average BLI radiance (p/sec/cm²/sr) showed slight initial decrease over first 15 days and then increased over remaining experimental timepoints in 3 mice. BLI radiance in the remaining 2 mice remained low at all timepoints after the initial decline. Note the scale is divided into low and high-value ranges for the BLI data. C) ¹⁸F-TFB PET SUV values (g/mL) exhibited the same trends as BLI for individual mice (i.e., mice with high BLI signal at a particular timepoint had high PET SUV values, and vice versa). (D-F) MPI, BLI, and PET measurements normalized to their initial measurement, respectively. (G-I) Grouped averages of the normalized data. Error bars represent +/- SD. G) a significant decrease of MPI signal at all imaging timepoints compared to day 0 was found (p<0.001; n=5). H) due to the high variability in BLI data across mice, significant differences over time were not found. I) significant increases in SUV values between MSC-injected hind limbs and control hind limbs were found on days 10, 17 and 30 (p<0.05; n=3).

BLI signal showed 2 trends in MSC engraftment: an early phase from days 1 to 9 where the number of viable cells decreased over time and a late phase from days 16 to 29 where the number of viable MSCs generally increased over time. As a result, we show comparisons of the individual mouse MPI and PET data to the corresponding BLI data for these early and late phases in Figure 3.4. MPI signal and BLI signal were correlated during the early phase ($R^2 = 0.677$; $p < 0.05$; Figure 3.4C), but not for the late phase as expected ($R^2 = 0.0022$; Appendices Figure 3.6). In contrast, BLI and PET measurements were significantly correlated during the late phase at comparable timepoints ($R^2 = 0.9817$; $p < 0.05$; Figure 3.4F).

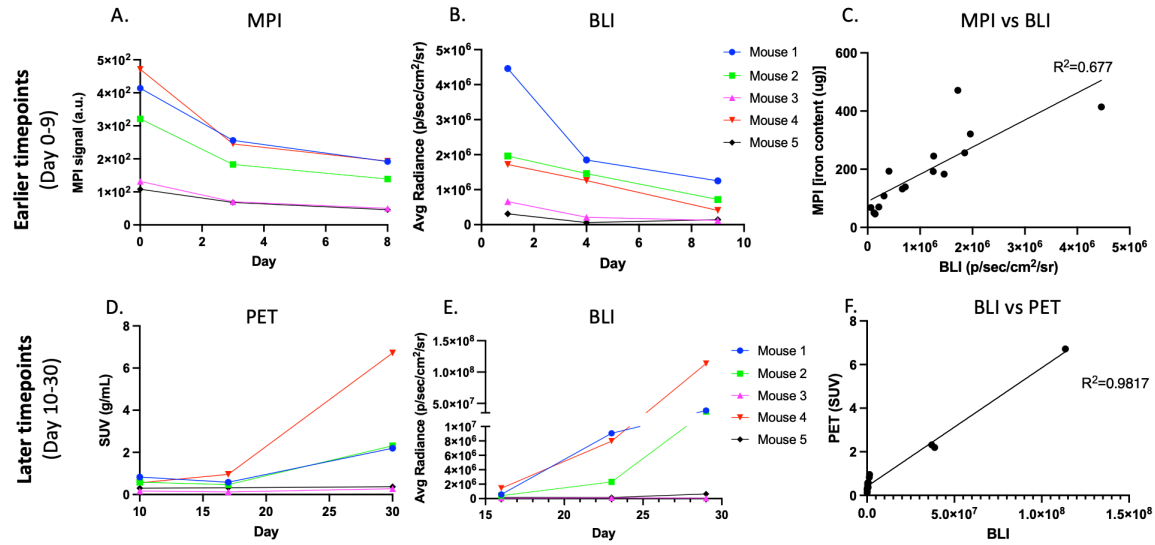


Figure 3.4: MPI (A) and BLI (B) signal from early imaging timepoints (days 0-9 post MSC injection), and correlational analysis of this data (C). ¹⁸F-TFB PET SUV values (D) and BLI signal (E) from later imaging timepoints (days 10-30 post MSC injection), and correlational analysis of this data (F).

Control and MSC-injected hind limbs were harvested at endpoint (day 35 post MSC implantation) for evaluation of iron presence and fluorescence protein expression, as shown in Figure 3.5. Iron staining was present in the MSC injected limb only (Fig. 3.5A/B). As expected, both tdTomato and zsGreen fluorescence were detectable only in the MSC injected limb (Fig. 3.5F/H.) and not in the control limb (Fig. 3.5E/G.).

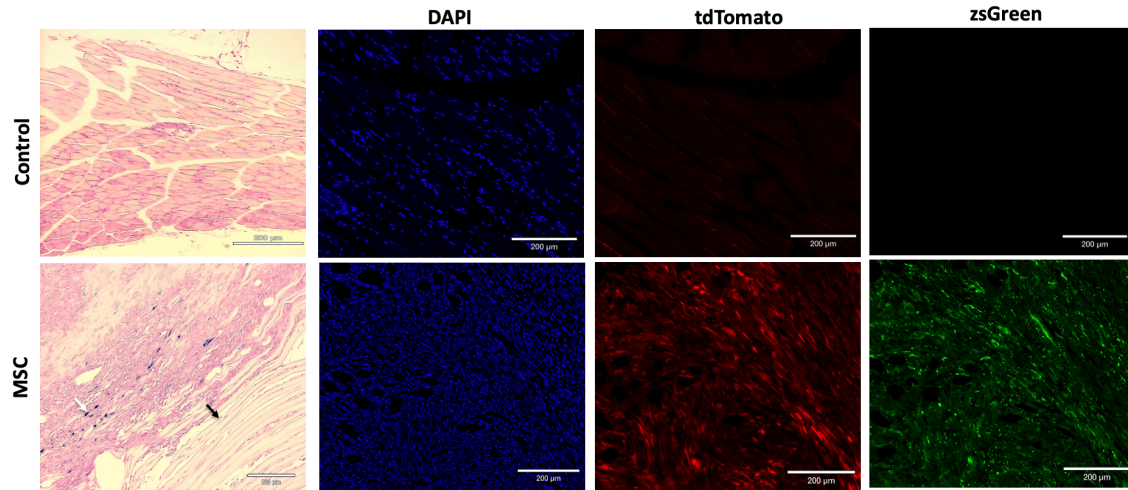


Figure 3.5: A) PPB iron staining with nuclear fast red counter stain of a control limb showing striated muscle cells and B) MSCs shown as darker and more dense cells with intracellular iron (white arrow) surrounded by muscle cells (black arrow) of the hind limb tissue harvested post-mortem (day 30). C) and D) show the DAPI staining of control and MSC cells, respectively. E) and G) shows the absence of tTtomato and zsGreen fluorescence in the control hind limb, while F) and H) show the presence of both fluorescence signals in the MSC-injected limb.

3.4 Discussion

Although MSCs have been clinically-effective for numerous conditions, MSCs have been observed to undergo either *in-vivo* apoptosis as a result of exposure to proapoptotic or cytotoxic factors present [40][41], influencing their therapeutic effectiveness due to insufficient grafting into host tissue. On the other extreme, MSCs can undergo malignant transformation over time [42][43][44], hindering their therapeutic use due to concerns of safety. These limitations of MSCs emphasize the importance of tracking these cell therapies to better understand their post-transplantation fate. Since the location, engraftment and survival of administered MSC-based therapies is a major determinant of clinical outcome, the goal of this study was to develop an MSC-monitoring system using a multi-modal imaging approach. Multimodal imaging is a common strategy that allows the collection of complementary information from multiple imaging technologies [45][36][46][47]. In this study, MPI and PET reporter imaging were combined for the first time to track MSCs in mice over a 30-day period, and showed the complementary nature of the two modalities by demonstrating their strengths in tracking MSCs at both early and late timepoints. The inclusion of bioluminescence imaging was important as it allowed comparison of MPI and PET metrics to a highly utilized preclinical modality that reports on relative cellular viability and proliferation, with superior sensitivity over time.

MPI is a relatively novel imaging modality developed in the early 2000s capable of directly detecting the magnetization of iron-oxide probes with the use of low-frequency magnetic fields [48]. Both prototype and commercial MPI scanners have been used in several studies for vascular imaging [49], oncology [50][51] and cell tracking applications [4][52]. MPI holds promise for clinical integration for cell-tracking applications as it has high depth penetration, produces linear quantification, provides hyperintense “hot-spot” contrast with nearly no background signal from

tissues, and can achieve high sensitivity [53][54]. Furthermore, SPIOs have been used clinically and have not been shown to have effects on biological mechanisms, such as proliferative capacity of cells [55][56][57]. Bulte et al. reported the first exploratory work with neural stem cells (NSCs) and rat mesenchymal stem cell detection using clinical SPIONs and reported an in-vivo cellular detection threshold of $3\text{-}5 \times 10^4$ NSCs [58]. Other studies have reported more sensitive detection thresholds as low as 200 SPIO-labeled neural cells [54] and 250 SPIO-labelled HeLa cells [52]. In our study, MPI showed high sensitivity in earlier phases and correlated with BLI data, enabling MPI to accurately report on viable cell number for very early time points (up to day 9 in this work). This is an essential benefit since one of the main limitations with MSC-based therapies is low and inefficient homing to target sites which ultimately results in reduced therapeutic efficacy [4]. However, as anticipated MPI signal declined steadily over time since the labelling agent dilutes when cells proliferate or as a result of agent clearance after apoptosis. MPI correlated with BLI at early imaging timepoints, where BLI showed a decline in radiance. The initial decrease observed with BLI can be mainly attributed to cell death post transplantation as MSCs have a typical “hit or die” mechanism post engraftment. Other studies have also reported on the clearance and short lifespan of MSCs post transplantation, although the mechanisms underlying post-transplantation survival remain unclear [40][59]. Our data emphasizes the utility of MPI at earlier timepoints, and its strong potential to assess successful MSC delivery, cell homing to target sites, as well as cell numbers. Importantly, our study also highlights that caution should be taken in converting iron measures in MPI with cell numbers at late imaging timepoints since mice with increasing BLI and PET signal still showed decreasing MPI measures. It is recommended that MPI cell tracking studies should include an independent measure of cell viability, like BLI or PET reporter gene imaging, if the study is attempting to track cell numbers with MPI at extended time periods.

PET has been widely used for cell-tracking applications in various cell types, both pre-clinically and clinically. Many studies have used direct-labelling techniques with 2'-[^{18}F]fluoro-2'-deoxy-D-glucose [^{18}F]-FDG [7][60], [^{18}F]-Fluorothymidine ([^{18}F]-FLT) [61], or [^{89}Zr]-Oxine [62] for PET detection of stem cells. Other studies have used genetic modifications to image stem cells with the use of a reporter genes such as the mutant herpes simplex virus 1 thymidine kinase HSV1-sr39tk [63], mutant human deoxycytidine kinase (hdCK3mut) [64], the dopamine type 2 receptor (D2R80A) [65], as well as the sodium iodide symporter (NIS) [66][67][68]. NIS is a popular reporter gene due to its minimal immunogenic risks due to its human-origin, the clinical use of its compatible [^{18}F]-TFB probe, as well as the restricted background expression of NIS in endogenous tissue (mainly thyroid). Fruhwirth's group reported a sensitive in-vivo cellular detection limit of 2,000 NIS-positive cancer cells in a volume of 5×10^5 cells using NIS/[^{18}F]-TFB [69]. Vandergaast, R. *et al.*, reported a similar detection limit of 2,500 NIS-expressing A549 cells in a pellet of 1×10^6 cells for consistent detection with PET using [^{18}F]-TFB [70]. In this work, PET showed the lowest sensitivity when compared with MPI and BLI at earlier timepoints with no significant difference noted between control and MSC-injected hind limbs uptake values (on day 2). However, at later timepoints PET signal was strongly correlated with increasing BLI signal, during which the MPI signal decreased monotonically. An increase of BLI radiance at later imaging timepoints (day 16-29) was observed in three of the five mice indicating the expansion of luciferase-expressing cells. However, it is difficult to accurately deduce if MSCs have differentiated in-vivo in this study. Other studies have assessed MSC in-vivo differentiation with the use of well-characterized differentiation promoters with various reporter gene imaging techniques [71][72][73]. Moreover, evidence suggests that MSCs can also undergo malignant

transformation, although the exact mechanism is still poorly understood [43]. In contrast, two mice did not show the rapid increase in BLI signal or PET uptake. It is important to note that the engineered MSCs were detectable with PET when the BLI average radiance was on the order of 10^7 p/sec/cm²/sr or higher. In the two mice with BLI signal of $\sim 10^6$ p/sec/cm²/sr, no detectable PET signal was observed throughout the duration of the study.

While we have successfully used MPI and PET to image an intramuscular-injection model of MSCs, a more clinically applicable disease model combined with MSC therapy would more accurately represent the detection capabilities of this tracking system. Furthermore, the optimization of genetic engineering with technologies such as CRISPR would improve the safety reporter genes by allowing site-selective integration as opposed to the random integration of lentiviral-transduced cells, as our group has shown previously [74]. It is important to note that the *in-vivo* environment can slightly influence PET and BLI signal intensity as vascularization to the local region has effects on the substrate delivery required for both reporters to generate signal. While MPI signal is proportional to the iron label, there are different fates of the SPIOs *in-vivo*. Dilution of the SPIOs occurs if MSCs are proliferating, and thus cannot accurately report on cell number long-term. Studies have also shown that long-lasting signal from SPIOs mainly originated from phagocytic cells (such as macrophages) that have engulfed the SPIOs found in the extracellular spaces after implanted cells have died [75].

To our knowledge, this is the first study to accomplish MSC tracking with MPI and PET reporter imaging. In accordance with the cellular detection thresholds reported in the literature, this work showed more sensitive detection of MSCs with MPI in comparison to PET. This data suggests that MPI has the potential to provide crucial early information on the success of accurate cell-delivery with local injection, cell-homing with systemic administration by providing quantitative measures

of cell number prior to excessive cell death or proliferation. However, at later imaging timepoints, MPI signal was no longer quantitatively accurate and did not reflect on cell viability and proliferation, while PET produced signal that strongly correlated with BLI, emphasizing the advantages of reporter gene imaging for longitudinal tracking applications. This study highlights the importance of multi-modal imaging and the how one imaging approach will likely not suffice in providing all the essential information, but rather can be combined with other imaging tools to provide complementary information and overcome the limitation of the other. This bi-modal imaging approach has the potential to report on cell biodistribution, homing, viability, and long-term survival of administered MSCs for both local and systemic administrations. Additionally, this system is not limited to MSCs and can be explored for its broad application for tracking of other therapeutic cell types such as immune cells.

3.5 References

- [1] Y. R. Murciano-Goroff, A. B. Warner, un J. D. Wolchok, "The future of cancer immunotherapy: microenvironment-targeting combinations", *Cell Res.* 2020 306, sēj. 30, nr. 6, lpp. 507–519, mai. 2020, doi: 10.1038/s41422-020-0337-2.
- [2] L. L. W. Wang *u.c.*, "Cell therapies in the clinic", *Bioeng. Transl. Med.*, sēj. 6, nr. 2, lpp. e10214, mai. 2021, doi: 10.1002/BTM2.10214.
- [3] "Global Cell Therapy Market Report 2021-2028 - Growing Adoption of Regenerative Medicine & Introduction of Novel Platforms and Technologies".
<https://ca.style.yahoo.com/global-cell-therapy-market-report-101300928.html> (skatīts nov. 25, 2021).
- [4] B. Zheng *u.c.*, "Quantitative Magnetic Particle Imaging Monitors the Transplantation, Biodistribution, and Clearance of Stem Cells In Vivo", *Theranostics*, sēj. 6, nr. 3, lpp. 291–301, 2016, doi: 10.7150/thno.13728.
- [5] Y. Wang, H. Yi, un Y. Song, "The safety of MSC therapy over the past 15 years: a meta-analysis", *Stem Cell Res. Ther.*, sēj. 12, nr. 1, lpp. 1–15, dec. 2021, doi: 10.1186/S13287-021-02609-X/FIGURES/6.
- [6] J. Gao, J. E. Dennis, R. F. Muzic, M. Lundberg, un A. I. Caplan, "The Dynamic in vivo Distribution of Bone Marrow-Derived Mesenchymal Stem Cells after Infusion", *Cells Tissues Organs*, sēj. 169, nr. 1, lpp. 12–20, 2001, doi: 10.1159/000047856.
- [7] N. Nose *u.c.*, "[18F]FDG-labelled stem cell PET imaging in different route of administrations and multiple animal species", *Sci. Rep.*, sēj. 11, nr. 1, lpp. 1–8, 2021, doi: 10.1038/s41598-021-90383-4.
- [8] V. Schönitzer *u.c.*, "In Vivo Mesenchymal Stem Cell Tracking with PET Using the Dopamine Type 2 Receptor and 18 F-Fallypride", *J Nucl Med*, sēj. 55, lpp. 1342–1347, 2014, doi: 10.2967/jnumed.113.134775.

- [9] T. Kim, J. E. Lemaster, F. Chen, J. Li, un J. V Jokerst, "Photoacoustic Imaging of Human Mesenchymal Stem Cells Labeled with Prussian Blue–Poly(L-lysine) Nanocomplexes", 2017, doi: 10.1021/acsnano.7b03519.
- [10] K. S. Dhada, D. S. Hernandez, un L. J. Suggs, "In Vivo Photoacoustic Tracking of Mesenchymal Stem Cell Viability", 2019, doi: 10.1021/acsnano.9b01802.
- [11] S. Rizzo *u.c.*, "In vitro labelling and detection of mesenchymal stromal cells: a comparison between magnetic resonance imaging of iron-labelled cells and magnetic resonance spectroscopy of fluorine-labelled cells", doi: 10.1186/s41747-017-0010-9.
- [12] C. H. Masterson, G. F. Curley, un J. G. Laffey, "Modulating the distribution and fate of exogenously delivered MSCs to enhance therapeutic potential: knowns and unknowns", 2019, doi: 10.1186/s40635-019-0235-4.
- [13] L. L. Israel, A. Galstyan, E. Holler, un J. Y. Ljubimova, "Magnetic iron oxide nanoparticles for imaging, targeting and treatment of primary and metastatic tumors of the brain", *J. Control. Release*, sēj. 320, lpp. 45–62, apr. 2020, doi: 10.1016/J.JCONREL.2020.01.009.
- [14] X. Y. Zhou *u.c.*, "Magnetic Particle Imaging for Radiation-Free, Sensitive and High-Contrast Vascular Imaging and Cell Tracking", *Curr. Opin. Chem. Biol.*, sēj. 45, lpp. 131, aug. 2018, doi: 10.1016/J.CBPA.2018.04.014.
- [15] M. Graeser *u.c.*, "Human-sized magnetic particle imaging for brain applications", *Nat. Commun.*, sēj. 10, nr. 1, 2019, doi: 10.1038/s41467-019-09704-x.
- [16] E. U. Saritas, P. W. Goodwill, G. Z. Zhang, un S. M. Conolly, "Magnetostimulation limits in magnetic particle imaging", *IEEE Trans. Med. Imaging*, sēj. 32, nr. 9, lpp. 1600–1610, 2013, doi: 10.1109/TMI.2013.2260764.
- [17] O. C. Sehl un P. J. Foster, "The sensitivity of magnetic particle imaging and fluorine-19 magnetic resonance imaging for cell tracking", *Sci. Rep.*, sēj. 11, nr. 1, lpp. 1–12, 2021, doi: 10.1038/s41598-021-01642-3.

- [18] J. J. Gevaert, C. Fink, J. Dikeakos, G. A. Dekaban, un J. Paula, "Magnetic Particle Imaging is a sensitive in vivo imaging modality for the quantification of dendritic cell migration", lpp. 1–29, 2021.
- [19] P. Vogel *u.c.*, "Synomag®: The new high-performance tracer for magnetic particle imaging", *Int. J. Magn. Part. Imaging*, sēj. 7, nr. 1, mar. 2021, doi: 10.18416/IJMPI.2021.2103003.
- [20] H. Paysen *u.c.*, "Cellular uptake of magnetic nanoparticles imaged and quantified by magnetic particle imaging", *Sci. Rep.*, sēj. 10, nr. 1, dec. 2020, doi: 10.1038/S41598-020-58853-3.
- [21] A. Antonelli, E. S. Scarpa, un M. Magnani, "Human Red Blood Cells Modulate Cytokine Expression in Monocytes/Macrophages Under Anoxic Conditions", *Front. Physiol.*, sēj. 12, febr. 2021, doi: 10.3389/FPHYS.2021.632682.
- [22] E. Jacquemin *u.c.*, "Expression cloning of a rat liver Na(+)-independent organic anion transporter.", *PNAS*, sēj. 91, nr. 1, lpp. 133–137, janv. 2014, doi: 10.1073/pnas.91.1.133.
- [23] N. N. Nyström, L. C. M. Yip, J. J. L. Carson, T. J. Scholl, un J. A. Ronald, "Development of a Human Photoacoustic Imaging Reporter Gene Using the Clinical Dye Indocyanine Green", *Radiol. Imaging Cancer*, sēj. 1, nr. 2, lpp. e190035, nov. 2019, doi: 10.1148/rycan.2019190035.
- [24] K. V. Keu *u.c.*, "Reporter gene imaging of targeted T cell immunotherapy in recurrent glioma", *Sci. Transl. Med.*, sēj. 9, nr. 373, janv. 2017, doi: 10.1126/scitranslmed.aag2196.
- [25] L. M. Lechermann *u.c.*, "Detection limit of ⁸⁹Zr-labeled T cells for cellular tracking: an in vitro imaging approach using clinical PET/CT and PET/MRI", *EJNMMI Res.*, sēj. 10, nr. 1, lpp. 82, dec. 2020, doi: 10.1186/s13550-020-00667-5.
- [26] S. S. Yaghoubi, D. O. Campbell, C. G. Radu, un J. Czernin, "Positron emission tomography reporter genes and reporter probes: Gene and cell therapy applications", *Theranostics*, sēj. 2, nr. 4, lpp. 374–391, 2012, doi: 10.7150/thno.3677.

- [27] B. C. Ahn, "Sodium iodide symporter for nuclear molecular imaging and gene therapy: From bedside to bench and back", *Theranostics*, sēj. 2, nr. 4. Ivyspring International Publisher, lpp. 392–402, 2012, doi: 10.7150/thno.3722.
- [28] C. Spitzweg, K. J. Harrington, L. A. Pinke, R. G. Vile, un J. C. Morris, "The Sodium Iodide Symporter and Its Potential Role in Cancer Therapy", *J. Clin. Endocrinol. Metab.*, sēj. 86, nr. 7, lpp. 3327–3335, jūl. 2001, doi: 10.1210/jcem.86.7.7641.
- [29] J. O'Doherty *u.c.*, "18F-Tetrafluoroborate, a PET Probe for Imaging Sodium/Iodide Symporter Expression: Whole-Body Biodistribution, Safety, and Radiation Dosimetry in Thyroid Cancer Patients.", *J. Nucl. Med.*, sēj. 58, nr. 10, lpp. 1666–1671, 2017, doi: 10.2967/jnumed.117.192252.
- [30] H. Jiang *u.c.*, "Safety, pharmacokinetics, metabolism and radiation dosimetry of 18F-tetrafluoroborate (18F-TFB) in healthy human subjects", *EJNMMI Res.*, sēj. 7, nr. 1, 2017, doi: 10.1186/s13550-017-0337-5.
- [31] S. B. Lee *u.c.*, "Tracking dendritic cell migration into lymph nodes by using a novel PET probe 18F-tetrafluoroborate for sodium/iodide symporter", *EJNMMI Res.*, sēj. 7, nr. 1, dec. 2017, doi: 10.1186/s13550-017-0280-5.
- [32] R. Sakemura *u.c.*, "Development of a clinically relevant reporter for chimeric antigen receptor t-cell expansion, trafficking, and toxicity", *Cancer Immunol. Res.*, sēj. 9, nr. 9, lpp. 1035–1046, sept. 2021, doi: 10.1158/2326-6066.CIR-20-0901/665804/AM/DEVELOPMENT-OF-A-CLINICALLY-RELEVANT-REPORTER-FOR.
- [33] J. W. Ostrominski *u.c.*, "CRISPR/Cas9-mediated introduction of the sodium/iodide symporter gene enables noninvasive in vivo tracking of induced pluripotent stem cell-derived cardiomyocytes", *Stem Cells Transl. Med.*, sēj. 9, nr. 10, lpp. 1203, okt. 2020, doi: 10.1002/SCTM.20-0019.
- [34] J. Nakayama *u.c.*, "High sensitivity in vivo imaging of cancer metastasis using a near-infrared luciferin analogue seMpai", *Int. J. Mol. Sci.*, sēj. 21, nr. 21, lpp. 1–8, 2020, doi:

10.3390/ijms21217896.

- [35] S. Iwano *u.c.*, "Single-cell bioluminescence imaging of deep tissue in freely moving animals.", *Science*, sēj. 359, nr. 6378, lpp. 935–939, febr. 2018, doi: 10.1126/science.aag1067.
- [36] O. C. Sehl, A. V. Makela, A. M. Hamilton, un P. J. Foster, "Trimodal cell tracking in vivo: Combining iron-and fluorine-based magnetic resonance imaging with magnetic particle imaging to monitor the delivery of mesenchymal stem cells and the ensuing inflammation", *Tomography*, sēj. 5, nr. 4, lpp. 367–376, 2019, doi: 10.18383/j.tom.2019.00020.
- [37] O. C. Sehl, B. Tired, M. A. Berih, A. V Makela, P. W. Goodwill, un P. J. Foster, "MPI region of interest (ROI) analysis and quantification of iron in different volumes", sēj. 8, nr. 1, lpp. 5–7, 2022.
- [38] H. Jiang *u.c.*, "Synthesis of ¹⁸F-Tetrafluoroborate via radiofluorination of boron trifluoride and evaluation in a murine C6-Glioma tumor model", *J. Nucl. Med.*, sēj. 57, nr. 9, lpp. 1454–1459, 2016, doi: 10.2967/jnumed.115.170894.
- [39] C. Mcfadden, C. L. Mallett, un P. J. Foster, "Labeling of multiple cell lines using a new iron oxide agent for cell tracking by MRI", *Contrast Media Mol. Imaging*, sēj. 6, nr. 6, lpp. 514–522, nov. 2011, doi: 10.1002/CMMI.456.
- [40] M. B. Preda *u.c.*, "Short lifespan of syngeneic transplanted MSC is a consequence of in vivo apoptosis and immune cell recruitment in mice", *Cell Death Dis. 2021 126*, sēj. 12, nr. 6, lpp. 1–12, jūn. 2021, doi: 10.1038/s41419-021-03839-w.
- [41] T. Thum, J. Bauersachs, P. A. Poole-Wilson, H. D. Volk, un S. D. Anker, "The Dying Stem Cell Hypothesis: Immune Modulation as a Novel Mechanism for Progenitor Cell Therapy in Cardiac Muscle", *J. Am. Coll. Cardiol.*, sēj. 46, nr. 10, lpp. 1799–1802, nov. 2005, doi: 10.1016/J.JACC.2005.07.053.
- [42] H. Y. Lee un I. S. Hong, "Double-edged sword of mesenchymal stem cells: Cancer-promoting versus therapeutic potential", *Cancer Sci.*, sēj. 108, nr. 10, lpp. 1939, okt. 2017,

doi: 10.1111/CAS.13334.

- [43] J. Sun *u.c.*, "MRI detection of the malignant transformation of stem cells through reporter gene expression driven by a tumor-specific promoter", *Stem Cell Res. Ther.*, sēj. 12, nr. 1, lpp. 1–14, 2021, doi: 10.1186/s13287-021-02359-w.
- [44] B. G. Cuiffo un A. E. Karnoub, "Mesenchymal stem cells in tumor development: Emerging roles and concepts", *Cell Adh. Migr.*, sēj. 6, nr. 3, lpp. 220, 2012, doi: 10.4161/CAM.20875.
- [45] P. Walczak *u.c.*, "Dual-modality monitoring of targeted intraarterial delivery of mesenchymal stem cells after transient ischemia", *Stroke*, sēj. 39, nr. 5, lpp. 1569–1574, mai. 2008, doi: 10.1161/STROKEAHA.107.502047.
- [46] M. Zaw Thin *u.c.*, "Multi-modal imaging probe for assessing the efficiency of stem cell delivery to orthotopic breast tumours", *Nanoscale*, sēj. 12, nr. 31, lpp. 16570–16585, aug. 2020, doi: 10.1039/D0NR03237A.
- [47] J. Hedhli *u.c.*, "Multimodal assessment of mesenchymal stem cell therapy for diabetic vascular complications", *Theranostics*, sēj. 7, nr. 16, lpp. 3876–3888, 2017, doi: 10.7150/THNO.19547.
- [48] B. Gleich un J. Weizenecker, "Tomographic imaging using the nonlinear response of magnetic particles", 2005, doi: 10.1038/nature03808.
- [49] P. Ludewig *u.c.*, "Magnetic particle imaging for assessment of cerebral perfusion and ischemia", *Wiley Interdiscip. Rev. Nanomedicine Nanobiotechnology*, sēj. 14, nr. 1, lpp. e1757, janv. 2022, doi: 10.1002/WNAN.1757.
- [50] A. Tomitaka, H. Arami, S. Gandhi, un K. M. Krishnan, "Lactoferrin conjugated iron oxide nanoparticles for targeting brain glioma cells in magnetic particle imaging", sēj. 7, lpp. 16890, 2015, doi: 10.1039/c5nr02831k.
- [51] D. Finas *u.c.*, "Lymphatic Tissue and Superparamagnetic Nanoparticles - Magnetic Particle Imaging for Detection and Distribution in a Breast Cancer Model", *Biomed. Tech.*

- (Berl)., sēj. 58 Suppl 1, nr. SUPPL.1, 2013, doi: 10.1515/BMT-2013-4262.
- [52] G. Song *u.c.*, "Janus Iron Oxides @ Semiconducting Polymer Nanoparticle Tracer for Cell Tracking by Magnetic Particle Imaging", *Nano Lett.*, sēj. 18, nr. 1, lpp. 182–189, 2018, doi: 10.1021/acs.nanolett.7b03829.
- [53] M. H. Pablico-Lansigan, S. F. Situ, A. Cristina, un S. Samia, "Magnetic particle imaging: advancements and perspectives for real-time in vivo monitoring and image-guided therapy", doi: 10.1039/c3nr00544e.
- [54] B. Zheng *u.c.*, "Magnetic particle imaging tracks the long-term fate of in vivo neural cell implants with high image contrast", *Sci. Rep.*, sēj. 5, nr. 1, lpp. 14055, sept. 2015, doi: 10.1038/srep14055.
- [55] H. Wei, Y. Hu, J. Wang, X. Gao, X. Qian, un M. Tang, "Superparamagnetic Iron Oxide Nanoparticles: Cytotoxicity, Metabolism, and Cellular Behavior in Biomedicine Applications", *Int. J. Nanomedicine*, sēj. 16, lpp. 6097, 2021, doi: 10.2147/IJN.S321984.
- [56] W. Bin Shen *u.c.*, "Human neural progenitor cells retain viability, phenotype, proliferation, and lineage differentiation when labeled with a novel iron oxide nanoparticle, Molday ION Rhodamine B", *Int. J. Nanomedicine*, sēj. 8, lpp. 4593–4600, nov. 2013, doi: 10.2147/IJN.S53012.
- [57] X. Wang *u.c.*, "Cancer stem cell labeling using poly(L-lysine)-modified iron oxide nanoparticles", *Biomaterials*, sēj. 33, nr. 14, lpp. 3719–3732, mai. 2012, doi: 10.1016/J.BIOMATERIALS.2012.01.058.
- [58] J. W. M. Bulte *u.c.*, "Quantitative “Hot-Spot” Imaging of Transplanted Stem Cells Using Superparamagnetic Tracers and Magnetic Particle Imaging", *Tomography*, sēj. 1, nr. 2, lpp. 91, dec. 2015, doi: 10.18383/J.TOM.2015.00172.
- [59] L. Li, X. Chen, W. E. Wang, un C. Zeng, "How to Improve the Survival of Transplanted Mesenchymal Stem Cell in Ischemic Heart?", *Stem Cells Int.*, sēj. 2016, 2016, doi: 10.1155/2016/9682757.

- [60] K. Stojanov, E. F. J. De Vries, D. Hoekstra, A. Van Waarde, R. A. J. O. Dierckx, un I. S. Zuhorn, "[18F]FDG Labeling of Neural Stem Cells for in Vivo Cell Tracking with Positron Emission Tomography: Inhibition of Tracer Release by Phloretin"., <http://dx.doi.org/10.2310/7290.2011.00021>, sēj. 11, nr. 1, lpp. 1–12, janv. 2012, doi: 10.2310/7290.2011.00021.
- [61] U. Großmann *u.c.*, "[18F]FLT - A new stem cell label for in vivo tracking with positron emission tomography", *J. Nucl. Med.*, sēj. 57, nr. supplement 2, 2016.
- [62] P. S. Patrick *u.c.*, "Lung delivery of MSCs expressing anti-cancer protein TRAIL visualised with 89Zr-oxine PET-CT", *Stem Cell Res. Ther.*, sēj. 11, nr. 1, lpp. 256, jūn. 2020, doi: 10.1186/S13287-020-01770-Z/FIGURES/5.
- [63] J. K. Willmann *u.c.*, "Imaging gene expression in human mesenchymal stem cells: From small to large animals", *Radiology*, sēj. 252, nr. 1, lpp. 117–127, jūl. 2009, doi: 10.1148/RADIOL.2513081616/ASSET/IMAGES/LARGE/R09JN29T01X.JPEG.
- [64] M. N. McCracken *u.c.*, "Long-term in vivo monitoring of mouse and human hematopoietic stem cell engraftment with a human positron emission tomography reporter gene", *Proc. Natl. Acad. Sci. U. S. A.*, sēj. 110, nr. 5, lpp. 1857–1862, janv. 2013, doi: 10.1073/PNAS.1221840110.
- [65] V. Schönitzer *u.c.*, "In vivo mesenchymal stem cell tracking with PET using the dopamine type 2 receptor and 18F-fallypride", *J. Nucl. Med.*, sēj. 55, nr. 8, lpp. 1342–1347, 2014, doi: 10.2967/jnumed.113.134775.
- [66] J. Terrovitis *u.c.*, "Ectopic expression of the sodium-iodide symporter enables imaging of transplanted cardiac stem cells in vivo by single-photon emission computed tomography or positron emission tomography", *J. Am. Coll. Cardiol.*, sēj. 52, nr. 20, lpp. 1652–1660, nov. 2008, doi: 10.1016/J.JACC.2008.06.051.
- [67] R. M. Dwyer *u.c.*, "Mesenchymal stem cell-mediated delivery of the sodium iodide symporter supports radionuclide imaging and treatment of breast cancer", *Stem Cells*, sēj. 29, nr. 7, lpp. 1149–1157, 2011, doi: 10.1002/stem.665.

- [68] C. Schug *u.c.*, "TGFB1-driven mesenchymal stem cell-mediated NIS gene transfer", *Endocr. Relat. Cancer*, sēj. 26, nr. 1, lpp. 89–101, 2019, doi: 10.1530/ERC-18-0173.
- [69] S. Diocou *u.c.*, "[18F]tetrafluoroborate-PET/CT enables sensitive tumor and metastasis in vivo imaging in a sodium iodide symporter-expressing tumor model", *Sci. Rep.*, sēj. 7, nr. 1, lpp. 946, dec. 2017, doi: 10.1038/s41598-017-01044-4.
- [70] R. Vandergaast *u.c.*, "Enhanced noninvasive imaging of oncology models using the NIS reporter gene and bioluminescence imaging", *Cancer Gene Ther.* 2019 273, sēj. 27, nr. 3, lpp. 179–188, janv. 2019, doi: 10.1038/s41417-019-0081-2.
- [71] D. W. Hwang un D. S. Lee, "Optical Imaging for Stem Cell Differentiation to Neuronal Lineage", *Nucl. Med. Mol. Imaging (2010)*., sēj. 46, nr. 1, lpp. 1, mar. 2012, doi: 10.1007/S13139-011-0122-8.
- [72] K. Fiedorowicz *u.c.*, "Tissue-specific promoter-based reporter system for monitoring cell differentiation from iPSCs to cardiomyocytes", *Sci. Reports 2020 101*, sēj. 10, nr. 1, lpp. 1–13, febr. 2020, doi: 10.1038/s41598-020-58050-2.
- [73] E. Wolfs *u.c.*, "Optimization of Multimodal Imaging of Mesenchymal Stem Cells Using the Human Sodium Iodide Symporter for PET and Cerenkov Luminescence Imaging", *PLoS One*, sēj. 9, nr. 4, lpp. e94833, apr. 2014, doi: 10.1371/JOURNAL.PONE.0094833.
- [74] J. J. Kelly *u.c.*, "Safe harbor-targeted CRISPR-Cas9 homology-independent targeted integration for multimodality reporter gene-based cell tracking", *Sci. Adv.*, sēj. 7, nr. 4, lpp. eabc3791, janv. 2021, doi: 10.1126/sciadv.abc3791.
- [75] X. Duan *u.c.*, "The long-term fate of mesenchymal stem cells labeled with magnetic resonance imaging-visible polymersomes in cerebral ischemia", *Int. J. Nanomedicine*, sēj. 12, lpp. 6705–6719, sept. 2017, doi: 10.2147/IJN.S146742.

CHAPTER 4

4 Imaging CAR-NK cells Targeted to HER2 Ovarian Cancer with Sodium Iodide Symporter-Based Positron Emission Tomography

The human epidermal growth factor receptor 2 (HER2) is overexpressed by a myriad of solid tumours and is associated with poor prognosis. Chimeric Antigen Receptor (CAR) cell therapies use a CAR to redirect immune cells to target and kill cancer cells expressing a particular antigen. Developing HER2-targeting CAR expressing immune cells (i.e. T cells of Natural Killer (NK) cells), has recently attracted attention. CAR T cell therapies have shown tremendous progress for treating hematological malignancies, while less effective in solid tumours. Furthermore, CAR T therapies are associated with cytokine release syndrome (CRS), graft versus host disease (GvHD), and neurotoxicity. Emerging CAR NK therapies are overcoming several limitations of CAR T cells related to their source, manufacturing, price, and potential cytotoxicity. There is also an unmet need for a robust, non-invasive clinically relevant imaging tool to track the *in vivo* fate of these immunotherapies. In this study, we developed HER2-targeted CAR-NK cells co-expressing the positron emission tomography (PET) reporter gene human sodium-iodide symporter (NIS). We evaluated the therapeutic potential of these cells in a mouse model of HER2 ovarian cancer as well as the ability to visualize these cells using PET.

Human NK-92 cells were engineered to express a HER2-targeted CAR, the bioluminescence imaging (BLI) reporter Antares, and NIS. Human SKOV3-ip1 ovarian cancer cells were engineered to express the BLI reporter Firefly luciferase (Fluc). SKOV3-ip1 were co-cultured with different NK constructs at different ratios to show *in vitro* NK lytic abilities. HER2 CAR NK cells exhibited significantly higher killing of co-cultured SKOV3-ip1 cells when compared to killing of naïve NK cells. Mice bearing Fluc-expressing SKOV3-ip1 tumors received intraperitoneal

injections of NIS⁺ Antares⁺ CAR NK cells. Tumour burden was tracked longitudinally with Fluc BLI, and NK cells were longitudinally imaged with Antares BLI and PET using the NIS-targeted tracer ¹⁸F-tetrafluoroborate ([¹⁸F]TFB) at endpoint. Mice receiving Antares-NIS-CAR-NK cells showed significantly reduced tumor burden (Fluc BLI signal; p<0.05) and survived significantly longer compared to control mice receiving either sham or naïve NK-92 cell injections (p<0.05). CAR-NK cells were visualized in the peritoneal space using both Antares BLI and PET. Significantly higher [¹⁸F]TFB PET signal was measured in mice receiving NIS cells compared to control mice (p<0.05). We demonstrate the ability to use PET to non-invasively visualize a HER2-targeted CAR-NK cell therapy that showed promising treatment responses in a highly aggressive ovarian cancer model.

4.1 Introduction

Ovarian cancer is the most lethal gynecological cancer in women, with more than 65% of diagnosed women expected to die from the disease [1]. While surgical tumour debulking remains the main treatment for ovarian cancer, sometimes in combination with chemotherapy at later disease stages, more than 70% of patients recur and develop drug resistant tumors [2][3]. New treatment strategies that have the potential to improve the survival of women with this devastating disease are needed.

Advancements in the understanding of important biological drivers of cancer have led to a new and ever-expanding options of approved targeted therapies with many more in development [4]. Human epidermal growth factor receptor-2 (HER2), also known as HER2/erbB2, is a tumor-associated antigen (TAA) that is over-expressed in ~10-20% of breast cancer cases, ~ 3% of cervical and uterine cancer cases [5], and ~27.6% of ovarian cancer cases [6]. HER2 initiates intracellular signaling pathways that promote tumour growth, survival and metastasis, and its

overexpression is associated with poor clinical outcomes making this a promising and important therapeutic target [7][8]. Trastuzumab (Herceptin) is a monoclonal therapeutic antibody directed against HER2 that has shown remarkable results against HER2 breast cancer [9]. However, it has not worked as well in HER2 ovarian cancer highlighting the need for exploring alternative HER2-targeted therapies in the hope of improving therapeutic responses [10].

Chimeric antigen receptor (CAR) cell immunotherapies involve administering immune cells that have been genetically modified outside the body to target a particular TAA and kill cancer cells. The extracellular binding domain of a CAR binds a TAA to initiate the activation of numerous intracellular signaling domains such as ζ -chain of the T cell receptor (TCR)/CD3 complex and the γ -chain of the high-affinity receptor for immunoglobulin E [11][12]. CAR-T cells have shown transformative and even curative clinical results in blood cancer patients, and six CAR-T cell therapies have been approved in the United States for the treatment of some patients with follicular lymphoma, mantle cell lymphoma, diffuse and primary mediastinal large B-cell lymphoma, B cell acute lymphoblastic leukemia, and multiple myeloma. In addition, many new CAR designs are being explored for the treatment of solid tumors in both preclinical models and clinical trials, [13][14]. Recent studies have developed HER2-directed CAR T cells for the treatment of colorectal cancer [15], breast cancer [16], gastric cancer [17], sarcoma [18], glioblastoma [19], ovarian cancer [20], osteosarcoma[21], and medulloblastoma [22].

Despite the remarkable clinical success, wider application of CAR-T cells have been hindered by life-threatening side effects such as cytokine release syndrome (CRS) and immune effector cell-associated neurotoxicity syndrome (ICANS) [23]. In addition, CAR-T cells have not demonstrated the same level of therapeutic efficacy against solid tumors as blood cancer. Finally, CAR T cells

can trigger graft-vs-host disease and thus autologous therapies derived from the patient are required. This increases production complexity, production times and overall cost [24]. In the last decade, natural killer (NK) cells have become a promising alternative to T cells that have several benefits. Endogenous NK cells have significant cancer cell killing potential through the recognition and binding of their activation receptors, causing the release of lytic granules [25][26][27]. NK cells also be used as an allogenic source to make an “off-the-shelf” therapy as they do not cause GvHD. Early studies in patients with B cell acute lymphoblastic leukemia have shown promising efficacy without evidence of severe CRS, ICANS, or GvHD [28][29][30][31][32][33]. In 2022, there were 31 global clinical trials registered to address the safety and efficacy of CAR-NK cells in patients with hematological cancer [29]. However, difficulties in isolation, purification and expansion of primary NK cells potentially limits their widespread clinical use [34]. As an alternative, many groups have used NK-92 cells, an interleukin-2 (IL-2) -dependent human NK cell line, that can be easily expanded, engineered, and have demonstrated sustainable cytotoxicity against many cancer types [35][36][37][38].

Methods to track cellular immunotherapies in the clinic are lacking. Rudimentary techniques such as blood tests to assess peripheral blood cytokines, or single-site biopsies are inadequate for assessing micrometastasis and evaluating therapeutic response [39]. Understanding CAR therapy kinetics and *in vivo* behavior of CAR therapies can enable interpretation of therapy response and shortcomings which can facilitate further therapeutic success and progress in the clinic. To optimize the efficacy of these therapies, non-invasive dynamic imaging to monitor CAR therapies is required. While some patients receiving the CAR therapy show therapeutic response, some patients experience tumour progression or pseudoprogression (followed by favorable tumour regression), which can oftentimes be misinterpreted by traditional imaging with CT or ¹⁸F-FDG

PET [40]. Thus, a non-invasive imaging platform that can accurately report on case-by-case response to CAR therapy would provide a clearer picture. To image the trafficking, infiltration and accumulation of CAR immunotherapies directed against solid tumours, a sensitive clinical imaging modality which provides 3D whole-body imaging using a non-immunogenic imaging approach that does not impact CAR functioning, would be the holy grail for treatment assessment. Previous studies have shown the use of PET imaging of CAR T [41][40][42]. Ponomarev *et al.*, transduced CAR T cells with the herpes simplex virus thymidine kinase (HSVtk) and correlated the BLI signal of MSLN+ tumours with PET signal of the MSLN-directed CAR T cells [40]. However, they reported that HSVtk-expressing CAR T cells were less effective in tumour killing than CAR T cells alone, and increased HSVtk expression affected CAR T cell viability. Pomper *et al.*, labeled CD19 targeted-CAR T cells with a truncated prostate specific membrane antigen (tPSMA) for imaging with PET and reported an *in vivo* detection limit of 2,000 CAR T cells [41]. However, there are potential issues with overexpression of PSMA in CAR T cells [43]. Sellmyer tested the expression of the *E. coli* dihydrofolate reductase enzyme (eDHFR) on CAR T cells and successfully imaged with PET [42]. In this study, we employ the human Sodium Iodide symporter (NIS) as a non-immunogenic PET reporter gene to visualize HER2 targeting CAR-NK therapy. NIS is an intrinsic membrane transporter that has seen significant attention as a PET reporter gene due to its human-origin (minimizing immunogenicity), its ability to function as a therapeutic gene, and its compatibility with many PET probes to allow for whole body PET imaging [44][45][46]. Thus, NIS was incorporated into the HER2-targeting CAR NK-92 therapy to enable non-invasive visualization of NK cells with PET. Furthermore, CAR-NK-92 cells were additionally engineered with Antares, which serves as a BLI reporter gene for sensitive *in-vivo* cellular tracking when administered with its optimized substrate fluoroflurimazine (FFZ) [47]. In this work, we developed

trackable HER2-targeted CAR NK-92 cells, which were non-invasively visualized using NIS-PET, that slowed the progression of HER2 positive ovarian cancer in mice.

4.2 Materials and Methods

4.2.1 Cell Lines

The HER2⁺ human ovarian cancer cell line, SKOV3-ip1, was a kind gift from Dr. Trevor Shepherd (University of Western Ontario) and cultured in McCoy's 5a Medium Modified (ThermoFisher Scientific, 16600-082, Massachusetts, USA) supplemented with 10% fetal bovine serum (FBS) (ATCC® 30-2020™, Virginia, USA). NK-92 cells were purchased from American Type Culture Collection (ATCC® CRL-2407™, Virginia, USA). NK-92 cells were maintained in α MEM (ThermoFisher Scientific, 12000-063, Massachusetts, USA,) supplemented with 1.5 g sodium bicarbonate (Sigma-Aldrich, S5761, Missouri, USA), 0.2 mM of Myo-inositol (Sigma-Aldrich, I-7508, Missouri, USA), 0.02 mM folic acid (Sigma-Aldrich, F-8758, Missouri, USA), 12.5% fetal bovine serum (not heat-activated, ATCC® 30-2020™, Virginia, USA), and 12.5% Horse Serum (not heat activated- ThermoFisher Scientific, 16050122, Massachusetts, USA). Complete media included 0.1 mM of 2-mercaptoethanol (ThermoFisher Scientific, MA, USA 21985-023) and 500 U/mL of recombinant human IL-2 (Sigma-Aldrich, I7908, Missouri, USA). All cells were kept in a humidified incubator with 5% CO₂ at 37°C and routinely confirmed to be mycoplasma-free using the MycoAlert mycoplasma detection kit (Lonza LT07-318, Basel, Switzerland).

4.2.2 Cloning and Lentiviral Production

All cloning was performed using an In-Fusion kit (Takara Bio USA, Inc. CA, USA). A lentiviral transfer plasmid was made encoding the human elongation factor α promoter (pEF1 α) driving an anti-HER2 CAR that uses a designed ankyrin repeat protein (DARPin) as the tumor-antigen

targeting domain (a kind gift from Dr. Jonathan L. Bramson and described previously in [48]). Downstream of this CAR, the bioluminescence imaging (BLI) reporter gene Antares (Addgene, MA, USA 74279) was cloned and separated by a T2A self-cleaving peptide sequence to make a pEF1 α -HER2CAR-Antares transfer plasmid. A second transfer plasmid also driven by the pEF1 contained zsGreen (ZsG) followed by the NIS gene (Origene technologies, Inc. MD, USA NM_000453) separated by the T2A self-cleaving peptide sequence (pEF1 α -ZsG-NIS). Finally, a previously made pEF1 α -tdT-Fluc lentiviral transfer plasmid containing a tdTomato (tdT) (from Addgene plasmid #48688) and the BLI reporter gene Firefly luciferase (Fluc) under the control of pEF1 was used (previously cloned and described in [49]).

For the pEF1-ZsG-NIS construct, lentivirus was produced by a commercial vendor at a titre of 10^8 IFU/ml (Origene technologies, Inc. MA, USA: custom made). The other viruses were produced in house using each of the above transfer plasmids with the packaging and envelope plasmids pMDLg/pRRE, pRSV-Rev, and pMD2.G (Addgene MA, USA plasmids #12251, #12253, and #12259, respectively). Human embryonic kidney (HEK 293T; ATCC, Virginia, USA) cells were transfected with Lipofectamine 3000 (Thermo Fisher Scientific, MA, USA) in accordance with the manufacturer's lentiviral production instructions (Thermo Fisher Scientific Inc., MA, USA). After 24-48 hours, viral-containing supernatant was collected and filtered with a 0.45 μ m filter and frozen at -80 °C until use.

4.2.3 Lentiviral Transductions

SKOV3-ip1 cells were transduced with the pEF1-tdT-Fluc lentiviral vector using 8- μ g/mL polybrene. Transduced cells were sorted for tdT using a FACS Aria III fluorescence-activated cell

sorter (BD Biosciences, Ontario, Canada) to obtain Fluc⁺tdT⁺SKOV3-ip1 cells with a purity of 98%.

NK-92 cells were either transduced with one or both the pEF1-HER2CAR-Antares and/or pEF1-ZsG-NIS lentiviral vectors at a multiplicity of infection of 70 and with 8 µg/mL of polybrene. NK cells transduced with EF1-HER2CAR-Antares virus were sorted for cyOFP1 in Antares and cells transduced with the EF1-zsG-NIS virus for zsG. The brightest 10% of engineered cells were collected with a purity of 93% for Antares⁺ CAR NK cells, 98% for NIS⁺ NK cells (No CAR), and 98% for NIS⁺ Antares⁺ CAR NK cells.

4.2.4 HER2 Analysis

For assessment of HER2 expression, SKOV3-ip1 cells were stained using an Alexa Fluor 488 anti-human CD340 (ErbB2/HER2; 5 µl per million cells in 100 µl staining volume; BioLegend California, USA 324410) prior to flow cytometric analysis using a FACS flow cytometer (BD Biosciences).

4.2.5 Cytotoxicity Assay

To evaluate immune cell cytotoxicity, Fluc⁺tdT⁺SKOV3-ip1 cells were cultured alone or with naïve NK cells, NIS⁺ NK cells, Antares⁺ CAR NK cells, or NIS⁺ Antares⁺ CAR NK cells at different effector: target (E:T) ratios. A 1:1 of effector to target ratio used 2x10⁵ cells of each cell type, and for different E:T ratios (2:1, 5:1), the number of effector NK cells was increased accordingly. After 24 hours of co-culturing, Fluc BLI was performed to assess cancer cell viability by adding 150-µg/mL D-luciferin to each well and imaging plates on an IVIS Lumina XRMS scanner (PerkinElmer, MA, USA). Regions of interest were drawn over each well using

LivingImage 4.5.2 software (PerkinElmer, Massachusetts, USA) and average radiance (p/s/cm²/sr) at peak signal was used.

Time-lapse fluorescence microscopy of Fluc⁺tdT⁺SKOV3-ip1 cells co-cultured with either NIS⁺ NK or NIS⁺ Antares⁺ CAR NK cells at a E:T of 2:1 was performed on a CytoSMART Lux3 FL incubator microscope (CytoSMART Technologies BV, AZ Eindhoven, Netherlands). Each image an exposure time of 1020 ms, gain of 45, and intensity of 36%, and were acquired every 15 minutes for 36 hours. The number of tdT-positive cancer cells over time were measured using the CytoSMART software.

4.2.6 Animal Model

Animals were cared for in accordance with the standards of the Canadian Council on Animal Care, and experiments were conducted as specified in our approved animal use protocol (AUP 2020-025). Fluc⁺tdT⁺SKOV3-ip1 cells (10⁵ in 100 µL) were injected intraperitoneally into immunocompromised female NOD scid gamma (NSG) mice and tumour progression was monitored with Fluc BLI as described below. One week post tumor inoculation, mice were administered intraperitoneally on days 8, 11 and 14 post cancer cell inoculation with either PBS (sham; n=4), 1.5x10⁷ of naïve NK cells (n=4), or 1.5x10⁷ NIS⁺ Antares⁺ CAR NK cells (n=6). Following NK cell delivery, all mice received daily intraperitoneal injections of interleukin-2 (IL-2; 12,500 IU) except on treatment days 8, 11, and 14 and up until day 35.

4.2.7 Fluc BLI of Tumour Burden

Mice were anesthetized with 2% isoflurane, injected intraperitoneally with D-luciferin (150 µg/mL) (Sigma Aldrich, Missouri, USA 808350) and imaged with an IVIS Lumina XRMS In Vivo Imaging System (PerkinElmer, Massachusetts, USA). Images with auto exposure times were

captured with a 60 second delay for 30 minutes, with a field of view of 12 cm. Regions of interest were drawn manually around the entire mouse body using the LivingImage software (PerkinElmer, Massachusetts, USA) to measure the average radiance (p/s/cm²/sr). Peak average radiance observed during the 30 minutes scan time was used for data analysis.

4.2.8 Antares BLI of NIS⁺ Antares⁺ CAR NK cells

BLI of mice receiving NIS⁺ Antares⁺ CAR NK cells was performed over 30 minutes following intraperitoneal injections of the Antares substrate fluoroflurimazine (FFZ) as previously described (50 μ L of stock solution diluted 50x in PBS; 50 μ L injected; FFZ was kindly gifted by Promega, Wisconsin, USA) [50]. Regions of interest were drawn manually around the entire mouse body and the peak average radiance (p/s/cm²/sr) over the 30-minute imaging window was determined.

4.2.9 [¹⁸F]TFB PET

PET imaging was performed to evaluate the ability of visualize NIS⁺ Antares⁺ CAR NK cells. Mice were anesthetized with 2% isoflurane, injected with 10-15 MBq of [¹⁸F]TFB in 100-150 μ L and imaged with a Siemens Inveon™ microPET system (Siemens Medical Solutions USA, Inc.). Animal breathing rate and body temperature were monitored and kept between 40-70 bpm and at 37°C, respectively, using a custom-made animal holder that allowed for simultaneous multi-mouse imaging. Dynamic PET images were acquired for 45 minutes post [¹⁸F]TFB tail vein injection. Images were reconstructed using ordered subset expectation maximization (OSEM). Quantification of PET signal was performed by manual segmentation of ROIs using Horos Project software v3.3.6. Maximum Activity Projections (MAPs). Standard Uptake Value (SUV) was calculated with the below equation:

$$SUV \left(\frac{g}{mL} \right) = \frac{Pixel\ value \left(\frac{Bq}{mL} \right) * weight\ (kg)}{Dose\ (Bq)} * 1000 \left(\frac{g}{kg} \right).$$

4.2.10 Peritoneal Lavage

Mice were euthanized by cervical dislocation and the peritoneal cavity was flushed with 1 mL of PBS using a 27-gauge syringe, followed by aspiration of the peritoneal fluid to assess for cellular composition. The aspirate was strained with a 70 µm nylon strainer, spun down at 200 relative centrifuge field(rcf) for 10 minutes, and resuspended in 1 mL of PBS buffer solution containing 2% FBS, 1 µM EDTA, and 25 µM HEPES. Cells suspensions were assessed for the presence of Fluc⁺tdT⁺SKOV3-ip1 and NIS⁺ Antares⁺ CAR NK cells using a FACSCanto flow cytometer and FlowJo v10 software (BD Biosciences, Ontario, Canada).

4.2.11 Histology and Microscopy

Tumour masses within the peritoneal space, as well as the ovaries, were collected and fixed in 4% paraformaldehyde for 24 hours. Half the tumour masses and one ovary from each mouse were embedded in paraffin, sectioned, and stained with hematoxylin-eosin. The remaining ovary and the other half of tumour tissue were immersed in increasing concentrations (10, 20 and 30%) of sucrose solutions for freezing. Frozen tissues were then cryosectioned and fluorescence microscopy was performed to visualize NIS⁺ Antares⁺ CAR NK cells (also express ZsG). Both bright-field and fluorescence images were acquired with a Revolve fluorescence microscope (Echo Microscopes, California, USA).

4.2.12 Statistical Analysis

Two-way repeated measures Analysis Of Variance (ANOVA) with multiple comparisons were used to compare Fluc and Antares BLI radiance over time between mouse cohorts. Mouse survival data were displayed on a Kaplan-Meier curve and a logrank Mantel-Cox test was used to compare survival between cohorts. For PET data analysis, an unpaired t test (assuming Welch correction) was used to compare the SUV values between cohorts. Statistical analysis was performed with GraphPad Prism Software (Version 7.00 for Mac OS X, GraphPad Software Inc., La Jolla California USA, www.graphpad.com). All data are expressed as mean \pm standard deviation of at least three independent experiments and a p-value less than 0.05 was considered statistically significant.

4.3 Results

The lentiviral construct in Figure 4.1A was used to make Fluc+ tdT+SKOV3-ip1 cells with a purity of 98%. Flow cytometry revealed the presence of HER2 expression in SKOV3-ip1 cells (Fig. 4.1B). Figure 4.1D shows the lentiviral constructs used to engineer NK-92 cells. First, NK cells were transduced with either a lentivirus encoding zsG and NIS to make NIS+ NK cells (98% purity after sorting; Fig. 4.1F) or a HER2-CAR-Antares lentivirus to make Antares+ CAR NK cells (93% purity after sorting; Fig. 4.1G). A subset of NK-92 cells was transduced with both vectors to produce NIS+ Antares+ CAR NK cells (purity of 98% after sorting; Fig. 4.1H). Figure 4.1I and 4.1J show a BLI cytotoxicity assay using the four effector NK cell phenotypes against Fluc+tdT+SKOV3-ip1 cells at different effector to target ratios. Average BLI radiance (p/sec/cm²/sr) of cells demonstrated significantly higher cytotoxicity with CAR-expressing NK cells in comparison to non-CAR expressing NK cells at all E:T ratios (p<0.05). No differences in

cytotoxicity were observed between non-CAR expressing NK cells (naïve NK cells and NIS⁺ NK cells) or CAR-expressing NK cells (Antares⁺ CAR NK cells and NIS⁺ Antares⁺ CAR NK cells).

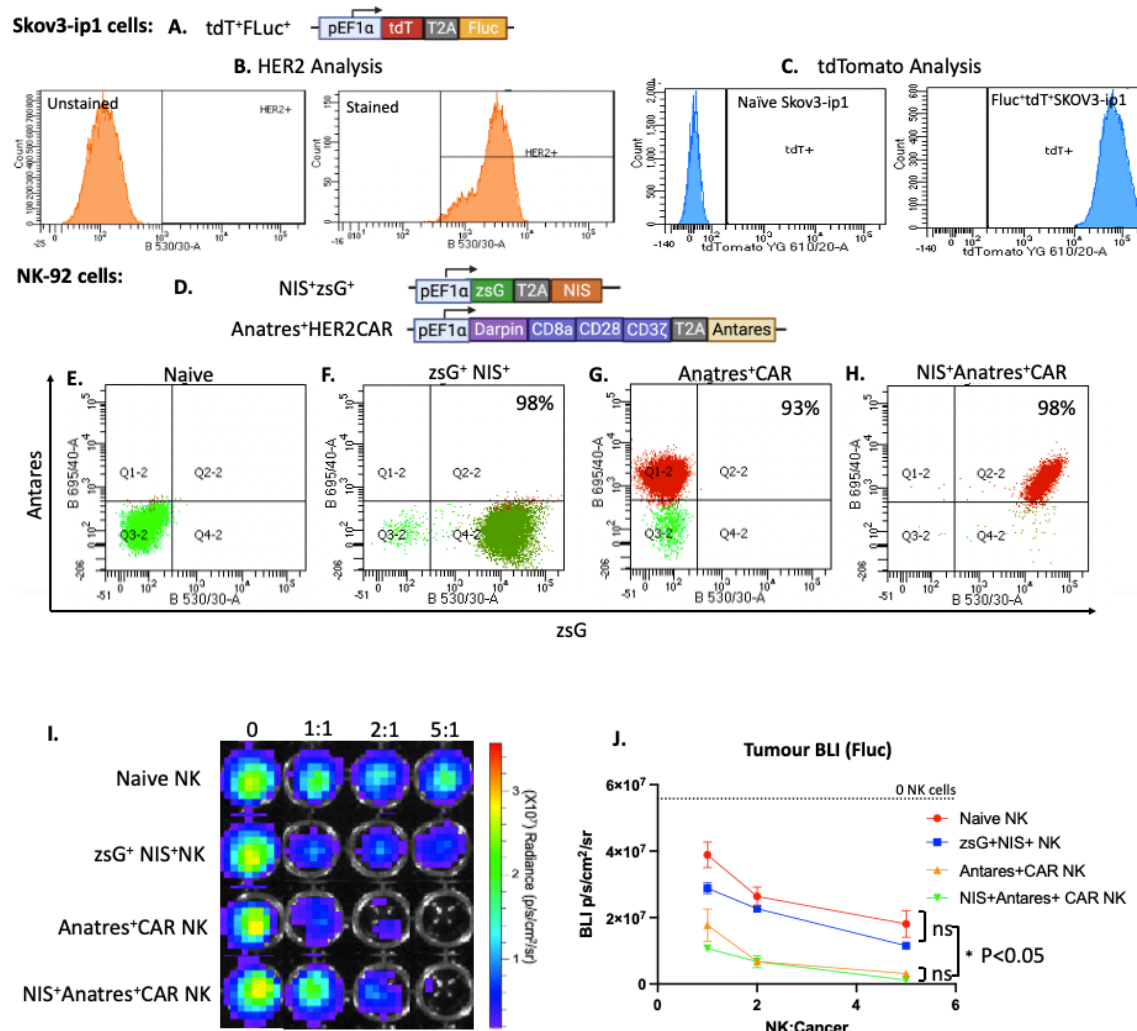


Figure 4.1: A) Lentiviral construct used to engineer SKOV3-ip1 ovarian cancer cells containing the human elongation factor 1 alpha promoter (pEF1a) to drive expression of tdTomato (tdT) and Firefly luciferase (Fluc) separated by a T2A peptide sequence. Flow plots showing Fluc⁺tdT⁺SKOV3-ip1 cells (B) without or with HER2 immunostaining. C) Flow plots showing naïve SKOV3-ip1 and Fluc⁺tdT⁺SKOV3-ip1. D) Lentiviral constructs used to engineer NK-92 cells. Describe constructs. E-H) Flow plots confirming the expression of zsG and Antares in NK-92 cells engineered with both constructs in D. I) Cytotoxicity assays by BLI-Fluc showing various levels of ovarian cancer killing upon co-culturing of Fluc⁺tdT⁺SKOV3-ip1 with NK cells at different effector to target ratios. Naïve NK and zsG⁺ NIS⁺ NK effectors showed no significant difference in cancer killing at all ratios, while CAR Antares⁺ NK and NIS⁺ Antares⁺ CAR NK cells showed more cancer killing (significantly higher than non-CAR-expressing NK effectors),

especially at higher ratios (J.). There was no significant difference in killing abilities between CAR Antares⁺ NK and NIS⁺ Antares⁺ CAR NK effector cells (J.).

For *in-vivo* experiments, 10^5 Fluc⁺tdT⁺SKOV3-ip1 cells were injected intraperitoneally into 14 NSG mice and tumour progression was monitored with Fluc BLI (Figure 4.2A). One week post inoculation, mice received either intraperitoneal injections of PBS (n=4), naïve NK cells (1.5×10^7 ; n=4), or NIS⁺ Antares⁺ CAR NK cells (1.5×10^7 ; n=6). These injections were repeated on days 11 and 14. Mice receiving either NK therapies also received daily intraperitoneal injections of IL-2 (12,500 units) except for therapy days. As demonstrated by Fluc BLI signal from Fluc⁺tdT⁺SKOV3-ip1 cells, mice receiving PBS or naïve NK cell injections showed continuous and rapid growth of tumours (Fig. 4.2B). Mice receiving NIS⁺ Antares⁺ CAR NK cells showed significantly reduced average BLI signal compared to both control groups on days 14, 18, 23 and 28 ($p < 0.05$; Fig. 4.2C). Additionally, the NIS⁺ Antares⁺ CAR NK cell therapy resulted in a significantly higher survival compared to mice receiving either PBS or naïve NK cells ($p < 0.001$; Fig. 4.2D).

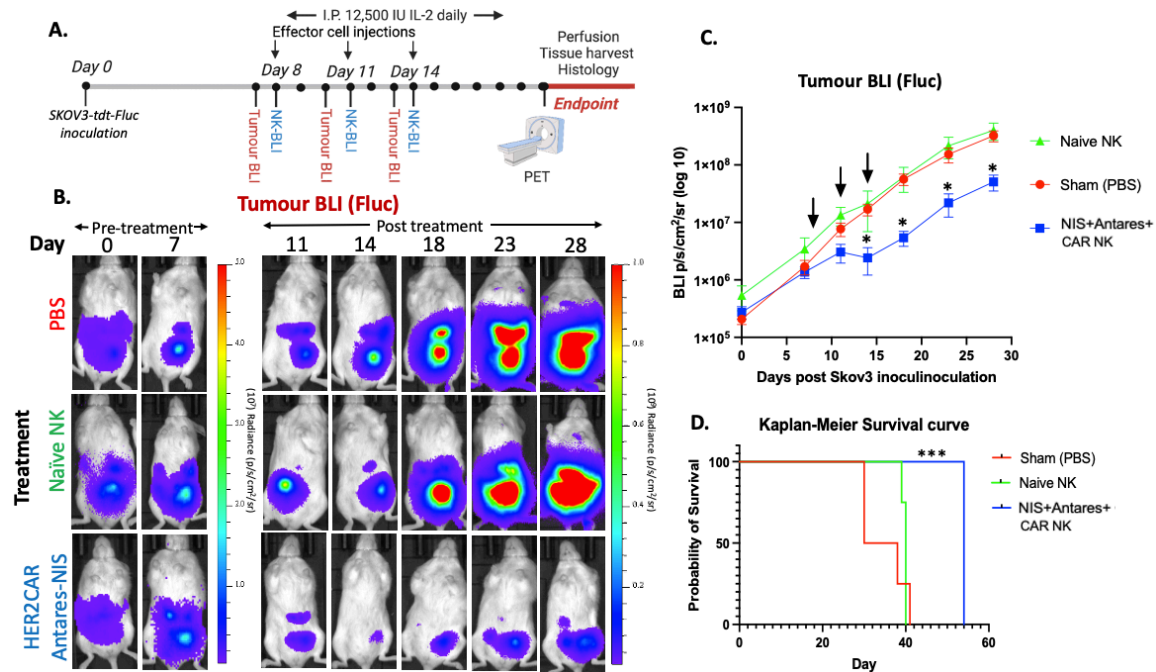


Figure 4.2: A) Experimental design of mouse studies. B) Fluc BLI images of tumor burden from a representative mouse from each cohort (PBS, Naïve NK and NIS⁺ Antares⁺ CAR NK). C) Average Fluc BLI radiance from all mice showed significantly lower tumour burden in mice receiving NIS⁺ Antares⁺ CAR NK cells compared to both other control cohorts at day 14, 18, 23 and 28 (*p<0.05). D) Kaplan-Meier curve analysis showed significantly increased survival in mice receiving NIS⁺ Antares⁺ CAR NK cells compared to mice receiving PBS or Naïve NK cells (***p<0.001).

Starting the day of NK cell administration (Day 8), mice receiving NIS⁺ Antares⁺ CAR NK cells were additionally imaged with Antares BLI twice per week (Fig. 4.3A). Antares signal fluctuates in response to the NK cell injections and stabilized once NK administration was halted. Daily injections of IL-2 to mice were halted on day 33 and the Antares BLI signal remained relatively stable thereafter. On Day 27, mice receiving either NIS⁺ Antares⁺ CAR NK cells (n=4) or PBS injections (n=3) were imaged with PET using the NIS tracer ¹⁸F[TFB] (Fig. 4.3 C & 4.3 D). Maximum activity projections (MAPs) are shown where mice receiving PBS injections display uptake in endogenous tissue expressing NIS such as the salivary glands, thyroid, and stomach, as well as signal from the bladder due to the urinary clearance of the ¹⁸F[TFB] probe. In contrast, mice receiving NIS⁺ Antares⁺ CAR NK cells showed additional ¹⁸F[TFB] uptake in regions within the peritoneal cavity. Regions of interest (ROIs) were drawn over these areas in the NIS⁺ Antares⁺ CAR NK cell group, as well as general peritoneal ROIs for the PBS group, and analysis showed significantly higher peritoneal PET signal (SUV) in treated mice (Fig. 4.3E).

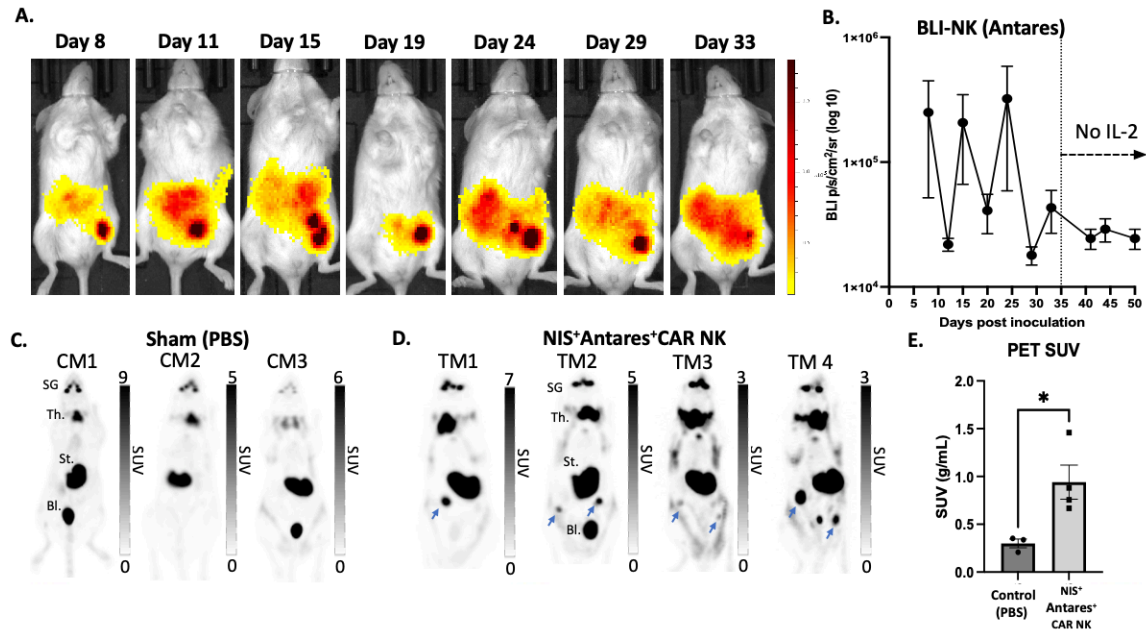


Figure 4.3: A) Longitudinal Antares BLI images of a representative mouse receiving NIS⁺ Antares⁺ CAR NK cells. B) Average radiance from Antares BLI images from all mice receiving NIS⁺ Antares⁺ CAR NK cells. Ceasing daily injections of IL-2 at day 35 resulted in stable Antares BLI signal from NIS⁺ Antares⁺ CAR NK cells. C and D) ¹⁸F[TFB] PET images of control mice (CM) receiving sham (PBS) injections and treated mice (TM) receiving NIS⁺ Antares⁺ CAR NK cells on day 27 post cancer cell inoculation. ¹⁸F[TFB] uptake is noted in NIS-expressing tissues and clearance routes (salivary glands (SG), thyroid (Th.), stomach (St.) and bladder (Bl.)) shows uptake of ¹⁸F[TFB]. Additional ¹⁸F[TFB] uptake is noted in the peritoneal of all mice receiving NIS⁺ Antares⁺ CAR NK cells. E) Significantly higher peritoneal PET signal (SUV) was measured in mice receiving NIS⁺ Antares⁺ CAR NK cells compared to mice receiving PBS injections (*p<0.05).

On day 30, one control mouse and one mouse receiving NIS⁺ Antares⁺ CAR NK cells were sacrificed, and peritoneal lavages were performed to assess the cellular composition within the peritoneal cavity (Fig. 4.4A). Assessment of the cellular aspirate with flow cytometry revealed tdtomato positive cancer cells in both mice but zsGreen positive cells only in the mouse receiving NK cell therapy (Fig. 4.4C and 4.4E). Following lavage, laparotomies were performed for gross assessment of the presence of ascites and tumors. The control mouse showed ascites within the peritoneal space and a larger tumour mass (Fig. 4.4B). In contrast, the mouse receiving NIS⁺ Antares⁺ CAR NK cells which showed no signs of ascites and had a visually smaller tumour lesion (Fig. 4.4D).

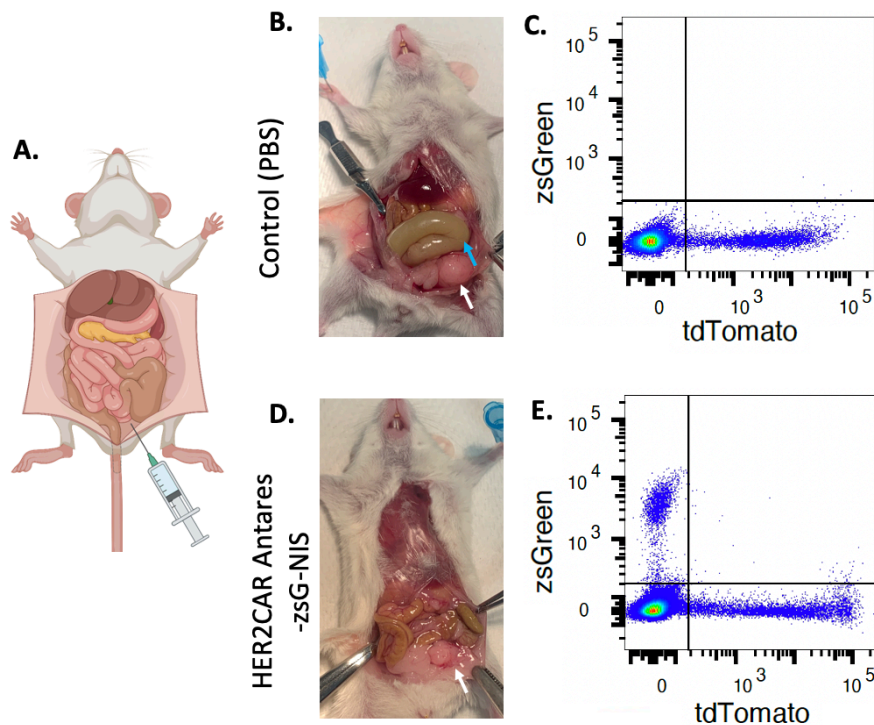


Figure 4.4: A) Peritoneal lavages performed with PBS injections into the peritoneal space followed by aspiration to collect and assess cellular composition. B) Control mouse receiving PBS injections showed larger cancer mass (white arrow) and ascites (blue arrow) within the peritoneal spaces. D) Mouse receiving the NIS⁺ Antares⁺ CAR NK cell therapy showed smaller tumour mass (white arrow) and no signs of ascites. C and E) Flow cytometry assessment of peritoneal lavage fluid showed tdTomato positive cells in both mice with additional zsGreen positive cells only in the mouse receiving the NIS⁺ Antares⁺ CAR NK cell therapy.

At endpoint, tumour masses and ovaries were harvested and preserved for H&E staining on paraffin sections, as well as fluorescence microscopy of frozen sections (Figure 4.5). Figure 4.5 shows representative sections of tumors and ovaries in mice receiving either PBS injections or NIS⁺ Antares⁺ CAR NK cell therapy.

Tdtomato fluorescence (from Fluc⁺tdT⁺SKOV3-ip1 cells) is present in both tumours of control mice and mice receiving NIS⁺ Antares⁺ CAR NK cells. Less tdTomato fluorescence is observed in the ovaries of both control mice and mice receiving NIS⁺ Antares⁺ CAR NK cells. Mice receiving NIS⁺ Antares⁺ CAR NK cells (also zsG-positive) showed zsG fluorescent cells in the cortex surrounding the ovaries (Fig.4.5J), but few zsG positive nuclei are present in the medulla of the ovary. Mice receiving NIS⁺ Antares⁺ CAR NK cells did not show zsGreen fluorescence within or around the tumour masses.

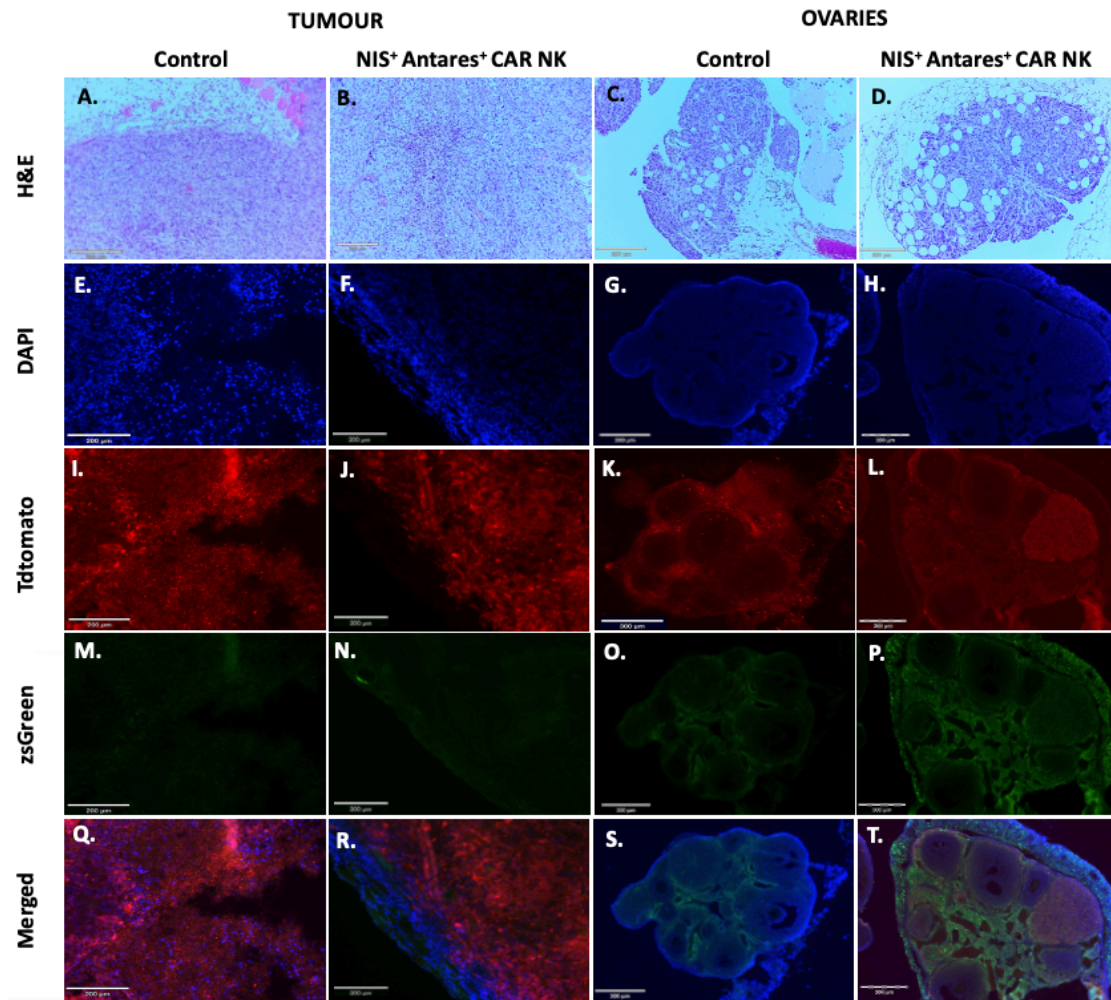


Figure 4.5: Tissue sections of tumour masses (A-B) and ovaries (C-D) stained with Hematoxylin and Eosin (H&E) of a control mouse and a mouse receiving the NIS⁺ Antares⁺ CAR NK therapy. Fluorescence images showing DAPI (nuclei; E-H), TdTomato (Fluc⁺tdT⁺SKOV3-ip1 cells; I-L), zsGreen (NIS⁺ Antares⁺ CAR NK; M-P), and the merged images (Q-T). ZsGreen positive cells are shown on the periphery of the ovaries in mice receiving the NK therapy (T). Few zsG positive cells are seen infiltrating inside the ovaries.

4.4 Discussion

Clinical use of CAR T cell therapies for the treatment of leukemia, lymphoma and myeloma has shown unprecedented outcomes in patients with relapsed/refractory disease [51][52][53][54]. However, CAR T cells undergo immense proliferation post-infusion, which is associated with cytokine release syndrome (CRS) and neurotoxicity [55][56]. Furthermore, there is poor therapeutic benefit of using CAR T cells for solid tumours due to poor penetration into tumour as well as inhibition by a hostile tumour microenvironment [57][58][59]. CAR NK cells are becoming attractive alternative therapeutics that can negate the above limitations due to their ability to circumvent CRS and graft versus host disease (GvHD), provide an “off the shelf” allogenic product via NK cell lines and iPSC-NK cells which culture an unlimited supply, and elicit anti-tumour effects in CAR-independent mechanisms through intrinsic activation receptors as well as via anti-body dependent cell-mediated cytotoxicity (ADCC) [60]. CAR NK cell also possess multiple mechanisms of cancer killing through both CAR-dependent and CAR-independent pathways [24]. Imaging tools that allow post-infusion tracking of these therapeutic cells could provide essential information such as sensitive and real-time tracking of cellular therapies, the potential to predict side effects due to rapid and uncontrolled proliferation, as well as predict therapeutic outcome, or lack thereof. In this study we develop a HER2 targeting-CAR NK therapy which can be visualized with the PET reporter gene, the Sodium-Iodide Symporter.

Several PET reporter genes have been used to track CAR-T cells such as herpes simplex virus-thymidine kinase (HSV1tk), *Escherichia coli* dihydrofolate reductase enzyme (eDHFR), somatostatin receptor 2 (SSTR2) and prostate-specific membrane antigen (PSMA) [41][61][42][62]. We employed NIS as our PET reporter gene as NIS is human-derived with minimal immunogenicity that is uniquely characterized by its ability to rapidly uptake radiotracers,

with the majority of its tracer up taken in the first 10 minutes post administration [63]. It is also compatible with a clinical fluorine-based PET tracer, ^{18}F -tetrafluoroborate (^{18}F -[TFB]) whose radionuclide has a short half-life (110 minutes), short positron diffusion range in tissue (< 2.4 mm), and high positron yield [64], to provide a sensitive approach for PET whole body imaging. Several groups have utilized the advantages of NIS for imaging of various immune cells [43][66][67]. Lee *et al.*, first employed the NIS to track migration of dendritic cells (DC) to lymph nodes with both ^{124}I and ^{18}F [TFB] for PET/CT detection [65]. Similarly, Emami-Shahri's *et al.*, has also developed NIS-expressing CAR T cells with administration of $^{99\text{m}}\text{Tc}$]TcO $_4^-$ radiotracer for SPECT/CT imaging [66]. To our knowledge, this is the first time NIS-expressing CAR-NK cells have been imaged with PET.

Our *in vitro* studies showed that CAR NK cells with or without NIS reporter gene showed similar levels of cytotoxicity towards SKOV3-ip1 cells, indicating NIS expression did not influence CAR lytic function. The addition of a CAR component increased cytotoxicity above NK-92 cell killing (Fig. 1). As performed previously [50] [68], we employed dual *in vivo* BLI to monitor both cancer cell and CAR NK cell populations in the same animals over time. Firefly luciferase (Fluc) was used to monitor SKOV3-ip1 cells, and we show mice receiving either PBS, or naïve NK injections showed significantly higher tumour burden when compared with mice receiving the NIS $^+$ Antares $^+$ CAR NK cell treatment (Fig. 4.2B). Thus, our HER2-targeted CAR-NK cells were able to significantly slow tumor progression in this highly aggressive model of HER2 ovarian cancer and prolonged the overall survival of treated mice (Fig. 4.2C). Although the HER2 CAR therapy did not cure the mice, future studies can look at optimizing CAR construct, increase CAR expression levels, or increase the dose of administered CAR NK therapy.

To monitor the CAR-NK cell population, we used the BLI reporter Antares, which is an optimized fusion of two orange-red fluorescent proteins called CyOFP1 excited by cyan light with NanoLuc [47]. Antares is a highly sensitive BLI reporter which can produce drastically brighter *in vivo* signal from deep tissues compared to FLuc and other BLI reporters. We also employed the Antares substrate FFZ which has been shown to strongly enhance bioluminescence signal *in vivo*, in comparison to other Antares-compatible substrates, to maximize sensitivity towards CAR NK detection [50]. Our Antares BLI data showed signal from CAR-NK cells present within the peritoneal spaces of mice, indicating the co-localization of both immunotherapy and tumour cells. NIS⁺ Antares⁺ CAR NK cells were longitudinally imaged using BLI with a stronger BLI signal originating from the bottom right quadrant of the animal (Fig. 4.3A.). This area also corresponds to the location of a large tumour mass observed in this and other sacrificed animals after exposure of their peritonea (Fig. 4.4A.), suggesting localized proliferation of therapeutic NK cells at the sites of tumours. To further validate this system *in vivo*, non-invasive imaging of the NIS-expressing CAR NK cells was performed. While uptake was observed in endogenous tissues as expected, mice receiving the NIS⁺ Antares⁺ CAR NK cell therapy also displayed uptake in other sites within the intraperitoneal cavity (Fig 4.3D, blue arrows). No uptake was observed in the right quadrant as was seen with Antares BLI which could indicate the lack of NIS⁺ Antares⁺ CAR NK cells present at the time of PET imaging (Day 27). Upon histological comparisons, no zsGreen fluorescence was observed at the primary tumour sites, matching the lack of PET uptake in those regions.

NK-92 cells are an Il-2 dependent cell line. While some studies have irradiated the NK-92 cells prior to implantation to prevent *in vivo* expansion, others have provided Il-2 without irradiation [28]. Similarly, studies have engineered NK-92 cells to endogenously express Il-2 and other

cytokines (i.e. IL-15) [69][70]. In our study, after day 33 IL-2 injections were halted to suppress the growth and expansion of NK cells *in vivo*. As seen in Figure 4B, Antares BLI signal showed stable levels until endpoint. In the future we will explore co-engineering our NK-92 cells with a suicide gene such as the Herpes simplex virus- thymidine kinase (HSV-tk) or human induced Caspase 9 (iCas9), to allow their selective killing following a defined treatment period [71][72]. Interestingly, NIS may also be explored as a suicide gene by administering mice with Iodide-131, which would limit the size of our lentiviral constructs [73][74][75]. However, this approach would result in cytotoxicity in NIS-expressing endogenous tissue (thyroid, stomach, salivary glands, and mammary glands).

After an average peak Antares BLI signal on day 25, PET was performed on day 27. Mice receiving either PBS or NIS⁺ Antares⁺ CAR NK cell injections were imaged with PET post IV injections of ¹⁸F-[TFB]. Assessment of SUV revealed significantly higher ($p < 0.05$) uptake in mice receiving NIS⁺ Antares⁺ CAR NK cells compared to mice receiving PBS injections in areas within the peritoneal space (Fig. 4.3E.). Although stand-alone PET is limited in providing anatomical context, it is believed that the increased SUV in the peritoneal spaces (in Fig. 4.3D blue arrows) corresponds to the ovaries as seen in figure 5J., indicating homing of NK cells to the ovaries in mice receiving the NIS⁺ Antares⁺ CAR NK treatment.

Peritoneal washes with PBS were performed on day 30 to collect cells from within the peritoneal space and assess for either the absence or presence of zsGreen positive cells in one mouse receiving PBS and another receiving NIS⁺ Antares⁺ CAR NK cells. As shown in figure 4.4C, the cell aspirate showed approximately 3% of cells to be tdTomato positive, indicating the presence of SKOV3-ip1 cells. The peritoneal wash from the mouse receiving NIS⁺ Antares⁺ CAR NK cell injections shows approximately 2% of cells expressing tdTomato and approximately 1% of cells were

zsGreen positive (Fig. 4.4E), indicating the presence of both SKOV3-ip1 and NIS⁺ Antares⁺ CAR NK cells. Upon exposure of peritoneal spaces of mice, a larger tumour mass, in addition to ascites along the inner peritoneal lining, were evident in the control mouse compared to the mouse from the treatment group (Fig. 4.4B and 4.4D.). Thus, while this therapy did not eliminate the entirety of tumour masses, it showed robust tumour lysis and can be used as an adjuvant therapy, post standard chemotherapy or surgical debulking.

Histological sections and tissue fluorescence of the ovaries and tumour sections were observed. Sections of ovaries in mice receiving sham injections show similar DAPI and tdTomato to mice receiving the NIS⁺ Antares⁺ CAR NK cell therapy. Mice receiving the NK therapy show additional zsGreen fluorescence along the cortex of the ovaries, indicating some peripheral infiltration of the therapy. Sections of tumour masses for mice receiving the sham injections as well as mice receiving the NIS⁺ Antares⁺ CAR NK cell therapy both show qualitatively similar DAPI and tdTomato fluorescence. Mice receiving the NIS⁺ Antares⁺ CAR NK cells therapy do not show zsGreen fluorescence within their tumour mass. Fluorescence sections of mice receiving NK therapy also imply that tumour infiltration is still a challenge for this therapy and methods to improve tumour penetration are needed. Furthermore, the incomplete eradication of the tumour in mice receiving the NIS⁺ Antares⁺ CAR NK cell therapy could indicate insufficient numbers of therapeutic cells (either at time of administration or their *in vivo* persistence).

4.4.1 Limitations

While NIS⁺ Antares⁺ CAR NK cell therapy showed effective antitumor activity, complete tumour clearance was not shown. To improve tumour lysis, enhancements to the CAR can be incorporated such as using more potent generation CARs which include intrinsic cytokine release from NK-92 cells to alleviate dependence on exogenous cytokines, or incorporate multiple tumour antigen

recognition domains to overcome antigen escape [11]. There are also limitations associated with the imaging platforms used for tracking the NIS⁺ Antares⁺ CAR NK cells. One of the limitations of the NIS reporter gene imaging is its background expression in organs such as the thyroid, stomach, and salivary glands, in addition to urinary clearance. This poses a challenge to visualize cell trafficking to these areas. To further exacerbate this limitation, PET lacks sufficient anatomical information to provide accurate distribution information on the cells. While this was not a major challenge for our peritoneal ovarian cancer model, it may restrict the use of this imaging reporter gene for other cancers with different biodistribution and metastatic spread. Another limitation with this cell theranostic system is the genetic incorporation of the CAR as well as the reporter genes using lentiviral vehicles, which poses clinical challenges. Further optimization of this cell system can be accomplished with more advanced genetic engineering using technologies such as CRISPR, which would improve the safety by enabling site-selective integration into the cells genome as opposed to the random integration of lentiviral-transduced cells [76].

4.4.2 Conclusions

To conclude, the natural killer cell line, NK-92 cells were genetically enhanced to incorporate a HER2 targeting CAR for treatment of HER2 positive ovarian cancer. Moreover, HER2-CAR NK cells were transduced to incorporate a BLI and PET reporter gene to accomplish non-invasive cell tracking with both imaging modalities in ovarian cancer bearing mice. SKOV3-ip1 ovarian cancer cells were engineered with Firefly Luciferase and imaged with BLI to monitor tumour burden within the same mice. The NIS reporter system was used to provide a clinically compatible, safe, quantitative, platform to non-invasively visualize CAR NK cells using ¹⁸F-TFB-PET imaging, while the Antares was used as a pre-clinical sensitive tool to enable long term tracking of NK cells. The NIS imaging platform has the potential to provide clinicians with missing information on the

number, localization, viability, therapeutic efficacy as well as side effects of the immunotherapeutic cells. Furthermore, with simple administration of the ^{18}F -TFB at trace doses, these cells can be tracked longitudinally over time. This comprehensive information will help clinicians better understand how women will respond to this therapy, as well as manage or intervene at earlier time points, to alleviate potential side-effects.

4.5 References

1. Cancer Tomorrow.
https://gco.iarc.fr/tomorrow/en/dataviz/trends?types=0_1&sexes=2&mode=population&group_populations=0&multiple_populations=1&multiple_cancers=0&cancers=25&populations=900.
Accessed 20 dec 2022
2. Surgery for Recurrent Ovarian Cancer May Help Selected Patients - NCI.
<https://www.cancer.gov/news-events/cancer-currents-blog/2022/ovarian-cancer-return-surgery-desktop-iii>. Accessed 20 dec 2022
3. Xin L, Xiao W, Che L, et al (2021) Label-Free Assessment of the Drug Resistance of Epithelial Ovarian Cancer Cells in a Microfluidic Holographic Flow Cytometer Boosted through Machine Learning. <https://doi.org/10.1021/acsomega.1c04204>
4. Itamochi H, Kigawa J Clinical trials and future potential of targeted therapy for ovarian cancer. <https://doi.org/10.1007/s10147-012-0459-8>
5. Yan M, Schwaederle M, Arguello D, et al (2015) HER2 expression status in diverse cancers: review of results from 37,992 patients. *Cancer Metastasis Rev* 34:157. <https://doi.org/10.1007/S10555-015-9552-6>
6. Pils D, Pinter A, Reibenwein J, et al (2007) In ovarian cancer the prognostic influence of HER2/neu is not dependent on the CXCR4/SDF-1 signalling pathway. *Br J Cancer* 2007 963 96:485–491. <https://doi.org/10.1038/sj.bjc.6603581>
7. Zidan J (2016) EGFR and HER2 expression in ovarian cancer compared to clinical and pathological features of the patients. https://doi.org/10.1200/JCO.2016.34.15_suppl.e23254 34:e23254–e23254. https://doi.org/10.1200/JCO.2016.34.15_SUPPL.E23254
8. Vallera DA, Oh F, Kodali B, et al (2021) A HER2 tri-specific NK cell engager mediates efficient targeting of human ovarian cancer. *Cancers (Basel)* 13:. <https://doi.org/10.3390/cancers13163994>

9. Gajria D, Chandarlapaty S (2011) HER2-amplified breast cancer: Mechanisms of trastuzumab resistance and novel targeted therapies. *Expert Rev Anticancer Ther* 11:263–275. <https://doi.org/10.1586/era.10.226>
10. Wilken JA, Webster KT, Maihle NJ (2010) Trastuzumab sensitizes ovarian cancer cells to EGFR-targeted therapeutics. *J Ovarian Res* 3:1–9. <https://doi.org/10.1186/1757-2215-3-7>
11. Sterner RC, Sterner RM (2021) CAR-T cell therapy: current limitations and potential strategies. *Blood Cancer J* 11:. <https://doi.org/10.1038/s41408-021-00459-7>
12. Dai H, Wang Y, Lu X, Han W (2016) Chimeric antigen receptors modified T-cells for cancer therapy. *J Natl Cancer Inst* 108:. <https://doi.org/10.1093/jnci/djv439>
13. Murciano-Goroff YR, Warner AB, Wolchok JD (2020) The future of cancer immunotherapy: microenvironment-targeting combinations. *Cell Res* 2020 306 30:507–519. <https://doi.org/10.1038/s41422-020-0337-2>
14. FDA-approved CAR T-cell Therapies | UPMC Hillman. <https://hillman.upmc.com/mario-lemieux-center/treatment/car-t-cell-therapy/fda-approved-therapies>. Accessed 5 nov 2021
15. Xu J, Meng Q, Sun H, et al (2021) HER2-specific chimeric antigen receptor-T cells for targeted therapy of metastatic colorectal cancer. *Cell Death Dis* 12:1–11. <https://doi.org/10.1038/s41419-021-04100-0>
16. Sun M, Shi H, Liu C, et al (2014) Construction and evaluation of a novel humanized HER2-specific chimeric receptor. *Breast Cancer Res* 16:1–10. <https://doi.org/10.1186/bcr3674>
17. Song Y, Tong C, Wang Y, et al (2018) Effective and persistent antitumor activity of HER2-directed CAR-T cells against gastric cancer cells in vitro and xenotransplanted tumors in vivo. *Protein Cell* 9:867–878. <https://doi.org/10.1007/s13238-017-0384-8>
18. Ahmed N, Brawley VS, Hegde M, et al (2015) Human epidermal growth factor receptor 2 (HER2) - Specific chimeric antigen receptor - Modified T cells for the immunotherapy of HER2-positive sarcoma. *J Clin Oncol* 33:1688–1696. <https://doi.org/10.1200/JCO.2014.58.0225>

19. Ahmed N, Salsman VS, Kew Y, et al (2010) HER2-specific T cells target primary glioblastoma stem cells and induce regression of autologous experimental tumors. *Clin Cancer Res* 16:474–485. <https://doi.org/10.1158/1078-0432.CCR-09-1322>
20. Lanitis E, Dangaj D, Hagemann IS, et al (2012) Primary Human Ovarian Epithelial Cancer Cells Broadly Express HER2 at Immunologically-Detectable Levels. *PLoS One* 7:. <https://doi.org/10.1371/journal.pone.0049829>
21. Rainusso N, Brawley VS, Ghazi A, et al (2012) Immunotherapy targeting HER2 with genetically modified T cells eliminates tumor-initiating cells in osteosarcoma. *Cancer Gene Ther* 19:212–217. <https://doi.org/10.1038/cgt.2011.83>
22. Ahmed N, Ratnayake M, Savoldo B, et al (2007) Regression of experimental medulloblastoma following transfer of HER2-specific T cells. *Cancer Res* 67:5957–5964. <https://doi.org/10.1158/0008-5472.CAN-06-4309>
23. Sakemura R, Bansal A, Siegler EL, et al (2021) Development of a Clinically Relevant Reporter for Chimeric Antigen Receptor T-cell Expansion, Trafficking, and Toxicity. *Cancer Immunol Res* 9:1035–1046. <https://doi.org/10.1158/2326-6066.CIR-20-0901>
24. Pan K, Farrukh H, Chittepu VCSR, et al (2022) CAR race to cancer immunotherapy: from CAR T, CAR NK to CAR macrophage therapy. *J Exp Clin Cancer Res* 41:1–21. <https://doi.org/10.1186/s13046-022-02327-z>
25. Shimasaki N, Jain A, Campana D (2020) NK cells for cancer immunotherapy. *Nat Rev Drug Discov* 2020 193 19:200–218. <https://doi.org/10.1038/s41573-019-0052-1>
26. Hu W, Wang G, Huang D, et al (2019) Cancer Immunotherapy Based on Natural Killer Cells: Current Progress and New Opportunities. *Front Immunol* 10:1205. <https://doi.org/10.3389/FIMMU.2019.01205>
27. Liu S, Galat V, Galat4 Y, et al (2021) NK cell-based cancer immunotherapy: from basic biology to clinical development. *J Hematol Oncol* 2021 141 14:1–17. <https://doi.org/10.1186/S13045-020-01014-W>

28. Liu E, Marin D, Banerjee P, et al (2020) Use of CAR-transduced natural killer cells in CD19-positive lymphoid tumors. *N Engl J Med* 382:545–553. <https://doi.org/10.1056/NEJMoa1910607>
29. Valeri A, García-Ortiz A, Castellano E, et al (2022) Overcoming tumor resistance mechanisms in CAR-NK cell therapy. *Front Immunol* 13:1–28. <https://doi.org/10.3389/fimmu.2022.953849>
30. Albinger N, Hartmann J, Ullrich E (2021) Current status and perspective of CAR-T and CAR-NK cell therapy trials in Germany. *Gene Ther* 2021 289 28:513–527. <https://doi.org/10.1038/s41434-021-00246-w>
31. Gong Y, Klein Wolterink RGJ, Wang J, et al (2021) Chimeric antigen receptor natural killer (CAR-NK) cell design and engineering for cancer therapy. *J Hematol Oncol* 14:. <https://doi.org/10.1186/S13045-021-01083-5>
32. Marofi F, Al-Awad AS, Sulaiman Rahman H, et al (2021) CAR-NK Cell: A New Paradigm in Tumor Immunotherapy. *Front Oncol* 0:2078. <https://doi.org/10.3389/FONC.2021.673276>
33. Xie G, Dong H, Liang Y, et al (2020) CAR-NK cells: A promising cellular immunotherapy for cancer. *EBioMedicine* 59:. <https://doi.org/10.1016/J.EBIOM.2020.102975>
34. Zhang L, Meng Y, Feng X, Han Z (2022) CAR-NK cells for cancer immunotherapy: from bench to bedside. *Biomark Res* 10:1–19. <https://doi.org/10.1186/s40364-022-00364-6>
35. Oelsner S, Friede ME, Zhang C, et al (2017) Continuously expanding CAR NK-92 cells display selective cytotoxicity against B-cell leukemia and lymphoma. *Cytotherapy* 19:235–249. <https://doi.org/10.1016/j.jcyt.2016.10.009>
36. Boissel L, Betancur M, Lu W, et al (2013) Retargeting NK-92 cells by means of CD19- and CD20-specific chimeric antigen receptors compares favorably with antibody-dependent cellular cytotoxicity. <https://doi.org/104161/onci26527> 2:e26527. <https://doi.org/10.4161/ONCI.26527>

37. Tang X, Yang L, Li Z, et al (2018) First-in-man clinical trial of CAR NK-92 cells: safety test of CD33-CAR NK-92 cells in patients with relapsed and refractory acute myeloid leukemia. *Am J Cancer Res* 8:1083
38. Pinz KG, Yakaboski E, Jares A, et al (2017) Targeting T-cell malignancies using anti-CD4 CAR NK-92 cells. *Oncotarget* 8:112783. <https://doi.org/10.18632/ONCOTARGET.22626>
39. S G, M T, C C (2018) Advances in oncological treatment: limitations of RECIST 1.1 criteria. *Q J Nucl Med Mol Imaging* 62:129–139. <https://doi.org/10.23736/S1824-4785.17.03038-2>
40. Skovgard MS, Hocine HR, Saini JK, et al (2021) Imaging CAR T-cell kinetics in solid tumors: Translational implications. *Mol Ther - Oncolytics* 22:355–367. <https://doi.org/10.1016/j.omto.2021.06.006>
41. Minn I, Huss DJ, Ahn HH, et al (2019) Imaging CAR T cell therapy with PSMA-targeted positron emission tomography. *Sci Adv* 5:eaaw5096. <https://doi.org/10.1126/sciadv.aaw5096>
42. Sellmyer MA, Richman SA, Lohith K, et al (2020) Imaging CAR T Cell Trafficking with eDHFR as a PET Reporter Gene. *Mol Ther* 28:42. <https://doi.org/10.1016/J.YMTHE.2019.10.007>
43. Sakemura R, Can I, Siegler EL, Kenderian SS (2021) In vivo CART cell imaging: Paving the way for success in CART cell therapy. *Mol Ther - Oncolytics* 20:625–633. <https://doi.org/10.1016/j.omto.2021.03.003>
44. Yaghoubi SS, Campbell DO, Radu CG, Czernin J (2012) Positron emission tomography reporter genes and reporter probes: Gene and cell therapy applications. *Theranostics* 2:374–391
45. Ahn BC (2012) Sodium iodide symporter for nuclear molecular imaging and gene therapy: From bedside to bench and back. *Theranostics* 2:392–402
46. Spitzweg C, Harrington KJ, Pinke LA, et al (2001) The Sodium Iodide Symporter and Its Potential Role in Cancer Therapy. *J Clin Endocrinol Metab* 86:3327–3335. <https://doi.org/10.1210/jcem.86.7.7641>

47. Chu J, Oh Y, Sens A, et al (2016) A bright cyan-excitable orange fluorescent protein facilitates dual-emission microscopy and enhances bioluminescence imaging in vivo. *Nat Biotechnol* 34:760–767. <https://doi.org/10.1038/nbt.3550>
48. Hammill JA, VanSeggelen H, Helsen CW, et al (2015) Designed ankyrin repeat proteins are effective targeting elements for chimeric antigen receptors. *J Immunother Cancer* 3:1–11. <https://doi.org/10.1186/s40425-015-0099-4>
49. Liu S, Nyström NN, Kelly JJ, et al (2022) Molecular Imaging Reveals a High Degree of Cross-Seeding of Spontaneous Metastases in a Novel Mouse Model of Synchronous Bilateral Breast Cancer. *Mol Imaging Biol* 24:104–114. <https://doi.org/10.1007/s11307-021-01630-z>
50. Su Y, Walker JR, Park Y, et al (2020) Novel NanoLuc substrates enable bright two-population bioluminescence imaging in animals. *Nat Methods* 17:852–860. <https://doi.org/10.1038/s41592-020-0889-6>
51. Turtle CJ, Hay KA, Hanafi LA, et al (2017) Durable Molecular Remissions in Chronic Lymphocytic Leukemia Treated With CD19-Specific Chimeric Antigen Receptor–Modified T Cells After Failure of Ibrutinib. *J Clin Oncol* 35:3010. <https://doi.org/10.1200/JCO.2017.72.8519>
52. Porter DL, Hwang WT, Frey N V., et al (2015) Chimeric antigen receptor T cells persist and induce sustained remissions in relapsed refractory chronic lymphocytic leukemia. *Sci Transl Med* 7:303ra139. <https://doi.org/10.1126/SCITRANSLMED.AAC5415>
53. Locke FL, Ghobadi A, Jacobson CA, et al (2019) Long-term safety and activity of axicabtagene ciloleucel in refractory large B-cell lymphoma (ZUMA-1): a single-arm, multicentre, phase 1–2 trial. *Lancet Oncol* 20:31–42. [https://doi.org/10.1016/S1470-2045\(18\)30864-7](https://doi.org/10.1016/S1470-2045(18)30864-7)
54. Locke FL, Neelapu SS, Bartlett NL, et al (2017) Phase 1 Results of ZUMA-1: A Multicenter Study of KTE-C19 Anti-CD19 CAR T Cell Therapy in Refractory Aggressive Lymphoma. *Mol Ther* 25:285–295. <https://doi.org/10.1016/J.YMTHE.2016.10.020>
55. Maude SL, Laetsch TW, Buechner J, et al (2018) Tisagenlecleucel in Children and Young Adults with B-Cell Lymphoblastic Leukemia. *N Engl J Med* 378:439–448. <https://doi.org/10.1056/nejmoa1709866>

56. Teachey DT, Lacey SF, Shaw PA, et al (2016) Identification of predictive biomarkers for cytokine release syndrome after chimeric antigen receptor T-cell therapy for acute lymphoblastic leukemia. *Cancer Discov* 6:664–679. <https://doi.org/10.1158/2159-8290.CD-16-0040/42478/AM/IDENTIFICATION-OF-PREDICTIVE-BIOMARKERS-FOR>
57. Guedan S, Ruella M, June CH (2018) Emerging Cellular Therapies for Cancer. <https://doi.org/10.1146/annurev-immunol-042718-041407> 37:145–171.
<https://doi.org/10.1146/ANNUREV-IMMUNOL-042718-041407>
58. Jiang Y, Li Y, Zhu B (2015) T-cell exhaustion in the tumor microenvironment. *Cell Death Dis* 6:e1792. <https://doi.org/10.1038/CDDIS.2015.162>
59. D'Aloia MM, Zizzari IG, Sacchetti B, et al (2018) CAR-T cells: the long and winding road to solid tumors. *Cell Death Dis* 2018 9:1–12. <https://doi.org/10.1038/s41419-018-0278-6>
60. Cao B, Liu M, Huang J, et al (2021) Development of mesothelin-specific CAR NK-92 cells for the treatment of gastric cancer. *Int J Biol Sci* 2021:3850–3861. <https://doi.org/10.7150/ijbs.64630>
61. Keu KV, Witney TH, Yaghoubi S, et al (2017) Reporter gene imaging of targeted T cell immunotherapy in recurrent glioma. *Sci Transl Med* 9:. <https://doi.org/10.1126/scitranslmed.aag2196>
62. Vedvyas Y, Shevlin E, Zaman M, et al (2016) Longitudinal PET imaging demonstrates biphasic CAR T cell responses in survivors. *JCI Insight* 1:. <https://doi.org/10.1172/jci.insight.90064>
63. Sakemura R, Bansal A, Siegler EL, et al (2021) Development of a clinically relevant reporter for chimeric antigen receptor t-cell expansion, trafficking, and toxicity. *Cancer Immunol Res* 9:1035–1046. <https://doi.org/10.1158/2326-6066.CIR-20-0901/665804/AM/DEVELOPMENT-OF-A-CLINICALLY-RELEVANT-REPORTER-FOR>
64. O'Doherty J, Jauregui-Osoro M, Brothwood T, et al (2017) ¹⁸F-Tetrafluoroborate, a PET Probe for Imaging Sodium/Iodide Symporter Expression: Whole-Body Biodistribution, Safety,

and Radiation Dosimetry in Thyroid Cancer Patients. *J Nucl Med* 58:1666–1671. <https://doi.org/10.2967/jnumed.117.192252>

65. Lee SB, Lee HW, Lee H, et al (2017) Tracking dendritic cell migration into lymph nodes by using a novel PET probe 18F-tetrafluoroborate for sodium/iodide symporter. *EJNMMI Res* 7:. <https://doi.org/10.1186/s13550-017-0280-5>

66. Emami-Shahri N, Foster J, Kashani R, et al (2018) Clinically compliant spatial and temporal imaging of chimeric antigen receptor T-cells. *Nat Commun* 9:1–12. <https://doi.org/10.1038/s41467-018-03524-1>

67. Seo JH, Jeon YH, Lee YJ, et al (2010) Trafficking macrophage migration using reporter gene imaging with human sodium iodide symporter in animal models of inflammation. *J Nucl Med* 51:1637–1643. <https://doi.org/10.2967/jnumed.110.077891>

68. Liu S, Su Y, Lin MZ, Ronald JA (2021) Brightening up Biology: Advances in Luciferase Systems for in Vivo Imaging. *ACS Chem Biol* 16:2707–2718. <https://doi.org/10.1021/acscchembio.1c00549>

69. Jochems C, Hodge JW, Fantini M, et al (2016) An NK cell line (haNK) expressing high levels of granzyme and engineered to express the high affinity CD16 allele. *Oncotarget* 7:86359–86373. <https://doi.org/10.18632/oncotarget.13411>

70. Klingemann H, Boissel L, Toneguzzo F (2016) Characterization of interleukin-15 gene-modified human natural killer cells: implications for adoptive cellular immunotherapy. *Front. Immunol.* 7

71. Marin V, Cribioli E, Philip B, et al (2012) Comparison of different suicide-gene strategies for the safety improvement of genetically manipulated T cells. *Hum Gene Ther Methods* 23:376–386. <https://doi.org/10.1089/hgtb.2012.050>

72. Dahlke J, Schott JW, Barbosa PV, et al (2021) Efficient genetic safety switches for future application of ipsc-derived cell transplants. *J Pers Med* 11:. <https://doi.org/10.3390/jpm11060565>

73. Penheiter AR, Russell SJ, Carlson SK (2012) The Sodium Iodide Symporter (NIS) as an Imaging Reporter for Gene, Viral, and Cell-based Therapies. *Curr Gene Ther* 12:33. <https://doi.org/10.2174/156652312799789235>
74. Ahmed KA, Davis BJ, Wilson TM, et al (2012) Progress in Gene Therapy for Prostate Cancer. *Front Oncol* 2:1–7. <https://doi.org/10.3389/fonc.2012.00172>
75. Ashmore-Harris C, Iafrate M, Saleem A, Fruhwirth GO (2020) Non-invasive Reporter Gene Imaging of Cell Therapies, including T Cells and Stem Cells. *Mol. Ther.* 28:1392–1416
76. Kelly JJ, Saeed-Marand M, Nyström NN, et al (2021) Safe harbor-targeted CRISPR-Cas9 homology-independent targeted integration for multimodality reporter gene-based cell tracking. *Sci Adv* 7:eabc3791. <https://doi.org/10.1126/sciadv.abc3791>

CHAPTER 5

5 Summary

This thesis presents multi-modal cell tracking of cancer cells, stem cells and immune cells in preclinical animal model. Cell tracking was accomplished using Positron Emission Tomography (PET), Magnetic Resonance Imaging (MRI), Magnetic Particle Imaging (MPI) and Bioluminescence Imaging (BLI). The use of multiple imaging modalities has enabled complementary information on cell's biodistribution, proliferation, and viability in the body, in a non-invasive, safe, sensitive, and quantitative approach. First, breast cancer cells were genetically encoded with two human-derived reporter genes; (1) the Organic Anion Transporter Polypeptide 1B3 (OATP1B3), and (2) the Sodium-Iodide Symporter (NIS), for detection with MRI and PET, respectively. This is the first highly translatable multi-modal system that uses human-derived (i.e. non-immunogenic) reporter genes and clinically-used imaging probes and contrast agents to provide sensitive and quantifiable information with PET, as well as fine spatial resolution and soft tissue contrast from MRI. Next, we transitioned to tracking a clinically-relevant cell based therapy; mesenchymal stem cells (MSCs), using NIS for PET detection, and superparamagnetic iron oxide nanoparticles (SPIOs) for MPI tracking for a duration of 30 days. We showed maximum sensitivity with MPI for early-phase MSC tracking, and optimal longitudinal imaging, viability and proliferation information using PET reporter gene imaging. Finally, we demonstrated multi-modal tracking of a novel cellular immunotherapy derived from Natural Killer (NK) cells which was used to target and treat a HER2 ovarian cancer model. NK therapy cells were image with both BLI and NIS-PET to monitor therapeutic efficacy, and visualize therapeutic cells' *in vivo* persistence, respectively. This thesis presents novel multi-modal imaging approaches for different preclinical and clinical applications that have enabled non-invasive visualization of cell fate *in vivo*.

5.1 Summary and Discussion

5.1.1 Chapter 2: Clinically translatable dual human-derived PET and MRI reporter genes

In this work, breast cancer cells were transduced to express OATP1B3 which enabled MRI imaging of cells when administered with 1 mmol/kg of the contrast agent, Gd-EOB-DTPA. Breast cancer cells were co-transduced with NIS to enable PET detection with 10-15 MBq of [^{18}F] TFB. This is the first reported clinically translatable multi-modal system, using (1) clinical imaging modalities; (2) human-derived reporter genes; and (3) clinically used contrast agent and tracer. PET provided sensitive information on breast cancer cells and enabled earlier cell detection compared to MRI. However, MRI provided soft tissue contrast and fine spatial resolution which enabled intratumoral visualization of OATP1B3-expressing cells. In this work, we also dynamically imaged the naïve and OATP1B3-expressing tumours in a mouse post both intravenous and intraperitoneal injection of Gd-EOB-DTPA for approximately 5 hours. The main findings of this work include: (1) demonstrating the complementary advantage of using multi-modal PET and MRI for cell tracking and (2) reporting the feasibility of using IP injections in small animal models which we have shown to have similar contrast enhancement when compared to the IV administration route. This proof-of-concept study showed the utility of using two powerful clinical modalities to rely sensitive, quantitative information with fine spatial resolution and soft tissue contrast.

5.1.2 Chapter 3: Early- and Late- Phase Multi-Modal Tracking of Mesenchymal Stem Cells

Mesenchymal stem cells (MSCs) are used clinically to treat a wide variety of pathologies due to their inherent renewal properties, anti-inflammatory capability, and regenerative capacity [1][2]. While MSCs are promising therapies, they can oftentimes undergo apoptosis or malignant

transformations, emphasizing the need to track MSCs and their fate *in vivo*. This chapter incorporates the human derived NIS from our first study, into MSCs to track cells with PET reporter gene imaging. Furthermore, MSCs were genetically modified to include a BLI reporter gene; Akaluc. BLI was used as a reference modality in this work to provide both sensitive and longitudinal tracking on MSCs. Finally, MSCs were directly labeled with SPIONs to allow sensitive detection with MPI in this intramuscular-injection model. MSC tracking was accomplished for 30 days post their administration. MPI is a relatively novel imaging modality that is currently in clinical development and has shown “hot spot” detection with high sensitivity. This is the first study to accomplish MSC tracking with MPI and PET reporter imaging. The main conclusions from this study: (1) we were able to visualize MSCs with MPI, BLI and PET and showed the complementary advantage of using a multi-modal approach; (2) at early time points, MPI showed high sensitivity and correlated with BLI data; while PET signal was not significant at these earlier time points; (3) later time points revealed inaccurate quantification of SPIO with MSCs which ceased to correlate with BLI data. Moreover, the PET data showed a strong correlation to BLI data at later time points, indicating its importance for long-term tracking and ability to provide viability and proliferation information on MSCs. This system enabled the comprehensive visualization of MSCs throughout their entire *in vivo* lifespan in a sensitive labeling approach in combination with reporter gene imaging to facilitate long-term tracking.

5.1.3 Chapter 4: Imaging a CAR NK cell-based therapy against HER2 ovarian cancer

Immunotherapies are immune cells that are modified to effectively target and lyse cancer cells. In this chapter, a novel immunotherapy, derived from Natural Killer (NK) cells of the immune system was genetically engineered to express a chimeric antigen receptor (CAR); a synthetic receptor

which can target tumour-associated antigens. In this work, we developed an NK immunotherapy expressing a CAR that targets the human epidermal growth factor receptor 2 (HER2), a protein overexpressed on a variety of solid tumours [3][4]. This immunotherapy was also genetically engineered to incorporate the NIS; PET reporter gene, used in the previous chapters. We have also integrated a BLI reporter gene; Antares, to describe the biodistribution, proliferation and *in vivo* persistence of our CAR NK therapy. Mice inoculated with HER2 positive ovarian cancer were treated with the CAR NK therapy and tumour regression was monitored longitudinally with BLI. Additionally, PET and BLI imaging of CAR NK therapy showed localization within the peritoneal spaces. This is the first HER2 targeting CAR NK therapy that has been imaged with a PET reporter gene. The main findings of this work include; (1) effective ovarian cancer treatment using a HER2 targeted CAR NK therapy, as shown by imaging tumour with BLI; (2) longitudinal persistence of CAR NK cells, as shown by imaging NK cells with BLI; (3) visualization of HER2 CAR NK cells in the peritoneal space of mice with NIS-PET. Although we concluded effective therapy that prolonged the overall survival of mice, CAR NK therapy did not completely abolish tumours mainly due to poor infiltration.

5.2 Challenges and Limitations

5.2.1 Limitations of reporter genes

In all projects within this thesis, reporter gene imaging was performed where cancer, stem and immune cells expressed various reporter genes compatible with different imaging modalities. Ideally, a reporter gene system should be non-toxic and non-destructive to cellular function, rely sensitive and quantifiable information, have minimal background expression levels, and provide high specificity to the target moiety [5]. However, no single reporter gene fulfils these criteria. For example, the NIS PET reporter gene, is human-derived and thus lacks immunogenicity. However,

with its endogenous expression in several tissues (i.e. thyroid, stomach, salivary glands and mammary glands), visualization of NIS-expressing cells would be difficult in these regions [6].

One of the main advantages of indirect labeling compared to direct labeling of cells, is the stable expression of reporter genes which gets inherited by daughter cells, enabling longitudinal tracking of expanding cell populations. However, epigenetic gene silencing, which can affect transcription of reporter genes, is possible. DNA methylation or histone deacetylation have been shown to suppress gene signal, which could lead to finite imaging of engineered cells [7]. However, this phenomenon is minimized with the addition of methyltransferase inhibitor during cell culture [8].

5.2.2 Lentiviral transduction of genes

All reporter genes in this thesis have been integrated using lentiviral transduction methods. Lentiviral delivery of genetic load results in permanent integration of the reporter genes into the host genome. This method has been optimized over the last couple of decades and has been extensively used for engineering therapies in the clinic [9]. While lentiviral transductions are the most common method of gene delivery due to its high transduction efficiencies seen in both proliferating and non-proliferating cells, they are not completely random in their genetic integration within the host genome and have been shown to preferentially integrate within transcriptional units, potentially disrupting cellular function and posing safety concerns [9]. Cells transduced with lentiviral vectors can become cancerous via activation of oncogenes or through mutations of tumour suppressor genes as a result of integrating within or near a coding region of the host's genome [10]. It is also important to note that insertional mutagenesis induced by viral vectors will also be passed down to the cell's progeny. Thus, methods to control the integration of gene into specific genetic loci, are highly desirable.

Another major risk associated with lentiviral vectors is the possible unintentional reconstitution of a replication-competent virus. Although this is an intrinsic risk associated with transgenes inserted by the viral vectors, different generations of lentiviral vectors where the design of the viral vector constructs can reduce this risk, have been developed [10]. In this work, third generation lentiviral vectors are used. Third generation viral vectors lack several accessory genes, and only included 3 plasmids, reducing the virulence of any replication-competent virus.

5.2.3 Dose Optimization

In chapter 2, the OATP1B3 was used as an MRI reporter gene due to its ability to uptake the clinical contrast agent, Primovist® (Bayer, Berlin, Germany). Primovist® is a Gadolinium containing MRI contrast agent clinically used for liver imaging. The recommended dose of Primovist® is 0.025 mmol/kg body weight of patient. The dose of Primovist® used for our preclinical animal models to visualize the OATP1B3-expressing cells was 1 mmol/kg weight of mouse, a dose 40 times higher than the recommended dose. This dose is not translatable to clinical settings as Gadolinium based contrast agents (GBCAs) have been associated with brain accumulation, especially with multiple administrations [11][12]. Furthermore, GBCAs increase the risk for Nephrogenic Systemic Fibrosis (NSF) in patients with kidney disease [13]. Reducing the administered dose in our study to clinical levels would decrease the overall sensitivity of this MRI reporter system. Similarly, [¹⁸F] TFB was used as the PET tracer for NIS detection in all our studies. The clinical dose used for [¹⁸F] TFB in patients is approximately 2.5-3 MBq/kg of patient weight, which translates to 0.05-0.06 MBq in a mouse of approximately 20 grams [14]. Our dose ranged from 10-20 MBq in all studies, indicating a significantly higher dose than clinically

translatable. Thus, other optimization methods, such as increasing reporter gene expression and optimizing imaging acquisition methods, are required.

To date, the dose of CAR NK cells which has been most effective in treating acute leukemia ranged from 10-100 million CAR NK cells/kg of patient weight [15], which converts to 200,000-2,000,000 cells in a mouse of average weight. Comparing to our dose of 15 million cells administered 3 times in each mouse, we utilized a dose that is not feasible in clinical settings. It is important to note that even with our high administered dose, full tumour eradication was not achieved. Thus, it is crucial to optimize the structure of these therapies to further improve their anti-tumour efficacy and enable significant dose reductions.

5.3 Future work

5.3.1 Optimization of CAR NK therapy

In chapter 4, an immunotherapy developed from the NK-92 cell line, originally derived from a lymphoma patient was used. This cell line is well characterized, and adoptive transfer of irradiated NK-92 cells has shown safe and effective treatment in patients. However, NK-92 cells are void of CD16 receptors, which are responsible for anti-tumour responses via antibody cell mediated cytotoxicity (ADCC). Jochems, et al., developed an NK-92 therapy that was genetically modified to endogenously produce interleukin-2 (IL-2) and express the CD16 receptor, which are associated with improved cytotoxicity [16]. This study showed similar cancer killing abilities with a 3-fold decrease in genetically modified NK cell dose, compared to standard NK cell dose. Other studies, motivated by the toxicity associated with high doses of IL-2 (i.e. capillary leak syndrome), have shown effective NK-92 cytotoxicity with the use of other endogenous cytokines, such as interleukin-15 (IL-15) [17]. This study showed higher affinity of IL-15 to its receptor compared to

the affinity of IL-2 to its receptor, resulting in higher toxicities and NK activation at relatively lower doses.

5.3.2 CAR design

While the design of CAR can be complex, the structure of the CAR is very modular and can be optimized to maximize its killing potential. Several studies have modified the CAR to improve its cytotoxicity by optimizing certain regions on the synthetic receptor (i.e. the linker and hinge regions), which resulted in more efficient cytokine production and proliferation of CAR-expressing cells [18]. Different derivations of the transmembrane domain of the CAR have also been shown to alter signaling formation with endogenous molecules, affecting cell activation and cytokine production [19]. Moreover, the intracellular signaling domain of the CAR has shown to be necessary for optimal CAR functioning and has been modified through different CAR generations to include one or more co-stimulatory domains, where newer generations combine potent and long-lasting lytic effects [20]. In addition to fine-tuning the CAR structure, further modifications can enable CAR-expressing cells to secrete cytokines, express costimulatory ligands, or secrete checkpoint-blocking scFvs have also shown to have increased *in vivo* persistence and better performance [21][22]. Multi-targeting CARs which can target more than one tumour associated antigen (TAA) to help battle the heterogenous tumour environment, have also been developed [23][24]. The heterogenous expression of TAAs in solid tumours greatly impacts the sensitivity of the CAR, especially for low-density antigens. In this regard, it is not only important to design an optimal CAR, but an ideal TAA should be targeted. An ideal TAA is; (1) overly expressed on tumour cells at high density; (2) expressed at low levels on normal cells to reduce off-target cytotoxicities; (3) has minimal shedding in the bloodstream; and has a key role in tumour development and progression [25]. In addition to high expression of TAAs, high CAR

density is also optimal for better antitumor responses. This can be accomplished via optimization of gene engineering techniques.

5.3.3 Genetic engineering methods

In this thesis, all studies accomplish gene engineering via lentiviral vectors to incorporate the gene of interest upstream of constitutive promoters. However, their semi-random integration presents translational limitations. Alternatively, clustered regularly interspaced short palindromic repeats (CRISPR) and CRISPR-associated protein 9 (Cas 9) systems enables precise gene integration into safe genomic harbours to overcome lentiviral vector limitations [26][27]. A well-established genomic safe harbor in the human genome is the adeno-associated virus site 1 (AAVS1) which supports long-term transgene expression [28]. Previously, our lab has built CRISPR/Cas9 technology to knock-in reporter genes (i.e. OATP1A1) in the AAVS1 site [27], supporting the safe integration of our reporter gene systems via safer genetic engineering.

5.3.4 Safety switches

Cell-based therapies hold great promise with potential for personalized medicine. In chapter 3 and 4, two cell-based therapies, derived from stem cells and natural killer (NK) cells, respectively, were used. Stem cells have a capacity to form teratomas as an indicator of their potency which implies a safety risk when transplanted into patients [29]. The risk of tumorigenicity limits their clinical applicability and effective strategies to remove the graft are needed. Likewise, the use of T-cell based therapies can result in severe toxicity and strategies to selectively destruct infused T-cells have been described [29]. A common safety switch mechanism employed to “turn off” cells involved the use of suicide genes. Suicide genes are genetic elements which cause cell death only when administered with a prodrug. Several suicide genes have been described, with the best characterized and most widely used being the Herpes simplex virus thymidine kinase (HSV-

tk)[29]. Once administered with its prodrug, ganciclovir, will phosphorylate nucleoside analogs inhibiting DNA synthesis and inducing apoptosis. Similarly, the Sodium Iodide Symporter (NIS) used in all studies of this thesis, is compatible with ^{131}I Iodine and can perform as a suicide gene. ^{131}I Iodine emits beta particles which can induce DNA damage and induce cellular apoptosis in NIS expressing cells. However, administration of ^{131}I Iodine would result in damage to all NIS expressing cells including the thyroid, stomach, salivary glands and mammary glands. Furthermore, endogenous NIS-expressing tissue have relatively higher NIS expression levels and thus more toxicity would be observed in these tissues relative to NIS transgenic cells [30]. Another common suicide gene is the human inducible caspase 9 (iCasp9), which will encode for a fusion protein that dimerizes upon introduction of a chemical inducer to trigger apoptosis of cells [31]. Other safety switch mechanisms which have slower, reversible, and modular control of cell therapies are also available. Dasatinib is a tyrosine kinase inhibitor which interferes with lymphocyte-specific tyrosine kinase, inhibiting signal from the intracellular CD3zeta, zeta chain of the TCR-associated protein, as well as costimulatory domains CD28 and 41BB of CARs [32]. Dasatinib induces an off state of lymphocytes halting proliferation, cytolytic effects, and cytokine production. The main advantage to Dasatinib is its ability to be titrated to achieve a partial or complete inhibition of cell function, and with discontinued use, the inhibitory effect can be reversed to resume therapeutic effect, which is advantageous for expensive therapies such as CAR T cell therapies.

5.3.5 Conclusion

In conclusion, the studies included in this thesis contribute to the field of multi-modal molecular imaging. Notably, we combined different imaging modalities to accomplish cell tracking for different applications. This work contributes to novel imaging approaches and techniques which

have utility in both preclinical settings (i.e. understanding fundamental and pathological mechanisms), and clinical applications (i.e. diagnostics, early detection, and assessing therapeutic response). Future work to further refine these approaches with respect to their safety and sensitivity, are in dire need to propel these strategies into the clinic.

5.4 References

- [1] R. Yahyapour *u.c.*, "Stem Cell Tracing Through MR Molecular Imaging", *Tissue Eng. Regen. Med.*, sēj. 15, nr. 3, lpp. 15, 2018, doi: 10.1007/s13770-017-0112-8.
- [2] J. M. Karp un G. S. Leng Teo, "Mesenchymal Stem Cell Homing: The Devil Is in the Details", *Cell Stem Cell*, sēj. 4, nr. 3, lpp. 206–216, mar. 2009, doi: 10.1016/J.STEM.2009.02.001.
- [3] W. Zhang *u.c.*, "Chimeric antigen receptor macrophage therapy for breast tumours mediated by targeting the tumour extracellular matrix", *Br. J. Cancer*, okt. 2019, doi: 10.1038/s41416-019-0578-3.
- [4] C. Gutierrez un R. Schiff, "HER2: Biology, detection, and clinical implications", *Arch. Pathol. Lab. Med.*, sēj. 135, nr. 1, lpp. 55–62, 2011, doi: 10.5858/2010-0454-rar.1.
- [5] H. D. Jones, "GENETIC MODIFICATION | Transformation, General Principles", B. B. T.-E. of A. P. S. Thomas, Red. Oxford: Elsevier, 2003, lpp. 377–382.
- [6] J. H. Kang *u.c.*, "Development of a Sodium/Iodide Symporter (NIS)-Transgenic Mouse for Imaging of Cardiomyocyte-Specific Reporter Gene Expression".
- [7] M. F. Kircher, S. S. Gambhir, un J. Grimm, "Noninvasive cell-tracking methods", *Nat. Rev. Clin. Oncol.*, sēj. 8, nr. 11, lpp. 677–688, 2011, doi: 10.1038/nrclinonc.2011.141.
- [8] M. Krishnan *u.c.*, "Effects of epigenetic modulation on reporter gene expression: implications for stem cell imaging.", *FASEB J. Off. Publ. Fed. Am. Soc. Exp. Biol.*, sēj. 20, nr. 1, lpp. 106–108, janv. 2006, doi: 10.1096/fj.05-4551fje.
- [9] M. C. Milone un U. O'Doherty, "Clinical use of lentiviral vectors", *Leukemia*, sēj. 32, nr. 7, lpp. 1529–1541, 2018, doi: 10.1038/s41375-018-0106-0.
- [10] R. Schlimgen *u.c.*, "Risks associated with lentiviral vector exposures and prevention strategies", *J. Occup. Environ. Med.*, sēj. 58, nr. 12, lpp. 1159–1166, 2016, doi: 10.1097/JOM.0000000000000879.

- [11] A. D. Sherry, P. Caravan, un R. E. Lenkinski, "Primer on gadolinium chemistry", no *Journal of Magnetic Resonance Imaging*, dec. 2009, sēj. 30, nr. 6, lpp. 1240–1248, doi: 10.1002/jmri.21966.
- [12] J. S. McDonald *u.c.*, "Acute adverse events following gadolinium-based contrast agent administration: A single-center retrospective study of 281 945 injections", *Radiology*, sēj. 292, nr. 3, lpp. 620–627, 2019, doi: 10.1148/radiol.2019182834.
- [13] J. W. M. Bulte, "In vivo MRI cell tracking: Clinical studies", *Am. J. Roentgenol.*, sēj. 193, nr. 2, lpp. 314–325, 2009, doi: 10.2214/AJR.09.3107.
- [14] J. O'Doherty *u.c.*, "¹⁸F-Tetrafluoroborate, a PET Probe for Imaging Sodium/Iodide Symporter Expression: Whole-Body Biodistribution, Safety, and Radiation Dosimetry in Thyroid Cancer Patients.", *J. Nucl. Med.*, sēj. 58, nr. 10, lpp. 1666–1671, 2017, doi: 10.2967/jnumed.117.192252.
- [15] L. Zhang, Y. Meng, X. Feng, un Z. Han, "CAR-NK cells for cancer immunotherapy: from bench to bedside", *Biomark. Res.*, sēj. 10, nr. 1, lpp. 1–19, 2022, doi: 10.1186/s40364-022-00364-6.
- [16] C. Jochems *u.c.*, "An NK cell line (haNK) expressing high levels of granzyme and engineered to express the high affinity CD16 allele", *Oncotarget*, sēj. 7, nr. 52, lpp. 86359–86373, 2016, doi: 10.18632/oncotarget.13411.
- [17] H. Klingemann, L. Boissel, un F. Toneguzzo, "Characterization of interleukin-15 gene-modified human natural killer cells: implications for adoptive cellular immunotherapy", *Frontiers in Immunology*, sēj. 7, nr. MAR. Frontiers Media S.A., mar. 14, 2016, doi: 10.3389/fimmu.2016.00091.
- [18] R. C. Larson un M. V. Maus, "Recent advances and discoveries in the mechanisms and functions of CAR T cells", *Nat. Rev. Cancer*, sēj. 21, nr. 3, lpp. 145–161, 2021, doi: 10.1038/s41568-020-00323-z.
- [19] R. C. Sterner un R. M. Sterner, "CAR-T cell therapy: current limitations and potential strategies", *Blood Cancer J.*, sēj. 11, nr. 4, 2021, doi: 10.1038/s41408-021-00459-7.

- [20] N. Albinger, J. Hartmann, un E. Ullrich, "Current status and perspective of CAR-T and CAR-NK cell therapy trials in Germany", *Gene Ther.* 2021 289, sēj. 28, nr. 9, lpp. 513–527, mar. 2021, doi: 10.1038/s41434-021-00246-w.
- [21] H. Dai, Y. Wang, X. Lu, un W. Han, "Chimeric antigen receptors modified T-cells for cancer therapy", *J. Natl. Cancer Inst.*, sēj. 108, nr. 7, 2016, doi: 10.1093/jnci/djv439.
- [22] M. M. D'Aloia, I. G. Zizzari, B. Sacchetti, L. Pierelli, un M. Alimandi, "CAR-T cells: the long and winding road to solid tumors", *Cell Death Dis.* 2018 93, sēj. 9, nr. 3, lpp. 1–12, febr. 2018, doi: 10.1038/s41419-018-0278-6.
- [23] M. Hegde *u.c.*, "Tandem CAR T cells targeting HER2 and IL13R α 2 mitigate tumor antigen escape", *J. Clin. Invest.*, sēj. 126, nr. 8, lpp. 3036–3052, aug. 2016, doi: 10.1172/JCI83416.
- [24] S. Guedan, M. Ruella, un C. H. June, "Emerging Cellular Therapies for Cancer", <https://doi.org/10.1146/annurev-immunol-042718-041407>, sēj. 37, lpp. 145–171, dec. 2018, doi: 10.1146/ANNUREV-IMMUNOL-042718-041407.
- [25] K. Watanabe, S. Kuramitsu, A. D. Posey, un C. H. June, "Expanding the therapeutic window for CAR T cell therapy in solid tumors: The knowns and unknowns of CAR T cell biology", *Front. Immunol.*, sēj. 9, nr. OCT, lpp. 1–12, 2018, doi: 10.3389/fimmu.2018.02486.
- [26] V. P. Dubois *u.c.*, "Safe Harbor Targeted CRISPR-Cas9 Tools for Molecular-Genetic Imaging of Cells in Living Subjects.", *Cris. J.*, sēj. 1, nr. 6, lpp. 440–449, dec. 2018, doi: 10.1089/crispr.2018.0030.
- [27] J. J. Kelly *u.c.*, "Safe harbor-targeted CRISPR-Cas9 homology-independent targeted integration for multimodality reporter gene-based cell tracking", *Sci. Adv.*, sēj. 7, nr. 4, lpp. eabc3791, janv. 2021, doi: 10.1126/sciadv.abc3791.
- [28] W. Y *u.c.*, "Genome editing of human embryonic stem cells and induced pluripotent stem cells with zinc finger nucleases for cellular imaging", *Circ. Res.*, sēj. 111, nr. 12, lpp. 1494–1503, dec. 2012, doi: 10.1161/CIRCRESAHA.112.274969.

- [29] J. Dahlke *u.c.*, "Efficient genetic safety switches for future application of ipsc-derived cell transplants", *J. Pers. Med.*, sēj. 11, nr. 6, 2021, doi: 10.3390/jpm11060565.
- [30] F. Galli, M. Varani, C. Lauri, G. G. Silveri, L. Onofrio, un A. Signore, "Immune cell labelling and tracking: implications for adoptive cell transfer therapies", *EJNMMI Radiopharm. Chem.*, sēj. 6, nr. 1, lpp. 7, dec. 2021, doi: 10.1186/s41181-020-00116-7.
- [31] V. Marin *u.c.*, "Comparison of different suicide-gene strategies for the safety improvement of genetically manipulated T cells.", *Hum. Gene Ther. Methods*, sēj. 23, nr. 6, lpp. 376–386, dec. 2012, doi: 10.1089/hgtb.2012.050.
- [32] Bryant Jeri L Boughter John D Gong Suzhen LeDoux Mark S Heck Detlef H, "The tyrosine kinase inhibitor dasatinib acts as a pharmacologic on/off switch for CAR-T cells", sēj. 32, nr. 1, lpp. 41–52, 2020, doi: 10.1126/scitranslmed.aau5907.The.

APPENDICES

Appendix A: Supplemental Figures

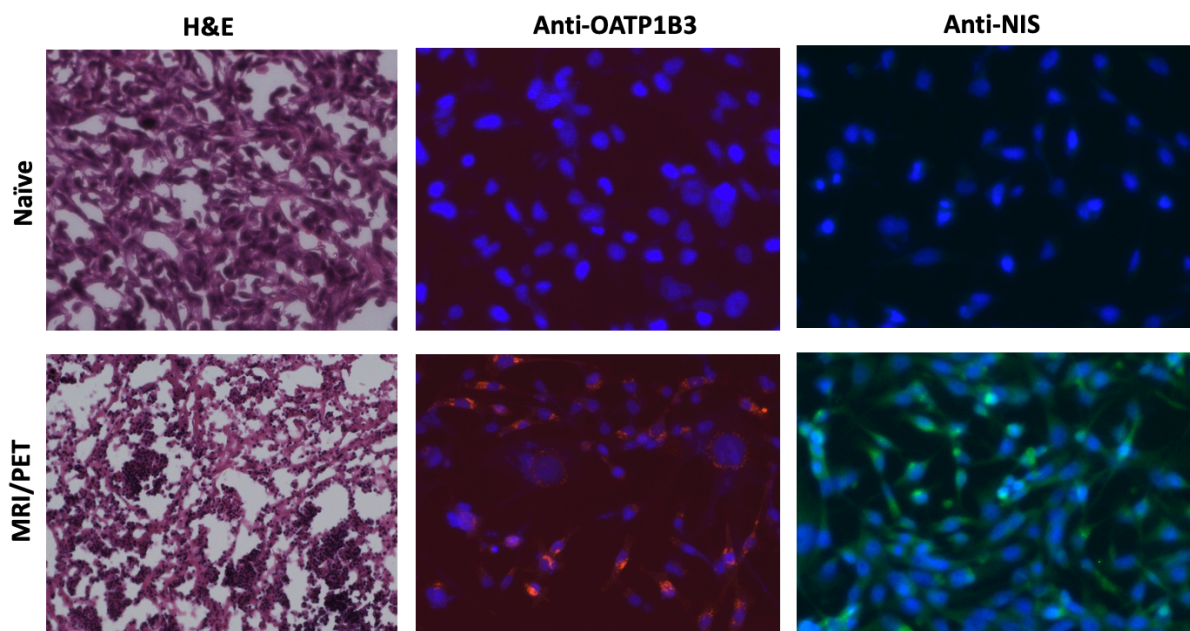


Figure 2.1: H&E, anti-OATP1B3 and anti-NIS staining of naïve (top) and MRI/PET (bottom) tumours. Anti-OATP1B3 showing transmembrane expression on MRI/PET cells. Anti-NIS staining showing NIS expression in MRI/PET cells.

Functionality test results for Gd-EOB-DTPA uptake

Appendices figure 2.2 shows Gd-EOB-DTPA uptake in naïve, NIS/zsG, OATP1B3/zsG and NIS/OATP1B3/zsG cells showing no significant difference between OATP1B3-only expressing cells and the dual NIS/OATP1B3-expressing cells. No significant difference was also noted between naïve and NIS-only expressing cells.

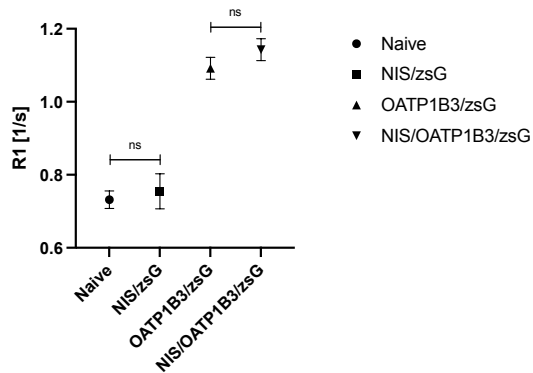


Figure 2.2: Gd-EOB-DTPA uptake in Naïve, NIS/zsG, OATP1B3/zsG and NIS/OATP1B3/zsG cells. No significant uptake between OATP1B3/zsG and NIS/OATP1B3/zsG cells is observed.

Gd-EOB-DTPA uptake in other organs

Appendices figure 2.3 shows uptake of the Gd-EOB-DTPA agent in other organs (liver, kidney, bladder, and muscle) with both methods of administration (IV and IP). Gd-EOB-DTPA uptake is initially highest in the kidneys and decreases over time, resulting in higher uptake in the bladder (a route of Gd-EOB-DTPA clearance). Stable signal intensity is observed in the muscle throughout both IV and IP dynamic studies. Gd-EOB-DTPA injected via IV shows peak liver signal at approximately three hours post injection, while in the IP route continues to increase due to the lag of the contrast agent reaching circulation.

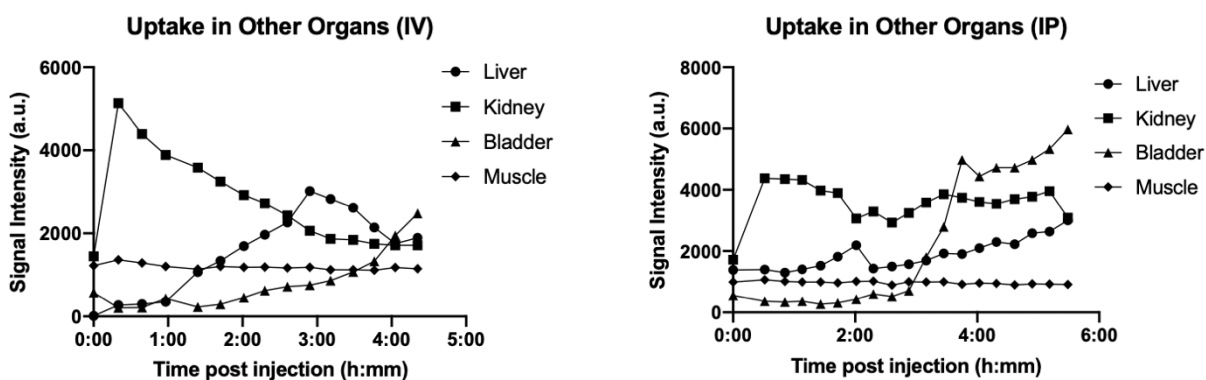


Figure 2.3: The kinetics of Gd-EOB-DTPA uptake in the muscle, liver, kidneys, and bladder with both IV and IP methods of administration.

Comparison of IV and IP at similar time points

Appendices figure 2.4 shows MR images at similar timepoints of the same mouse with IV (top) and IP (bottom) Gd-EOB-DTPA injections, using the same imaging parameters. Comparable contrast enhancement was observed between administration routes.

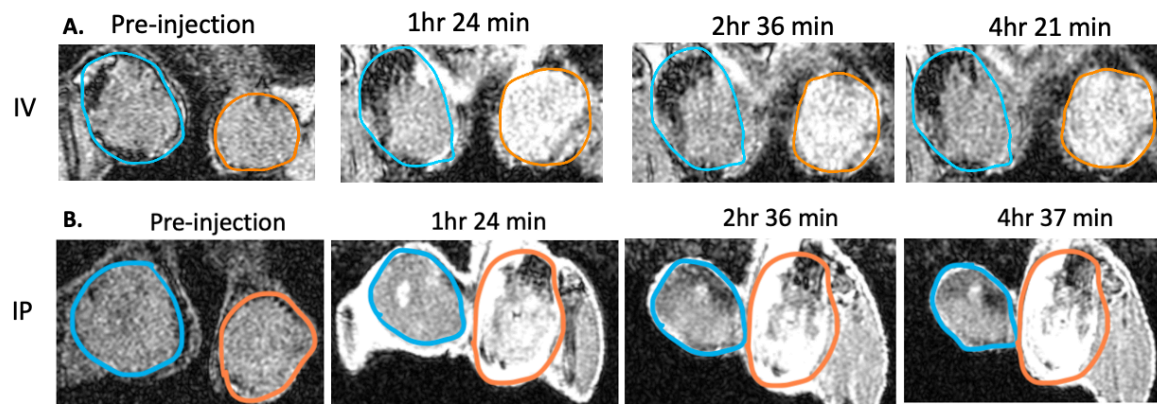


Figure 2.4: A direct comparison of coronal $T1$ -w MRI images of the same mouse with (A) IV and (B) IP administration of Gd-EOB-DTPA at similar time points post agent injection.

Differences in signal intensity between MRI/PET and naïve tumours in IV and IP injections

Appendices figure 2.5 shows the difference in signal intensity between the control and MRI/PET tumour divided by the average standard deviations, in the dynamic imaging for IV- and IP injections, showing the maximum difference in signal intensity at approximately 2.5 hours, for the IV injection, and at approximately 4.5 hours after the IP injection of Gd-EOB-DTPA.

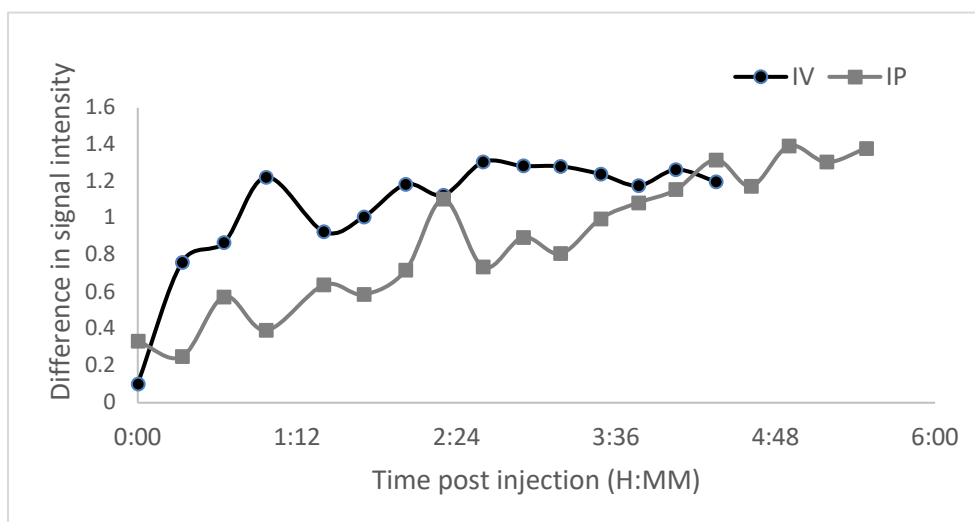


Figure 2.5: The difference in signal intensity (between MRI/PET and naïve tumour) plotted as a function of time, for both IV- and IP- GD-EOB-DTPA injection methods in the same mouse.

PET uptake in other organs

Appendices figure 2.6 shows the increasing SUV values in endogenous NIS-expressing tissue (thyroid and stomach) over the 40-minute dynamic PET imaging.

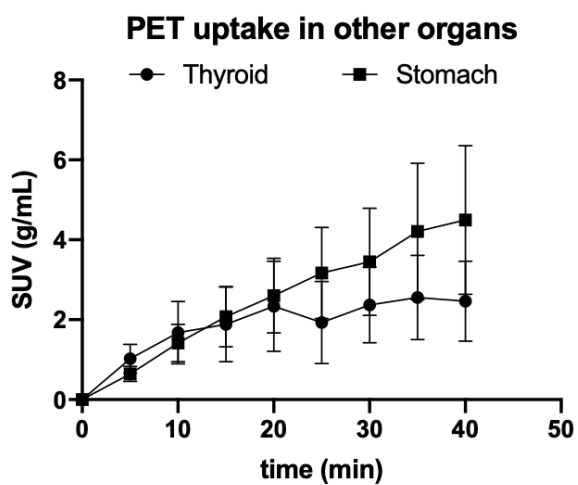


Figure 2.6: SUV (g/mL) of [^{18}F]TFB in tissue with endogenous NIS expression (thyroid and stomach).

PET SUV Effect Size:

Appendices figure 2.7 shows the effect size for the PET SUVs calculated as the difference between the MRI/PET and naïve tumour SUVs divided by the average standard deviations, showing the maximum effect size at 30 minutes.

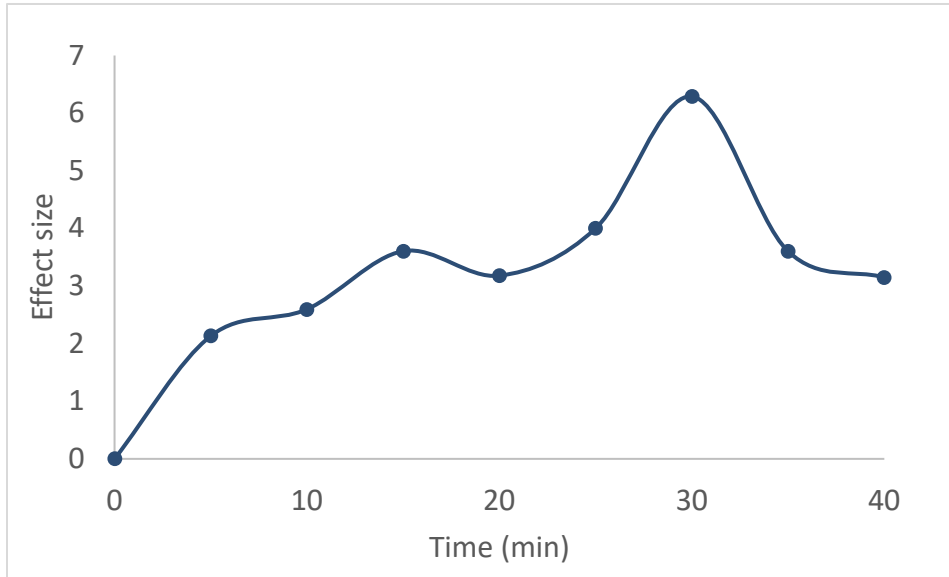


Figure 2.7: The effect size, measured as the difference between MRI/PET and naïve tumour SUVs divided by the average standard deviations is plotted.

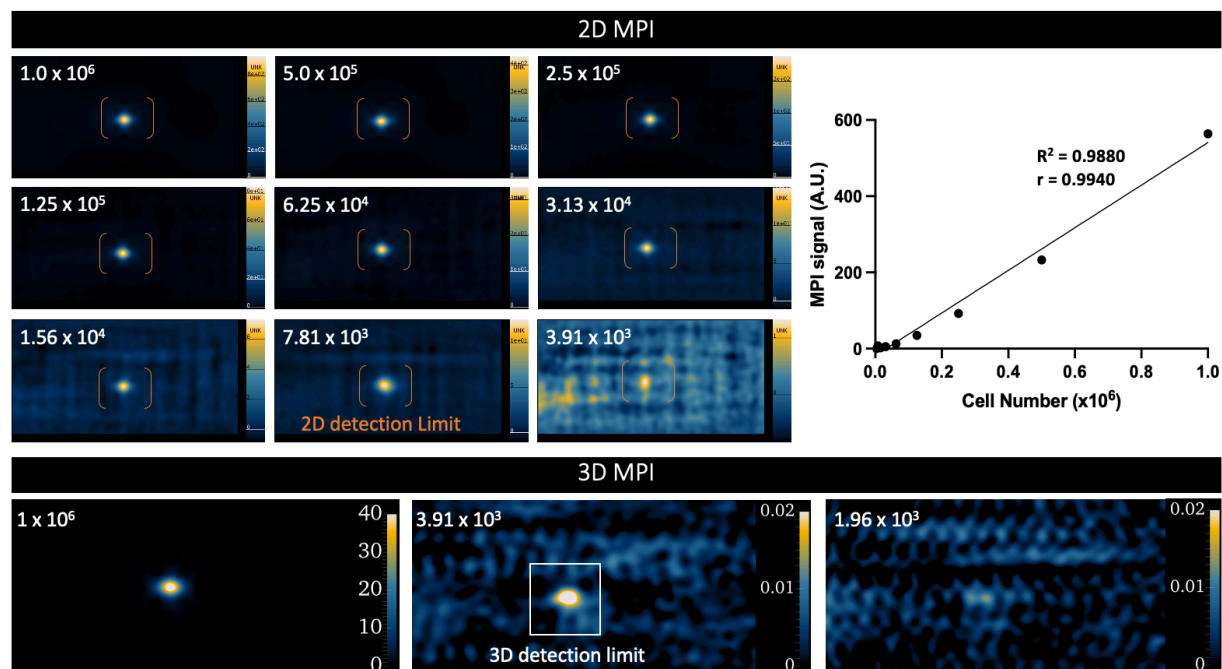
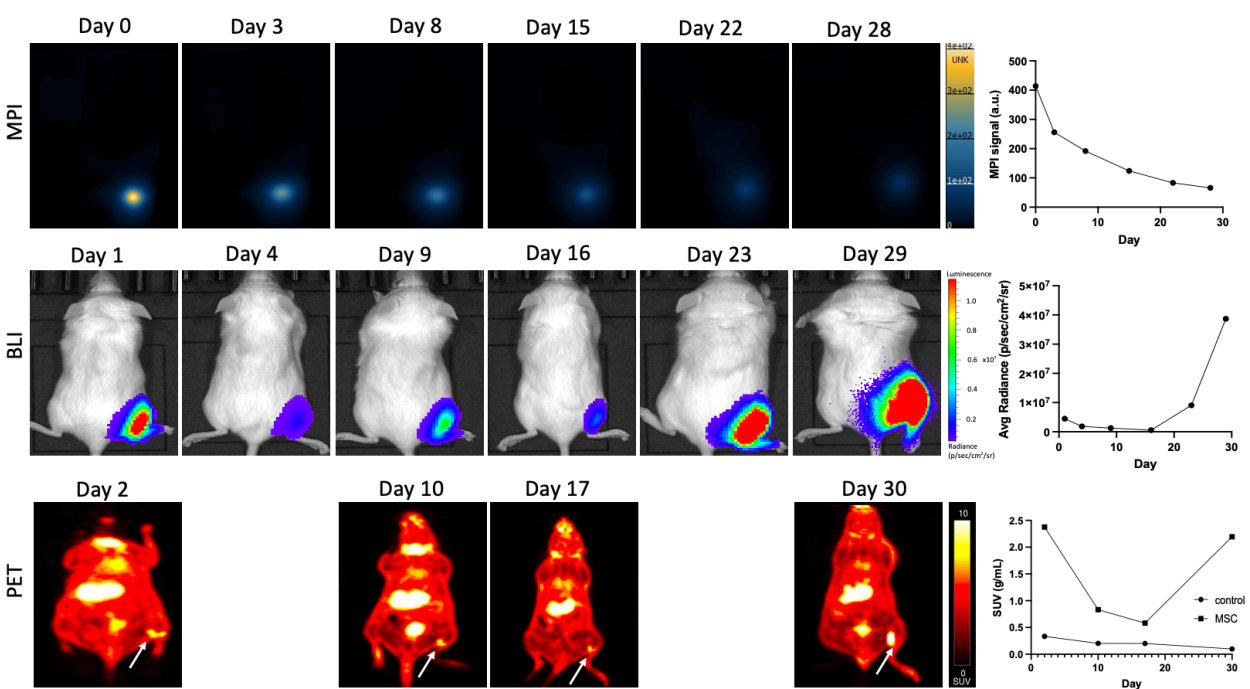
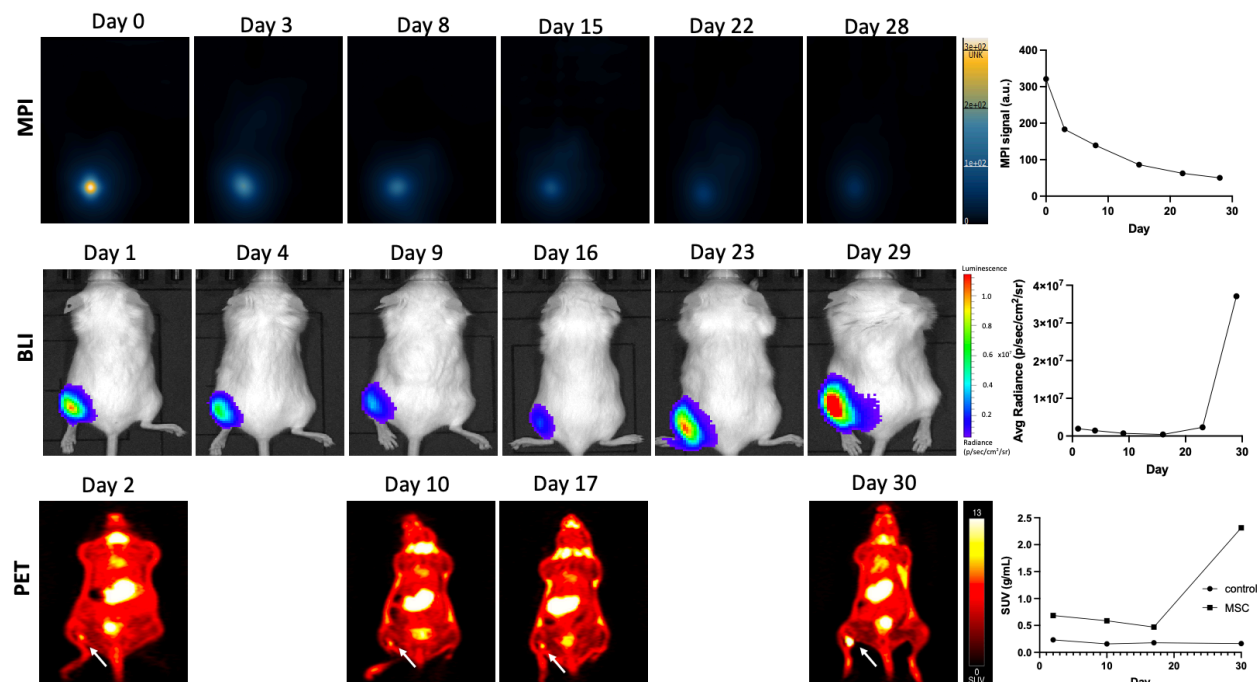


Figure 3.1: Calibration images for MPI quantification and detection threshold estimation of Synomag-D-labelled cells. In-vitro MPI detection of various numbers of Synomag-D-labelled MSCs (ranging from 10^6 -<4,000 cells), showing a 2D cellular detection limit of <8,000 cells, and a 3D detection limit of <4,000 cells. MPI signal was shown to strongly correlate with cell number ($R^2=0.9880$).

Appendices Figures 3.2 and 3.3 below show the in-vivo tracking of the tri-modally detectable MSCs in two additional mice. In-vivo detection of MSCs in the hind limb with MPI (top), BLI (middle) and PET (bottom) in each mouse over a 30-day period. MPI shows the brightest signal on day 0 and steadily decreases over time. BLI signal shows fluctuating radiance (initial signal reduction due to cell death), followed by an ultimate increase in BLI signal thereafter. PET SUV shows a similar pattern to BLI radiance at the comparable imaging timepoints of the engineered MSCs (arrows). Additional uptake also present in thyroid and stomach (organs with endogenous NIS expression).

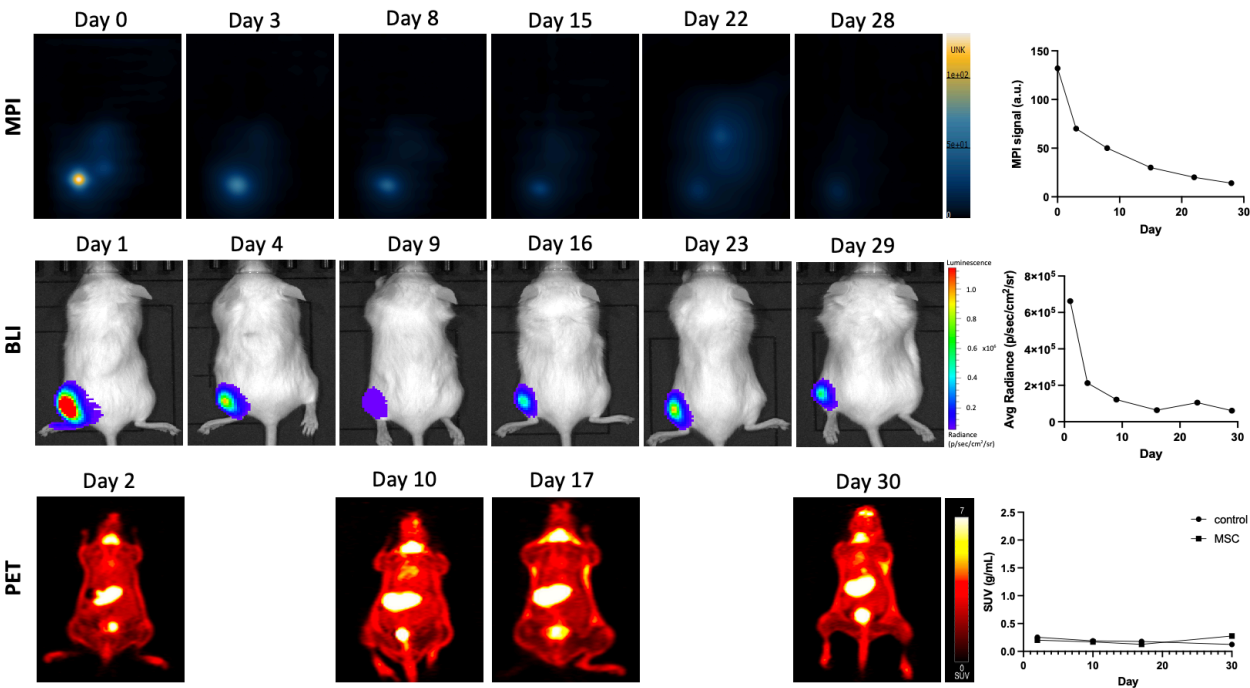


Appendices Figure 3.2: Mouse Identifier: Mouse 1

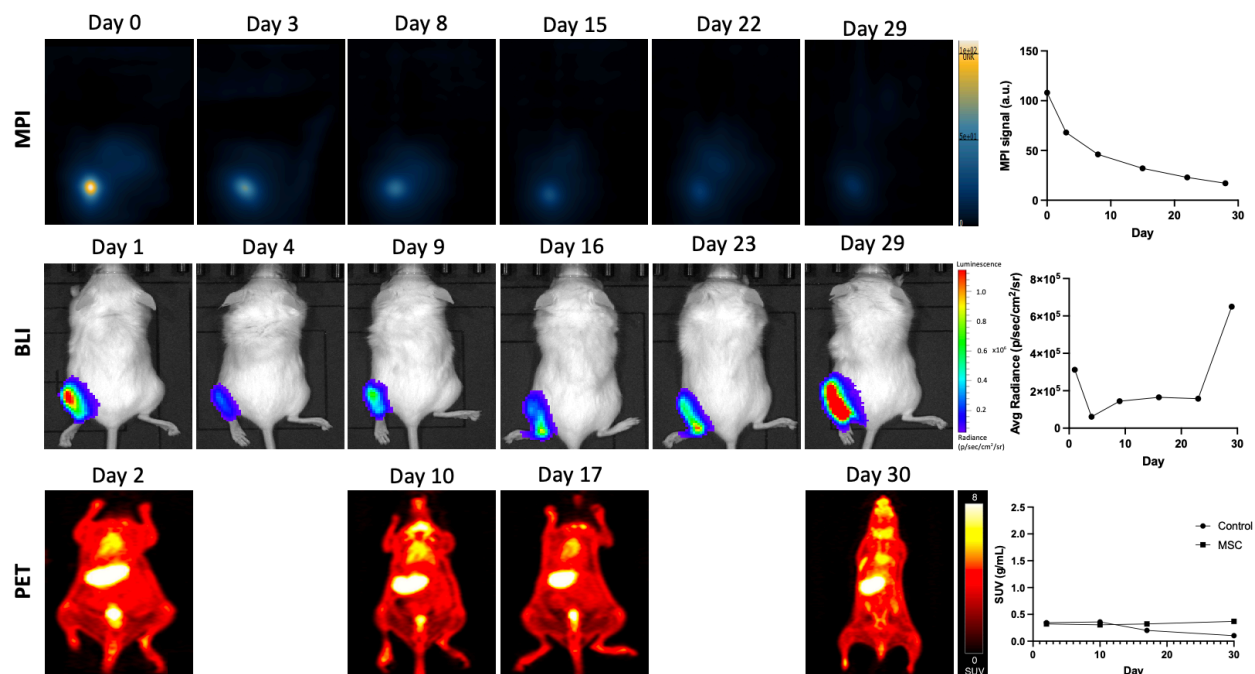


Appendices Figure 3.3: Mouse Identifier: Mouse 2

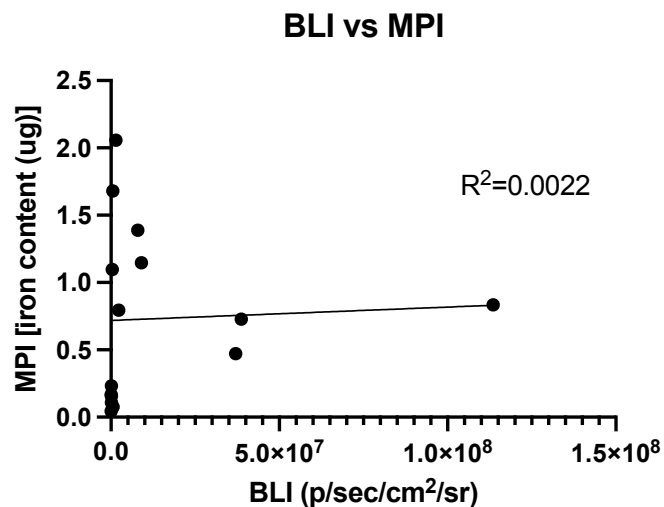
Appendices Figures 3.4 and 3.5 below show the in-vivo tracking of the MSCs in the remaining two mice. Imaging MSCs with MPI (top), BLI (middle) and PET (bottom) was performed. Similar to previous mice, MPI signal showed bright signal on day 0 that steadily decreased over time. BLI signal also allowed the detection of MSCs and showed fluctuating patterns but with overall lower radiance (on the order of 10^6 p/sec/cm²/sr for all imaging time points in comparison to the previous mice. This decrease in MSC signal can be mainly attributed to eventual cell death and clearance. Mice represented in figures 4 and 5 did not display detectable MSC PET signal.



Appendices Figure 3.4: Mouse Identifier: Mouse 3



Appendices Figure 3.5: Mouse Identifier: Mouse 5



Appendices Figure 3.6: Correlation plot between BLI signal and MPI signal at later imaging time points (day 10-30). Plot showing weak correlation between MPI signal and BLI radiance at late phase imaging ($R^2=0.0022$).

Appendices B: Permissions

Decision on submission to Nanoscale - NR-ART-07-2022-003684.R2

2+ 🔍 📧



Nanoscale (shared) <nanoscale@rsc.org>

To: Nourhan Shalaby

😊 ↩️ ⏪ ⏩ ⋮

Fri 2023-01-20 7:08 AM

Dear Nourhan,

Thank you for your email.

Permission is granted to reproduce your article in your thesis as long as it is fully acknowledged and includes a link back to the article on our website. Please ensure that all authors are aware that it is being included.

If you have any further questions, please let me know.

Best wishes,
Lee

Lee Colwill (they/them)
Publishing Assistant, Journals
Royal Society of Chemistry

www.rsc.org

The Royal Society of Chemistry

Advancing excellence, connecting chemical scientists and shaping the future of the chemical sciences for the benefit of humanity.

www.rsc.org



Dear Nourhan –

That should be no problem at all – when used for a thesis I think the citation covers it.

The very best of luck

Jason

...

Please note that this e-mail and any files transmitted from Memorial Sloan Kettering Cancer Center may be privileged, confidential, and protected from disclosure under applicable law. If the reader of this message is not the intended recipient, or an employee or agent responsible for delivering this message to the intended recipient, you are hereby notified that any reading, dissemination, distribution, copying, or other use of this communication or any of its attachments is strictly prohibited. If you have received this communication in error, please notify the sender immediately by replying to this message and deleting this message, any attachments, and all copies and backups from your computer.

Nourhan Shalaby

RESEARCH INTERESTS

Molecular and cellular imaging, positron emission tomography (PET), magnetic resonance imaging (MRI), magnetic particle imaging (MPI), reporter gene imaging, nuclear medicine, radiotherapy, cell therapy, theranostic, bioengineering, health informatics, data visualization, image analysis

EDUCATION

- September 2018 – August 2022 **Western University**, London, ON
Candidate for Doctor of Philosophy (PhD), Medical Biophysics
Cellular and Molecular Imaging Group
CAMPEP-accredited
Supervisor: Dr. John Ronald, PhD and Dr. Timothy Scholl, PhD
- September 2015 – April 2017 **McMaster University**, Hamilton, ON
Master of Science, Medical Physics
Supervisor: Dr. Michael Farquharson, PhD
- September 2009 – April 2012 **Western University**, London, ON
Bachelor of Science, Honors Medical Science and Biology

SCHOLARSHIPS AND AWARDS

- May 2020- April 2023 **NSERC Postgraduate Doctoral Scholarship**
Natural Science and Engineering Research Council
of Canada
- September 2019-2021 **Translational Breast Cancer PhD Research Scholarship**
Breast Cancer Society of Canada
- September 2018-2022 **Western Graduate Research Scholarship (\$4500/year CAD)**
Western University

September 2022 (\$200)	Women In Molecular Imaging Network (WIMIN) Scholar Award World Molecular Imaging Congress 2022
September 2022	Student Travel Stipend Award (\$500) World Molecular Imaging Congress 2022
June 2021 Research (\$4,500)	Drs. Madge and Charles Macklin Fellowship for Teaching and Department nomination Schulich School of Medicine and Dentistry
June 2019	Top Oral Presentation (\$200) Windsor Cancer Research Group
August 2016/2017 (nominee)	GSA Keith Leppmann Teaching Assistant Excellence Award McMaster University
September 2017	Distinguished TA Award of Science Faculty (\$400) McMaster University
May 2017	Dean's Award for Excellence in Communicating Graduate Research McMaster University
April 2017	First Place Graduate Award at Radiology Research Day (\$500) Radiology Research Day
February 2017	Three Minute Thesis winner (\$250) McMaster University

PUBLICATIONS

1. **Shalaby, N.**, Xia, Y., Kelly J., Sanchez, R., Martinez F., Fox M., Thiessen J., Hicks J, Scholl T.J., Ronald J.A. Non-invasive Imaging of a HER2-CAR NK-cell immunotherapy for Ovarian Cancer with Positron Emission Tomography (PET) and Bioluminescence Imaging (BLI). Status: In preparation

2. **Shalaby, N.**, Kelly J., Sehl, O.S., Gevaert, J.J., Fox M., Qi, Q., Foster, P.J., Thiessen J., Hicks J, Scholl T.J., Ronald J.A. Complementary short-term Magnetic Particle Imaging and long-term Positron Emission Tomography. *Nanoscale*. Published: January 2023
3. **Shalaby N.**, Kelly J., Martinez F., Fox M., Qi, Q., Thiessen J., Hicks J, Scholl T.J., Ronald J.A. (2021).
A Human-Derived Dual MRI/PET Reporter Gene System with High Translational Potential for Cell Tracking. *Molecular Imaging and Biology*. Published: January 2022
4. **Shalaby N.**, Dubois V.P., Ronald J.A. (2021). Molecular Imaging of Cellular Immunotherapies in Experimental and Therapeutic Settings. *Cancer Immunology, Immunotherapy*. Published: October 2021
5. **Shalaby N.**, Al-Ebraheem A.A., Le D., Fang Q., Farrell T., Lovrics P., Farquharson M. (2018). A Pilot Clinical Study of Time-Resolved Fluorescence (TRF) and Diffuse Reflectance Spectroscopy (DRS) between Fresh and Pre-frozen Breast Tissue. *Lasers in Surgery and Medicine*. Published: March 2018

THESIS/DISSERTATION

1. Fluorescence and Diffuse Reflectance Spectroscopy for Margin Analysis in Breast Cancer. (2017). McMaster University. Supervisor: Michael Farquharson

CONFERENCE PRESENTATIONS

International

1. **Shalaby N.**, Scholl T., Ronald, J.A., Dynamic Trimodal Imaging of Mesenchymal Stem Cells with Magnetic Particle Imaging, Positron Emission Tomography, and Bioluminescence Imaging. *World Molecular Imaging Congress 2022*. **Oral Presentation. Award Recipient.**
2. **Shalaby N.**, Scholl T., Ronald, J.A., Trimodal Tracking of Mesenchymal Stem cells (MSCs) with Magnetic Particle Imaging (MPI), Bioluminescence Imaging (BLI) and

- Positron Emission Tomography (PET). *European Molecular Imaging Meeting 2022*. March 2022. Thessaloniki, Greece. **Poster Presentation. Poster Award.**
3. **Shalaby N.**, Scholl T., Ronald, JA., The first clinically relevant PET and MRI reporter gene system for cell tracking. *World Molecular Imaging Congress 2021*. October 2021. Virtual. Oral Presentation
 4. Kelly, J., **Shalaby, N.**, Xia, Y., Francisco, MS., Hicks, J., Scholl, T., Ronald, JA. High Efficiency CRISPR Editing of Chimeric Antigen Receptor T (CAR-T) Cells Expressing Human-Derived MRI and PET Reporter Genes. *World Molecular Imaging Congress 2021*. October 2021. **Oral Presentation**

National

1. **Shalaby N.**, Scholl T., Ronald, JA., Development of a Human-Based Dual PET/MR Reporter Gene System for Cell Tracking. *Imaging Network of Ontario 2020*, Toronto, Canada. April 2021 **Oral Presentation**
2. **Shalaby N.**, Scholl T., Ronald, JA., The first clinically-relevant PET/MRI reporter gene system for cell tracking. *Ontario Institute for Cancer Research*. March 2021. **Oral Presentation**
3. **Shalaby N.**, Scholl T., Ronald, JA., A dual PET/MRI reporter gene system for cell tracking. *Windsor Cancer Research Group*, Windsor, Canada. February 2021. **Oral Presentation. First place oral presentation.**
4. **Shalaby N.**, Scholl T., Ronald, JA., A PET/MRI Reporter Gene System for Cell Tracking. *Imaging Network of Ontario, London*. March 2019. **Poster Presentation**

Regional

1. **Shalaby N.**, Scholl T., Ronald, JA., Towards translationally-relevant PET/MRI reporter gene imaging of cellular therapies. *Immuno-Oncology Symposium*, London, Canada. July 2020. **Oral Presentation**
2. **Shalaby N.**, Scholl T., Ronald, JA., PET/MRI Reporter Gene System for Cell Tracking. *Robarts Research Retreat*, Western University. June 2020. **Oral Presentation**

3. **Shalaby N.**, Farquharson M., Differentiation of Tumour and Normal Breast Tissue using an Optical Spectroscopy System. *Radiology Research Day*, Hamilton, Canada. April 2017. **Invited Talk**
4. **Shalaby N.**, Farquharson M., Breast Cancer Margin Analysis using Optical Spectroscopy. *3 Minute Thesis Competition*, Hamilton, Canada. February 2017. **Oral Presentation**
5. **Shalaby N.**, Farquharson M., Comparison Study of Time-Resolved Fluorescence (TRF) and Diffuse Reflectance Spectroscopy (DRS) between Fresh and Defrosted Breast Tissue. *McMaster Symposium on Physics in Medicine and Biology*, Hamilton, Canada. February 2016. **Invited Talk**

TEACHING EXPERIENCE

Course Instruction

January 2021 – April 2021	Curriculum Developer Fanshawe College, London, ON Department of Public Health and Safety
September 2019 – April 2021	Pre-Calculus Instructor Fanshawe College, London, ON Department of Applied Science and Technology
September 2019 – April 2021	Statistics Instructor Fanshawe College, London, ON Department of Public Health and Safety
September 2018 – April 2020	Physics Instructor Fanshawe College, London, ON Department of Applied Science and Technology

Graduate Teaching Assistantships (GTA)

January 2017– April 2017	Graduate Teaching Assistant , McMaster University, Hamilton, ON Faculty of Science, Department of Life Sciences Courses: Bio 3X03: Fundamental Concepts of Pharmacology Course Co-ordinator: Dr. Kim Dej, PhD
Sep. 2016– Dec. 2016	Graduate Teaching Assistant , McMaster University, Hamilton, ON Faculty of Science, Department of Medical Physics and Applied Radiation Sciences Courses: MedRad 1C03: Physics for Medical Radiation Science Course Co-ordinator: Dr. Jennifer Lemon, PhD
January 2016– April 2016	Graduate Teaching Assistant , McMaster University, Hamilton, ON Faculty of Science, Department of Medical Physics and Applied Radiation Sciences Courses: MedPhys 1E03: Physics in Medicine and Biology Course Co-ordinator: Dr. Michael Farquharson, PhD
Sep. 2015– Dec. 2015	Graduate Teaching Assistant , McMaster University, Hamilton, ON Faculty of Science, Department of Biology Courses: Bio 3A03: Laboratory Methods in Molecular Biology Course Co-ordinator: Dr. Rosa Da Silva, PhD

Guest Lectures

February 2022	Guest Lecturer , Western University, London, ON Department of Medical Biophysics (Schulich School of Medicine and Dentistry) Course: Medical Biophysics 9518B Lecture Title: Genome Editing using CRISPR
March 2021	Guest Lecturer , Western University, London, ON Department of Medical Biophysics (Schulich School of Medicine and Dentistry) Course: Medical Biophysics 2582B: Imaging in Biology Lecture Title: Molecular MRI and MR Reporter Genes

Teaching Certifications

February 2021	Western Certificate in University Teaching and Learning Centre for Teaching and Learning
---------------	--

Western University

January 2019

Advanced Teaching Program
Centre for Teaching and Learning
Western University

August 2019

Teaching Assistant Training Program
Centre for Teaching and Learning
Western University

Professional Development Workshops

June 2020

Western University
June 2020
Western University

**Teaching with a Trauma and Violence-Informed Approach,
Developing a Culturally Affirming Teaching Practice,**

June 2020
University

Leadership in Wellness: Mental Health Conversations, Western

June 2020

Western University
March 2020

**Leadership in Wellness: Cultivating Student Mental Health,
Gender Pronouns and Teaching,** Western University

March 2020

Self-Care Strategies for Graduate Students, Western University

March 2020

Self-Care Strategies for Teaching Assistants, Western University

December 2019

Teaching Mentor Program, Western University

October 2019

Western University
October 2019
Western University

**Universal Design for Inclusive Classrooms,
Preparing Your Teaching Dossier,**

MENTORSHIP EXPERIENCE

December 2019 – April 2020

Mentor, Western University, London, ON
Course: Medical Biophysics 3970Z
Independent Research Project
Student: Phillip Guevorguian
Project: *“Inversion Recovery for MRI reporter gene with the uptake of a Gadolinium-based MRI contrast agent”*

January 2017 – April 2017

Mentor, McMaster University, Hamilton, ON
Student: Julia Gevaert & Sarah Auberge

Project: “*Diffuse Reflectance and Scattering of human hair follicles using X-ray fluorescence*”

LEADERSHIP EXPERIENCE

June 2021-April 2022 University, ON	Medical Biophysics Teaching Initiative co-chair , Western
October 2019 – April 2020 London, ON	Social Media Liaison , Let’s Talk Science/Let’s Talk Cancer,
October 2019 Congress, Montreal	Organizing committee member , World Molecular International
September 2019 – April 2021 Teams, London, ON	Social Media Co-ordinator , Research Information Outreach
October 2019 – May 2020	Fundraising Volunteer , Breast Cancer Society of Canada

PROFESSIONAL MEMBERSHIPS

September 2022-Present Student	American Association of Physicists in Medicine ,
September 2021-Present Student	Canadian Organisation of Medical Physicists ,
September 2018-Present May 2019 - Present Trainee	Cellular Molecular Imaging Group , Trainee World Molecular International Congress ,

CERTIFICATIONS

February 2022	Radiological Society of North America: Ethics of Research
February 2022	Radiological Society of North America: Conflict of Interest
February 2022	Radiological Society of North America: Historical Evolution and Principles of Medical Professionalism (2021)
February 2022	Radiological Society of North America: Professionalism in Everyday Practice: A physician Charter
February 2021	Western Certificate for Graduate Teaching
February 2019	Radiation Safety Training

November 2019	Advanced Teaching Program
September 2018	Level 2 MRI Personnel
September 2018	Mouse Handling, IP, SQ, and IV Injection, and Gas Anesthesia
September 2018	X-ray Safety Training
September 2018	Biosafety Training
September 2018	Laboratory and Environmental Waste Management
September 2018	Comprehensive WHMIS Training